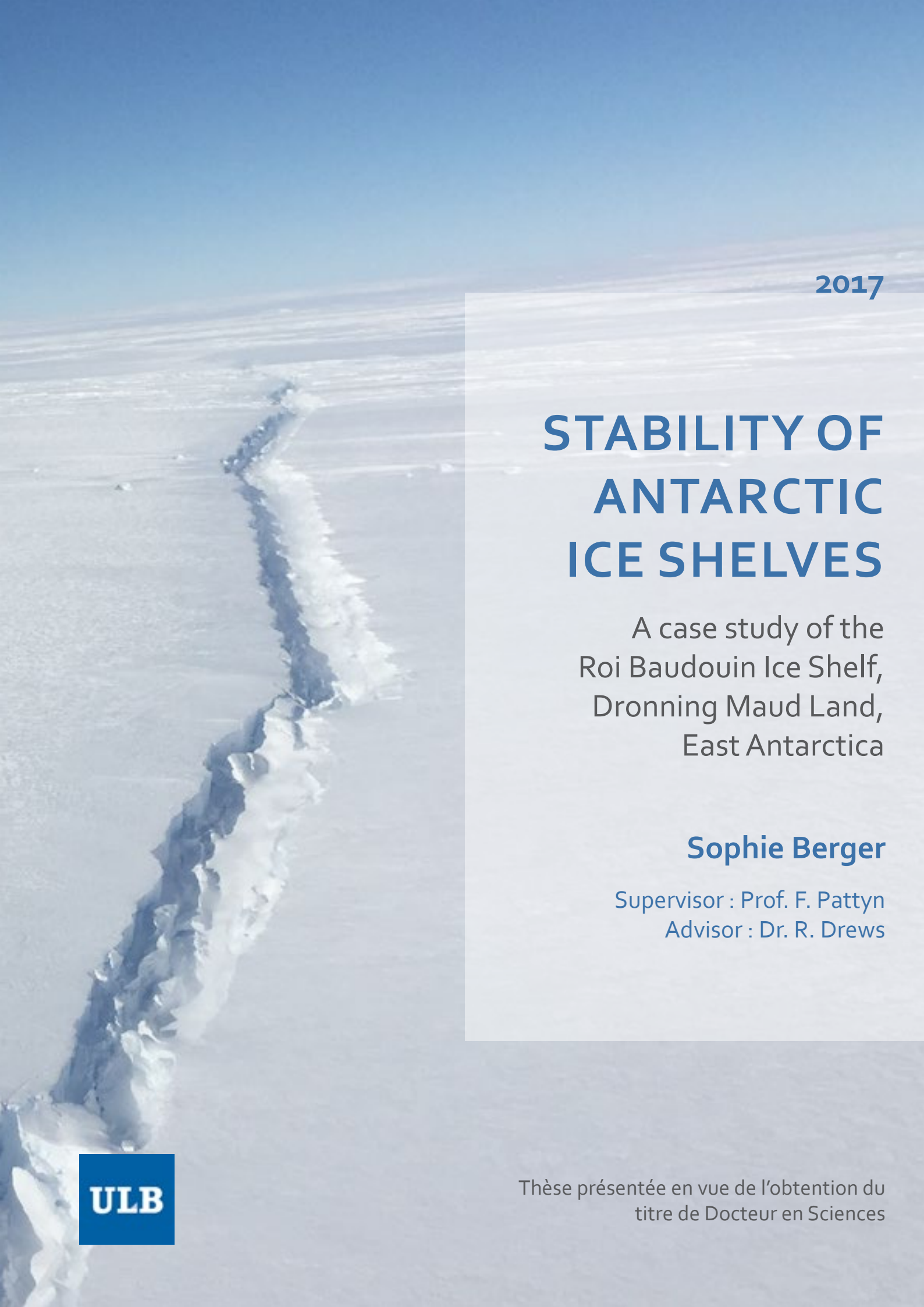

2017

STABILITY OF ANTARCTIC ICE SHELVES

A case study of the Roi Baudouin Ice Shelf, Dronning Maud Land, East Antarctica

Sophie Berger

Supervisor : Prof. F. Pattyn
Advisor : Dr. R. Drews

ULB

Thèse présentée en vue de l'obtention du titre de Docteur en Sciences

UNIVERSITÉ LIBRE DE BRUXELLES

FACULTÉ DES SCIENCES

Laboratoire de Glaciologie

Stability of Antarctic ice shelves

A case study of the Roi Baudouin Ice Shelf, Dronning Maud Land, East Antarctica

Author:
Sophie BERGER
Supervisor:
Frank PATTYN
Advisor:
Reinhard DREWS

Other jury members:
Jean-Louis TISON
Pierre-François COHEUR
Geir MOHOLDT

Thèse présentée en vue de l'obtention du titre de Docteur en Sciences

October 2017

Financial support was provided by the F.R.S-FNRS (the Belgian French-speaking fund for scientific research) through an *Aspirant* fellowship.

Design of the cover page by Florence Lepoudre. Cover picture : large rift on the Pine Island Ice Shelf, West Antarctica. The photo is flipped compared to the original shot, which was acquired on November 2016 during Operation IceBridge. Credit: NASA/Nathan Kurtz (licensed under CC BY 2.0 license).

Acknowledgments/Remerciements

I cannot believe that I am already at the very end of my PhD. Here, at the laboratoire de glaciologie, I have spent four years full of challenges and amazing opportunities. Four years that have forced me to constantly surpass myself to achieve things that I would have never imagined I would be capable of. Four years of laughter (and sometimes a little bit of cries) that will remain in any case a memorable experience. I would be lying if I were to tell that pursuing a PhD is always an easy ride. Luckily, I managed to make it to the finish line, thanks to the help and support of many individuals and groups.

First and foremost, I offer my sincerest gratitude to my supervisors Reinhard Drews and Frank Pattyn, who have always supported me throughout my PhD. I have immensely benefited from their different but complementary supervision styles. While Reinhard's selfless time, care and enthusiasm were sometimes all that kept me going, Frank's more sporadic but always timely and often humorous interventions provided completing backing. Both Reinhard and Frank have showed me that it is possible to be outstanding scientists, while remaining great people to work and spend time with. I have learned so much from both them : I know now how to avoid making "bubus", I can properly shake hands and I am aware that 42 is the answer to everything :-). One could simply not wish for better PhD supervisors.

I am grateful to the other members of my PhD jury – Jean-Louis Tison, Pierre-François Coheur and Geir Moholdt – for their time, insightful questions and constructive comments during the private defence. Thanks also to my supervisory committee (including Dominique Derauw) for their attention and advice.

I thank the F.R.S-FNRS, which made this thesis possible by providing financial support throughout my PhD through diverse funds (Apirant fellowship, operating credit and travel support). I am also grateful to the Antarctic Science Bursary for providing money to acquire satellite data. Belspo, InBev Baillet Latour Antarctica Fellowship, the Belgian Military, AntarctiQ and the International Polar Foundation all provided financial or logistical support to acquire ground data used in this thesis.

I would like to acknowledge that this thesis has been improved thanks to the combined efforts of my supervisors and co-authors, my thesis committee, Florence who made the cover and my proofreaders Loïc, Caroline and Marie.

S'ils sont bien sûr des conditions indispensables, un financement convenable, des données, une bonne supervision et un manuscrit sans fautes ne sont cependant pas des critères suffisants pour mener à l'aboutissement de son doctorat. Ainsi, je remercie chaleureusement tous les membres du laboratoire de glaciologie pour m'avoir permis de passer 4 années inoubliables. Il n'est pas donné à tout le monde de pouvoir évoluer dans un environnement qui soit à la fois agréable à vivre (et agrémenté de nombreux canelés (merci Jean-Louis) et autres délicieux cakes) tout en conservant une grande qualité scientifique. Quel honneur d'avoir fait partie d'un tel labo. Merci à Lionel d'avoir été un si bon ami, collaborateur et compagnon de bureau. Sa motivation, ses éclats de rire ainsi que son fond d'écran n'attendant qu'à être modifié me manquent déjà. Merci à Brice pour sa bonne humeur, sa disponibilité et son support, qu'il soit psychologique, scientifique ou technique. En 9 ans, il n'a jamais manqué à son rôle de "parrain géographe", même lorsqu'il s'agissait de trouver des gens à placer dans ses nombreuses commissions :-). Merci à Célia pour toutes les petites fêtes organisées chez elle et qui ont grandement contribué à la cohésion du labo. Merci à Caro pour son enthousiasme et son soutien moral inestimable lors du sprint final. La fameuse carioca de Denis et Mathieu, le "naked bar" et la rando à Chamonix resteront parmi mes meilleurs souvenirs de thèse. Merci à Momo, pour un lasemo qui restera inoubliable. Huge thanks to Ceri for having been my favourite (and never grumpy) English teachers for so long. Thanks to Sainan for making us win a pétanque. *Merci à Claire pour son aide inestimable, toujours prête à rendre service et à l'affût du petit détail pratique qui vous aurait si facilement échappé. Enfin merci à Claudia, dont je n'ai découvert le support sans faille*

que tardivement. Les nombreuses discussions autour d'une tasse de bon thé avec Marie, Fanny et tous les autres vont me manquer. Merci au pickwick qui, grâce à sa proximité avec l'ULB, nous a permis de joyeusement célébrer toutes sortes de réussites scientifiques et personnelles autour d'une bonne bière. Merci à Saida, Gauthier, Heiko, Boris, Jiayun and co pour la bonne ambiance qu'ils mettent/ont mis au labo et bonne chance à Violaine et Elise les dernières recrues du labo.

I am deeply grateful to Wolfgang Rack, the "ice nerds" (Chris, Michelle, Sandrine) and the rest of the people from Gateway Antarctica for their warm welcome. My research stay in New Zealand has been arguably the most enjoyable period of my PhD. Huge thanks also to all the friends I have met in New Zealand and who have made this few months so memorable.

I would like to acknowledge the great work of my co-authors and collaborators, it has been a pleasure to work with them all. *Je tiens d'ailleurs tout particulièrement à exprimer ma gratitude envers Jean-Jacques Derwael, celui que je surnomme "mon papy d'adoption" depuis presque 4 ans. Sa soif de connaissance, son enthousiasme, dévouement pour la recherche Antarctique Belge, sont exemplaires. Ce n'est pas donné à tout le monde de compter parmi ses co-auteurs celui qui a donné son nom au fameux "Derwael Ice Rise".*

I am grateful to the EGU, IGS, ESA and Karthaus organising committee for convening all sorts of scientific meetings ranging from workshops to symposia and summer schools. Such meetings have been fruitful far beyond any of my expectations on both scientific and personal levels.

For adding a lot of cryo-fun to my PhD, I would like to acknowledge my partners in blog crimes, in particular the ones with whom I have run the EGU cryoblog. Thanks Nanna for introducing me to the world of blogging and for teaching me how to find happy volunteers (**cough** corner victims :-D). I am also grateful to Emma and Clara for their enthusiasm and shared passion for puns, bullet points and unicorns of course. Thanks for taking care of everything to let me focus on writing up my thesis. My PhD would definitely not have been as fun without me spamming you so much.

If there is something that I didn't expect when I undertook this PhD, it is the fact that I would meet so many friendly people and make so many friends across Europe. I don't have the time to name them all but I would like to acknowledge a few. I am grateful to Kristof, Tiree and Delphine for all the good time in Frascati and for having remained *golden* friends since then. Thanks to T.J. for providing me the best way to cheer myself up : watching friends episodes. I thank Sarah for her crazy awesomeness and for not being judgemental when people sit on the floor like hobos! She literally enlightened my first EGU general assembly.

Merci aux habitants du "Sexy flat" – Tim, Pauline et François. Je ne sais pas comment comment j'aurais tenu le coup sans leur soutien psychologique (et alimentaire). Ils ont réussi à rendre la fin de ma thèse beaucoup moins pénible! Merci à mes amis géographes qui ont toujours été là pour moi, depuis mes débuts à l'ULB et qui, j'en suis certaine, le resteront encore pendant de nombreuses années. Merci à Caro et Aline d'être parties en vacances avec moi aux moments où j'en avais le plus besoin, c'est-à-dire juste avant de commencer à rédiger et après avoir déposé ce manuscrit. Merci à Flo et Lola de me laisser un but dans la vie un fois ma thèse finie : visiter Berlin :-). Merci à tous mes amis d'avoir veillé à mon équilibre mental pendant toutes ces années. Merci à petit Tom d'être si mignon, même quand il est malade et qu'il empêche sa marraine d'écrire ses remerciements de thèse. Enfin, je tiens à remercier mes beaux-parents, frères et parents pour leur support inconditionnel.

Abstract

The Antarctic ice sheet is increasingly contributing to sea-level rise because of accelerated mass losses at its floating extensions – its ice shelves. By floating while remaining attached to the grounded ice sheet, ice shelves buttress (i.e. restrain) the inland ice in such a way that ice-shelf losses lead to accelerated ice discharge in the ocean.

This thesis investigates the stability of Antarctic ice shelves – so crucial for the stability of the entire ice sheet – using the Roi Baudouin Ice Shelf (RBIS), Dronning Maud Land, East Antarctica, as a case study. The RBIS has remained relatively stable over the last millennia and presents various kilometre-scale features (pinning point, ice-shelf channels and englacial lakes) with potential impact on its present and future stability.

We first derive a horizontal velocity field, combining interferometry and speckle tracking with Synthetic Aperture Radar images from ERS 1/2 and ALOS-PALSAR, respectively. The resulting velocities and associated shear-strain rates represent the most detailed fields, currently available for the RBIS and clearly resolve small-scale features of the RBIS: significant slow-down and shearing are observed upstream of a small pinning point and ice converges at ice-shelf channels.

We then combine our flow field with high-resolution elevations from TanDEM-X to infer the Basal Mass Balance (BMB) of the RBIS. This method relies on mass conservation in a Lagrangian frame and enables us to finely detect spatial variability in the BMB. We show that the BMB of the RBIS varies substantially on sub-kilometre scales. Our technique is promising and could easily be applied more widely.

Additionally, the flow field is used to investigate how considering/ignoring small pinning points in observations (geometry and velocities) impacts data initialisation of poorly known parameters (e.g. basal friction, ice viscosity) and subsequent ice-sheet modelling with BISICLES. We find that overlooking the pinning point in the bathymetry leads to erroneous ice-shelf properties whereas accurately capturing the pinning point in velocities is of secondary importance.

Finally, before concluding the thesis, we discuss the stability of the RBIS and its neighbouring ice shelves. Most studies agree that the ice shelf has remained stable over the last decades to millennia and would likely remain so in the absence of external forcing. We however point out to three potential triggers of instabilities: (i) large quantities of surface meltwater are formed in the grounding zone and subsequently stored on the ice shelf, thereby providing fuel for hydrofracturing; (ii) ice-shelf channels are found to significantly incise the ice inland and (iii) a bathymetric trough beneath the RBIS forms a potential gateway for warm water intrusions the ice-shelf cavity, which could destabilise the ice shelf from below.

We close with a short essay on the importance of outreach, where we argue that public engagement as a scientist should be considered as being part of science and should be valued for its worth. This chapter gives us the opportunity to present outreach activities undertaken in the frame of this thesis. We conclude that, just like ice shelves control Antarctic ice losses, science communication determines transfers of scientific expertise to public knowledge.

Résumé

La calotte de glace en Antarctique contribue de plus en plus au niveau marin par pertes accélérées de masse à ses extensions flottantes : les plateformes de glace flottante ou *ice shelves*. Parce qu'ils flottent tout en restant rattachés au reste de la calotte, les ice shelves retiennent (*buttressent*) les flux de glace venant du continent. Ainsi, toute perte de masse des ice shelves entraine un perte de buttressing, elle-même menant à un décharge accrue de glace dans l'océan et donc à une augmentation du niveau marin.

Cette thèse explore la stabilité des ice shelves en Antarctique en utilisant le cas de l'ice shelf Roi Baudouin (ISRB), Dronning Maud Land, Antarctique de l'Est, qui est resté relativement stable au cours des derniers millénaires.

Nous commençons par dériver un champ de vitesse de l'ice shelf en combinant interferométrie et traçage du chatoiement (*speckle tracking*) sur des images de radar à synthèse d'ouverture, provenant des satellites ERS 1/2 et ALOS-PALSAR. Notre champ de vitesse montre l'impact de petites structures: la glace décélère et se cisaille en amont d'un point d'ancrage et le flux converge au niveau de chenaux.

Nous combinons ensuite le champ de vitesse à des élévations à haute résolution (TanDEM-X) afin de déduire le bilan de masse basal (BMB) de l'ice shelf. Cette méthode est basée sur le principe de conservation de masse dans un cadre Lagrangien et nous permet de détecter très finement la variabilité spatiale du BMB sous l'ISRB. Ainsi, nous montrons que le BMB varie fortement au niveau sub-kilométrique. Notre technique est prometteuse et pourrait être facilement appliquée plus largement, comme le montre des tests préliminaires.

Le champ de vitesse nous sert également à examiner comment la prise en compte/l'omission de petits points d'ancrage dans les observations (de vitesse et de géométrie) impacte l'initialisation des modèles d'écoulement de glace et leurs prédictions. Nous trouvons que, lorsque le point d'ancrage n'apparaît pas dans la bathymétrie, l'assimilation des données produit des propriétés de l'ice shelf qui sont erronées.

Une partie de la thèse est en enfin consacrée à discuter la stabilité de l'ISRB et de ses voisins. La plupart des études s'accordent à dire que l'ice shelf est resté stable sur les derniers millénaires et le restera probablement, en l'absence de forçage externe. Nous trouvons cependant 3 sources potentielles d'instabilité. Primo, une grande quantité d'eau de fonte est produite à la surface de la calotte, près de la ligne d'ancrage, ce qui pourrait favoriser de l'hydrofracturation. Secundo, les chenaux dans l'ice shelf commencent déjà à se former en amont de la ligne d'ancrage, ce qui pourrait contribuer à fragiliser la glace posée sur le continent. Tertio, une dépression bathymétrique sous l'ice shelf a le potentiel d'amener des eaux chaudes en dessous de ce dernier, ce qui pourrait augmenter fortement la fonte à la base de l'ice shelf et le déstabiliser.

Enfin, avant de conclure cette thèse, nous dissertons sur l'importance de la communication et vulgarisation scientifique. Cette partie est pour nous l'occasion de valoriser les activités de communication réalisées dans le cadre de cette thèse. Tout comme les ice shelves contrôlent les pertes de glace en Antarctique, la communication scientifique détermine les transferts de connaissances scientifiques vers le savoir public.

Contents

List of Figures

List of Boxes

Acronyms

ASW	Antarctic Surface Water
ACC	Antarctic Circumpolar Current; *Eastward flowing oceanic current around Antarctica*
AIS	Antarctic Ice Sheet
ALOS	Advanced Land Observing System; *satellite*
BMB	Basal Mass Malance
CDW	Circumpolar Deep Water; *Relatively warm and saline water mass in the Southern ocean*
DEM	Digital Elevation Model
DInSAR	Differential Interferometric Synthetic Aperture Radar
DIR	Derwael Ice Rise
DML	Dronning Maud Land; *region in East Antarctica*
DSW	Dense Shelf Water
EAIS	East Antarctic Ice Sheet
EGU	European Geoscience Union
ERG	East Ragnhild Glacier
ERS 1/2	European Remote Sensing; *2 satellite in tandem*
ESA	European Space Agency
ESW	Eastern Shelf Water
FAC	Firn-Air Content
FDM	Firn Density Model
GCP	Ground Control Point
GIS	Geographic Information System
GNSS	Global Navigation Satellite System; *generic term for positioning systems like GPS*
GPS	Global Positioning System

GRACE Gravity and Recovery And Climate Experiment; *satellite mission (2 satellites in tandem)*

InSAR Interferometric Synthetic Aperture Radar

IPCC Intergovernmental Panel on Climate Change

LBMB Lagrangian basal mass balance

LOS Line of Sight

MB Mass Balance

mCDW modified Circumpolar Deep Water

MICI Marine Ice Cliff Instability

MISI Marine Ice Sheet Instability

OLI Operational Land Imager; *sensor on-board satellite Landsat-8*

PALSAR Phase Array Type L-band Synthetic Aperture Radar; *SAR sensor on-board satellite ALOS*

QDInSAR Quadruple difference interferometric synthetic aperture radar; *Technique to locate grounding lines*

RACMO Regional Atmospheric Climate MOdel

Radar RAdio Detection And Ranging

RAMP Radarsat Antarctic Mapping Project

RBIS Roi Baudouin Ice shelf

SAR Synthetic Aperture Radar

SLC Single Look Complex

SMB Surface Mass Balance

SNR Signal-to-Noise Ratio

TanDEM-X TerraSAR-X add-on for Digital Elevation Measurement; *Satellite mission*

WAIS West Antarctic Ice Sheet

WP Western Promontory

WRG West Ragnhild Glacier; *Ice stream feeding the Roi Baudouin Ice Shelf*

WDW Warm Deep Water; *Relatively warm and saline water mass that can be seen as a variant of the Circumpolar Deep Water*

List of Publications

Published in peer reviewed journals

- **Berger, S.**, Favier, L., Drews, R., Derwael, J. J., and Pattyn, F. (2016). The control of an uncharted pinning point on the flow of an Antarctic ice shelf. *Journal of Glaciology*, 62(231):37–45

- Drews, R., Pattyn, F., Hewitt, I. J., Ng, F. S. L., **Berger, S.**, Matsuoka, K., Helm, V., Bergeot, N., Favier, L., and Neckel, N. (2017). Actively evolving subglacial conduits and eskers initiate ice shelf channels at an Antarctic grounding line. *Nature Communications*, 8:15228

- Favier, L., Pattyn, F., **Berger, S.**, and Drews, R. (2016). Dynamic influence of pinning points on marine ice-sheet stability: a numerical study in Dronning Maud Land, East Antarctica. *The Cryosphere*, 10(6):2623–2635

- Lenaerts, J. T. M., Lhermitte, S., Drews, R., Ligtenberg, S. R. M., **Berger, S.**, Helm, V., Smeets, C. J. P. P., van den Broeke, M. R., van de Berg, W. J., van Meijgaard, E., Eijkelboom, M., Eisen, O., and Pattyn, F. (2017). Meltwater produced by wind–albedo interaction stored in an East Antarctic ice shelf. *Nature Climate Change*, 7(1):58–62

Accepted for publication

- **Berger, S.**, Drews, R., Helm, V., Sun, S., and Pattyn, F.(2017). Detecting high spatial variability of ice-shelf basal mass balance (Roi Baudouin ice shelf, Antarctica), *The Cryosphere Discussions*, doi:10.5194/tc-2017-41, in press.

In preparation

- Sun, S., Drews, R., Pattyn, F., **Berger, S.** and Nicholls, K. (2017). Basal melt rate variability across ice-shelf channels in Dronning Maud Land, Antarctica
  in preparation for *Journal of Glaciology*

- Neckel et al.

Chapter 1

Introduction

1.1 Rationale

Antarctica is a land of superlatives: it is the most remote continent, the coldest place on Earth, the driest desert... But, more importantly, its ice sheet is the largest, yet most uncertain potential contributor to future sea-level rise, in response to on-going climate change.

Antarctica and future sea-level rise

In its latest assessment report (AR5, Church et al., 2013), the Intergovernmental Panel on Climate Change (IPCC) concluded that the global sea level was unlikely to rise by more than one meter by 2100. Less than one seventh of the projected sea-level rise was then attributed to the Antarctic ice sheet, which presented nevertheless the highest likely range, spanning[1] from -8 to 16 cm (Fig. 1.1).

Those projections however sharply contrast with geologic records, which indicate (i) that sea level of previous warm periods was several meters higher than today (Dutton et al., 2015) and (ii) that rapid phases of sea-level rise occurred in the past. For instance, sea-level reconstruction of the last deglaciation highlights a period of rapid global sea-level rise – meltwater pulse 1A (14,500 years ago) – during which sea-level jumped by 14-16 m in ~350 years (Deschamps et al., 2012). During meltwater pulse 1A, sea level rose by 46 mm a^{-1}, which contrasts with the current rate of 3 mm a^{-1} (Church et al., 2013) and implies rapid ice-sheet collapses – including a possible substantial contribution from Antarctica (Deschamps et al., 2012, Weber et al., 2014). Geologic archives therefore suggest that the Antarctic ice sheet responds quicker to climate change than predicted in the latest IPCC report.

If, back in 2013, the IPCC admitted that abrupt and irreversible collapses of marine sectors in Antarctica – known as marine ice sheet instability or MISI – could raise the sea level beyond the likely range (Church et al., 2013), lacking evidence and understanding of those processes prevented their incorporation in sea-level projections. Both observations and modelling have since then suggested that the Amundsen Sea sector (the Antarctic region currently losing the most ice (Shepherd et al., 2012)) is undergoing a MISI triggered by ocean melting (Rignot et al., 2014, Favier et al., 2014, Joughin et al., 2014). Similarly, more recent studies have found that many other marine sectors in Antarctica are susceptible to destabilise over the coming centuries (e.g. Mengel and Levermann, 2014, Ritz et al., 2015).

Using a processed-based statistical approach, Ritz et al. (2015) assessed the uncertainties associated with destabilisation of marine sectors in Antarctica. They found a likely contribution of the ice sheet of 10 cm by 2100 with an upper bound uncertainty range of 30 cm (95% probability). Their results therefore discredit the higher values found in previous work (e.g. Bindschadler

[1] In 2100, compared to 1986-2005, across all scenarios and within the 2/3 likely range.

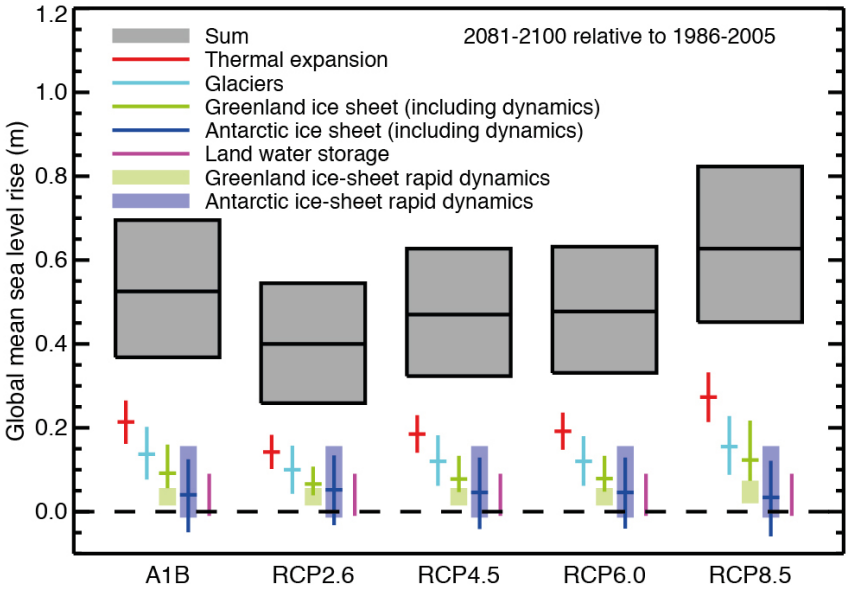

Figure 1.1: Sea-level rise projections with likely range and median values (67 % probability), under different scenarios (RCP–Representative Concentration Pathways). Rapid dynamics Credit: Fig. 13.10 from Church et al. (2013).

et al., 2013, Nowicki et al., 2013, Bamber and Aspinall, 2013). In other words, Ritz et al. (2015) managed to effectively reduce sea-level rise uncertainties associated with Antarctica. They concluded that, to be reliable, higher predictions and uncertainties in Antarctic sea-level rise would require new mechanisms and MISI triggers.

One year later however, DeConto and Pollard (2016) re-opened the debate with higher and more uncertain predictions of Antarctic ice losses (Le Bars et al., 2017). By including new physical processes and instability (cliff instability) in their model, they found the Antarctic ice sheet to be much more sensitive to atmospheric warming, predicting sea-level contribution greater than 1 m by 2100 in high-emission scenarios (RCP 8.5). Although their model correctly reproduces Antarctic losses during past warm periods, some of the mechanisms proposed by DeConto and Pollard (2016) have yet to be verified and refined. As a consequence, it remains to be seen whether this study is a precursor that forewarns higher sea-level projections from Antarctica, or an outlier that will soon be disproven.

Combining observation and modelling

Increasingly available satellite observations have played a crucial role in recent improvements in both our knowledge and our understanding of ice-sheet dynamics. On the one hand, observations showing higher Antarctic mass loss than anticipated, have forced ice-sheet modellers to adapt in order to reproduce and explain the observed changes. Observations are therefore critical to evaluating ice-sheet models by testing their adequacy and quantifying their uncertainties (e.g. Ritz et al., 2015). On the other hand, increasingly available observations better constraint ice-sheet models (initialisation), providing opportunities for better data assimilation, ultimately improving model performances and predictions.

Deriving reliable observations and combining them with modelling are therefore essential to better understand and predict Antarctic contribution to future sea-level rise, ultimately reducing and quantifying uncertainties associated with it. Both concepts are at the core of this thesis. In the rest of this chapter, we lay out the bases for understanding the stability of the Antarctic ice sheet (Section 1.2), we then present our area of interest (Section 1.3) and finish by outlining the rest of the thesis (Section 1.4).

1.2 Importance of ice shelves in the Antarctic Mass Balance

In this section, we first introduce the basic principles that are necessary to understand the mass balance of the Antarctic ice sheet (Section 1.2.1) and its critical ice shelves (1.2.2). We then present ice-atmosphere (Section 1.2.3) and ice-ocean (Section 1.2.4) interactions and close the section with a brief presentation of instabilities currently threatening the ice sheet (Section 1.2.5).

1.2.1 Antarctic Mass balance – background information

The Antarctic ice sheet

The Antarctic ice sheet (AIS) is a perennial mass of (freshwater-)ice and snow that covers an area of 13.9 million km^2, representing 8% of the global land surface (Fretwell et al., 2013, Vaughan et al., 2013). With a mean thickness of ~2000 m, the AIS contains enough ice to raise the global sea level by 58 m (Fretwell et al., 2013).

Schematically (Fig. 1.2), ice in Antarctica originates from gradual compaction of snowfalls in the ice-sheet's interior. Driven by gravity, ice then slowly flows seawards. As it approaches the coast, ice progressively accelerates and collects in fast *ice streams* (Fig. 1.5a), until it reaches the ocean, where it starts to float and form the *ice shelves*. Unlike the Greenland ice sheet – where meltwater runoff is significant – the AIS virtually loses all its ice in contact with the ocean either by melting beneath the ice shelves or by iceberg calving (i.e. breaking off). Ice shelves surround three-quarters of the AIS (Bindschadler et al., 2011a) and connect to the grounded ice sheet with the *grounding line*, the boundary where ice becomes afloat.

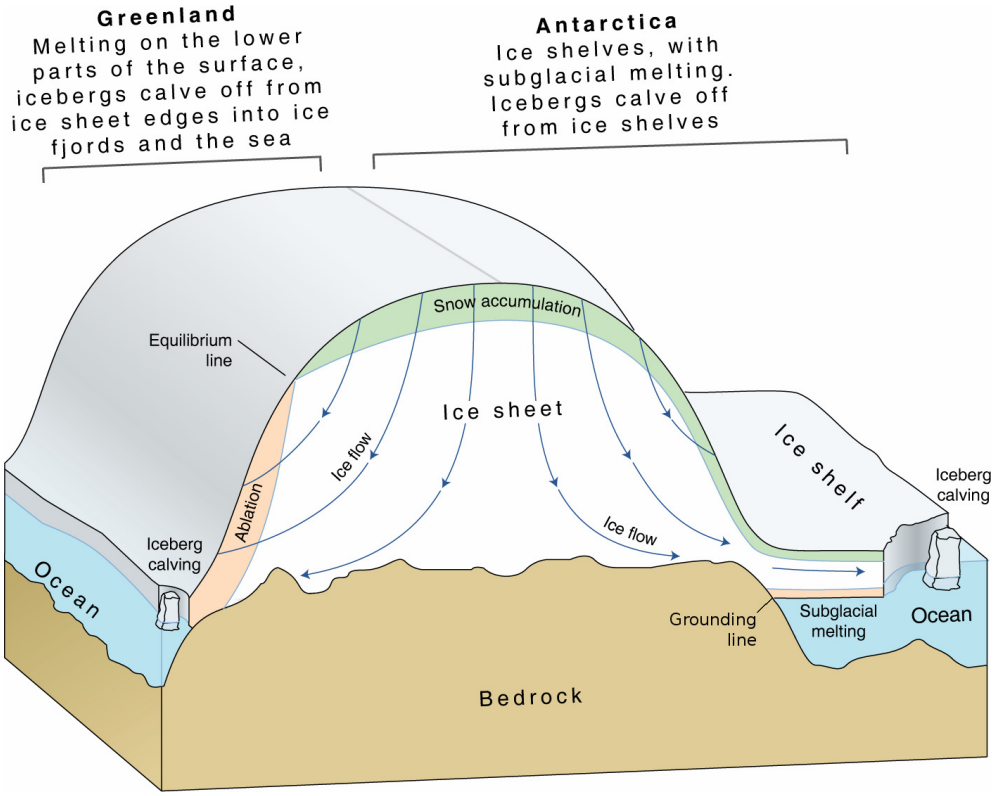

Figure 1.2: Schematic ice sheet illustrating how an ice sheet gains and loses mass and flows towards the coast to form ice shelves. Credit: Hugo Ahlenius, UNEP/GRID-Arendal.

The mass balance

The mass balance measures the health status of an ice sheet. It represents the net balance (i.e. difference) between mass gains and losses on the entire ice sheet. A negative mass balance indicates that the ice sheet loses mass and therefore shrinks. Despite large uncertainties (Hanna et al., 2013), most of recent estimates, from various techniques and data, agree that the AIS has been losing mass for the last two decades at an accelerating pace (Fig. 1.3e and Martín-Español et al., 2016, Scambos and Shuman, 2016, Harig and Simons, 2015, McMillan et al., 2014, Velicogna et al., 2014, Williams et al., 2014, Schrama et al., 2014, Shepherd et al., 2012).

In practice, Antarctic-wide mass balance (MB) is determined as the difference between the surface mass balance (SMB), the net ice accumulation at the ice-sheet's surface, and the solid ice discharge to the ocean (D):

$$MB = SMB - D \tag{1.1}$$

The surface mass balance results from atmospheric processes. In Antarctica, it is positive and driven by snowfalls. Surface mass balance and ice-atmosphere interactions are further discussed in Section 1.2.3.

Its positive surface mass balance implies the AIS loses most of its ice in contact with the ocean (by basal melting or calving). However, ice losses appear in Eq. (1.1) as discharge at the grounding line, with no discrimination between basal melting and calving. This is because ice raises the sea level when it becomes afloat rather than when it is removed from the ice shelf. By analogy, if you have a glass filled to the brim with water and you would like to add an ice cube to it, the glass will overflow when the ice cube is added rather than when it melts. Before discovering in the next section (Section 1.2.2), why ice-shelf losses indirectly increase the sea level, let us first quickly look into spatial and temporal variability of the Antarctic mass balance.

Regional disparities and temporal variability of the mass balance

If Antarctica as a whole is losing ice at an accelerating rate, the continental mass balance conceals however significant regional disparities and high inter-annual variations (Fig. 1.3). The overall negative mass balance is largely driven by mass losses in the Amundsen Sea sector, West Antarctica (Fig. 1.3-map and Fig. 1.5 for place names). Losses in this region are attributed to persistent melting below ice shelves (Depoorter et al., 2013, Rignot et al., 2013), which is thought to have destabilised Pine Island and Thwaites glaciers (Favier et al., 2014, Rignot et al., 2014, Joughin et al., 2014). All the other coastal regions of Antarctica lose mass, with the notable exception of Dronning Maud Land, East Antarctica, where gains are attributed to increasing snowfalls (Boening et al., 2012, Lenaerts et al., 2013, Philippe et al., 2016). Large inter-annual variations are mainly driven by variability in the surface mass balance.

1.2.2 Ice shelves: the gatekeepers of the Antarctic ice sheet

By floating while remaining attached to grounded ice, ice shelves *buttress* – i.e. restrain – the ice from upstream (Dupont and Alley, 2005, Gagliardini et al., 2010, Fürst et al., 2016, Fig. 1.5b). The buttressing strength exerted on the inland ice-flow comes from lateral friction with ice-shelf embayments and/or basal drag by local sea-mounts – i.e. pinning points (Fig. 1.4) – that locally re-attach the ice shelf from below (Goldberg et al., 2009, Favier et al., 2012). Pinning points are ubiquitous in Antarctica and are called *ice rises*, when their ice flow is totally disconnected from the surrounding ice shelf, and *ice rumples* when ice dynamics are controlled by the surrounding shelf (Matsuoka et al., 2015).

Ice-shelf thinning (Pritchard et al., 2012, Paolo et al., 2015) or disintegration (Berthier et al., 2012) have dramatically decreased their volume over the last decades (Fig. 1.5b), reducing the buttressing they exert on the inland flow. In reaction, their tributary glaciers have sped up, their

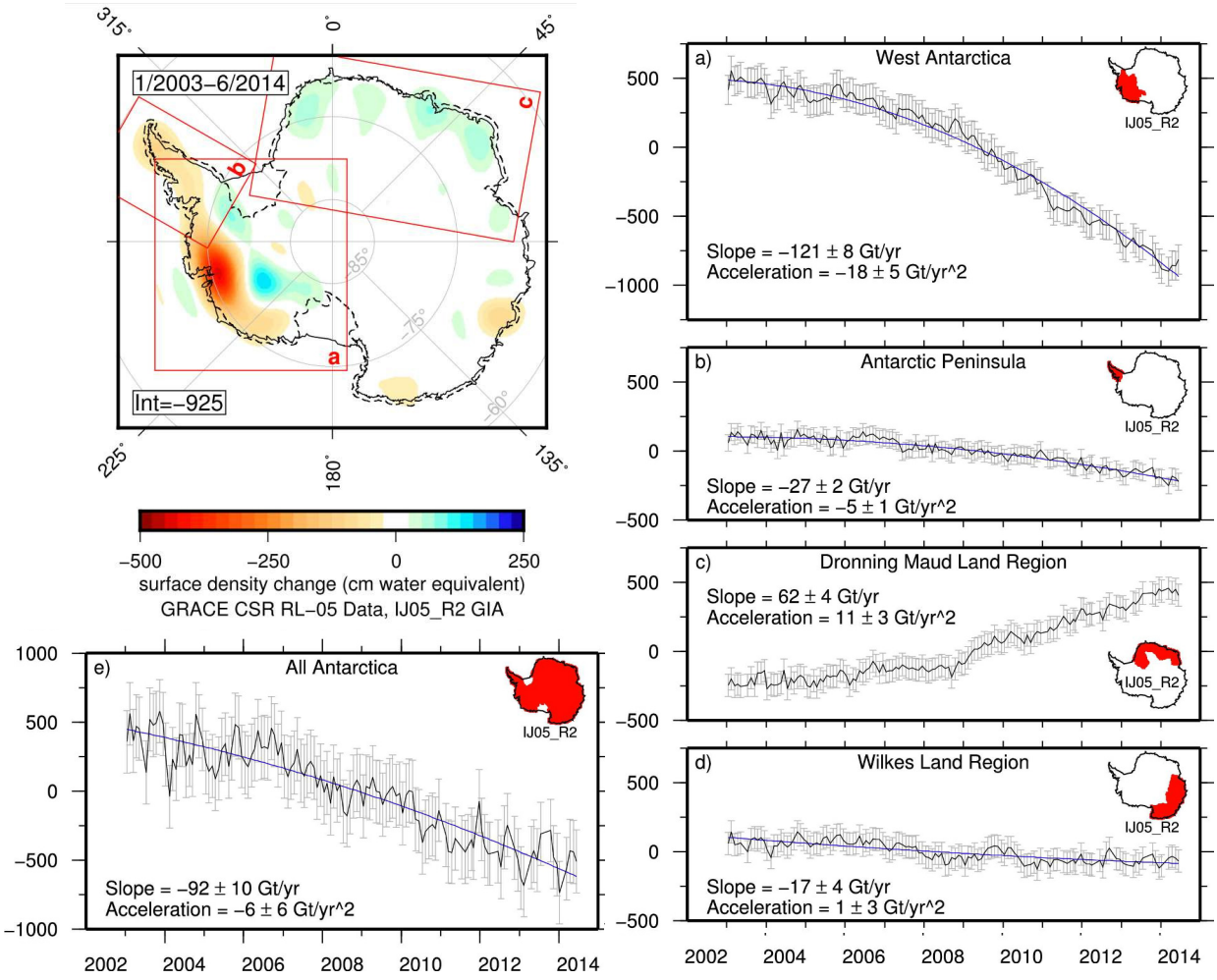

Figure 1.3: Antarctic ice-mass change in space and time, estimated from satellite gravimetry (GRACE), over the period 2003-2014. (**Map**) Spatial pattern of ice-mass change (**a-e**) Time-series of ice mass changes (in Gt) for various regions of Antarctica and for the whole ice sheet (**e**). The black lines are monthly GRACE observations with 2σ error bars. Credit: Figs. 1 and 2 from Harig and Simons (2015). [Reprinted with permission from Elsevier].

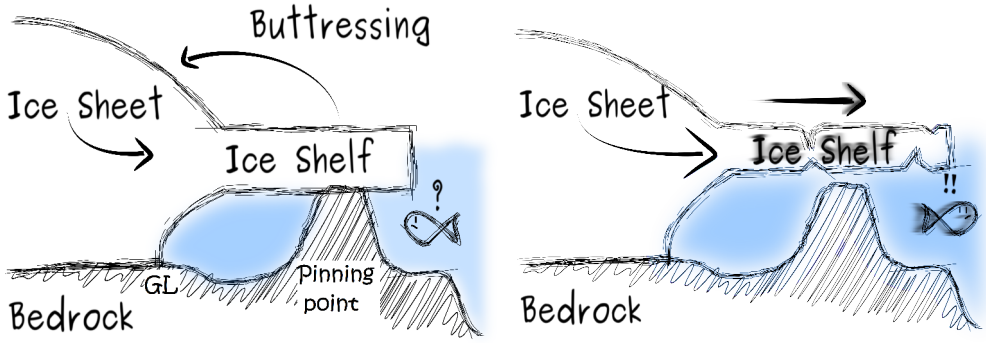

(a) Ice shelf buttressed by a pinning point. (b) Ice shelf unpinned

Figure 1.4: Pinned and unpinned ice shelf. (**a**) A pinning point buttresses the ice shelf, de facto restraining the ice discharge from the continent. (**b**) The ice shelf has thinned and has lost contact with the pinning point. This results in a loss of buttressing, which speeds up the ice coming from upstream and enhances ice discharge to the ocean. "GL" denotes the grounding line, the point where ice starts to float. Credit: R. Drews.

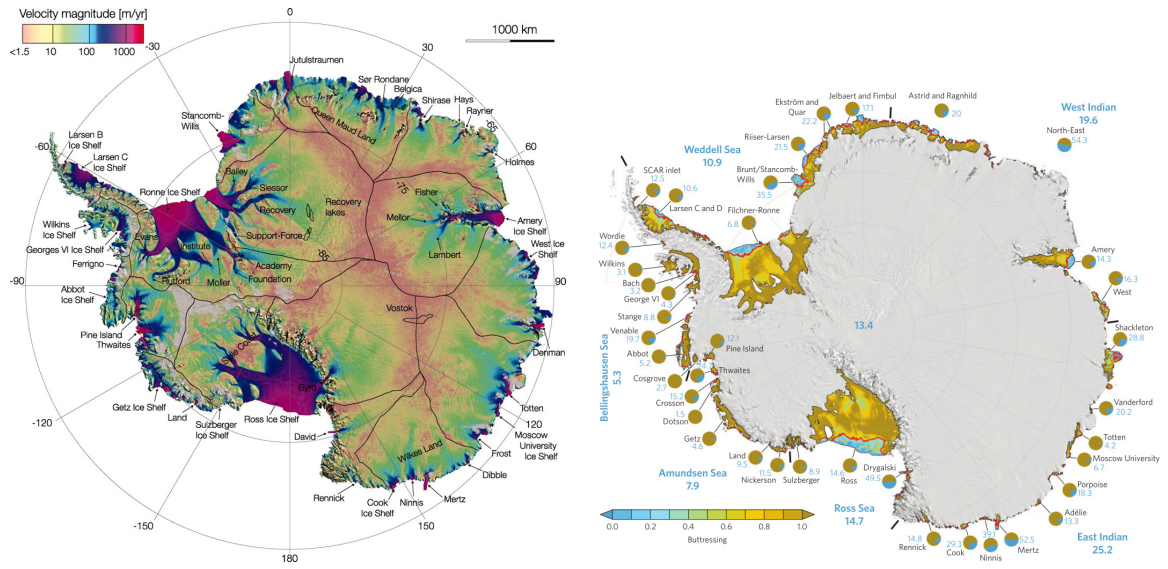

(a) Surface velocities (b) Ice-shelf buttressing

Figure 1.5: Ice-sheet flow and ice-shelf buttressing. (**a**) Surface velocity from satellite radar interferometry. (**b**) Maximum buttressing of ice shelves, with red contours delineating the *passive shelf ice*, the ice-shelf area which has little or no dynamical influence, so that it can be removed from the ice shelf with minimal dynamical implications. Numbers and pie charts refer to percentage of passive shelf-ice area, with respect to the total ice-shelf area. Credit: (a) Fig. 1 from Rignot et al. (2011) [Reprinted with permission from The American Association for the Advancement of Science] and (b) Fig. 1 from Fürst et al. (2016) [Reprinted with permission from Nature Publishing Group].

grounding lines have retreated and discharge in the ocean has significantly increased, leading to sea-level rise (Fig. 1.4). Put simply, mass losses at ice shelves are driving the current Antarctic contribution to sea-level rise.

Given their peripheral positions, ice shelves are vulnerable to both atmospheric and oceanic warming. In the following, we detail ice-atmosphere (section 1.2.3) and ice-ocean (section 1.2.4) interactions, which control the stability of the ice shelves.

1.2.3 Ice-atmosphere interactions

Ice-atmosphere interactions are summarised by the surface mass balance (SMB – Fig. 1.6a), which encompasses precipitations (snow and rain), meltwater runoff, erosion/deposition and sublimation[2] (e.g. Lenaerts et al., 2012).

Snowfalls largely control the SMB and exceed the other components by one to two orders of magnitude (Lenaerts et al., 2012). As a result, the Antarctic SMB is widely positive, with less than 1% of the ice-sheet's surface experiencing ablation ($SMB < 0$) (Winther et al., 2001, Lenaerts et al., 2012). In those ablation areas, ice is mainly lost through sublimation.

The surface mass balance varies however considerably both spatially and temporally. Coastal areas (especially in the Antarctic Peninsula and in West Antarctica) show high accumulation as opposed to the very low SMB in the interior (Fig. 1.6a and Lenaerts et al., 2012, Arthern et al., 2006). Variable topography also influences the SMB on more local scales by modulating precipitations and snow erosion/deposition (Lenaerts et al., 2014, Frezzotti et al., 2007). It is also important to note the strong inter-annual variability in the SMB, controlled by very variable snowfalls (Lenaerts et al., 2012, 2013).

[2] *Sublimation* is the phase transition from solid to gas.

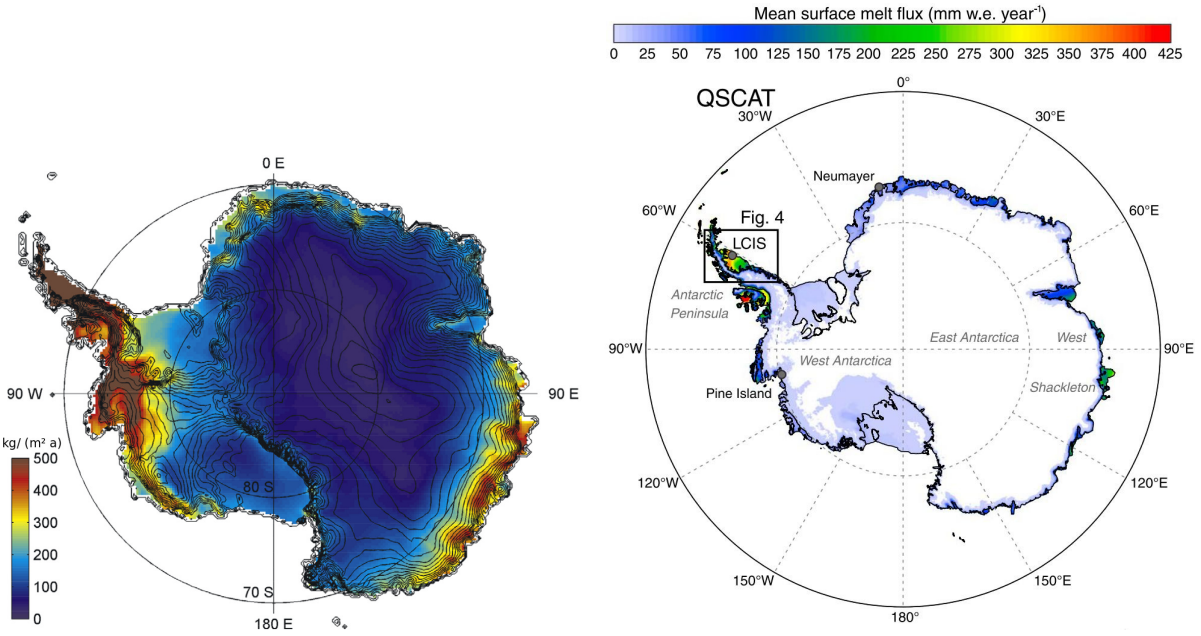

(a) Surface Mass Balance (b) Surface melting

Figure 1.6: Antarctic surface processes. (**a**) Observed surface mass balance from satellite and ground-based measurements. (**b**) Surface melt fluxes from satellite measurements (QuikSCAT). Credit: (a) Fig. 4 from Arthern et al. (2006) [Reprinted with permission from John Wiley and Sons] and (b) Fig. 2a from Trusel et al. (2013) [Reprinted with permission from John Wiley and Sons]

Although mass loss due to surface meltwater runoff is negligible because almost all meltwater refreezes in the snow and firn[3] (Lenaerts et al., 2012, Kuipers Munneke et al., 2012a), surface meltwater can however impact ice shelves and their stability in at least 3 different ways. First, refreezing of meltwater releases latent heat and warms the ice, which therefore becomes less viscous and accelerates, leading to a loss of buttressing (Hubbard et al., 2016). Second, meltwater influences firn-densification (Helsen et al., 2008), which impacts ice-shelf-elevation changes detected by satellites (Holland et al., 2015). Additionally, denser ice can resist better to tensile fracturing (i.e. by stretching) and therefore become less prone to across-flow crevassing (Hubbard et al., 2016). Third, meltwater ponding can weaken the ice shelves by (i) hydrofracturing – a process whereby fractures are filled with water and widen by subsequent increase in hydrostatic pressure (Scambos et al., 2000, Kuipers Munneke et al., 2014)– or by (ii) fracturing from lake drainage and following hydrostatic rebound (MacAyeal and Sergienko, 2013, Banwell et al., 2013).

Although meltwater and hydrofracturing have been linked to ice-shelves disintegration (Scambos et al., 2009, and Section 1.2.5), meltwater volume has not changed significantly over the last 20 years (Kuipers Munneke et al., 2012a). This suggests that atmospheric forcing alone is not the main driver of the recent and rapid mass losses observed in Antarctica. Instead, ocean forcing needs to be considered. Before addressing ice-ocean interactions (Section 1.2.4), we briefly outline in Box 1.1 the predicted future changes in surface mass balance and surface melting.

[3] *Firn* is compacted snow that as not yet been fully compressed into ice.

Box 1.1: Future changes in ice-atmosphere interactions

During the 21st century, atmospheric warming is expected to intensify snowfalls in Antarctica through (i) enhanced moisture-carrying capacity of a warmer atmosphere, (ii) higher water availability in coastal regions less covered by sea ice; and (iii) changing cloud properties (Lenaerts et al., 2016). Climate models in line with current satellite observations (CALIPSO) predict an increase in Antarctic precipitation of 7.4-29.3%, with a precipitation sensitivity of 7.1 %/°C of atmospheric warming (Palerme et al., 2017).
At the same time, surface melting is expected to intensify exponentially with near-surface atmospheric warming in summer (Trusel et al., 2015). As a result, Trusel et al. (2015) predict a doubling or tripling of Antarctic surface melt by 2050, which will affect almost all ice shelves.
All in all, the overall Antarctic surface mass balance is predicted to increase driven by higher winter snowfalls, whereas warmer summer will intensify surface melting (Lenaerts et al., 2016).

1.2.4 Ice-ocean interactions

The ocean interacts with an ice sheet either beneath its ice shelves (where ice mostly melts but sometimes refreezes) or at the ice-shelf front (where icebergs calve). The AIS loses between half and two-third of its ice through basal melting, whereas icebergs calving accounts for the remaining part (Depoorter et al., 2013, Rignot et al., 2013, Liu et al., 2015). As seen in Section 1.2.2, both processes modulate the buttressing exerted by ice shelves on the inland flow and therefore influence the total ice discharge in the ocean.

In the following, we first briefly depict the ocean circulation around Antarctica (Section A)), before delving more deeply into the processes of basal melting (Section B)) and calving (Section C)).

A) Ocean circulation around Antarctica

As shown in Fig. 1.7, the eastward flowing *Antarctic Circumpolar Current* (ACC) dominates the circulation of the Southern Ocean (Rintoul et al., 2001). This current is driven by winds, water density and Coriolis effect but its path relies heavily on land and seafloor bathymetry (Williams, 2015). Most of the Antarctic Circumpolar Current is formed by *Circumpolar Deep Water* (CDW), a relatively warm and saline water mass that circulates around Antarctica between ~1,400 m and >3,500 m depths but that can rise along the Antarctic continental shelf-breaks and shelves[4] (Carter et al., 2008, Williams, 2015).

As the bathymetry deflects the Antarctic Circumpolar Current to the north in the Weddell and Ross seas, local gyres form[5]. Those two gyres are complemented by a third one, south of Australia (Bindoff et al., 2000).

Close to the coast, water is circulating westwards, driven by easterly (westward flowing) winds and geostrophic[6] processes to form the coastal and slope-front currents.

[4] *Continental shelves*, not to be confused with ice shelves, are areas of shallow seafloor, in the vicinity of continents. They are separated from the deep ocean by *continental shelf-breaks*.

[5] A subpolar *gyre* is a clockwise-rotating ocean current, driven by wind and Coriolis, beneath persistent region of low atmospheric pressure.

[6] *Geostrophic* flow occurs when the pressure gradient and Coriolis forces, which both drive ocean flow, balance each other

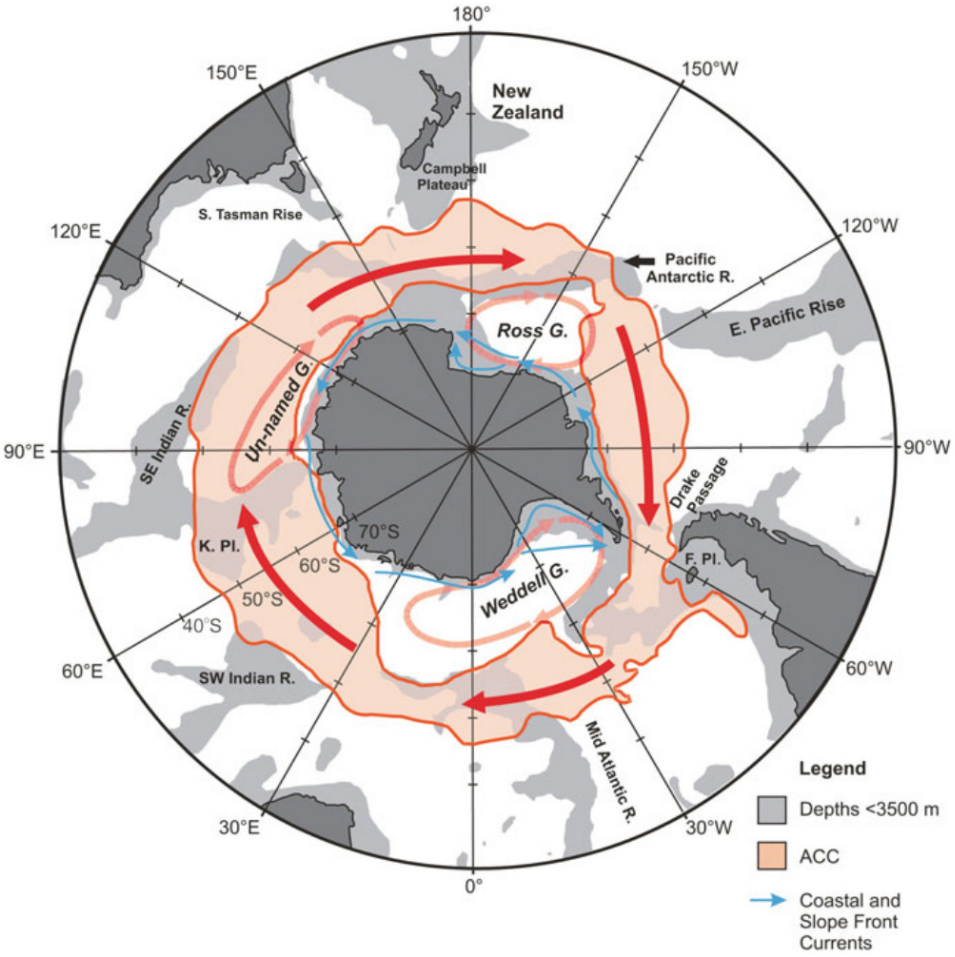

Figure 1.7: Ocean circulation in the Southern Ocean. ACC and G. stand for Antarctic Circumpolar Current and Gyre, respectively. Note that Antarctica is rotated, compared to previous figures. Credit: Fig. 7.4 from Williams (2015) (modified from Carter et al., 2008) [Reprinted with permission from Springer].

B) Sub-shelf melting (and refreezing)

Mechanisms driving melting

Ice-ocean interactions underneath ice-shelves are mainly controlled by 3 factors occurring at different scales: (i) the regional oceanographic conditions beyond the ice front, (ii) the local water circulation beneath the ice shelves (iii) the micro-scale interactions in the layer at the interface between the ice and the seawater, i.e. the boundary layer (e.g. Dinniman et al., 2016).

The regional ocean circulation determines which water masses are present at the ice front and therefore the heat supply that can potentially enters in the ice-shelf cavity (the space between the seafloor and the ice shelf). For instance, the Antarctic Circumpolar Current flows along the coast in the Amundsen Sea (120° – 90° W) but is located much more off-shore in the Weddell Sea (60°W–30°W) (Fig. 1.7). If total melting beneath ice shelves does not solely depend on the oceanographic conditions at its front, Rignot and Jacobs (2002) have nevertheless found a strong correlation between ocean temperatures and basal melt rates.

However, to melt the ice, the potential heat supply at the ice-shelf front needs to enter the ice-shelf cavity and reach the ice-shelf base. This is determined by the local circulation underneath the ice shelves, which depends on the bathymetry and ice-shelf base, thus on the geometry of the cavity.

While the latter processes supply potential heat beneath the ice shelves, the actual melt-rates are controlled by micro-scale processes, which depend on 3 factors. First, ice-melting and

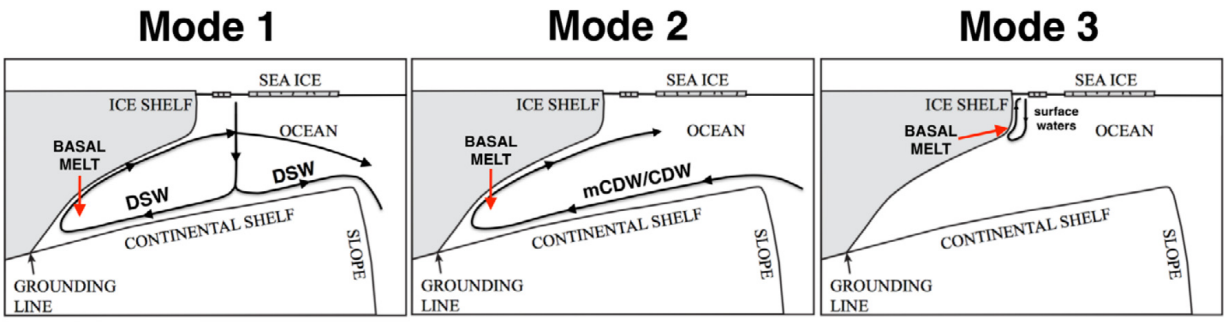

Figure 1.8: 3 melting modes beneath ice shelves: Credit: Fig. 2 from Silvano et al. (2016)

seawater-freezing points depend on pressure. The melting point of ice decreases with the pressure – hence depth – at a rate of ~0.75°C per kilometre (Foldvik and Kvinge, 1974). This pressure-dependence of the melting point explains why higher melt-rates are observed where ice is thicker, i.e. close to the deep grounding lines (e.g. Rignot et al., 2013). Second, the freezing point of seawater depends on its salinity. As a result, saltier water masses have a colder freezing point and therefore refreeze less easily than fresher water. Third, the effective melt rates are determined by the temperature of the seawater directly in contact with the ice (i.e. in the boundary layer). This depends on how fast heat and salt are transferred across the boundary layer, which is itself controlled by parameters such as basal ice roughness, ocean flow speed and temperature, tides and turbulence (Silvano et al., 2016).

The interplay between different processes at different scales results in complex ice-ocean interactions that can substantially vary over sub-kilometre scales (e.g. Stanton et al., 2013, Marsh et al., 2016). Ice-shelf melting however has been grouped under three different modes (Fig. 1.8 and Jacobs et al., 1992), which we describe now.

Melting modes

1. *Mode 1* is typical of "cold cavities". In winter, cooling of seawater and salt rejections from sea-ice freezing form the Dense Shelf Water (DSW). This dense and cold water mass then sinks and intrudes in the ice-shelf cavity. In the deep parts of the ice shelf (i.e. near the grounding line), the DSW is locally warmer than the freezing point because of its pressure dependence. As a result, DSW melts the ice-shelf base and mixes with the meltwater to form the lighter Ice-Shelf water, which rises along the ice-shelf base. As its depth decreases, ice-shelf water becomes supercooled (i.e. below freezing point) and refreezes to form marine ice. This melting mode produces overall low melting and is typical of large ice shelves such as Ross, Filchner-Ronne and Amery ice shelves (e.g. Joughin and Padman, 2003).

2. In *Mode 2*, the relatively warm (1°C) Circumpolar Deep Water mixes with surrounding water to form modified CDW (mCDW), which intrudes in the ice-shelf cavity. As the temperature of the CDW is >4°C above the in-situ freezing point, the mCDW melts vigorously the ice-shelf base (at intermediate depths), even after mixing with meltwater. This melt mode drives the rapid thinning of ice shelves such as Pine Island, Thwaites or Totten ice shelves (e.g. Jenkins et al., 2010, Greenbaum et al., 2015, and Figs. 1.9a and 1.9b).

3. In *Mode 3*, surface waters seasonally warmed in summer are transported in the ice-shelf cavity by tides, eddies, ocean currents, etc. and melt the shallow ice close to the calving front.

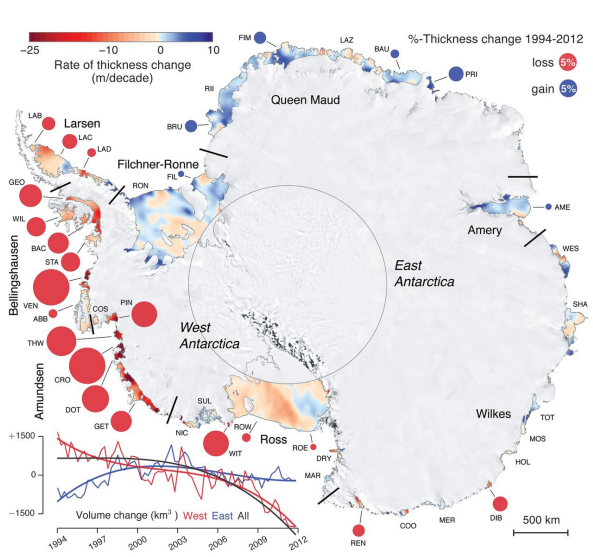

(a) Ice-shelf thinning and volume loss

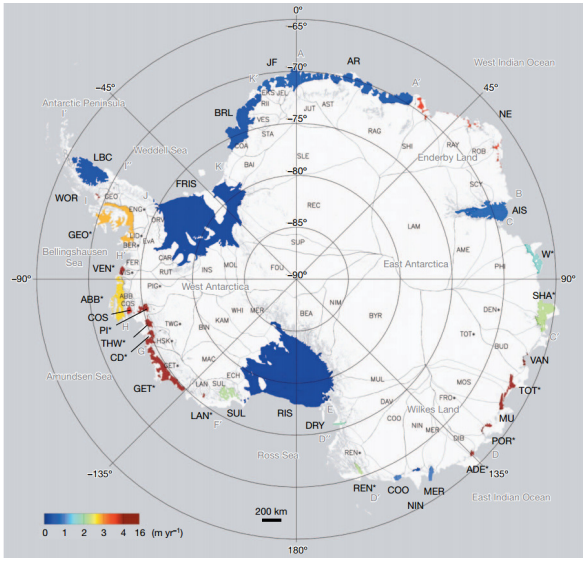

(b) Ice-shelf melting

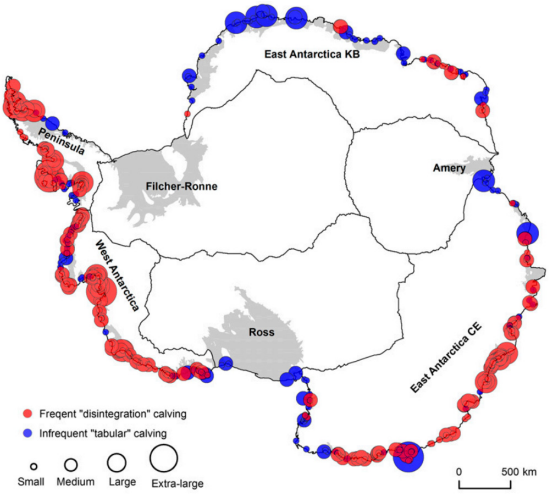

(c) Iceberg calving

Figure 1.9: Ice-ocean interactions around Antarctica : ice-shelf thinning, melting and calving.
Credit: (a) Fig. 1 from Paolo et al. (2015) [Reprinted with permission from The American Association for the Advancement of Science], (b) Fig. 2 from Depoorter et al. (2013) [Reprinted with permission from Macmillan Publishers Ltd], (c) Fig. S1 from Liu et al. (2015).

C) Calving

Despite its importance, iceberg calving is a complex process, which is hard to measure directly and difficult to accurately reproduce in models. Calving occurs in two stages: (i) fractures isolate a chunk of ice from the rest of the ice shelf, (ii) the iceberg must be transported away from the ice front (Bassis and Jacobs, 2013). The first step is most efficient in regions of large stress or when crevasses are advected from upstream, while export is facilitated by a deep bathymetry below ice shelves. In Antarctica, Liu et al. (2015) have recently distinguished two types of calving: *tabular* and *disintegrating* calving (Fig. 1.9c).

Tabular calving corresponds to the sporadic detachment of very large tabular icebergs (Bassis and Jacobs, 2013, Bassis et al., 2008, Fricker et al., 2002, Joughin and MacAyeal, 2005), followed by years to decades of inactivity. Tabular icebergs are formed by the propagation of rifts, which are large through-cutting fractures in the ice (as opposed to crevasses that do not sever the entire

ice thickness). Tabular calving is typical of Dronning Maud Land, Ross and Amery sectors (Liu et al., 2015).

In contrast, disintegrating calving produces smaller icebergs (<100 km^2) of similar size that detach frequently from the same neighbourhood (Bassis and Jacobs, 2013, Scambos et al., 2003, 2009, MacAyeal et al., 2003). Liu et al. (2015) have recently linked disintegrating calving to climate forcing, suggesting that the thinning associated with vigorous ocean melting is also related to enhanced calving and retreating ice-shelf fronts (Fig. 1.9). As a result, disintegrating calving dominates in West Antarctica, the Antarctic Peninsula and Wilkes Land, where mass losses due to calving are comparable in magnitude with basal melting (Liu et al., 2015). In the most extreme cases, disintegrating calving can even lead to the abrupt collapse of almost entire ice shelves, as will be explained in the next section.

1.2.5 Abrupt and irreversible ice losses

The AIS can be destabilised by at least three mechanisms that accelerates mass losses through loss of buttressing, grounding-line retreat and increased discharge (Fig. 1.11):

1. Ice-shelf collapse
2. Marine ice sheet instability
3. Cliff failure/marine ice cliff instability

Based on the information provided in the previous sections, we briefly present these 3 instabilities.

A) Ice-shelf collapse

Ice-shelf collapse – or disintegration – is a rapid retreat of the ice-shelf front, where successive calving events (disintegrating calving) drastically reduce the size of ice shelves over a short period of time. So far, collapses have only been observed in the Antarctic Peninsula, where several ice shelves spectacularly disintegrated in the last decades (Cook and Vaughan, 2010). Since the 1950s, the Peninsula has been affected by strong atmospheric warming that has been (i) unprecedented in the past millennium and (ii) unseen in other regions of Antarctica (Vaughan et al., 2003, Zazulie et al., 2010, Abram et al., 2013).

Ice-shelf collapses have been followed by an acceleration of their tributary glaciers (Rignot et al., 2004, Rott et al., 2011), leading to continuous mass loss since then (Berthier et al., 2012). Ice-shelves disintegration is responsible for the current acceleration of mass loss in the Antarctic Peninsula (Shepherd et al., 2012, Harig and Simons, 2015, Fig. 1.3).

Many of those collapses follow a specific 4-step pattern. First, atmospheric warming exposes the ice shelves to intense surface melting (e.g. Hubbard et al., 2016), gradually depleting the firn from its air content (pore space). Second, the firn then becomes saturated and can no longer accommodate additional water. Therefore, lakes start to form at the surface of the ice and/or water start to fill pre-existing fractures. Third, existing fractures deepen and new ones form by hydrofracturing (Scambos et al., 2003) or by release of pressure when the lake drain and the ice is suddenly lifted up by "hydrostatic rebound" (MacAyeal and Sergienko, 2013, Banwell and Macayeal, 2015). Finally, repeated over several years, this cycle of lake filling and drainage has sufficiently fractured the ice shelf that has gradually become weak enough for the final act: the break-up. After a long and intense melt event (van den Broeke, 2005), hundreds of lakes form at the surface of the ice shelf. The sudden drainage of one lake can cause the surrounding lakes to drain, triggering a chain reaction that eventually leads to the sudden collapse of the ice shelf by disintegrating calving (Banwell et al., 2013, Banwell and Macayeal, 2015).

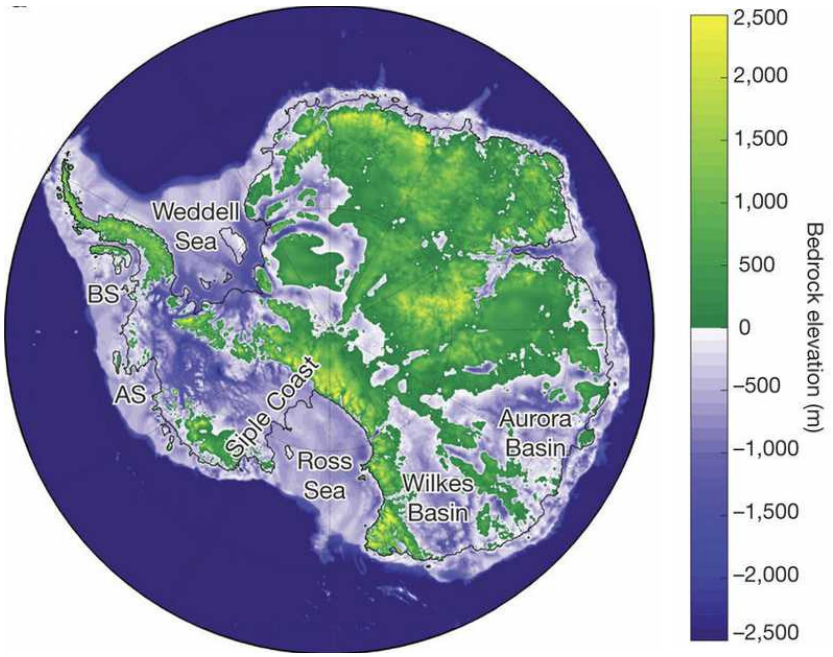

Figure 1.10: Bed topography and bathymetry from Bedmap2 (Fretwell et al., 2013). The grounding line is in black. BS: Bellinghausen Sea, AS: Amundsen Sea. Credit: Fig 1a from DeConto and Pollard (2016) [Reprinted with permission from Nature Publishing Group].

However, atmospheric warming is not the only factor causing collapses: prior to their disintegration, basal melting (Holland et al., 2015, Shepherd et al., 2003) had been weakening those ice shelves from below for decades (Paolo et al., 2015). Therefore, the picture emerging is that the collapse of an ice shelf is primarily caused by its thinning, mainly controlled by the ocean, whereas surface melting triggers the disintegration (Kuipers Munneke et al., 2012a).

B) Marine Ice Sheet Instability

The numerous marine sectors of the AIS (in blue in Fig. 1.10) – which lie below sea level with inland-sloping bed (i.e. retrogrades slope) – are even more sensitive to oceanic forcing than the Antarctic Peninsula. This configuration can lead to unstable and irreversible retreat, known as marine ice sheet instability (Mercer, 1978, Schoof, 2007). The instability is triggered when the loss of ice-shelf buttressing (e.g. due to oceanic melting or ice-shelf collapse) causes the grounding line to retreat and reach retrograde bed slope (Fig. 1.11-top). Then, as the grounding line retreats on the retrograde slope, ice gets thicker at the new grounding-line position, so that more ice is discharged to the ocean. Because ice flux coming from upstream of the grounding line does not increase, this higher discharge is not compensated. Ice therefore locally thins at the grounding line and becomes thin enough to float, which pushes the grounding line further inland, and so on. This process self-maintains itself until the grounding line reaches a new stable position (e.g. bedrock high). If the concept of MISI has been known for decades (Mercer, 1978), there is a growing evidence in both modelling (Favier et al., 2014, Joughin et al., 2014) and observations (Rignot et al., 2014, Wouters et al., 2015) that a marine ice sheet instability is currently under way in West Antarctica. Although West Antarctica is the most vulnerable marine-based region of the AIS, many other sectors of the much bigger East Antarctic ice sheet are also prone to marine ice sheet instability in the long term (Mengel and Levermann, 2014, Ritz et al., 2015, DeConto and Pollard, 2016, and Fig. 1.10).

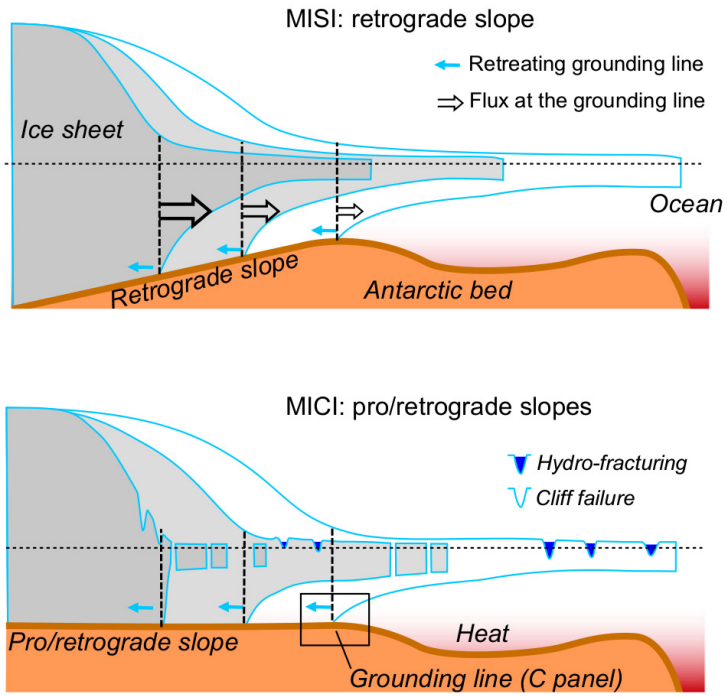

Figure 1.11: Marine Ice Sheet (MISI) and Ice Cliff (MICI) instabilities. (**top**) MISI: unstable retreat of the grounding line on a bed sloping towards the interior. (**bottom**) MICI: collapse of exposed ice cliffs, formed after ice-shelf disintegration due to hydrofracturing. Credit: Fig 1b from Pattyn et al. (2017) [Reprinted with permission from Springer].

C) Marine Ice Cliff Instability

More recently, DeConto and Pollard (2016) have proposed the concept of Marine Ice Cliff Instability (MICI) (Fig 1.11-bottom) to better reproduce past Antarctic contribution to sea-level rise (Section 1.1). This instability leads to rapid grounding-line retreat due to structural collapse of marine-terminating ice cliffs under their own weight (Pollard et al., 2015, DeConto and Pollard, 2016). Cliff instability can occur on prograde bed slopes but necessitates a prior disintegration of ice shelves (e.g. by submarine melting and hydrofracturing).

Furthermore, cliff instability could catalyse the marine ice sheet instability, destabilising significant parts of the AIS. If this theoretical concept of cliff instability is validated, it will imply the Antarctic ice sheet to be much more vulnerable to atmospheric warming that previously assumed (DeConto and Pollard, 2016).

1.3 Roi Baudouin Ice Shelf, Dronning Maud Land, East Antarctica

Coastal Dronning Maud Land (20° W - 45° E), in East Antarctica, is characterised by various outlet glaciers feeding into small ice shelves, whose extents are limited by relatively close and shallow continental-shelf breaks (Arndt et al., 2013, Fig. 1.12). Many of these ice shelves are stabilised and buttressed by numerous pinning points (Matsuoka et al., 2015, Favier and Pattyn, 2015).

Although not as vulnerable as the West Antarctic ice sheet, the bed in some parts of Dronning Maud Land lies below sea level and dips towards the interior (Fretwell et al., 2013). As a result, some basins are prone to marine ice sheet instability over the coming centuries (Ritz et al., 2015).

Among the ice shelves of Dronning Maud Land, stands the Roi Baudouin Ice Shelf (RBIS –

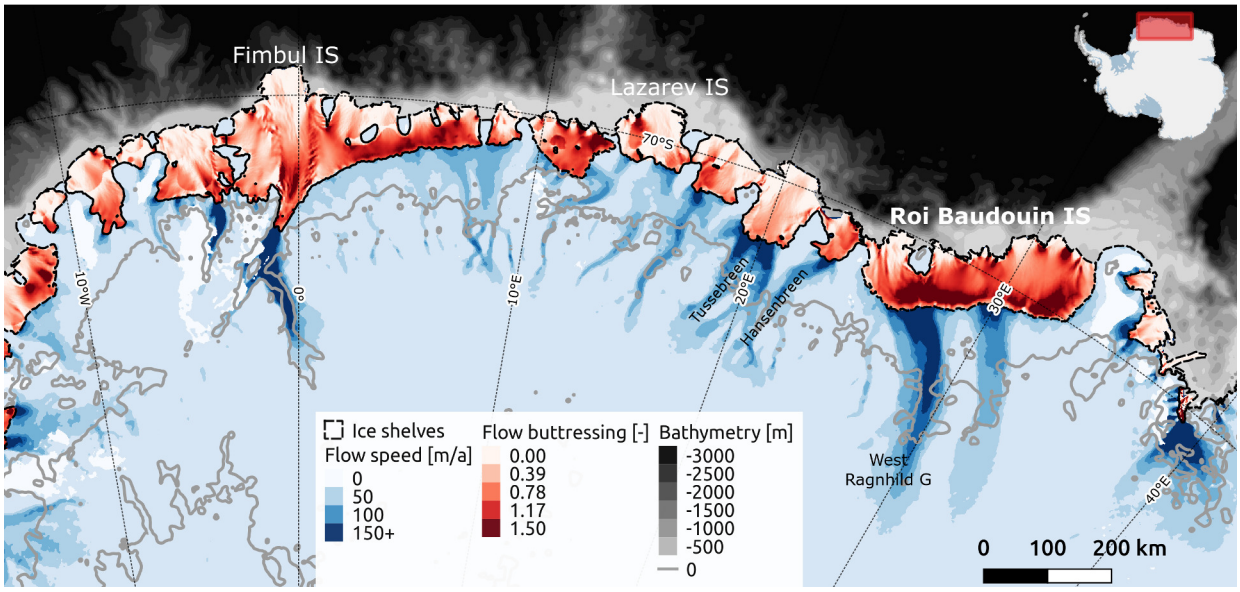

Figure 1.12: Coastal Dronning Maud Land. **Ice shelves** (red): buttressing in the direction of ice flow from Fürst et al. (2016) (ice-shelf outlines from Rignot et al., 2013, Mouginot et al., 2016). **Grounded ice** (blue): flow speed from Rignot et al. (2011). **Seaward side** (grey): seabed from Fretwell et al. (2013). IS and G stand for ice shelf and glacier, respectively.

Fig. 1.13). Discovered by the Norwegians Isachsen and Rijser-Larsen in 1931, the RBIS extends over almost 33,000 km^2 – an area comparable in size to Belgium – on the Princess Ragnhild Coast. Only mapped with aerial photographs by the Norwegians in 1937-1936 (Lars Christensen Expedition) then by the Americans in 1946-1947 (Operation High jump Kearns, 2005), the region remained little documented until the late 1950s. Then, in 1958, the Belgian Antarctic Expedition established its research station, the base Roi Baudouin, on the ice shelf that now bears its name. For slightly more than one decade, the Belgians, later aided by the Dutch, surveyed the whole area (e.g. Van Autenboer, 1964), until the Base Roi Baudouin was vacated in 1967 (Derwael, pers. com.). Research in the area was subsequently carried out by the Japanese who installed and maintained, between 1985 and 1992, the Asuka research station in the Sør Rondane Mountain range, 100 km inland from the Roi Baudouin ice shelf (e.g. Nishio and Uratsuka, 1991). In 2008, after decades of absence, the Belgians opened a new research station – the Princess Elisabeth station – ~50 km inland from the abandoned Japanese station. This has revived the Belgian research interests in the region in general and in the Roi Baudouin Ice Shelf in particular.

The western part of the Roi Baudouin Ice Shelf (hereafter referred to as RBIS, Fig 1.13) is of particular interest:

- It is fed by the West Ragnhild Glacier (WRG), one of the three largest outlet glaciers in Dronning Maud Land (Callens et al., 2014).

- The RBIS is covered by several ice-shelf channels, which are curvilinear tracts visible both at the surface and base of the ice shelf (Fig. 1.13). In the case of the RBIS, channels start at the grounding line and stretch over hundreds of kilometres to the ice-shelf front. Channels are carved by localised ocean melt at the base of the ice shelf. They become visible in satellite imagery because their surface tends to sag, to adjust hydrostically to the ice removed at the base. Ice-shelf channels attest therefore to very active but localised ice-ocean interactions (Chapter 3 and Section 5.3.1).

- The Roi Baudouin ice shelf is laterally constrained by the Western Promontory (WP) on its west, by Derwael Ice Rise (DIR) on its East and by a small pinning point at its front (Fig

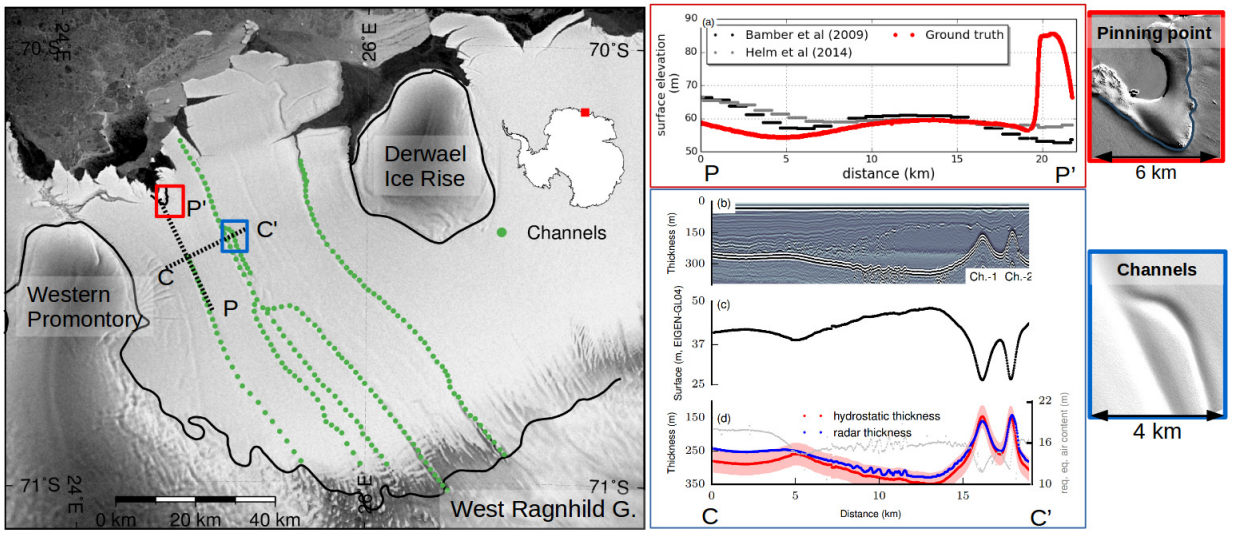

Figure 1.13: Western part of the Roi Baudouin Ice Shelf. (**Map**) Satellite view of the ice shelf with ice-shelf channels and the pinning point outlined. (**a**) Elevation upstream and on top of the pinning point, along the profile P-P'. (**b**), (**c**), (**d**), ice penetrating radar profile, surface elevation and ice thickness of the profile C-C', respectively. Credit: (c-d) subset of Fig. 5 from Drews (2015).

1.13, Chapter 4 and Section 5.3.2).

- A significant volume of ice is melted (and stored) at the (sub)surface of the ice shelf (Section 5.3.5).

For all the reasons listed above and because of its proximity to the Belgian research station (which facilitates the collection of ground-truth data), the RBIS has become a good laboratory to investigate the stability of ice shelves at high resolution. The relative steadiness of the RBIS provides a different perspective than fast changing ice shelves in the Antarctic Peninsula or in West Antarctica.

1.4 Objectives and outline

This thesis investigates the stability of ice shelves in general, using the Roi Baudouin Ice Shelf as a case study. The RBIS exemplifies how small-scale features (e.g. pinning point, ice-shelf channels, Fig. 1.13) can be easily overlooked whereas their effect will be imprinted on larger scales. The overall goal of the thesis is to investigate the impact of small-scale features on ice-shelf stability. To do so, (i) we try to accurately capture the effect of those sub-kilometre features in observations and (ii) we investigate the impact of (in)accurate observations on ice-sheet modelling.

The core of the thesis is made of two scientific papers (Chapter 3 and 4), provided "as is", i.e. under their current publication status, which, unfortunately, makes repetition with other chapters unavoidable. Apart from using the same velocity field, the two papers differ and complement one another both methodologically and topically.

The first paper, Chapter 3, is oriented towards the development/refinement of a methodology to detect basal melting beneath ice shelves, mainly based on satellite observations. This piece of research falls within the scope of the thesis because, as we have seen, basal melting of ice shelves is a key process that controls ice-shelf stability. Yet, ice-ocean interactions are complex, hard to observe directly and therefore poorly constrained in ice-sheet models. While this Chapter is oriented towards observations, it takes nevertheless a step towards inverse modelling, as it combines many datasets and uses physical assumptions to produce secondary observations.

The second paper, Chapter 4, for its part, specifically investigates the relationship between observations and models through initialisation with data assimilation. This study focuses on another key part of the ice shelves: their buttressing, i.e. the mechanism by which basal melting actually leads to increased mass loss from Antarctica.

In addition to this introduction and the two paper-chapters, this thesis includes four other chapters that give more substance to the thesis. Before delving into the papers, Chapter 2 provides background information about the methodology adopted in the papers, to enable non-specialists to understand them. The two papers are then followed by Chapter 5, which provides a methodological outlook and discusses more broadly the stability of the Roi Baudouin Ice Shelf. We then include a short essay (Chapter 6) on science outreach and its link to science, using the specific case of the cryosphere blog of the European Geoscience Union. This essay is an attempt to value outreach work as part of a scientific work. Finally, we summarise our main findings and conclude this research in Chapter 7.

Chapter 2

Methodology

This chapter is structured as follows: the first section (Section 2.1) focuses on radar remote sensing whereas the second part (Section 2.2) presents how to derive the basal mass balance of ice shelves, mainly based on remotely sensed radar data.

2.1 Spaceborne radar imaging of the Antarctic ice sheet

Spaceborne remote sensing[1] is particularly well-suited to study large and remote places like the Antarctic ice sheet. Over the last decades, a wide range of satellites and remote sensing techniques have flourished, enabling us to understand Polar Regions like never before (see Massom and Lubin, 2006, Tedesco, 2015, for an overview of existing techniques). Among all those techniques, spaceborne radar imaging has emerged as one of the most powerful tool for observing polar ice sheets.

In what follows, we briefly introduce the concept of radar imaging and present why this technique is so useful for studying the Antarctic Ice sheet (Section 2.1.1). We next focus on synthetic aperture radar, the most widely used type of spaceborne radar (Section 2.1.2) and then explain the concepts of radar interferometry (Section 2.1.3) and speckle tracking (Section 2.1.4). Those two techniques, which both rely on synthetic aperture radar data, provide elevations and velocities subsequently used in Chapters 3 and 4. This section ends with a quick summary highlighting the work conducted for this thesis (Section 2.1.5).

2.1.1 Basics and benefits of radar imaging to study Polar Regions

RAdio Detection And Ranging sensors – better known as *radar*s – are active sensors that emit microwave pulses (with a wavelength of 1 mm to 1 m) towards the Earth. Each pulse reaches the surface of the Earth and interacts with it. Part of the signal is backscattered (i.e. returned) to the satellite, where the sensor records the power of the returned echo. The time lag between the emission and reception of the radar signal can then be converted into distance separating the sensor from the target. Satellite-based radar sensors present many advantages:

- Being on-board satellites, radar sensors can acquire data over wide areas with high spatial sampling.
- Microwaves are relatively unaffected by cloud cover – very frequent at the poles – and atmospheric conditions.
- As radar are active sensors, they illuminate the Earth with their own energy. As a result,

[1] *Remote Sensing* is an ensemble of techniques used to derive information about a target without physical contact with it.

images can be acquired all day long, even during the long polar night.

These three reasons combined make radar sensors a perfect tool for observing the remote Polar Regions where the cloud cover is frequent and daylight lacks in winter.

2.1.2 Synthetic Aperture Radar: underlying principle and terminology

Synthetic Aperture Radar (SAR) is a technique that has been developed to improve the resolution of radar images. It takes advantage of the *Doppler* effect, caused by the forward motion of the spacecraft. Here, we restrict ourselves to presenting the geometry of SAR imaging systems (Box 2.1) and key features of SAR signals. Both are necessary to understand the rest of the thesis. For more thorough information about SAR systems, we refer to numerous textbook (e.g. Richards, 2009, Curlander and McDonough, 1991, Lacomme et al., 2001).

Box 2.1: Geometry of a SAR imaging system

Figure 2.1 describes the acquisition geometry of a SAR sensor, which is a side-looking system whose antenna points towards the Earth's surface with a fixed angle relative to the vertical, i.e. the *look angle*. Radar images are subsequently characterised by three main directions (i) the *slant range*, which is the radar look direction, perpendicular to the satellite track; (ii) the *ground range*, which corresponds to the projection of the slant range on the ground; and (iii) the *azimuth*, which corresponds to the along-track direction of the satellite. Finally, the *swath* corresponds to the ground area imaged by the sensor, whose typical width is about 50 to 100 kilometres (Bamler and Hartl, 1998, Furuya, 2011).

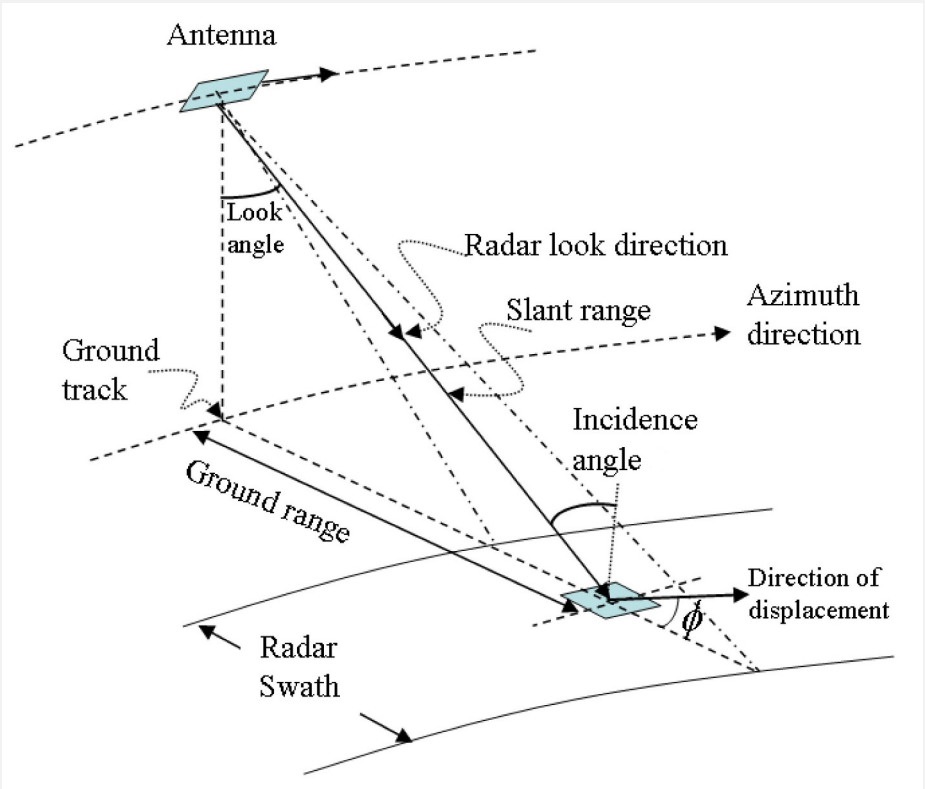

Figure 2.1: Acquisition geometry of a SAR sensor. Credit: Fig. 1 in Zhou et al. (2009).

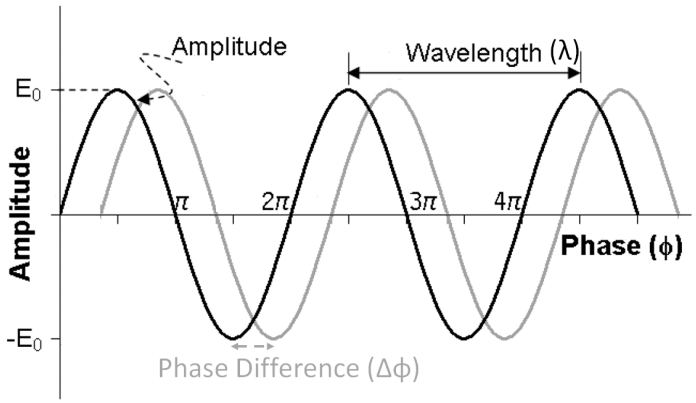

Figure 2.2: Schematic representation of an electromagnetic wave. The figure shows the relation between amplitude, wavelength and phase in a wave. The phase shift between two waves is shown in grey. Credit: adapted from Fig.2 in Zhou et al. (2009).

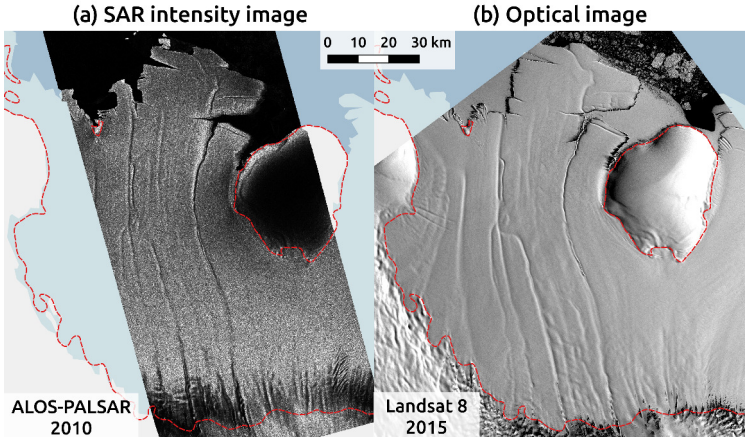

Figure 2.3: SAR intensity and optical images of the Roi Baudouin Ice Shelf (a) ALOS-PALSAR intensity image from 2010 and (b) Landsat-8 panchromatic image from 2015. The red dashed line outlines the grounded areas (Depoorter et al., 2013).

Like every other electromagnetic wave, a microwave (or radar wave) can be described by its amplitude, its wavelength and its phase (Fig. 2.2). The wavelength depends on the SAR system emitting the wave, whereas its amplitude and phase depend on surface properties and how they change. In practice, raw SAR data are first processed into Single Look Complex (SLC) images, which are two-dimensional grids where each pixel is a complex number storing two independent pieces of information: the amplitude (real part) and phase (imaginary) of the backscattered signal.

The amplitude of a particular pixel is determined by the sum of the energy backscattered by all the individual reflectors within the pixel. Note that the squared amplitude – the intensity – is often used for practical purposes, as this value is directly measured by the SAR sensor. Unlike optical data, radar images present a *speckle* pattern, which gives a "salt and pepper" effect on the images because neighbouring pixels present different intensities (Fig. 2.3). Speckle is pseudo-random: it appears random but is deterministic, as it results from interactions with the surface. In other words, if two SAR images are acquired in the exact same conditions (i.e. with no temporal changes and from the exact same geometry) they will show the exact same speckle pattern.

Phase, on the other hand, records the distance travelled by the wave between its emission and reception. Due to the periodic nature of a wave, its phase is wrapped, meaning that its values range between $[-\pi; \pi]$. A phase image appears random, because it is formed by the contribution of many elementary scatterers. However, if the surface remains relatively stable – i.e. *coherent*

– differencing the phase of two waves (related to the same information) removes the random contribution and leaves a signal that measures relative distances. This technique is called SAR interferometry or *InSAR* and is further developed in the following section.

2.1.3 Interferometric SAR

A) Common processing steps

Interferometric SAR is used to map ground displacement and topography from the phase information of several SAR images. As the phase depends on the travel path of the waves, phase shift between two images of the same area originates either from different paths to the target (different satellite points of view – topographic applications (Fig. 2.5)) or from changes at the surface (different times of acquisition – motion retrieval (Fig. 2.6)).

Both motion tracking and topographic applications present similarities in their processing. Those similarities are outlined below, before we focus on the particularities of both approaches in (Sections C) and B)). Schematically, InSAR processing starts with 2 single-look complex images of the exact same area, which are processed as follows:

1. **Co-registration of the two images**: one image (the slave) is resampled to match the geometry of the other one (the master). In other words, both images need to locate the same targets at the same pixel coordinates.

2. **Interferogram generation** by differencing the phase of the two co-registered single-look complex images. Interferograms display the interferometric phase (i.e. phase difference $\Delta\phi$), which is proportional to the difference in distance travelled by the 2 radar beams:

$$\Delta\phi = \frac{4\pi}{\lambda}(R_1 - R_2) = \frac{4\pi}{\lambda}\Delta R \tag{2.1}$$

   Equation (2.1) is made of 3 contributions: (i) the term $\frac{\Delta R}{\lambda}$ represents the difference in slant-range distance (ΔR) of the two waves, expressed as the fraction of a wavelength; (ii) the factor of 2 represents the round-trip of the waves (they have to hit the target and return to the sensor); and (iii) the factor of 2π accounts for the number of radians per wavelength (i.e. per wave cycle). To exploit the interferometric phase, its information needs to be decomposed in its different contributions:

$$\Delta\phi = \Delta\phi_{flat} + \Delta\phi_{topo} + \Delta\phi_{disp} + \Delta\phi_{noise} \tag{2.2}$$

   where $\Delta\phi_{topo}$ and $\Delta\phi_{disp}$ are the contributions due to topography and displacement in the slant range direction. $\Delta\phi_{flat}$ is a phase shift that arises because of the Earth's curvature and because of variations in the sensor(s) position. $\Delta\phi_{noise}$ is an unwanted phase shift due to various phenomena, such as atmospheric delay, instrumental noise, changing surface properties etc. (Zebker et al., 1994).

3. **Interferogram flattening** aims at removing the linear phase trend ($\Delta\phi_{flat}$) that stands out from interferograms. The interferogram is flattened by subtracting the expected phase from a surface of constant elevation on an ellipsoidal earth ($\Delta\phi_{flat}$).

4. **Phase unwrapping and calibration** to convert the interferometric phase into absolute unbounded phase shift (Fig. 2.4). Because the interferometric phase is confined between $[-\pi;\pi]$, it must be unwrapped to remove the ambiguity. Phase unwrapping consists in adding the correct multiple of 2π to the interferometric phase. This operation yields relative values, as the starting unwrapping point (where the interferometric phase is set zero) is

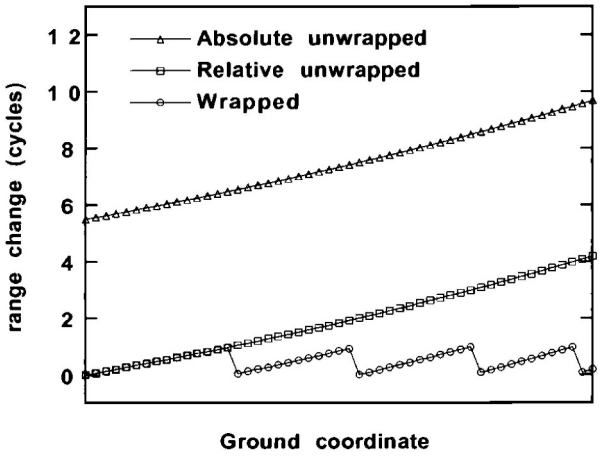

Figure 2.4: 3 types of phase measurements: wrapped, absolute unwrapped and relative unwrapped phases. The wrapped phase is confined between $[-\pi, \pi]$ and corresponds to modulo 2π of the relative phase. Discontinuities of the wrapped phase aside, all three curves have the same slope. Credit: Fig. 5 from Massonnet and Feigl (1998) [Reprinted with permission from John Wiley and Sons].

arbitrary. As a result, the unwrapped phase must be calibrated by a constant offset to reflect absolute values.

5. **Conversion to physical units**: elevations (Section B)) or displacement (Section C)) are then isolated in the unwrapped phase and converted to physical units.

6. **Post-processing**: geometric correction, georeferencing, etc.

B) Interferometry for topography

Topographic mapping with InSAR relies on a principle very similar to conventional stereoscopy, with the particularity that it exploits phase information, which makes InSAR more accurate than the latter (Rosen et al., 2000).

In the configuration laid out in Fig. 2.5 (i.e. single pass bistatic system), the topographic contribution to the interferometric phase in Eq. (2.2) can be expressed as follows (e.g. Rott, 2009, Zhou et al., 2009)[2]:

$$\Delta\phi_{topo} = \frac{2\pi}{\lambda}\Delta z \frac{B_n}{R_1 \sin\theta} \tag{2.3}$$

where B_n is the perpendicular baseline (the component of the Baseline B, perpendicular to the slant range direction) and Δz is the elevation with respect to a reference surface. To deduce the topography from interferometry, all the non-topographic contributions must then be removed ($\Delta\phi_{flat}$), minimised ($\Delta\phi_{disp}$) or neglected ($\Delta\phi_{noise}$) from the topographic phase. As a result, topographic InSAR works best with single-pass interferometer where both SAR images are acquired at the same time from slightly different points of view (Fig. 2.5). This configuration avoids any phase shift due to surface displacement or temporal changes.

In this thesis, we use external TanDEM-X digital elevation models (DEMs) (Section 2.2 and Chapter 3). Those DEMs are processed from SAR images acquired in single-pass bistatic mode, where two satellite fly close to each other, one (S_1) emits a radar beam and both (S_1,S_2) record the backstattered signal (R_1, R_2) (Fig. 2.5).

[2]Note the term 2π from Eq. (2.2) is replaced by π in a single-pass bistatic system because the radar wave is emitted by one antenna and recorded by 2.

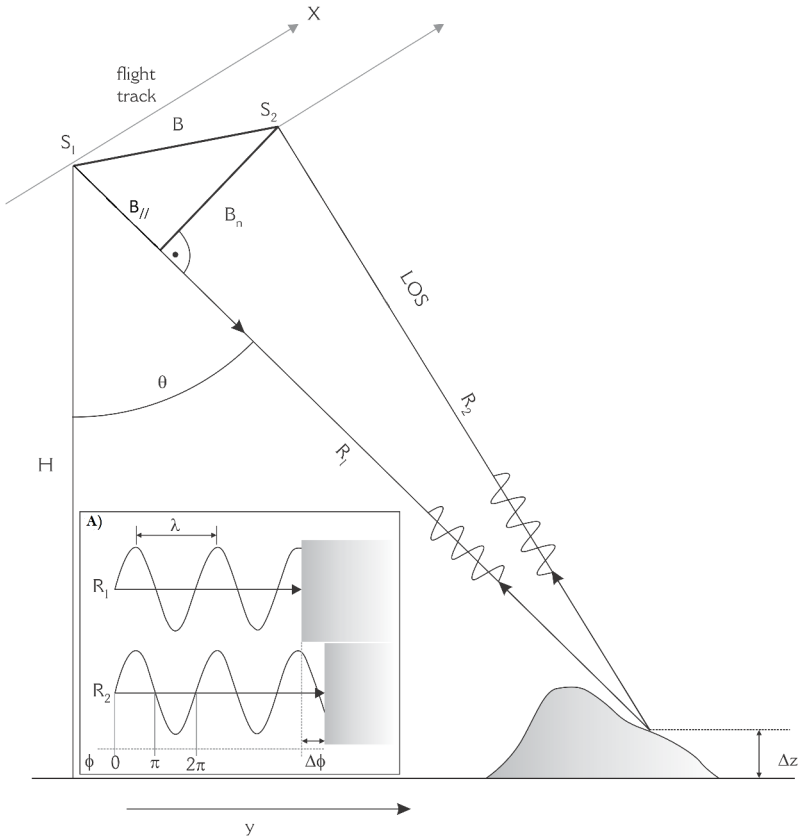

Figure 2.5: Configuration of single-pass bistatic SAR interferometer. The two SAR images are acquired at the same time by two sensors (S_1 and S_2) separated by a baseline B ($B_{//}$ and B_n being parallel and perpendicular components of baseline, respectively). The sensor S_1 illuminates the surface and the backscattered signal is recorded by both sensors simultaneously. R_1 and R_2 correspond to the slant range distances travelled by the signal between the surface and the sensors S_1 and S_2, respectively. θ is the satellite look-angle and LOS the Line of Sight. Inset A) illustrates the phase shift ($\Delta\phi$) between the two echoes. The path difference measured by $\Delta\phi$ depends on the orbital configuration of S_1 and S_2; the altitude Δz; atmospheric wave delay and other kinds of noise. Credit: adapted from Fig. 1 in Rott (2009)[Reprinted with permission from H. Rott]

C) Interferometry for surface displacements

When SAR images are acquired from the same satellite path (viewpoint) but at different times, i.e. in repeat-pass (Fig. 2.6), the interferometric phase is sensitive to surface displacements in the slant range direction ($\Delta r_{s.r}$):

$$\Delta\phi_{disp} = \frac{4\pi}{\lambda}\Delta r_{s.r} \tag{2.4}$$

It results from Eq. (2.4) that the motion sensitivity of an InSAR system only depends on the radar wavelength and on the direction of motion, both influenced by sensors' characteristics. A 2π phase shift is thus induced by a displacement with a magnitude of half a wavelength in the slant-range direction. Interferometric SAR is completely insensitive to motion in the azimuth direction (as it is perpendicular to the slant-range direction) and its sensitivity to vertical and ground-range displacement depends on the look angle of the SAR sensor. Both, horizontal and vertical movements have useful glaciological applications, namely grounding line-detection and horizontal velocity derivation, which are detailed below.

It should be noted however that before extracting motion information, the topography must be removed from the interferometric phase. In this thesis, we use a very common approach that

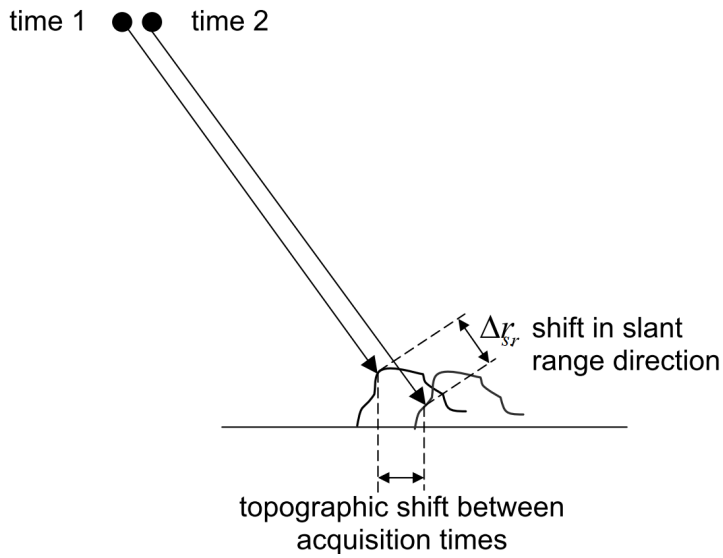

Figure 2.6: Configuration of repeat-pass SAR interferometer. Such a configuration is optimal to detect displacements (in the slant-range direction). Credit: adapted from Fig. 6.16 in Richards (2009) [Reprinted with permission from Springer].

simulates the topographic phase with a DEM and removes it from the interferogram (Massonnet et al., 1993). To do so we use an Antarctic-wide DEM from radar altimetry (Bamber et al., 2009) to map the velocities of the Roi Baudouin Ice Shelf with ERS 1/2 and ALOS-PALSAR images (Chapter 4). We also use the aforementioned TanDEM-X DEMs to remove the topography and locate the grounding line of the RBIS with ERS 1/2 and ALOS-PALSAR data (Section 5.3.3).

Grounding zone detection

We have seen in Chapter 1 that grounding zones are crucial areas for the Antarctic ice sheet, as they control its discharge in the ocean. (Figure 2.7a describes the different parts of a grounding zone.) Interferometric SAR provides a very efficient tool to locate grounding zones and monitor their evolution. If constant horizontal velocities can be assumed, differencing interferograms removes the component of horizontal motion from the interferometric phase, and therefore isolates the vertical displacement in the interferogram (e.g. Goldstein et al., 1993, Gray et al., 2002, Fricker et al., 2009, Hogg et al., 2016, Rankl et al., 2017, Drews et al., 2017). This is all the more true, given that steep look-angle of most radar system (e.g. 23° with the satellites ERS 1/2, used here) makes the slant-range displacement more sensitive to vertical displacement than horizontal motion (Goldstein et al., 1993). As tides rise and fall, floating ice shelves are lifted up and down, contrary to the grounded ice. Differential interferograms can therefore be used to locate the grounding zone, as the transition between the grounded ice and floating ice shelf is characterised by large gradients in vertical displacement (Fig. 2.7). This technique, a.k.a *quadruple difference interferometric synthetic aperture radar* (QDInSAR), can locate the landward limit of tidal flexure (H in Fig. 2.7) with a precision of 30 m (Rignot, 1998a,b).

Horizontal velocity

With Eq. (2.4), unwrapped and calibrated interferograms are easily converted to displacement and velocity fields. Those fields however only reflect displacement/velocity in the satellite's line of sight. This unidirectional sensitivity has several implications: (i) it is impossible to unambiguously separate the horizontal and vertical components of the displacement and (ii) observations in 3 linearly independent directions are needed to resolve 3D-velocity fields. Unfortunately, many SAR satellites (e.g. ERS 1/2) look on a fixed side and can therefore only provide observations

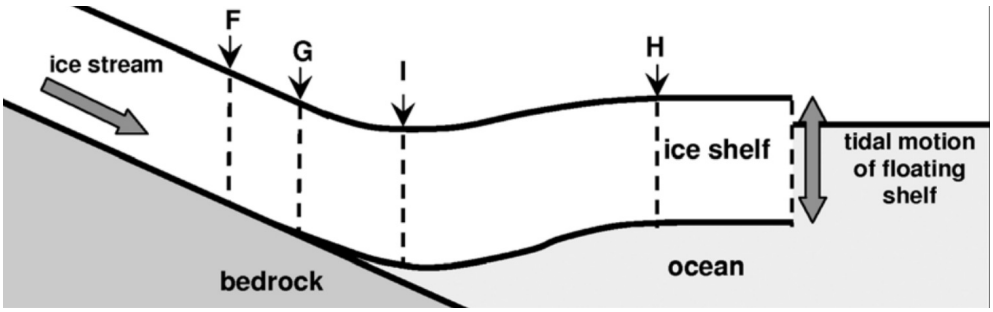

(a) Schematic grounding zone of an ice sheet-shelf system

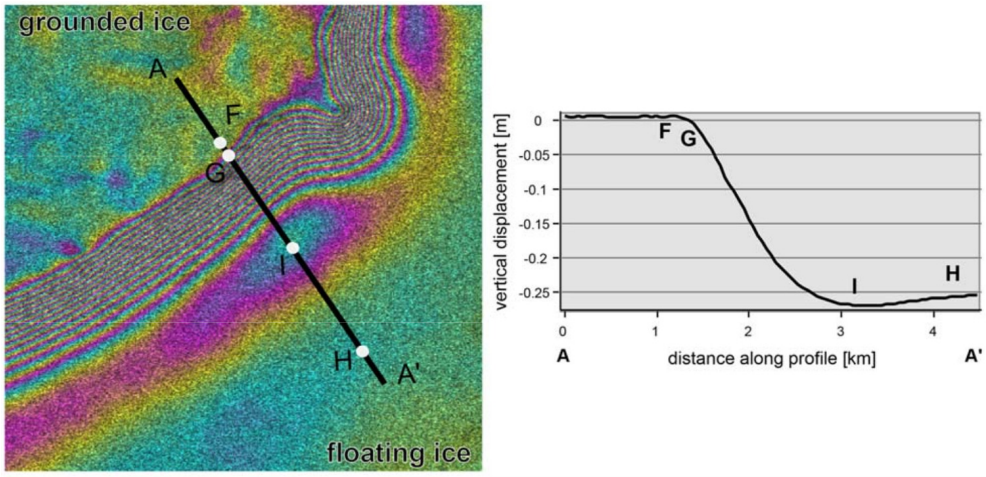

(b) Differential interferogram and vertical displacement in the grounding zone of Wilkins Ice Shelf

Figure 2.7: Grounding zone and vertical displacement of an ice shelf. F is the landward limit of tidal flexure. G is the grounding line, i.e. the limit where ice becomes afloat. I is the inflexion point, i.e. the local elevation minimum due to longitudinal stresses associated with ice-shelf bending. H is the seaward limit of tidal flexure. Credit: (a) Fig. 1 from Fricker and Padman (2006) [Reprinted with permission from John Wiley and Sons] (b) Fig. S2 from Rankl et al. (2017)

from 2 independent directions: the ascending and descending satellite passes. It is possible to overcome this limitation and unequivocally resolve horizontal-velocity fields by combining ascending and descending passes with a DEM, provided that ice flow is assumed parallel to the surface (Joughin et al., 1998, Kwok et al., 1996). Whereas tidal uplift of ice-shelf is exploited to accurately locate grounding lines (see previous paragraph), spatial variation in the vertical movement can corrupt the detected horizontal displacement (Rignot, 1996). This is avoided here by unwrapping and calibrating the grounded and floating areas separately.

As we have seen, interferometric SAR is a very powerful tool able to accurately detect very small motions. This accuracy however comes at the price that a lot of conditions need to be met: to get one velocity field, InSAR requires 2 pairs of coherent[3] SAR images from ascending and descending passes. These requirements practically limit the applicability of interferometry, by lack of suitable data and loss of coherence if the time lag between data acquisition is too long. Fortunately, an alternative technique has emerged : *speckle tracking*.

[3] *Coherence* measures the degree of correlation between two SAR images and is therefore a quality measure of the interferometric phase.

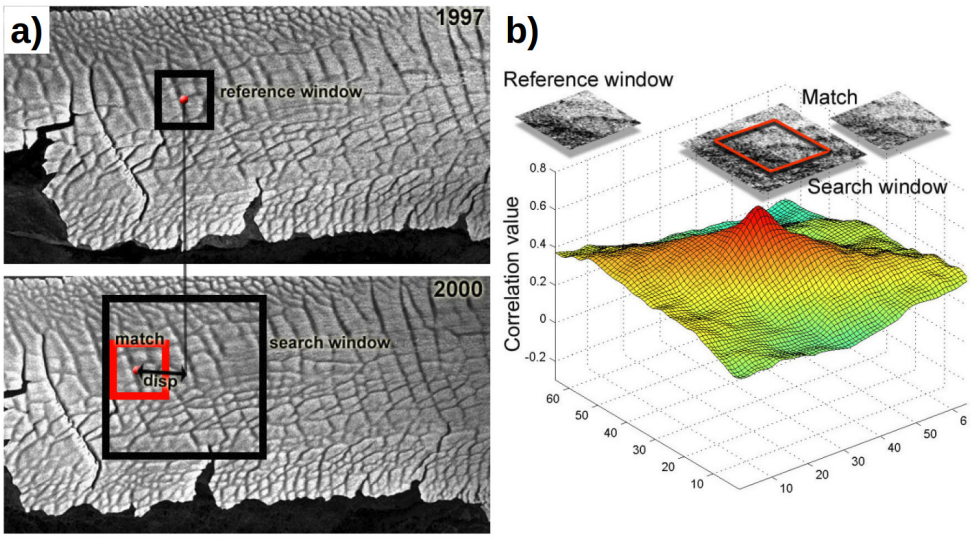

Figure 2.8: Principle of offset/speckle tracking. (**a**) Matching procedure of a reference window within a larger search window. (**b**) 2-D cross-correlation obtained after comparing a reference window with all the possible combinations in a larger search window. The match (offset) is located at the maximum of the correlation. Credit: (a) Fig. 3.5 and (b) Fig. 3.6 from Wuite (2006). [Reprinted with permission from J. Wuite].

2.1.4 Speckle tracking

Speckle tracking [4], sometimes called intensity tracking (Strozzi et al., 2002), is an offset tracking procedure that provides horizontal velocity fields by cross-correlating small image patches between 2 SAR images (Gray et al., 1998, 2001, Michel and Rignot, 1999). The wider applicability of the technique, which only requires two images (and less coherence) comes at the expense of a lower accuracy and poorer spatial resolution.

The conceptual principle of speckle tracking (and other offset tracking procedures) can be seen as a refinement of the co-registration used for InSAR and is illustrated in Fig. 2.8. Two SAR images of the same ice shelf from different times are compared. The displacement that occurred between the first (Fig. 2.8 a-top) and the second (Fig. 2.8 a-bottom) images is computed by taking a reference window in the first scene and comparing it against a larger search window in the second image. The matching window (red) is found at the peak in correlation (Fig. 2.8 b). The location of the matching window is then converted to displacement and horizontal velocity. This specific example tracks visible features in the ice shelf but one could also track the speckle with much smaller search windows.

In practice, speckle tracking occurs in three steps:

1. The two SAR images acquired in the same viewing geometry first need to be precisely co-registered to account for shifts due to slightly different orbit configurations (Fig. 2.9). As orbits of ALOS-PALSAR (the sensor used here) are not constrained well enough, the general/orbital offset are determined from stable reference points in the images (Strozzi et al., 2002). If conceptually simple, this step is nevertheless tricky for ice shelves like the RBIS, where virtually every pixel is moving, and where rocky outcrops are absent. We overcome this issue by only using the grounded and slow-moving parts of the scenes – namely the pinning point, Derwael Ice Rise and the western promontory (Fig. 1.13 and

[4] Speckle-, intensity-, coherence-, SAR feature- tracking are many names for similar – but slightly different – concepts that are gathered under the generic term of *offset tracking*. As a result, different authors use the same terms for different concepts (e.g. Gray et al., 2001, Rott, 2009, with speckle tracking). Here, we consider speckle tracking as the offset-tracking procedure that exclusively relies on the amplitude/intensity of SAR images. See Strozzi et al. (2002) for a thorough discussion of speckle and coherence tracking.

Section 1.3) – to determine and remove the orbital offset with a 2D-polynomial based on the cross-correlation. This is further discussed in Section 5.1.1.

2. A similar matching procedure is then re-applied but this time on the two co-registered images, assuming that residual offsets ('K' in Fig.2.9) are caused by displacement.

3. Ground-range and azimuth offsets fields are converted to X and Y velocities, calibrated and post-processed (e.g. filtering, georeferencing, etc.).

Note that speckle tracking relies on the same principle as *feature tracking* with optical images. The only difference is that instead of tracking visible features (e.g. crevasses), speckle tracking cross-correlates the pseudo-random but deterministic speckle pattern (Section 2.1.2). Accuracy of speckle tracking is one order of magnitude better than feature tracking, simply because the size of the patches needed to cross-correlate the speckle pattern can be much smaller than for visible features (Gray et al., 1998).

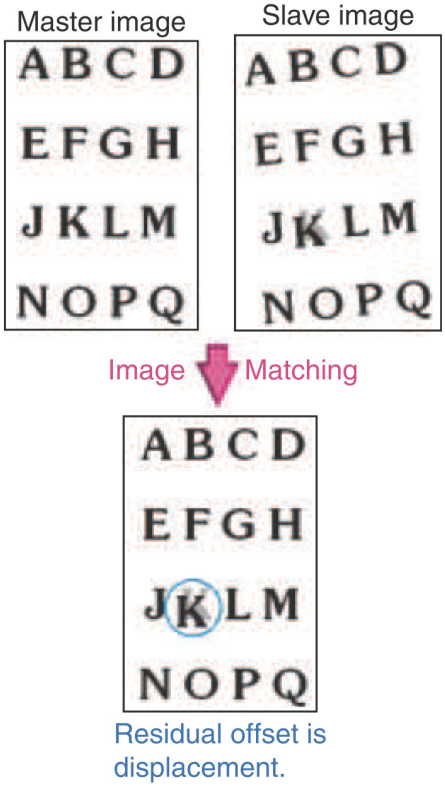

Figure 2.9: Co-registration before speckle tracking. One of the two image (the slave) is resampled to match the other one (the master). The residual offset is considered as displacement. Credit: Fig. 3 from Furuya (2011) [Reprinted with permission from Springer].

2.1.5 Summary and work conducted for this thesis

Spaceborne SAR images are more suited than optical images to study polar places, such as the RBIS because (i) SAR images are not affected by cloud-cover or lack of day-light, very frequent in Polar Regions; (ii) processing techniques based on SAR images are either not applicable to optical imagery (displacement tracking with InSAR) or provide a better accuracy/resolution than their optical counterparts (Topographic InSAR vs stereoscopy and speckle tracking vs feature tracking).

In this thesis, we map the velocities of the Roi Baudouin Ice shelf by combining InSAR on ERS 1/2 images from 1996 and speckle tracking on ALOS-PALSAR images from 2010. Both techniques are summarised in Fig. 2.10 and specific processing details are provided in Chapter 4 and the velocity field is subsequently used in Chapters 3 and 4. The choice of the sensor and techniques was constrained by the available data (and their coherence) at the beginning of the thesis. The major limitations in deriving the velocity field – the co-registration and lack of coherent SAR images – are further discussed in Section 5.1.1. Additionally, we also locate the grounding line of the RBIS, based on QDInSAR (Section 5.3.3 and Drews et al. (2017)). Although, we do not derive the TanDEM-X DEMs used in Chapter 3 ourselves, explanations about topographic InSAR have been provided here, as the DEMs play a central role in the following section.

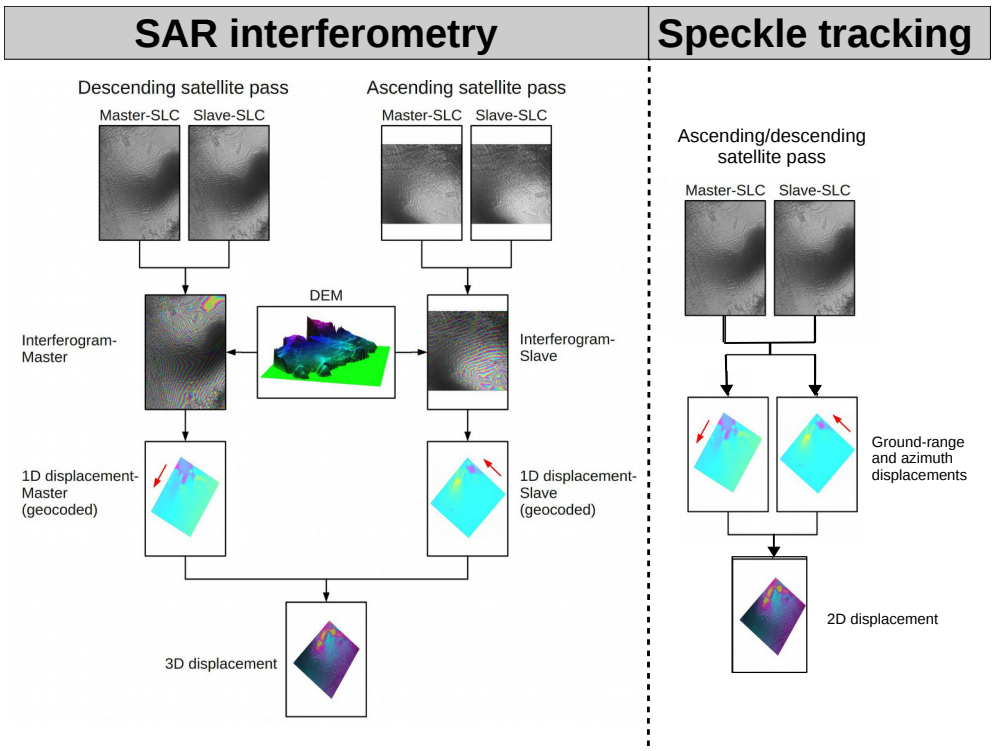

Figure 2.10: SAR interferometry vs speckle tracking. Credit: partly adapted from Neckel (2010) (with permission from N. Neckel).

2.2 Detecting the basal mass balance of ice shelves from space

2.2.1 Introduction

We have seen in Section 1.2 that melting beneath the Antarctic ice shelves regulates the ice-sheet's contribution to sea-level rise, through ice-shelf thinning and subsequent loss of buttressing. We also know that basal refreezing of marine ice can partially counteract basal melting, stabilising ice shelves (Khazendar et al., 2009). Those competing processes are brought together by the basal mass balance (BMB), a measure of the net accumulation at the ice-shelf base. Detecting the BMB of ice shelves is therefore crucial to monitor the stability of the Antarctic ice sheet. Direct BMB measurements are only obtainable from phase-sensitive radar (e.g. Nicholls et al., 2015, Marsh et al., 2016, Sun et al, in prep), which only provides point measurements. Alternatively, line-measurements of BMB are obtainable from ice-penetrating radar measurements (e.g. Bindschadler et al., 2011b, Khazendar et al., 2016). Unfortunately, point and line estimations from ground-based/airborne measurements provide limited information about spatial variations in the BMB. Spatial variability can either be obtained by combining remote sensing datasets (assuming mass conservation) or from ocean circulation models (e.g. Hattermann et al., 2014, Schodlok et al., 2016). The main hurdles of ocean modelling it that (i) it requires a good knowledge of ice-shelf cavities (not well constrained at the moment) and (ii) it is relatively coarse compared to glaciological datasets (for instance high-resolution ocean simulations are gridded to 1.5 km in Hattermann et al. (2014), while high-resolution satellite observations can be gridded to 10-125 m).

In the following we explain how we use various remote sensing datasets to map ice-shelves BMB at high resolution in a Lagrangian framework. We first present the specificities of the Lagrangian approach compared to the more traditional Eulerian method (Section 2.2.2). Then we explain how the BMB is derived from mass conservation (Section 2.2.3). Next, we focus on deriving ice-thickness – the main input to compute the BMB – from hydrostatic equilibrium

Figure 2.11: Lagrangian vs Eulerian approaches for a steady-state ice shelf. The red star is at point A at time t_0 and moves to B at time t_1. The Lagrangian frame follows the star flow and considers changes at point B (at time t_2), whereas the Eulerian frame stays fixed in space and considers changes at point A'.

(Section 2.2.4) and we close the section with a short summary of the methodology, emphasising what was carried out as part of this thesis.

Although the topic of this section is very similar to that of Chapter 3 (with some overlap in content), this section aims at providing background information for readers less familiar with concepts mentioned in the following chapter (e.g. mass conservation, Lagrangian frameworks, hydrostatic equilibrium, etc.).

2.2.2 Lagrangian and Eulerian methods

There are two ways of approaching ice-dynamics: problems can either be treated in Eulerian or Lagrangian frameworks. In the first case – the Eulerian approach – ice properties are determined at some specific points in space, where the temporal evolution of those properties are also determined. Eulerian frames are thus fixed in space. The other approach – the Lagrangian method – consists in "tagging" ice particles and following them on their journey through space. Instead of being fixed in space, Lagrangian properties and their rate-of-change move with the particles as they flow downstream.

Figure 2.11 illustrates the two different approaches, for an ice shelf in steady state. At time t_0, the ice thickness at point A has certain value. In an Eulerian frame, the thickness at time t_1 will be considered at the same location (A'). Because the ice shelf is in steady state, the Eulerian thickness does not change. On the other hand, the Lagrangian frame follows the particles and the thickness at t_1 is not considered at point A' but at point B (where the star has moved). In this case, the Lagrangian thickness change is negative, because the ice shelf spreads under its own weight and thins downstream.

Eulerian approaches are more commonly used because ice properties are more easily measured in a fixed frame (e.g. geo-referenced datasets from remote sensing). With an ice thickness H, Lagrangian and Eulerian approaches are related as follows:

$$\frac{\mathrm{D}H}{\mathrm{D}t} = \frac{\partial H}{\partial t} + \vec{u} \cdot \nabla H \tag{2.5}$$

where $\frac{\mathrm{D}H}{\mathrm{D}t}$ is the material (Lagrangian) time derivative; $\frac{\partial H}{\partial t}$ is the local (Eulerian) time derivative and $\vec{u} \cdot \nabla H$ is the convective derivative. In practice, the convective derivative is an advective term that accounts for the motion of the particles.

2.2.3 Basal mass balance and mass conservation

The principle of mass conservation is that local temporal changes of ice thickness ($\frac{\partial H}{\partial t}$) are only due to external input/output of ice (i.e. local mass balance $\dot{M}_{tot}$) and divergence in ice flux

$$\frac{\mathrm{D}H}{\mathrm{D}t} = \quad - H\,(\nabla \cdot \vec{u}) \quad + \dot{M}_s \quad + \dot{M}_b$$

Figure 2.12: Mass conservation in a Lagrangian framework. Schematic illustration of Eq. (2.7).

($\nabla \cdot (H\vec{u})$, $\vec{u}$ being the horizontal ice-velocity):

$$\frac{\partial H}{\partial t} = -\nabla \cdot (H\vec{u}) + \dot{M}_{tot} \tag{2.6a}$$

$$\frac{\partial H}{\partial t} = -\left(\vec{u} \cdot \nabla H + H\nabla \cdot \vec{u}\right) + \dot{M}_{tot} \tag{2.6b}$$

The divergence term in Eq. (2.6) is preceded by a minus sign because a negative divergence at a specific parcel of ice reflects local thickening, as more ice is entering the parcel than leaving it.

Combining Eq. (2.5) with Eq. (2.6b) and decomposing the total mass balance into its surface ($\dot{M}_s$) and basal ($\dot{M}_b$) components, we can formulate mass conservation in its Lagrangian form:

$$\frac{\mathrm{D}H}{\mathrm{D}t} = -H\,(\nabla \cdot \vec{u}) + \dot{M}_s + \dot{M}_b \tag{2.7}$$

In other words, Eq. (2.7) and Fig. 2.12 indicate that if we follow a section of an ice shelf (that does not calve), changes in ice thickness only result from external inputs and outputs at the boundaries of the ice shelf (surface and base) or from dynamic processes (ice-flow divergence). It is therefore easy to calculate the Lagrangian BMB of an ice shelf by deriving and combining the three other terms of Eq. (2.7), namely (i) surface mass balance, (ii) Lagrangian thickness change and (iii) ice-flow divergence fields. Computing those terms requires: an ice-velocity field; several thickness fields ; and a technique to follow the ice flow to be in a Lagrangian frame. The derivation of the velocity field is based on radar remote sensing, which has already been outlined (Sections 2.1.3 and 2.1.4). The Lagrangian frame is ensured with 2D cross-correlation, which relies on the same principle as co-registration and speckle tracking (Section 2.1.4). The only input that is still needed is therefore the computation of thickness, which we do in the following.

2.2.4 Hydrostatic thickness

While thickness and its evolution are essential variables to compute the BMB of ice shelves from mass conservation, current remote sensing techniques cannot map those variables directly from space. A work around consists in applying hydrostatic equilibrium to surface freeboards, themselves derived from surface elevations. While the latter has been detailed in Section 2.1.3, we detail the two former steps in the following.

A) Hydrostatic equilibrium

The hydrostatic equilibrium relies on Archimedes' Principle:

> "*Any object, wholly or partially immersed in a fluid, is buoyed up by a force equal to the weight of the fluid displaced by the object.*"
>
> Archimedes – On floating bodies

In practice, this means that for a cross section of an ice shelf, the weight of its ice is balanced by the weight of water it has displaced. Let us consider the simple case depicted in Fig. 2.13, where a cube of ice has a total thickness H and a column-averaged density $\overline{\rho}$. The ice floats over seawater of density ρ_w. We know from hydrostatic equilibrium that:

$$\overline{\rho} g H = \rho_w g H_d \tag{2.8a}$$

$$\overline{\rho} H = \rho_w (H - h_{asl}) \tag{2.8b}$$

where the total thickness is decomposed in two layers h_{asl} and H_d, the freeboard (above sea level) and draft (below sea level) heights, respectively. As the acceleration of gravity (g) cancels out in Eq. (2.8a), the hydrostatic thickness is thus given by:

$$H = \frac{\rho_w h_{asl}}{\rho_w - \overline{\rho}} \tag{2.9}$$

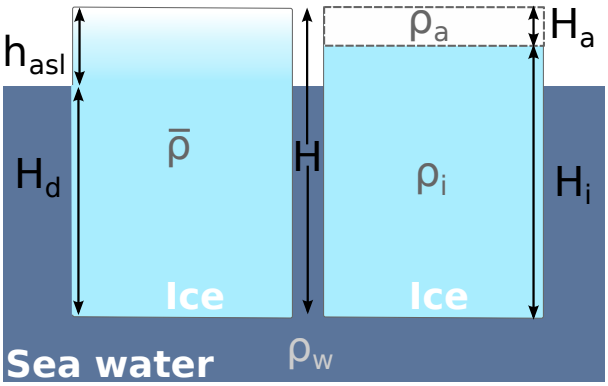

Figure 2.13: Hydrostatic thickness of an ice shelf. (**Left**) block of ice with vertically variable density due to firn compaction. (**Right**) same block of ice where the firn pack is represented as one layer of air and one layer of ice. The different variables are explained in the text.

As we can see in Fig. 2.13 (left), progressive snow compaction into firn causes vertical gradients in ice-shelf density, which laterally fluctuates because accumulation and subsequent depth of the firnpack can vary spatially. As a result, determining the column-averaged density becomes challenging. This is overcome by subdividing the thickness into one layer of air H_a with a known density ρ_a and one layer of pure ice H_i with a known density ρ_i, so that $H_i + H_a = H$ and $\overline{\rho} H = \rho_i H_i + \rho_a H_a$ (Fig. 2.13 (right)). This way the real and ice-equivalent thicknesses become:

$$H = \frac{\rho_w h_{asl}}{\rho_w - \rho_i} - \frac{H_a(\rho_i - \rho_a)}{\rho_w - \rho_i} \quad \text{and} \quad H_i = \frac{\rho_w h_{asl}}{\rho_w - \rho_i} - \frac{H_a(\rho_w - \rho_a)}{\rho_w - \rho_i} \tag{2.10}$$

The layer of air – often referred to as the firn-air content – can be obtained from atmospheric modelling (e.g. Ligtenberg et al., 2011, 2014), from ice cores (e.g. Hubbard et al., 2013) or from ground-based radar measurements (e.g. Drews et al., 2016). In this thesis, we rely on regional atmospheric modelling (Lenaerts et al., 2017) because it is the only spatially exhaustive dataset. This is further discussed in Section 5.1.2.

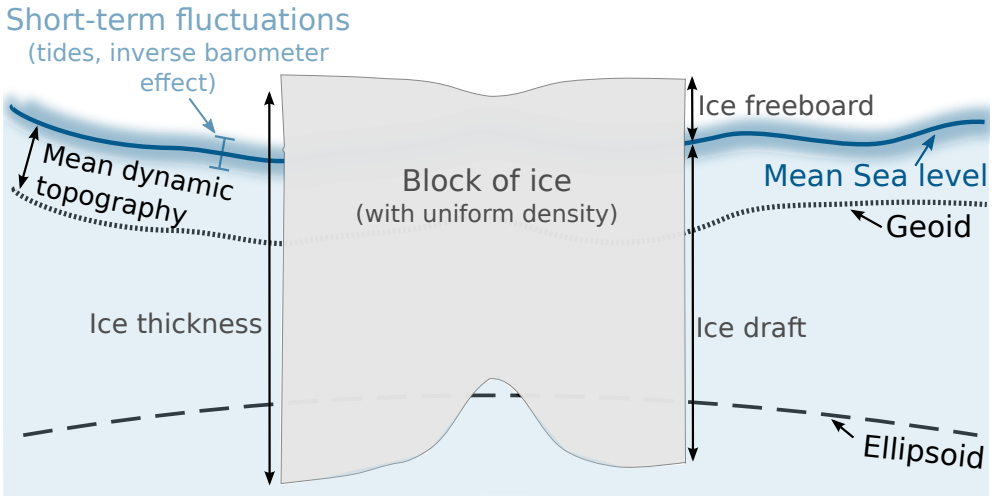

Figure 2.14: Converting elevation to freeboard heights

B) Freeboard heights

Digital elevation models from InSAR are typically referenced to the ellipsoid WGS84 (h_{WGS84}), which is an idealised mathematical representation of the Earth. Elevations must however be referenced to the mean sea level to be further converted into thicknesses (Fig. 2.14). The easiest way to do so, is to use a geoid (G) (e.g. Förste et al., 2014), which is an equipotential surface of the Earth's gravity field that approximates the mean sea level. Additionally, the mean dynamic topography (M_{DT}) (e.g. Knudsen et al., 2011) corrects small deviations between the mean sea level and the geoid, due to oceanic circulation for instance. Remotely sensed elevations are thus transformed to freeboard heights as follow:

$$h_{asl} = h_{WGS84} - (G + M_{DT}) \tag{2.11}$$

It should be noted that the actual sea level fluctuates over very short time scales (Fig. 2.14), due to tides and variable atmospheric pressure (inverse barometer effect). Those effects are nevertheless often implicitly corrected during the calibration of the DEMs.

2.2.5 Summary and work conducted for this thesis

All the processing steps of the Lagrangian BMB are summarised in Fig. 2.15 with the orange boxes indicating the external datasets used. Note that details about filtering, calibration and detrending of the DEMs are laid out in Chapter 3.

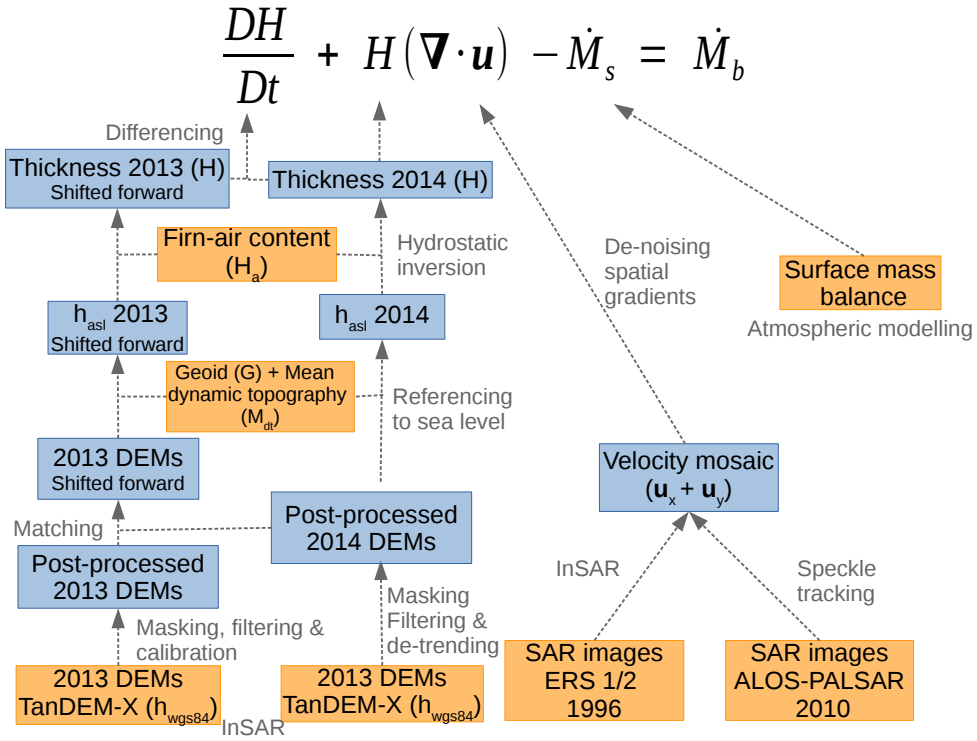

Figure 2.15: Deriving Lagrangian basal mass balance from remote sensing. This flowchart shows in blue the data processed as part of this thesis and in orange the external datasets used. Grey annotations describe processing steps.

Chapter 3

Combining satellite observations to detect ice-shelf basal mass balance

This standalone chapter is taken from a paper currently accepted and in typesetting for *The Cryosphere*:

Berger, S., Drews, R., Helm, V., Sun, S., and Pattyn, F.(2017). Detecting high spatial variability of ice-shelf basal mass balance (Roi Baudouin ice shelf, Antarctica), *The Cryosphere Discussions*, doi:10.5194/tc-2017-41, accepted.

Here we combine observations (and atmospheric modelling) to derive the basal mass balance of the Roi Baudouin Ice Shelf at high resolution. This chapters provides insight on ice-ocean interactions on sub-kilometre scales.

Part of the content of this Chapter overlaps with Section 2.2, although the scope here is different. While Section 2.2 presents the general principle of our basal mass balance-detecting technique, this chapter applies the method to the Roi Baudouin Ice Shelf. As such, we provide here specific details about the methodology. This chapter also presents and discusses the results for the specific case of the RBIS. Upscaling and broader applicability are further discussed in Section 5.1.2.

Because we combine different observations and rely on various assumptions to detect the basal mass balance of the RBIS, the outcome of this study can be viewed as a "secondary observation", an intermediary between direct observations (e.g. the flow field) and modelling initialisation (e.g. inverted basal friction), which is the focus of the next chapter (Chapter 4).

Detecting high spatial variability of ice-shelf basal mass balance, Roi Baudouin ice shelf, Antarctica

Sophie Berger[1], Reinhard Drews[2], Veit Helm[3], Sainan Sun[1], and Frank Pattyn[1]

[1]Laboratoire de glaciologie, Université libre de Bruxelles, Brussels, Belgium
[2]Department of Geosciences, University of Tübingen, Tübingen, Germany
[3]Alfred Wegener Institute, Bremerhaven, Germany

Correspondence to: S. Berger (sberger@ulb.ac.be)

Abstract.

Ice shelves control the dynamic mass loss of ice sheets through buttressing and their integrity depends on the spatial variability of their basal mass balance (BMB), i.e., the difference between refreezing and melting. Here, we present an improved technique – based on satellite observations – to capture the small-scale variability in the BMB of ice-shelves. As a case study, we apply the methodology to the Roi Baudouin Ice Shelf, Dronning Maud Land, East Antarctica and derive its yearly-averaged BMB at 10 m horizontal gridding. We use mass conservation in a Lagrangian framework based on high-resolution surface velocities, atmospheric-model surface mass balance and hydrostatic ice-thickness fields (derived from TanDEM-X surface elevation). Spatial derivatives are implemented using the total-variation differentiation, which preserves abrupt changes in flow velocities and their spatial gradients. Such changes may reflect a dynamic response to localised basal melting and should be included in the mass budget. Our BMB field exhibits much spatial detail and ranges from -14.7 to 8.6 m a^{-1} ice equivalent. Highest melt rates are found close to the grounding line where the pressure melting point is high, and the ice-shelf slope is steep. The BMB field agrees well with on-site measurements from phase-sensitive radar, although independent radar profiling indicates unresolved spatial variations in firn density. We show that an elliptical surface depression (10 m deep and with an extent of 0.7×1.3 km) lowers by 0.5 to 1.4 m a^{-1}, which we tentatively attribute to a transient adaptation to hydrostatic equilibrium. We find evidence for elevated melting beneath ice-shelf channels (with melting being concentrated on the channel's flanks). However, farther downstream from the grounding line, the majority of ice-shelf channels advect passively (i.e. no melting nor refreezing) toward the ice-shelf front. Although the absolute, satellite-based BMB values remain uncertain, we have high confidence in the spatial variability on sub-kilometre scales. This study highlights expected challenges for a full coupling between ice and ocean models.

1 Introduction

Approximately 74% of the Antarctic ice sheet is surrounded by floating ice shelves (Bindschadler et al., 2011a) providing the interface for interactions between ice and ocean. Marine ice sheets – characterized by a bed elevation below sea level and sloping down towards the interior – can be destabilised leading to a marine ice sheet instability (Mercer, 1978; Schoof, 2007; Tsai et al., 2015). However, ice shelves that are laterally constrained through embayments (or locally regrounded from below),

mitigate the marine ice sheet instability (Gudmundsson et al., 2012), thus regulating the ice flux from the inland ice sheet through buttressing. Over the last decade, major advances in our understanding of the processes at this ice-ocean interface have emerged, both theoretically (e.g. Pattyn et al., 2013; Favier et al., 2012, 2014; Ritz et al., 2015) as well as from observations (e.g. Rignot et al., 2014; Wouters et al., 2015). It is now established that ice-shelf integrity plays an important part in explaining sea-level variations in the past (Golledge et al., 2014; DeConto and Pollard, 2016), enabling improved projections of future sea-level rise (Golledge et al., 2015; Ritz et al., 2015).

Ice-shelf integrity can be compromised by atmospheric driven surface melt-ponding (Lenaerts et al., 2017) and hydrofracturing (Banwell et al., 2013; Scambos et al., 2004; Hulbe et al., 2004). From the ocean side, ice shelves may thin or thicken (Paolo et al., 2015) due to changes in basal mass balance (BMB), i.e. the difference between refreezing and melting. Point measurements with phase-sensitive radars (Marsh et al., 2016; Nicholls et al., 2015), global navigation satellite system (GNSS) receivers (Shean et al., 2017), observations from underwater vehicles (Dutrieux et al., 2014) and analysis from high-resolution satellites (Dutrieux et al., 2013; Wilson et al., 2017) have shown that BMB varies spatially on sub-kilometre scales. Ice-shelf channels are one expression of localised basal melting (Stanton et al., 2013; Marsh et al., 2016) which, after hydrostatic adjustment, form curvilinear depressions visible at the ice-shelf surface (Fig. 1). These surface depressions reflect basal incisions resulting in curvilinear tracts of thin ice. In some areas, ice-shelf channels are twice as thin as their surroundings (Drews, 2015). However, the impact of ice-shelf channels on ice-shelf integrity is yet unclear because, on the one hand, excessive basal melting beneath ice-shelf channels may prevent ice-shelf-wide thinning (Gladish et al., 2012; Millgate et al., 2013) but, on the other hand, increased crevassing due to channel carving may structurally weaken the ice shelf (Vaughan et al., 2012).

Here we attempt to derive the BMB of the Roi Baudouin Ice Shelf (RBIS), Dronning Maud Land, East Antarctica, at 10 m gridding, based on mass conservation in a Lagrangian framework. The RBIS (Fig.1) is constrained by an ice promontory to the West and by Derwael Ice Rise in the East, blocking the tributary flow from Western Ragnhild Glacier – one of the largest outlet glaciers in Dronning Maud Land (Callens et al., 2014). Analyses on Derwael Ice Rise (Drews et al., 2015; Callens et al., 2016) and the larger catchment area (Favier et al., 2016) suggest that the RBIS is a relatively stable sheet-shelf system on millennial time scales. The RBIS contains a number of ice-shelf channels (Drews, 2015, and arrows in Fig. 2e), many of which start at the grounding line and extend over 230 km to the ice-shelf front.

We outline our approach of deriving the BMB, with focus on attaining high spatial resolution. Resolving BMB is challenging, because it is computed as the residual of several uncertain quantities and it relies on spatial derivatives, which amplify noise in the input data. The latter can be accounted for with spatial averaging (e.g. Neckel et al., 2012; Moholdt et al., 2014), which, however, may smear out the imprint of processes acting on sub-kilometre scales. Here, we use spatially well-resolved input data combined with total-variation regularization of the velocity gradients. This avoids spatial averaging, but still mitigates the noise in the input data. As a result, our BMB field shows high detail over different spatial scales that are validated with phase-sensitive radar, GNSS observations and ground-penetrating radar.

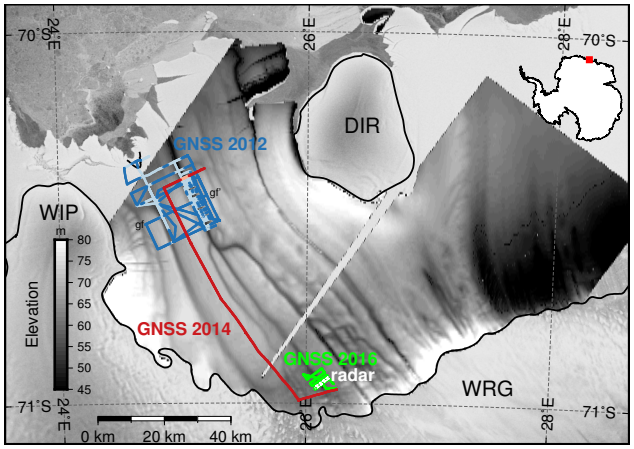

Figure 1. Overview of the topography (grey shading) of the Roi Baudouin Ice Shelf (from TanDEM-X 2014) and ground-truth datasets presented and discussed in the text (Sect 2.7 and 4). Acronyms stand for DIR: Derwael Ice Rise, WIP : Western Ice Promontory and WRG: West Ragnhild Glacier. The profile gf-gf' is shown in Fig. S2. Light blue and light red are the low-lying parts of the ice-shelf, which are excluded from the GNSS-TanDEM-X comparison in Fig. 9. "Radar" denotes both ground-penetrating and phase sensitive radars. The background is from the Radarsat mosaic (Jezek and RAMP-Product-Team, 2002) and the black line delineates the grounding line (Depoorter et al., 2013).

2 Data and methods

2.1 Basal mass balance from mass conservation

We derive the basal mass balance ($\dot{M}_b$) from mass conservation, i.e.,

$$\dot{M}_b = \frac{\partial H_i}{\partial t} + \nabla \cdot (H_i \boldsymbol{u}) - \dot{M}_s \tag{1a}$$

$$= \frac{\partial H_i}{\partial t} + (\boldsymbol{u} \cdot \nabla H_i + H_i \nabla \cdot \boldsymbol{u}) - \dot{M}_s \tag{1b}$$

$$= \frac{\mathrm{D}H_i}{\mathrm{D}t} + H_i (\nabla \cdot \boldsymbol{u}) - \dot{M}_s \tag{1c}$$

where $\dot{M}_s$ is the surface mass balance (SMB, positive values for mass gain), H_i is the ice thickness and $\boldsymbol{u}$ the column-average horizontal velocity of the ice. $\dot{M}_b$, $\dot{M}_s$ and H_i are given in ice-equivalent units. $\partial H_i/\partial t$ and $\mathrm{D}H_i/\mathrm{D}t$ represent the Eulerian and Lagrangian thickness change, respectively and $\nabla \cdot (H_i \boldsymbol{u})$ denotes the flux divergence, that includes advection of thickness gradients ($\boldsymbol{u} \cdot \nabla H$) and ice-flow divergence ($H_i \nabla \cdot \boldsymbol{u}$). In principle, Eq. (1) does not depend on the reference frame and can be calculated in both a fixed coordinate system (i.e. Euler coordinates) or with a moving coordinate system that follows the ice flow (i.e. Lagrange coordinates). In practice, however, both approaches differ: Eulerian studies are often based on one thickness field and either assume steady-state (Rignot and Steffen, 2008; Neckel et al., 2012) or rely on an external dataset (Depoorter et al., 2013; Rignot et al., 2013) to account for the thickness changes $\partial H_i/\partial t$ (e.g. Pritchard et al., 2012; Paolo et al., 2015).

Table 1. Key features of the main input datasets used to compute the variables of Eq. (1c).

Type of data	**Observations/Modelling** Reference	Dataset/Model	gridding	Use (Eq.)	Average (min ; max)
Surface elevation	**Observations** this study	TanDEM-X	10 m	$\frac{\mathrm{D}H_i}{\mathrm{D}t}$, H_i	63.8 m (19.8 ; 117.4)
Velocity	**Observations** Berger et al. (2016)	ERS1/2 ALOS PALSAR	125 m	$\nabla \cdot \boldsymbol{u}$	189.7 m a^{-1} (0.1 ; 378.2)
Surface Mass Balance	**Modelling** Lenaerts et al. (2017, 2014)	RACMO 2.3	5.5 km	$\dot{M}_s$	0.3 m a^{-1} (0.0 ; 1.0)
Firn-air content	**Modelling** Lenaerts et al. (2017) Ligtenberg et al. (2011)	RACMO 2.3	5.5 km	H_i	12.8 m (0.0 ; 22.5)
Mean Dynamic topography	**Modelling & observations** Knudsen and Andersen (2012)	DTU12MDT	0.125°	H_i	-0.1 m (-0.9 ; 0.6)
Geoid	**Modelling & observations** Förste et al. (2014)	EIGEN-6C4	0.125°	H_i	17.0 m (14.6 ; 19.8)

The Lagrangian approach, on the other hand, requires two thickness fields covering different time periods from which the Lagrangian thickness change is calculated implicitly ($\mathrm{D}H_i/\mathrm{D}t$). As shown below, the key difference between both approaches is how the advection of thickness gradients ($\boldsymbol{u} \cdot \nabla H$) is accounted for. The Lagrangian approach is best-suited in areas with rough surface and significant advection (e.g. near ice-shelf channels). We refer to previous publications (Dutrieux et al., 2013; Moholdt et al., 2014; Shean et al., 2017) that further explain differences between Eulerian and Lagrangian approaches.

In the following, we describe surface velocities in Sect. 2.2, surface mass balance in Sect. 2.3, the derivation of hydrostatic ice thickness in Sect. 2.4 and Lagrangian thickness change in Sect. 2.5. Key features of the input datasets are summarised in Table1. As a novelty compared to previous studies, we base our hydrostatic thickness field on high-resolution digital elevation models (DEMs) derived from TanDEM-X images from 2013 and 2014. Section 2.6 explains the implementation of spatial velocity gradients ($\nabla \cdot \boldsymbol{u}$ in Eq. (1)), which is non-trivial when derivatives are taken over short distances with noisy input data. We compare the derived Lagrangian Basal Mass Balance (LBMB) with field measurements of phase-sensitive radar and GNSS profiling (Sect. 2.7). Although this is not a direct validation, as the field data cover a different period, the comparison is insightful to understand the spatial variability in our LBMB field. The derived LBMB is only valid in freely floating areas, which excludes the grounding zone, but also other small-scale features such as ice-shelf channels where viscous inflow can occur (Humbert et al., 2015; Drews, 2015). (Examples where this may be the case are discussed in Sect. 5).

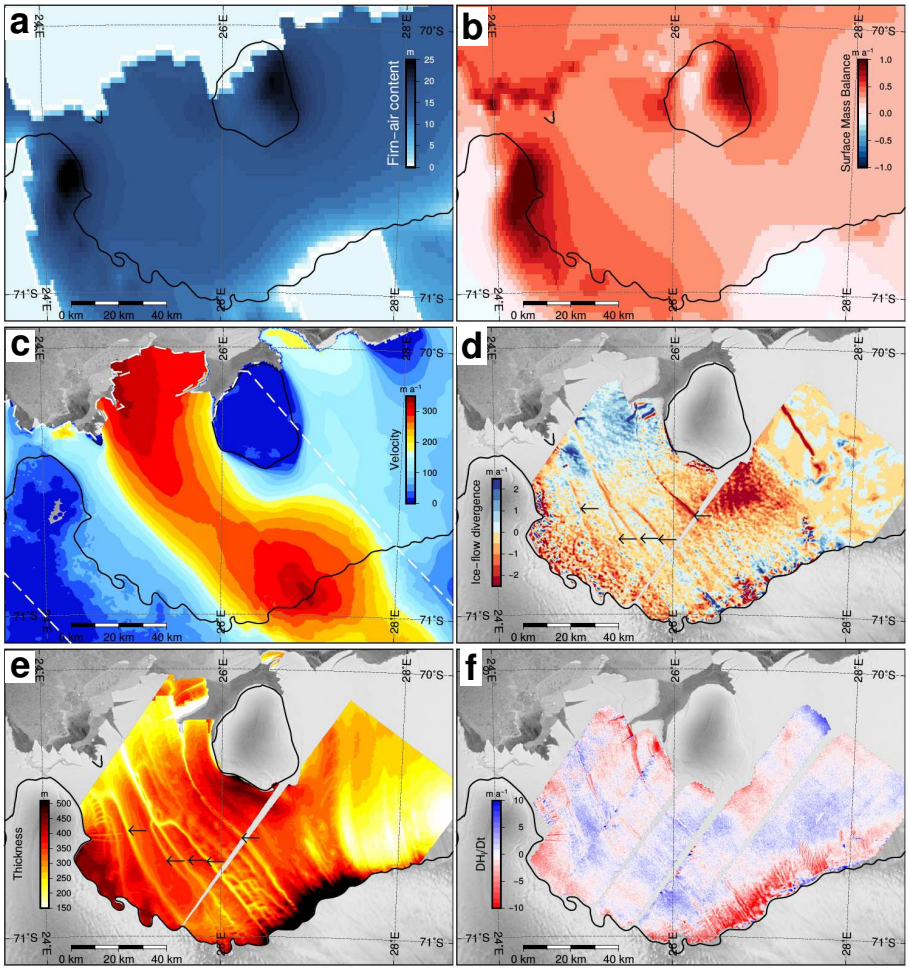

Figure 2. (a, c, e) Variables entering Eqs. (1) and (2) and (b, d , f) terms needed to calculate the LBMB in Eq. (1).
(a) Firn-air content (H_a); (b) surface mass balance ($\dot{M}_s$); (c) surface velocities ($\boldsymbol{u}$) (the white dashed line delinates the flow field from Berger et al. (2016)); (d) ice-flow divergence ($H_i\,(\nabla \cdot \boldsymbol{u})$) (Note: the red band 30km east of Derwael ice rise is caused by a seam in Rignot et al. (2011b)'s flow field); (e) hydrostatic ice thickness of 2014 (H_i) and (f) Lagrangian thickness change ($\mathrm{D}H_i/\mathrm{D}t$). Arrows in (d) and (e) locate ice-shelf channels. The background is from the Radarsat mosaic (Jezek and RAMP-Product-Team, 2002) and the black line delineates the grounding line (Depoorter et al., 2013). Key features regarding the input datasets are summarised in Table 1.

2.2 Surface velocities from satellite radar remote sensing

Assuming that velocities do not vary with depth, we use surface velocities that were previously derived by combining interferometric Synthetic Aperture Radar (InSAR) and speckle tracking (Berger et al., 2016). The velocities are mosaicked and gridded to a 125 m posting and are based on images from the European Remote Sensing satellites (ERS 1/2) from 1996 and the Advanced Land Observing System Phased Array type L-band Synthetic Aperture Radar (ALOS-PALSAR) from 2010. As shown in Berger et al. (2016), comparison with on-site measurements collected in 1965-1967 and 2012-2014 yields no evidence of prominent changes in the ice velocities over the last decades, which supports the combination of data from different dates. The velocity mosaic covers 75% of our area of interest (dashed line in Fig. 2c). The remaining areas are filled with an Antarctic-wide flow field (Rignot et al., 2011b) gridded to 900 m postings (the 450 m gridded velocities are too noisy in our area of interest). We reduce seams – as high as 60 m a^{-1} in some places – using linear feathering (e.g. Joughin, 2002; Neckel et al., 2012) over 4.5 km.

2.3 Surface mass balance from atmospheric modelling

We use the surface mass balance from a high-resolution (5.5 km posting) simulation of the Regional Atmospheric Climate MOdel (RACMO) version 2.3, centred on Dronning Maud Land ($25\,^{\circ}\mathrm{W}$ and $45^{\circ}\mathrm{W}$) and averaged over the period 1979–2015 (Lenaerts et al., 2014, 2017). The SMB field correctly reproduces asymmetries across Derwael Ice Rise originating from orographic uplift and also simulates a corresponding shadowing effect on the Roi Baudouin Ice Shelf (Fig. 2b and Lenaerts et al., 2014). Moreover, the simulation explains observed surface melting near the grounding zone due to a wind-albedo feedback caused by persistent katabatic winds in this area (Lenaerts et al., 2017).

2.4 Hydrostatic Ice Thickness

We calculate the ice thickness (Fig. 2e) by imposing hydrostatic equilibrium on surface freeboard (Bindschadler et al., 2011b; Chuter and Bamber, 2015; Drews, 2015) derived from the TanDEM-X satellites. The details of hydrostatic inversion are presented in the following two sections.

Surface elevations

The digital elevation models are processed from 43 image pairs (Fig. S1) of the TanDEM-X mission (Krieger et al., 2007), in which the TerraSAR-X and TanDEM-X satellites image the surface simultaneously from different viewing angles. This allows to infer topography interferometrically without the need to correct for ice flow. Images from the austral winters of 2013 and 2014 are processed to single-look complex scenes, using SARscape®. After coregistration using the CryoSat-2 DEM (Helm et al., 2014), the pairs are differenced in phase. The resulting interferograms are then unwrapped and the phase difference is re-flattened before being geo-referenced in polar stereographic coordinates. The processing provides 43 single DEMs (32 from 2013 and 11 from 2014) gridded to 10 m. They cover time spans of June-October 2013 and June-July 2014 (Fig. S1), with time separations ranging from 231 to 379 days in areas where thickness rates where calculated between the two years.

Digital elevation models from the same date and satellite path are concatenated together, with a linear taper on overlapping zones. Grounded areas are masked out using the composite grounding line from Depoorter et al. (2013), based on differential InSAR with Radarsat and PALSAR (Rignot et al., 2011a) at RBIS. To correct for small elevation shifts between the different frames, which we assume to be uniform over the ice shelf, we tie the 2013 concatenated frames to each other and to the CryoSat-2 DEM (Helm et al., 2014), using constant offsets. We attribute these small shifts to tides, inverse barometric effects or different calibrations during the SAR processing.

All DEMs are smoothed with a Gaussian filter to remove small-scale surface roughness. The standard deviation of the filter is set to 7 pixels (or 70 m) in all directions. This means that points lying within that distance are weighted with 0.68. To determine the size of the Gaussian filter, we investigated standard deviations from 1-10 pixels and found that using 7 pixels minimises the elevation discrepancy between 2012 GNSS and TanDEM-X surface elevation (Sect. 2.7). As shown in Fig. S2, the applied smoothing does not affect the shape of the surface depressions linked to ice-shelf channels (with a typical width of 1-2 km).

The difference fields of the 2013-2014 overlapping DEMs exhibit a linear trend aligned with the satellite trajectory. We attribute this signal to the interferometric processing, which can leave a flawed elevation trend due to imprecise information about the satellite orbits or due to ill-constrained parameters during the SAR processing (Drews et al., 2009). To account for this effect, we subtract a plane from the 2014 DEM using the difference fields of 2013-2014 overlapping fields. The plane fit and the offset correction applied earlier mask absolute $\partial H_i/\partial t$ changes, which we assume to be small in the following.

To assess the relative vertical accuracy of the final DEMs (Sect. 4.1) (i) we use the difference fields of overlapping, unconcatenated TanDEM-X frames from the same date and satellite path (Fig. S3), and (ii) we compare the DEMs to kinematic GNSS profiling. We estimate the relative vertical accuracy to be better than 1 m, although elevation differences in some areas are systematically higher (Sect 2.7). The offset and plane fitting corrections are further discussed in Sect. 4.1, as they strongly impact the quality of our ice-thickness fields and the resulting LBMB rates.

Hydrostatic equilibrium

We invert hydrostatic thickness from freeboard heights (h_{asl}) with densities of ρ_w=1027 kg m^{-3}, ρ_i=910 kg m^{-3} and ρ_a=2 kg m^{-3}, for seawater, ice and firn air, respectively :

$$H_i = \frac{\rho_w h_{asl}}{\rho_w - \rho_i} - \frac{H_a(\rho_w - \rho_a)}{\rho_w - \rho_i}. \quad (2)$$

The firn-air content H_a accounts for the lower firn and snow densities by subdividing the ice column in air- and ice-equivalent layers. We use simulated values from the firn-densification model 'IMAU-FDM' (Fig. 2a and Ligtenberg et al., 2011; Lenaerts et al., 2017), which is forced by the SMB, exists on the same spatial grid (5.5 km, Sect. 2.3) and is averaged over the same time-period (1979-2015). For converting ellipsoidal heights to freeboard elevations we employ the EIGEN-6C4 geoid (Förste et al., 2014) and the DTU12MDT mean dynamic topography model (Knudsen and Andersen, 2012). The hydrostatic ice thickness is most sensitive to the firn-air content and the freeboard heights, resulting in an estimated uncertainty of at least $\pm$ 25 m (Drews, 2015). However, as discussed in Sect. 4.1, uncertainties can be much higher in areas where firn density is ill-constrained.

2.5 Lagrangian thickness change

As the Lagrangian framework moves with the flow, computing the Lagrangian thickness change $\mathrm{D}H_i/\mathrm{D}t$ requires to shift one thickness field to match the geometry of the second one. Consequently, this approach implicitly accounts for advection of thickness gradients ($\boldsymbol{u} \cdot \nabla H_i$). Here, the 2013 TanDEM-X frames are shifted forward with a normalized correlation-coefficient matching algorithm from the computer vision library OpenCV (Bradski and Kaehler, 2008). Each 2013 concatenated frame is divided in 5×5 km patches that are sampled every kilometre in both directions. Each 2013 patch is then compared with any possible 5×5 km patch within a slightly bigger search region (6.6×6.6 km) in the 2014 DEMs that overlap with the 2013 DEM. Comparison is based on normalized cross-correlation coefficients technique, a more robust variant of 2D normalised cross correlation (Marengoni and Stringhini, 2011). The shift of the 2013 patches is found where the correlation coefficient is maximal. Mismatches are discarded when the correlation-coefficient is smaller than 0.8, or when the detected offset is well beyond what would be expected from the available flow-field. All the 2013 shifted patches are then mosaicked to construct a shifted 2013 frame that matches the geometry of its overlapping 2014 frame. The process is applied to each overlapping pair of 2013-2014 TandDEM-X frames before conversion to hydrostatic thickness.

In Sect. 4.1, we investigate an alternative approach using observed surface velocities to shift the DEMs with a 10 day time-step (as in Moholdt et al., 2014). We also apply this alternative approach to shift the 2016 GNSS profiles (Sects. 2.7, 3.2 and 5).

2.6 Spatial derivatives of noisy input data

Taking spatial gradients in Eq. (1) is not straightforward as naive discretization schemes (e.g. forward, backward or central differences) greatly amplify the signal-to-noise ratio if the input data are noisy. This issue can be accounted for by smoothing the input data (e.g. Moholdt et al., 2014) and/or by increasing the lateral distances over which the derivative is approximated (e.g. Neckel et al., 2012). However, smoothing prior to taking the derivative can lead to smearing out of the derivative in areas where the derived quantity changes abruptly (or discontinuously). We expect such abrupt changes in the surface velocities across ice-shelf channels that experience strong basal melting (Drews, 2015). To circumnavigate this problem, we applied the total-variation regularization, a technique that suppresses noise from spatial derivatives while preserving abrupt changes (Chartrand, 2011). Noise is removed from the data by reducing the total variation of the signal to a certain degree controlled by a regularization parameter α (Chartrand, 2011). The α value we use (10^5) is given by the variance of the velocities, following the discrepancy principle (Chartrand, 2011). Figure 3 compares regularized derivatives with derivatives based on velocity fields that were smoothed to varying degrees prior to taking the derivatives using central differences. It should be noted that some ambiguity about the specific choice of α remains but this is inherent to regularization in general. We discuss the benefits and trade-offs of the different derivative schemes further in Sect. 4.2.

Figure 3. Velocity divergence at an ice-shelf channel located in Fig 4. (a) Profile showing elevation and velocity divergence for various degree of smoothing (w = window width) and after regularization ($\alpha = 10^5$). (b -f) corresponding spatial pattern of the velocity-divergence profiles shown in (a) . The background image is from Landsat 8, acquired in 2014 and the maps are overlain with elevation contour lines of 1 m.

2.7 On-site geophysical measurements

Remote-sensing and modelling data are complemented by a series of geophysical measurements (ground-penetrating radar, GNSS profiling and phase-sensitive radar measurements) carried out in December 2012, December 2014 and January 2016 (Fig. 1).

The ground-penetrating radar profile shown in Fig. 8a (located in Fig. 1) was acquired in 2016 with a 20 MHz pulsed radar (Matsuoka et al., 2012). The data are geolocated with kinematic GNSS and migrated using Kirchoff-depth migration with a velocity-depth function that accounts for the low firn-air content in this area. More details about acquisition and processing of the radar data are given in Drews et al. (2015). We use the radar ice thickness to validate the hydrostatic ice thickness (Sect. 4.1).

We use three sets of kinematic GNSS profiles that were recorded at 1 Hz intervals with geodetic, multi-channel receivers moving at a speed below 12 km h^{-1}. In December 2012, a 20×25 km GNSS network was acquired at the front of the ice shelf (Drews, 2015). The profiles cross ice-shelf channels multiple times. Two years later in December 2014, a 100 km-long North-South GNSS transect was acquired (Lenaerts et al., 2017). The last GNSS dataset was acquired in January 2016, along and across an elliptical surface depression (Sect 3.2). All GNSS elevations are de-tided using the circum-Antarctic tide model (CATS2008a_opt) from Padman et al. (2002, 2008). Datasets from 2012 and 2016 are processed differentially, relative to a non-moving base station (Drews et al., 2015), while data from 2014 are post-processed with Precise Point Positioning. Elevations from GNSS are used (i) to determine the size of the Gaussian filter applied to the TanDEM-X DEMs (2012 survey, Sect. 2.4), (ii) to assess the accuracy of the TanDEM-X DEMs (2012 and 2014 surveys, Sect. 4.1) and (iii) to extend the time period of surface elevation change detected by the TanDEM-X mission (2016 survey, Sect. 3.2 and 5; Figs. 7 and 8).

BMB was measured at point locations using a phase-sensitive radar. Processing and acquisition schemes are as outlined previously (Nicholls et al., 2015; Marsh et al., 2016). The radar antennas were positioned at 22 sites. Each site was remeasured after 10 days at the same location at the surface (in a Lagrangian framework). This way, relative thickness changes due to strain thinning and basal melting can be detected within millimetres. Strain thinning is corrected using a linear approximation of the vertical strain rate with depth, based on tracking the relative displacement of internal reflectors. The strain correction of the BMB rates is small (6.6×10^{-3} a^{-1} on average), because strain thinning is small.

3 Results

3.1 Large-scale pattern of the basal mass balance

The LBMB rates range from -14.7 to 8.6 m a^{-1} (excluding outliers with 0.1 and 0.99 percentiles) and average -0.8 m a^{-1} (negative values signify melting, positive values refreezing). For the 9227 km^2 covered by the TanDEM-X DEMs, net mass loss at the ice-shelf bottom is 6.7 Gt a^{-1}. Most melting occurs just seaward of the grounding zone where the western Ragnhild Glacier feeds into the Roi Baudouin Ice Shelf (Fig. 4, label A). This area corresponds to the thickest and fastest part of the

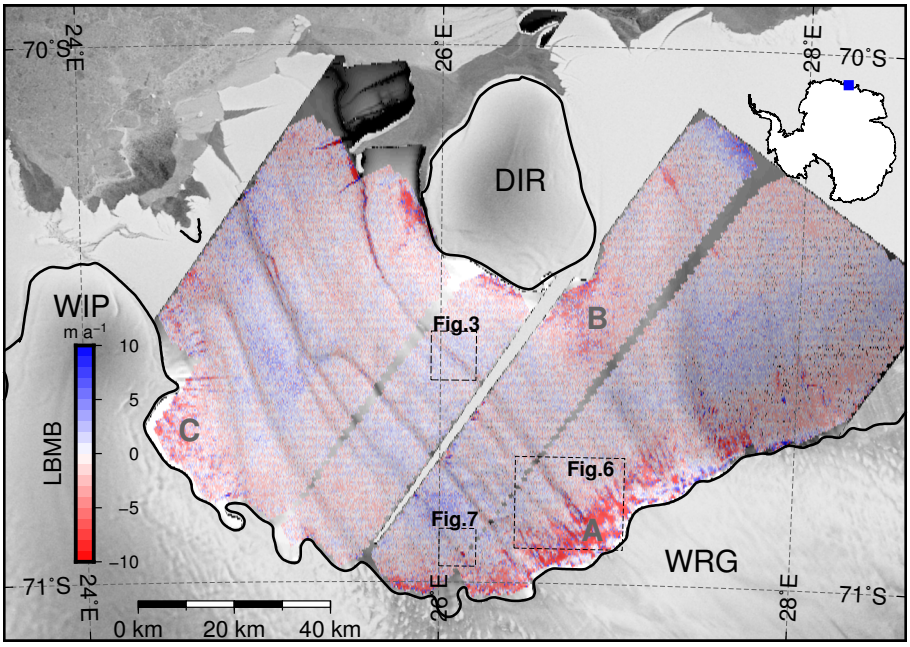

Figure 4. Lagrangian Basal Mass Balance (LBMB) of the Roi Baudouin Ice Shelf. Red and blue colours indicate basal melting and refreezing, respectively. The 3 dashed boxes locate the close-ups presented in Figs. 3, 6 and 7. Labels A-C pinpoint areas discussed in the text. Acronyms stand for DIR: Derwael Ice Rise, WIP : Western Ice Promontory and WRG: West Ragnhild Glacier. The LBMB overlays the 2014 TanDEM-X DEM. The background is from the Radarsat mosaic (Jezek and RAMP-Product-Team, 2002) and the black line delineates the grounding line (Depoorter et al., 2013).

grounding zone (Fig. 2e and c). We also find elevated melting close to the western ice promontory (Fig. 4, label C) and on the southern side of Derwael Ice Rise (Fig. 4, label B).

The uncertainties of the absolute LBMB are typically higher than the LBMB itself, because errors unfavourably propagate in mass budgets (Moholdt et al., 2014). Here, we assess a lower bound of the LBMB errors by using the difference fields of the individual LBMB frames in overlapping areas. These show no systematic patterns and the standard deviation amounts to 2.3 m a^{-1}. Moreover, comparing the (yearly averaged) LBMB values with the 22 on-site phase-sensitive radar measurements, reveals differences of 1.1 ± 2.6 m a^{-1} in mean and standard deviation, respectively. We discuss this comparison in more detail in Sect. 3.2. Figures 2b,d,f illustrate the terms entering Eq. (1c), namely surface mass balance, ice-flow divergence and Lagrangian thickness change, whereas Figs. 2a,c,e display the most critical input variables needed to compute those different terms, i.e., firn-air content, ice velocity and hydrostatic thickness. For the RBIS, the Lagrangian thickness change dominates the BMB (as in Shean et al., 2017), while ice-flow divergence and SMB are both one order of magnitude lower. Qualitatively the large-scale pattern agrees well with the results from Rignot et al. (2013) who also found the highest melt rates close to the grounding line, both for steady state or transient approximations.

To illustrate the advantages of the Lagrangian approach, Fig. 5 shows the Eulerian thickness change, flux divergence and Eulerian BMB. While the large-scale pattern of the Eulerian BMB agrees very well with that of the LBMB, the Eulerian approach fails in the vicinity of ice-shelf channels (arrows in Fig. 5). Advecting topographic features imprint the Eulerian thickness changes (Fig. 5a), however, the Eulerian approach does not fully account for this advection of thickness gradients ($\boldsymbol{u} \cdot \nabla H_i$) in the flux divergence (Fig. 5b). This results in spurious Eulerian BMB in the vicinity of ice-shelf channels (Fig. 5c). These spurious signals in the Eulerian BMB become even stronger when thinning/thickening rates are taken from external datasets which are spatially less well resolved. Using ice-shelf wide, average values (e.g. repeat satellite altimetry) does not account for the advection of ice-shelf channels and other (transient) features in the ice-shelf, hence introducing artifacts in the basal mass balance pattern.

3.2 Small-scale variability of the basal mass balance

The larger scale LBMB pattern (>10 km) is overlain by smaller-scale variability. Ice-shelf channels appear most clearly in the DEMs and thus in the hydrostatic thickness fields (arrows in Fig. 2e). In some places, they also co-locate with areas of lateral inflow (i.e., negative flow divergence; arrows in Fig. 2d) and Lagrangian thinning (i.e., negative Lagrangian thickness change in Fig. 2f). In the LBMB, ice-shelf channels appear partially as narrow bands of intense melting. Figure 6 shows one example where ice preferentially melts at the flanks of an ice-shelf channel. LBMB rates drop to -5 m a^{-1} at both flanks, whereas outside the channel the LBMB is close to zero. The slight refreezing found at the channel's apex (1.5 m a^{-1}) is very close to the detection limit and its magnitude is 3 times lower than what is observed at the flanks.

Another example of a small-scale feature is illustrated in Figs. 7 and 8. Here, we observe a 0.7×1.3 km elliptical surface depression that is up to 10 m lower than its surroundings and located on the upstream end of an ice-shelf channel. The surface topography also exhibits secondary elongated surface depressions that are shaped like fingers merging into the elliptical depression. We surveyed this area in 2016 with kinematic GNSS profiles, ground-penetrating radar and 22 point-measurements of the BMB with phase-sensitive radar (Sect. 2.7). Lenaerts et al. (2017) identified this feature as one of the 55 features on the Roi Baudouin Ice Shelf, that can be linked to the formation of englacial lakes near the grounding line. They proposed that these features are initially formed as supra-glacial lakes in the grounding zone due to katabatic wind-albedo feedback. Freezing at the lake surface and subsequent burial by snowfalls form at first englacial lakes that are advected farther downstream. As a function of the advection time the liquid water then likely fully refreezes. For the elliptical surface depression considered here, the radar data show a bright reflector at approximately 30 m depth and no coherent signals appear at larger depths (Fig. 8a). We tentatively interpret the bright radar reflector as a refrozen surface of a former supra-glacial lake. The specularity of this interface hinders deeper penetration of the radar signal. However, a more detailed radar analysis is warranted to unambiguously clarify the origin and history of this feature. Here, we restrict ourselves to the elliptical surface depression where we observe significant surface lowering.

The elliptical depression appears prominently in our LBMB field with rates as low as -12 m a^{-1} (Figs. 7b and 8b). On the eastern side of the depression, the BMB from the phase-sensitive radar (Fig. 8b) agrees well with the LBMB estimate, both methods averaging about -0.5 m a^{-1} with little spatial variability. On the western side – which contains the finger-shaped

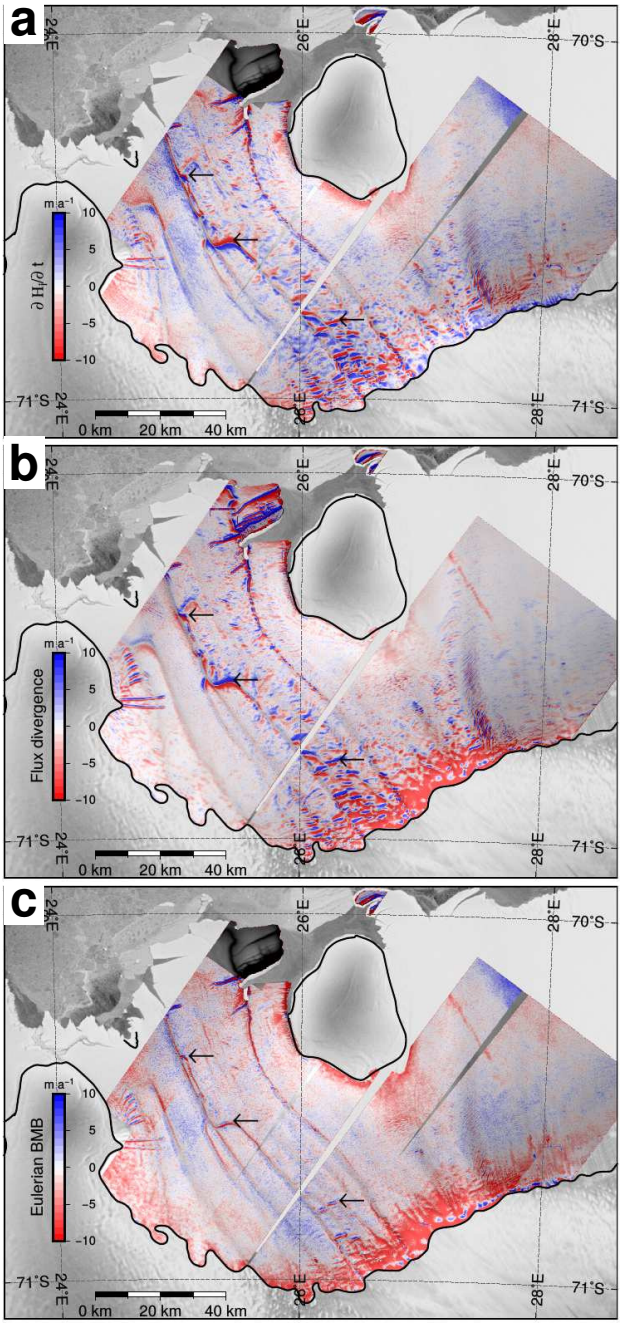

Figure 5. (a) Eulerian thickness change ($\partial H_i/\partial t$) (b) Flux divergence ($\nabla \cdot (H_i \boldsymbol{u})$) and (c) Eulerian basal mass balance (BMB). Arrows point to spurious signal due to advection of ice-shelf channels. The background is from the Radarsat mosaic (Jezek and RAMP-Product-Team, 2002) and the black line delineates the grounding line (Depoorter et al., 2013).

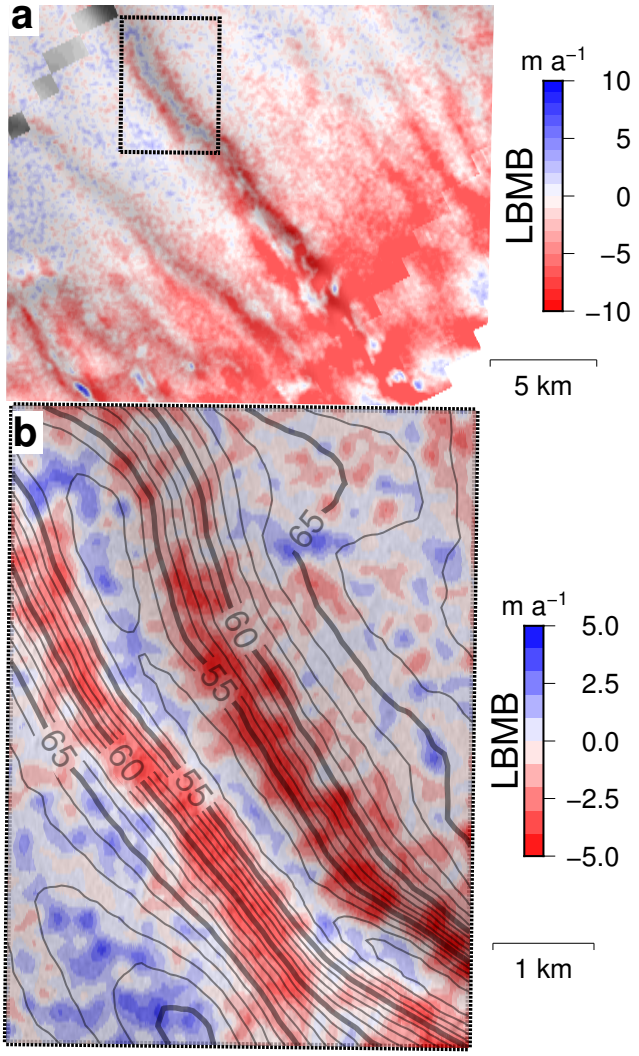

Figure 6. (a) Lagrangian basal mass balance around an ice-shelf channel near the grounding line. The box is located in Fig. 4. (b) Close-up view of the box delineated in (a), with 1 m elevation contour lines. Enhanced melting is observed at the channel's flanks.

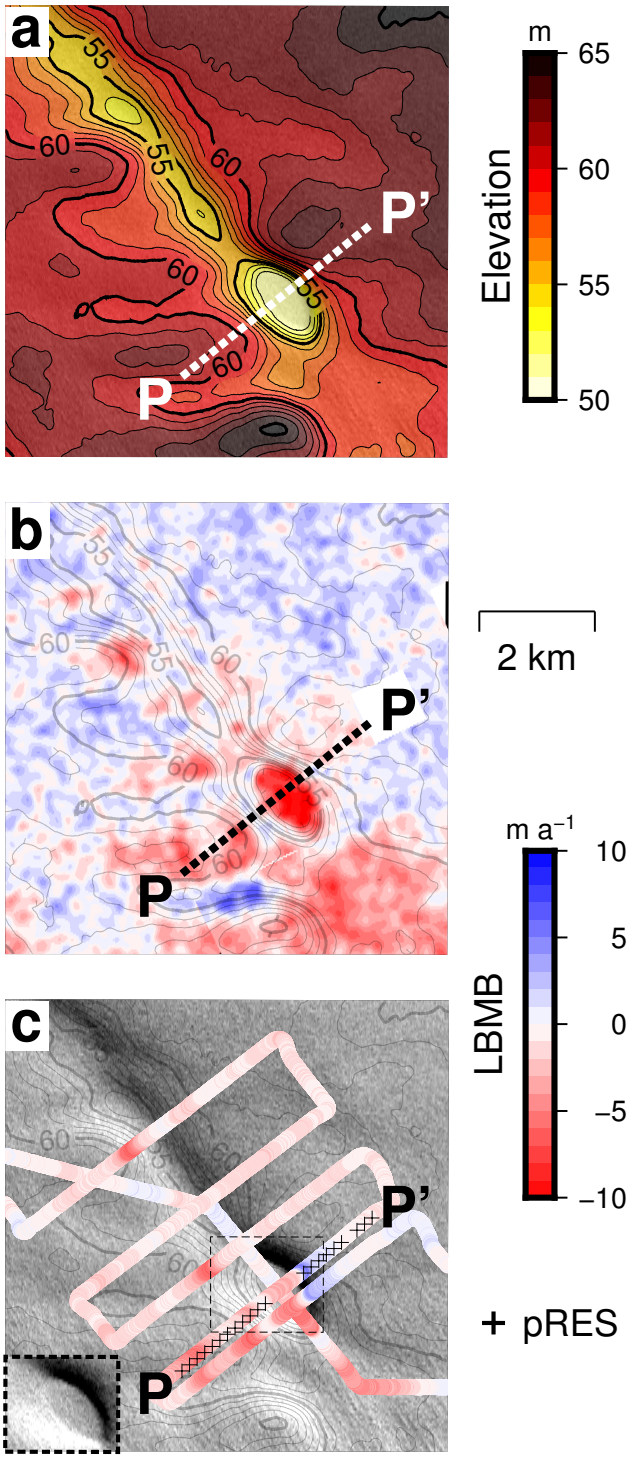

Figure 7. Close-up of the elliptical surface depression, located in Fig. 4. (a) Surface elevation from TanDEM-X DEMs from 2014. (b) LBMB (c) Landsat image of 2014 overlaid with the LBMB computed with elevations from the 2014 TanDEM-X DEMs and the 2016 GNSS profiles (using velocities to shift GNSS elevations backward). The crosses locate phase-sensitive radar (pRES) points. The profile PP' is shown in Fig. 8. All subfigures are overlain with the surface elevation contour lines of 1 m.

surface features – larger differences and variability occur. The differences could reflect the more complex topography and/or temporal variations. The large negative LBMB rates in the elliptical depression reflect persistent surface lowering of 0.5 to 1.4 m a^{-1}. Ice-flow divergence is negligible at that location. We extend the time series from the TanDEM-X DEMs to 2016 with the GNSS profiles (Fig. 8c) where we find the same localised lowering. This indicates that the high-resolution TanDEM-X DEMs reliably pick up surface elevation changes on sub-kilometre scales. Some of the finger-shaped surface depressions also show surface lowering, but less pronounced than what is seen in the elliptical depression itself. The flanks of the surface depression are significantly steeper on the eastern compared to the western side. Unlike the elliptical depression, the ice-shelf channel located farther downstream does not actively experience melting or refreezing. Away from ice-shelf channels or other surface depressions, our assumptions for the LBMB (such as hydrostatic equilibrium) likely hold explaining the comparatively good fit with the phase-sensitive radar measurements. Inside the elliptical depression, the observed surface lowering cannot unambigously be attributed to basal melting. Regardless of the specific mechanisms causing the surface lowering, this example highlights that much of the small-scale variability seen in the resulting LBMB field can be used to investigate sub-kilometre-scale ice-shelf processes that do not necessarily occur at the ice-shelf base.

4 Error sources

4.1 Hydrostatic thickness and Lagrangian thickness change

The Lagrangian thickness change is the dominant error source of the LBMB for the Roi Baudouin Ice Shelf, since the magnitude of both ice-flow divergence and SMB are one order of magnitude smaller (Fig. 2). The Lagrangian thickness change depends (i) on factors controlling the hydrostatic ice thickness, i.e. the surface elevation (above sea level), the seawater and ice densities, the depth of the firnpack and temporal variations thereof; and (ii) on the Lagrangian matching of the DEMs following the ice flow. It should also be clear that our approach is only able to detect basal changes reflected in the surface elevations, because ice thickness is derived from hydrostatic equilibrium.

Calibration and accuracy of TanDEM-X elevations

The interferometric DEMs provide excellent spatial resolution at the cost that they require calibration. It is straightforward to offset the DEMs to account for the relative phase unwrapping using Antarctic-wide DEMs based on altimetry. More challenging are residual phase trends that may originate from imprecise satellite orbits/SAR processing (Drews et al., 2009) or represent unaccounted tilting of the ice-shelf surface due to tides. In our case, these trends are near-linear and become evident in the difference fields of overlapping DEMs from both different years and from the exact same date and satellite path. In the former, systematic biases extend in the azimuth direction with residual height differences typically ranging from -0.5 to +0.5 m. Such biases strongly imprint the corresponding LBMB fields resulting in a mosaic with linear trends typically ranging from -10 to +10 m a^{-1} in the azimuth direction and differences exceeding 13 m a^{-1} across seams. To account for this, we correct the 2014 DEMs with plane fitting (Sect. 2.4).

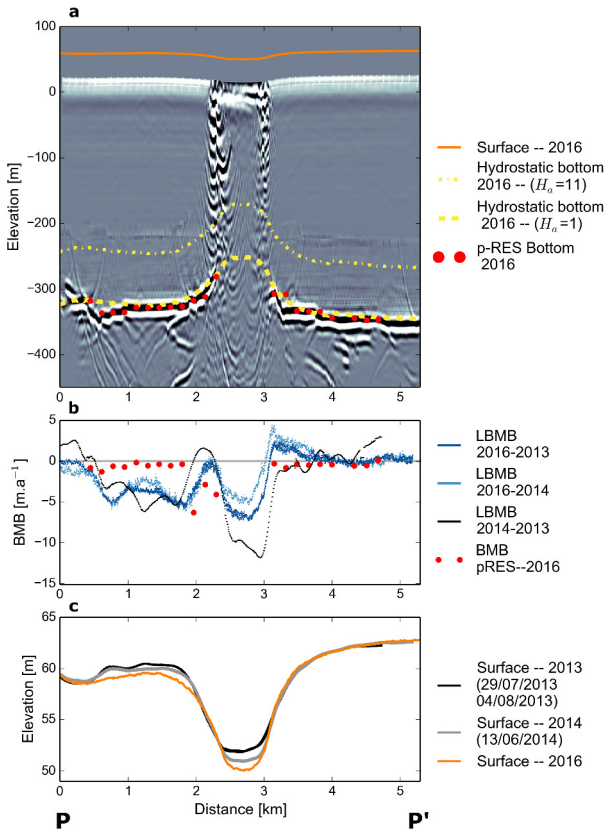

Figure 8. Profile PP' across the elliptical surface depression located in Fig. 7. (a) Ice thickness from profiling and phase-sensitive radars together with the hydrostatically inverted surfaces from 2016, measured with GNSS. (b) Different time slices of the basal mass balance. Data from 2013 and 2014 are based on the TanDEM-X DEMs, data from 2016 use GNSS surface elevations. (c) Surface lowering at the elliptical depression: surface elevation between the 2016 GNSS profile and the TanDEM-X profiles from 2013 and 2014. Elevations are referenced to the WGS84 ellipsoid and all profiles are shown in Lagrangian coordinates

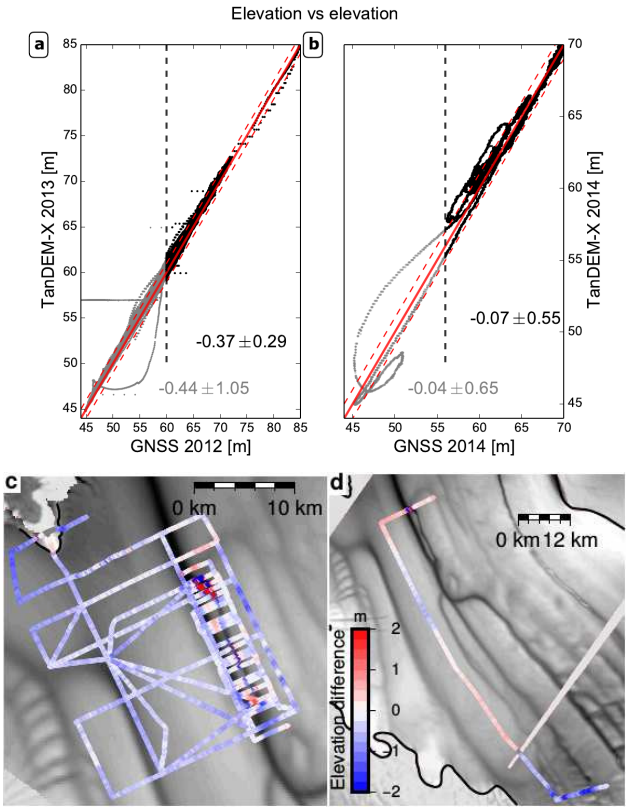

Figure 9. (a – b) Comparison between GNSS 2012 – TandDEM-X 2013 and GNSS 2014 – TanDEM-X 2014, respectively. The GNSS data are located in Fig. 1. The grey points, on the left on the vertical dashed lines, lie in ice-shelf channels and are shown in light blue and light red in the profiles in Fig. 1. The plain and dashed red lines show the perfect equality between the two elevations datasets and the ±1 m difference, respectively. (c – d) spatial variations of elevation differences between GNSS 2012 – TandDEM-X 2013 and GNSS 2014 – TanDEM-X 2014, respectively. Background is from TanDEM-X elevations.

We do not correct for systematic trends in individual TanDEM-X frames from the same dates (Fig. S3), not only because the discrepancies are smaller, but also because the small overlapping areas would amplify plane-fitting errors dozens of kilometres away. The standard deviation of the difference fields reduces to 0.3 m after plane fitting. An exception is the two northernmost difference fields, where a trend ranging from -0.8 to 0.8 m remains. In addition to residual phase trends, discrepancies of ~0.5 m can occur in areas where surface slope is locally elevated (e.g ice-shelf channels or surface ridges). Altogether, we therefore estimate the SAR processing uncertainties to be in the order of 0.5 m.

Next, we compare the 2013 and 2014 DEMs with kinematic GNSS profiles from 2012 and 2014, respectively. The time lag between the satellite data acquisition and the collection of ground-truth data is hereby 8-10 months for the 2013 DEMs, and 5-6 months for the 2014 DEMs. For 2012-2013, differences are -0.44±1.05 m, and for 2014 -0.04±0.65 m. The largest discrepancies occur in both datasets near ice-shelf channels were ice advection within the multiple months time lag is significant

(Figs 9). Removing those areas reduces the discrepancies to -0.37±0.29 m in 2012-2013, and -0.07±0.2 m in 2014. Ignoring the dynamic influence of ice-shelf channels, the highest discrepancies are found in the most upstream part of the 2014 GNSS profile (Fig. 9d). There, TanDEM-X elevations are systematically overestimated by up to 2 m near the grounding line. We attribute this bias to decreasing penetration of the TanDEM-X signal, as the firn-air content decreases towards the grounding zone (Fig. 2a). The X-band radar signal can penetrate up to 8-10 m in cold dry snow (Humbert and Steinhage, 2011), and the bulk part of such a signal penetration would be accounted for during our offset correction. However, errors due to spatial variations of signal penetration remain but affect both the 2013 and 2014 DEMs. To conclude, we estimate that in most areas the relative accuracy of the TanDEM-X DEMs is in the sub-meter range. Errors are slightly elevated in areas where the local surface slope is high, and surface elevation is systematically and significantly overestimated by up to 2 m in a narrow belt close to the grounding line.

Hydrostatic inversion

The main uncertainties for the hydrostatic inversion are referencing the surface elevation to height above sea level, and accounting for density variations. The former depends on the geoid, the mean dynamic topography, tides, atmospheric pressure variations and eustatic sea level. Drews (2015) estimates errors in the geoid and the dynamic topography for RBIS to be within ±1 m. We account for tides and atmospheric pressure variations implicitly by offsetting the TanDEM-X DEMs to the CryoSat-2 DEM, which contains these corrections. The smallest component in the error budget are changes in eustatic sea level rise, which we neglect.

Variations in firn-air content are important because these propagate with a factor of 9 into the hydrostatically inverted ice thickness (Eq. 2). We illustrate this point along profile PP' where the inferred thickness from radar profiling and from phase-sensitive radar agree closely, but the hydrostatic thickness is >80 m thinner (Fig. 8a). Because surface elevation is well constrained by our kinematic GNSS profiles (Fig. 8c), we attribute this large, unphysical mismatch to an overestimation of the firn-air content. The firn densification model predicts a value of 11 m at that location. However, in the field it became evident that this area is close to a spatially extensive blue-ice area where firn-air content is negligible. Reducing the firn-air content to 1 m reconciles the hydrostatic ice thickness with the observed radar ice thickness (Fig. 8a). Such a large deviation of the modelled firn-air content may be site-specific because it is located in the transition zone where turbulent mixing by the katabatic winds and a wind-albedo feedback form a micro-climate that causes extensive surface melting with not yet fully understood effects on the firn densification (Lenaerts et al., 2017). The impact of the firn-air-content misestimation on the derivation of the hydrostatic ice thickness is further discussed in Lenaerts et al. (2017). Moreover, Drews et al. (2016) used wide-angle radar measurements in conjunction with ice coring and found that firn density varies spatially over tens of kilometres scales, in particular across ice-shelf channels, where surface melt water collects in the corresponding surface depressions and locally refreezes. Therefore, we anticipate that at least some of the variability seen in the LBMB field is due to unresolved variations in firn density.

Because of unaccounted variations in firn density, and uncertainties in referencing the freeboard height, our ice thickness field has a lower bound error of at least ±25 m (Drews, 2015). In some areas the error can be considerably larger. However,

the corresponding impact on the inferred LBMB rates is mitigated by the low ice-flow divergence rendering the magnitude of ice thickness less important (Eq. (1c)).

Lagrangian matching

Computing the Lagrangian thickness change, requires matching the DEMs to account for ice advection. We use a normalised cross-correlation to match 5×5 km patches from 2013 to the 2014 geometry (Sect. 2.5). Alternatively, the matching can be based on the surface flow field (Moholdt et al., 2014). For the DEMs, this methods yields similar results in terms of the large-scale LBMB pattern, but introduces erroneous positive/negative patterns near ice-shelf channels. This is because the flow velocities are not sufficiently constrained for the flow direction, and tilts by a few degrees cause a significant mismatch in areas where thickness gradients are larger. On the other hand, the 2016 GNSS have to be matched with the velocities, because 2D cross-correlation fails with profiles.

4.2 Ice-flow divergence: the benefits of regularized derivatives

The high-resolution velocity field is too noisy in magnitude to approximate the derivatives in the flow divergence with finite differencing of neighbouring cells (gridded to 125 m posting). This can be accounted for by smoothing the velocity field prior to taking the derivative. However, this type of smoothing can blur abrupt changes in the flow velocities and corresponding strain rates. This is important, because we suspect that ice-flow velocities change abruptly in ice-shelf channels that experience strong basal melting (Drews, 2015). We, therefore, explore the use of total-variation regularization which treats abrupt (and discontinuous) changes more accurately (Chartrand, 2011). Figure 3 illustrates a close-up of an ice-shelf channel (inset "Fig.3" in Fig. 4) where we compare the "Normal" (unsmoothed) velocity divergence (b) with its regularized (c) and smoothed (c-e) versions. For the latter, we applied average filters of 375×375 m, 1,125×1,125 m and 1,875×1,875 m (i.e. kernels of 3×3, 9×9 and 15×15 pixels, respectively) to the velocity field, before computing the gradients. The enhanced velocity-divergence has a similar magnitude in the regularized and the smoothed version using a 375×375 m window. However, the latter is noisier outside the ice-shelf channel than the regularized version. In the regularized case, velocity divergence at the channel's apex is 8%, 24% and 40% lower than for the 375×375 m, 1,125×1,125 m and 1,875×1,875 m kernels, respectively. However, the inferred LBMB rates are insensitive to the technical implementation of the derivatives, because the Lagrangrian thickness change controls the signal at RBIS. Nevertheless, in order to study the dynamics of the smaller-scale ice-shelf channels, efficiently denoising the derivatives becomes increasingly important, in particular for ice shelves where the dynamic thinning terms is more important.

4.3 Surface mass balance

Both the firn-air content and the SMB are spatially less well resolved than our ice thickness and velocity fields. Consequently, we do not capture their spatial (and temporal) variations on the length scales associated with ice-shelf channels. Both Drews et al. (2016) and Langley et al. (2014) found evidence in the shallow radar stratigraphy that the SMB may be locally elevated

in those areas, potentially reflecting the deposition of drifting snow at the bottom of surface slopes (Frezzotti et al., 2007). If this holds true, then the systematic underestimation of the SMB would result in a positive bias of the LBMB in those areas.

5 Discussion

The large-scale patches of enhanced basal melting (Sect. 3.1; labels A-C in Fig. 4) are sufficiently far away from the tidal bending zone so that we can safely assume hydrostatic equilibrium. These regions are also detected by Rignot et al. (2013), based on different input datasets (i.e. Eulerian thickness change based on ICESat-1). Patches A-C line up with deepest parts of the ice-shelf base and the largest gradients in the hydrostatic ice thickness. A large ice draft fosters basal melting because the freezing point is lower with depth (e.g. Holland et al., 2008). The steep basal slopes facilitate entrainment of heat in the mixed layer beneath the ice shelf increasing basal melting (Jenkins and Doake, 1991; Little et al., 2009).

The smaller-scale variations in LBMB are more difficult to interpret, because these are overlain by unaccounted variations in firn density, SMB, and ice that is not in hydrostatic equilibrium. Nevertheless, the comparison with the phase-sensitive radar data and the kinematic GNSS profiling increases our confidence that much of the relative variability that we observe here is meaningful. The surface lowering of the elliptical surface depression is consistently observed over a 3-year time period marking this zone as dynamically active. Two other options are: (i) a transient adjustment of the surface towards hydrostatic equilibrium (Humbert et al., 2015) as a response to some unknown event in the past which locally reduced the ice thickness, and (ii) the surface lowering may reflect vertical creeping of a liquid water body through the ice column. In any case, the surface lowering is restricted to a small area and the ice-shelf channel farther downstream appears passive (i.e. does not show significant melting nor refreezing).

In most areas, ice-shelf channels at RBIS seem to advect passively and basal melt rates there do not significantly stand out from those in the larger surrounding. Exceptions are the locally elevated basal melt rates in ice-shelf channels in the interior of the RBIS (e.g. inset “Fig. 3” in Fig. 4) and close to the grounding zone (Fig.6 and its corresponding inset in Fig. 4). Almost all ice-shelf channels at RBIS are connected to the grounding line and may arise from water-filled subglacial conduits injecting subglacial-melt water into the ice-shelf cavity, driving a spatially localised buoyant melt-water plume (Jenkins, 2011; Le Brocq et al., 2013; Drews et al., 2017; Sergienko, 2013). Such localised melting near the grounding zone has been previously observed on Pine Island Ice Shelf using similar methods as done here (Dutrieux et al., 2013). However, on Pine Island Ice Shelf, background melt rates are an order of magnitude larger than what is observed here (Depoorter et al., 2013; Rignot et al., 2013) and Dutrieux et al. (2013) analysed DEMs separated by 3 years (compared to the 1 year time period used here). This explains why locally elevated BMB values appear more clearly on other ice shelves. We find some evidence that basal melting is concentrated on the flanks, rather than on the apex (Fig. 6). This accords both with observations (Dutrieux et al., 2014) and modelling (Millgate et al., 2013). Dutrieux et al. (2014) suggest that the presence of a colder water blocks the heat flux from below near the apex of the channel. Alternatively, modelling suggests (Millgate et al., 2013) that a geostrophic current develops beneath the channels (if the channels are wide enough) which preferentially melts at the channel’s flanks. This seems less likely here because ice-shelf channels near the grounding line are narrow (i.e. a few hundred meters wide and high).

In summary, our observations suggest that the LBMB varies on multiple spatial scales which has several implications. First, point measurements with phase-sensitive radars are not necessarily representative for a larger area. Particularly in areas where thickness gradients are large, phase-sensitive radar measurements are best understood in combination with satellite-based estimates covering larger spatial scales. On the other hand, on-site point measurements are crucial to estimate the quality of the satellite-based BMB estimates, which are uncertain in their magnitude. Second, this sub-kilometre variability in ice-ocean processes poses challenges for coupling ice flow with ocean models, because highly resolved ocean models and community efforts, such as the Marine Ice Sheet–Ocean Model Intercomparison Project (MISOMIP), are typically gridded with 1-2 km (Dinniman et al., 2016; Asay-Davis et al., 2016). This is too coarse to capture the spatial variability that we observe here.

6 Conclusions

We derived the Lagrangian Basal Mass Balance (LBMB) of the Roi Baudouin Ice Shelf by combining TanDEM-X DEMs of 2013 and 2014 with high-resolution surface velocities and atmospheric modelling outputs. On a large scale, the LBMB shows the highest basal melt rates where the ice draft is deepest and steepest, i.e. close to the grounding line and near Derwael Ice Rise and the Western Ice Promontory. This pattern is overlain with significant sub-kilometre scale variability, as witnessed by localised surface lowering of an elliptical surface depression and large basal melting rates below some sections of ice-shelf channels. For the latter, we find evidence that at least in some areas, basal melting is concentrated on the channel's flanks as opposed to its apex. Key advancements in our methodology to elucidate this variability are (i) the calibration of the DEMs to account for residual trends from the interferometric processing, (ii) the quality of the matching procedure – using normalised cross-correlation coefficients – for calculating the Lagrangian thickness change , and (iii) the total-variation regularization of the spatial derivatives that preserves abrupt changes in flow velocities that are sometimes observed across ice-shelf channels. New satellites (such as TanDEM-X or Sentinel 1) will continue to provide highly-resolved datasets of surface elevation and ice velocity. In comparison, atmospheric modelling does not (yet) provide the required spatial resolution on firn-density and SMB to solve the mass budget reliably on sub-kilometre scales. Although the uncertainty of the absolute LBMB values remains high, we find a good fit with on-site measurements from phase-sensitive radar, and we demonstrate that much of the spatial LBMB variability contains information about ice-shelf processes occurring at sub-kilometre scales. This variability highlights the complexity of the ice-ocean and ice-atmosphere interactions on small spatial scales on ice shelves, which need to be accounted for by glaciologists, oceanographers and atmospheric scientists.

Acknowledgements. This paper forms a contribution to the Belgian Research Programme on the Antarctic (Belgian Federal Science Policy Office), project SD/CA/06A (Constraining Ice Mass Change in Antarctica, IceCon). S. Berger is supported by a FRS-FNRS (Fonds de la Recherche Scientifique) "Aspirant" PhD fellowship. R. Drews was partially supported by the Deutsche Forschungsgemeinschaft (DFG) in the framework of the priority programme "Antarctic Research with comparative investigations in Arctic ice areas" by the grant MA 3347/10-1. S. Sun is supported by the FNRS-PDR (Fonds de la Recherche Scientifique) project MEDRISM. TanDEM-X data originate from German Aerospace Center (ATI-GLAC0267). We thank Nicolas Bergeot (Royal Observatory Belgium) who helped with GNSS processing and K.

Nicholls for his valuable help in processing of the phase-sensitive radar. We received excellent logistic support by the Belgian Military, AntarctiQ and the International Polar Foundation during the field campaigns. Finally, we thank J. Lenaerts and S. Ligtenberg for sharing results from atmospheric modelling, as well as D. Shean and G. Moholdt for their constructive comments on this manuscript.

References

Asay-Davis, X. S., Cornford, S. L., Durand, G., Galton-Fenzi, B. K., Gladstone, R. M., Hilmar Gudmundsson, G., Hattermann, T., Holland, D. M., Holland, D., Holland, P. R., Martin, D. F., Mathiot, P., Pattyn, F., and Seroussi, H.: Experimental design for three interrelated marine ice sheet and ocean model intercomparison projects: MISMIP v. 3 (MISMIP +), ISOMIP v. 2 (ISOMIP +) and MISOMIP v. 1 (MISOMIP1), Geoscientific Model Development, 9, 2471–2497, doi:10.5194/gmd-9-2471-2016, 2016.

Banwell, A. F., MacAyeal, D. R., and Sergienko, O. V.: Breakup of the Larsen B Ice Shelf triggered by chain reaction drainage of supraglacial lakes, Geophysical Research Letters, 40, 5872–5876, doi:10.1002/2013GL057694, 2013.

Berger, S., Favier, L., Drews, R., Derwael, J. J., and Pattyn, F.: The control of an uncharted pinning point on the flow of an Antarctic ice shelf, Journal of Glaciology, 62, 37–45, doi:10.1017/jog.2016.7, 2016.

Bindschadler, R., Choi, H., Wichlacz, A., Bingham, R., Bohlander, J., Brunt, K., Corr, H., Drews, R., Fricker, H., Hall, M., Hindmarsh, R., Kohler, J., Padman, L., Rack, W., Rotschky, G., Urbini, S., Vornberger, P., and Young, N.: Getting around Antarctica: New high-resolution mappings of the grounded and freely-floating boundaries of the Antarctic ice sheet created for the International Polar Year, The Cryosphere, 5, 569–588, doi:10.5194/tc-5-569-2011, 2011a.

Bindschadler, R., Vaughan, D. G., and Vornberger, P.: Variability of basal melt beneath the Pine Island Glacier ice shelf, West Antarctica, Journal of Glaciology, 57, 581–595, doi:10.3189/002214311797409802, 2011b.

Bradski, G. and Kaehler, A.: 07 Learning OpenCV: Computer Vision with the OpenCV Library, vol. 1, doi:10.1109/MRA.2009.933612, 2008.

Callens, D., Matsuoka, K., Steinhage, D., Smith, B., Witrant, E., and Pattyn, F.: Transition of flow regime along a marine-terminating outlet glacier in East Antarctica, The Cryosphere, 8, 867–875, doi:10.5194/tc-8-867-2014, 2014.

Callens, D., Drews, R., Witrant, E., Philippe, M., and Pattyn, F.: Temporally stable surface mass balance asymmetry across an Ice rise derived from radar internal reflection horizons through inverse modeling, Journal of Glaciology, 62, 525–534, doi:10.1017/jog.2016.41, 2016.

Chartrand, R.: Numerical Differentiation of Noisy, Nonsmooth Data, ISRN Applied Mathematics, 2011, 1–11, doi:10.5402/2011/164564, 2011.

Chuter, S. J. and Bamber, J. L.: Antarctic ice shelf thickness from CryoSat-2 radar altimetry, Geophysical Research Letters, 42, 10,710–721,729, doi:10.1002/2015GL066515, 2015.

DeConto, R. M. and Pollard, D.: Contribution of Antarctica to past and future sea-level rise, Nature, 531, 591–597, doi:10.1038/nature17145, 2016.

Depoorter, M. A., Bamber, J. L., Griggs, J. a., Lenaerts, J. T. M., Ligtenberg, S. R. M., van den Broeke, M. R., and Moholdt, G.: Calving fluxes and basal melt rates of Antarctic ice shelves., Nature, 502, 89–92, doi:10.1038/nature12567, 2013.

Dinniman, M., Asay-Davis, X., Galton-Fenzi, B., Holland, P., Jenkins, A., and Timmermann, R.: Modeling Ice Shelf/Ocean Interaction in Antarctica: A Review, Oceanography, 29, 144–153, doi:10.5670/oceanog.2016.106, 2016.

Drews, R.: Evolution of ice-shelf channels in Antarctic ice shelves, The Cryosphere, 9, 1169–1181, doi:doi:10.5194/tc-9-1169-2015, 2015.

Drews, R., Rack, W., Wesche, C., and Helm, V.: A Spatially Adjusted Elevation Model in Dronning Maud Land, Antarctica, Based on Differential SAR Interferometry, IEEE Transactions on Geoscience and Remote Sensing, 47, 2501–2509, doi:10.1109/TGRS.2009.2016081, 2009.

Drews, R., Matsuoka, K., Martín, C., Callens, D., Bergeot, N., and Pattyn, F.: Evolution of Derwael Ice Rise in Dronning Maud Land, Antarctica, over the last millennia, Journal of Geophysical Research: Earth Surface, 120, 564–579, doi:10.1002/2014JF003246, 2015.

Drews, R., Brown, J., Matsuoka, K., Witrant, E., Philippe, M., Hubbard, B., and Pattyn, F.: Constraining variable density of ice shelves using wide-angle radar measurements, The Cryosphere, 10, 811–823, doi:10.5194/tc-10-811-2016, 2016.

Drews, R., Pattyn, F., Hewitt, I. J., Ng, F. S. L., Berger, S., Matsuoka, K., Helm, V., Bergeot, N., Favier, L., and Neckel, N.: Actively evolving subglacial conduits and eskers initiate ice shelf channels at an Antarctic grounding line, Nature Communications, 8, 15 228, doi:10.1038/ncomms15228, 2017.

Dutrieux, P., Vaughan, D. G., Corr, H. F. J., Jenkins, A., Holland, P. R., Joughin, I., and Fleming, A.: Pine Island Glacier ice shelf melt distributed at kilometre scales, The Cryosphere, 7, 1591–1620, 2013.

Dutrieux, P., Stewart, C., Jenkins, A., Nicholls, K. W., Corr, H. F. J., Rignot, E., and Steffen, K.: Basal terraces on melting ice shelves, Geophysical Research Letters, 41, 5506–5513, 2014.

Favier, L., Gagliardini, O., Durand, G., and Zwinger, T.: A three-dimensional full Stokes model of the grounding line dynamics: effect of a pinning point beneath the ice shelf, The Cryosphere, 6, 101–112, doi:10.5194/tc-6-101-2012, 2012.

Favier, L., Durand, G., Cornford, S. L., Gudmundsson, G. H., Gagliardini, O., Gillet-Chaulet, F., Zwinger, T., Payne, A. J., and Le Brocq, A. M.: Retreat of Pine Island Glacier controlled by marine ice-sheet instability, Nature Climate Change, 4, 117–121, doi:10.1038/nclimate2094, 2014.

Favier, L., Pattyn, F., Berger, S., and Drews, R.: Dynamic influence of pinning points on marine ice-sheet stability: a numerical study in Dronning Maud Land, East Antarctica, The Cryosphere, 10, 2623–2635, doi:10.5194/tc-10-2623-2016, 2016.

Förste, C., Bruinsma, S., Abrikosov, O., Flechtner, F., Marty, J.-C., Lemoine, J.-M., Dahle, C., Neumayer, H., Barthelmes, F., König, R., and Biancale, R.: EIGEN-6C4 - The latest combined global gravity field model including GOCE data up to degree and order 1949 of GFZ Potsdam and GRGS Toulouse, in: EGU General Assembly Conference Abstracts, vol. 16 of *EGU General Assembly Conference Abstracts*, p. 3707, 2014.

Frezzotti, M., Urbini, S., Proposito, M., Scarchilli, C., and Gandolfi, S.: Spatial and temporal variability of surface mass balance near Talos Dome, East Antarctica, Journal of Geophysical Research, 112, F02 032, doi:10.1029/2006JF000638, 2007.

Gladish, C. V., Holland, D. M., Holland, P. R., and Price, S. F.: Ice-shelf basal channels in a coupled ice/ocean model, Journal of Glaciology, 58, 1227–1244, doi:10.3189/2012JoG12J003, 2012.

Golledge, N. R., Menviel, L., Carter, L., Fogwill, C. J., England, M. H., Cortese, G., and Levy, R. H.: Antarctic contribution to meltwater pulse 1A from reduced Southern Ocean overturning, Nature Communications, 5, 1–10, doi:10.1038/ncomms6107, 2014.

Golledge, N. R., Kowalewski, D. E., Naish, T. R., Levy, R. H., Fogwill, C. J., and Gasson, E. G. W.: The multi-millennial Antarctic commitment to future sea-level rise, Nature, 526, 421–425, doi:10.1038/nature15706, 2015.

Gudmundsson, G. H., Krug, J., Durand, G., Favier, L., and Gagliardini, O.: The stability of grounding lines on retrograde slopes, The Cryosphere, 6, 1497–1505, doi:10.5194/tc-6-1497-2012, 2012.

Helm, V., Humbert, A., and Miller, H.: Elevation and elevation change of Greenland and Antarctica derived from CryoSat-2, The Cryosphere, 8, 1539–1559, doi:10.5194/tc-8-1539-2014, 2014.

Holland, P. R., Jenkins, A., and Holland, D. M.: The Response of Ice Shelf Basal Melting to Variations in Ocean Temperature, Journal of Climate, 21, 2558–2572, doi:10.1175/2007JCLI1909.1, 2008.

Hulbe, C. L., MacAyeal, D. R., Denton, G. H., Kleman, J., and Lowell, T. V.: Catastrophic ice shelf breakup as the source of Heinrich event icebergs, Paleoceanography, 19, n/a–n/a, doi:10.1029/2003PA000890, 2004.

Humbert, A. and Steinhage, D.: The evolution of the western rift area of the Fimbul Ice Shelf, Antarctica, The Cryosphere, 5, 931–944, doi:10.5194/tc-5-931-2011, 2011.

Humbert, A., Steinhage, D., Helm, V., Hoerz, S., Berendt, J., Leipprand, E., Christmann, J., Plate, C., and Müller, R.: On the link between surface and basal structures of the Jelbart Ice Shelf, Antarctica, Journal of Glaciology, 61, 975–986, doi:10.3189/2015JoG15J023, 2015.

Jenkins, A.: Convection-driven melting near the grounding lines of ice shelves and tidewater glaciers, Journal of Physical Oceanography, 41, 2279–2294, 2011.

Jenkins, A. and Doake, C. S. M.: Ice-ocean interaction on Ronne Ice Shelf, Antarctica, Journal of Geophysical Research, 96, 791, doi:10.1029/90JC01952, 1991.

Jezek, K. and RAMP-Product-Team: RAMP AMM-1 SAR Image Mosaic of Antarctica, Fairbanks, AK: Alaska Satellite Facility, in association with the National Snow and Ice Data Center, Boulder, CO. Digital media, 2002.

Joughin, I.: Ice-sheet velocity mapping: a combined interferometric and speckle-tracking approach, Annals of Glaciology, 34, 195–201, 2002.

Knudsen, P. and Andersen, O. B.: A global mean ocean circulation estimation using goce gravity models - the DTU12MDT mean dynamic topography model, in: 20 Years of Progress in Radar Altimetry Symposium, p. 123, 2012.

Krieger, G., Moreira, A., Fiedler, H., Hajnsek, I., Werner, M., Younis, M., and Zink, M.: TanDEM-X: A Satellite Formation for High-Resolution SAR Interferometry, IEEE Transactions on Geoscience and Remote Sensing, 45, 3317–3341, doi:10.1109/TGRS.2007.900693, 2007.

Langley, K., Deschwanden, A., Kohler, J., Sinisalo, A., Matsuoka, K., Hattermann, T., Humbert, A., Nøst, O. A., and Isaksson, E.: Complex network of channels beneath an Antarctic ice shelf, Geophysical Research Letters, 41, 1209–1215, 2014.

Le Brocq, A. M., Ross, N., Griggs, J. A., Bingham, R. G., Corr, H. F. J., Ferraccioli, F., Jenkins, A., Jordan, T. A., Payne, A. J., Rippin, D. M., and Others: Evidence from ice shelves for channelized meltwater flow beneath the Antarctic Ice Sheet, Nature Geoscience, 6, 945–948, 2013.

Lenaerts, J., Brown, J., Van Den Broeke, M. R., Matsuoka, K., Drews, R., , Callens, D., Philippe, M., Gorodetskaya, I. V., Van Meijgaard, E., Reijmer, C. H., and Others: High variability of climate and surface mass balance induced by Antarctic ice rises, Journal of Glaciology, 60, 1101, 2014.

Lenaerts, J. T. M., Lhermitte, S., Drews, R., Ligtenberg, S. R. M., Berger, S., Helm, V., Smeets, C. J. P. P., van den Broeke, M. R., van de Berg, W. J., van Meijgaard, E., Eijkelboom, M., Eisen, O., and Pattyn, F.: Meltwater produced by wind–albedo interaction stored in an East Antarctic ice shelf, Nature Climate Change, 7, 58–62, doi:10.1038/nclimate3180, 2017.

Ligtenberg, S. R. M., Helsen, M. M., and van den Broeke, M. R.: An improved semi-empirical model for the densification of Antarctic firn, The Cryosphere, 5, 809–819, doi:10.5194/tc-5-809-2011, 2011.

Little, C. M., Gnanadesikan, A., and Oppenheimer, M.: How ice shelf morphology controls basal melting, Journal of Geophysical Research, 114, C12 007, doi:10.1029/2008JC005197, 2009.

Marengoni, M. and Stringhini, D.: High Level Computer Vision Using OpenCV, in: 2011 24th SIBGRAPI Conference on Graphics, Patterns, and Images Tutorials, pp. 11–24, IEEE, doi:10.1109/SIBGRAPI-T.2011.11, 2011.

Marsh, O. J., Fricker, H. A., Siegfried, M. R., Christianson, K., Nicholls, K. W., Corr, H. F. J., and Catania, G.: High basal melting forming a channel at the grounding line of Ross Ice Shelf, Antarctica, Geophysical Research Letters, pp. n/a–n/a, doi:10.1002/2015GL066612, 2016.

Matsuoka, K., Pattyn, F., Callens, D., and Conway, H.: Radar characterization of the basal interface across the grounding zone of an ice-rise promontory in East Antarctica, Annals of Glaciology, 53, 29–34, doi:10.3189/2012AoG60A106, 2012.

Mercer, J. H.: West Antarctic ice sheet and CO2 greenhouse effect: a threat of disaster, Nature, 271, 321–325, doi:10.1038/271321a0, 1978.

Millgate, T., Holland, P. R., Jenkins, A., and Johnson, H. L.: The effect of basal channels on oceanic ice-shelf melting, Journal of Geophysical Research: Oceans, 118, 6951–6964, doi:10.1002/2013JC009402, 2013.

Moholdt, G., Padman, L., and Fricker, H. A.: Basal mass budget of Ross and Filchner-Ronne ice shelves, Antarctica, derived from Lagrangian analysis of ICESat altimetry, Journal of Geophysical Research: Earth Surface, 2014.

Neckel, N., Drews, R., Rack, W., and Steinhage, D.: Basal melting at the Ekström Ice Shelf, Antarctica, estimated from mass flux divergence, Annals of Glaciology, 53, 294–302, doi:10.3189/2012AoG60A167, 2012.

Nicholls, K. W., Corr, H. F., Stewart, C. L., Lok, L. B., Brennan, P. V., and Vaughan, D. G.: A ground-based radar for measuring vertical strain rates and time-varying basal melt rates in ice sheets and shelves, Journal of Glaciology, 61, 1079–1087, doi:10.3189/2015JoG15J073, 2015.

Padman, L., Fricker, H. A., Coleman, R., Howard, S., and Erofeeva, L.: A new tide model for the Antarctic ice shelves and seas, Annals of Glaciology, 34, 247–254, 2002.

Padman, L., Erofeeva, S. Y., and Fricker, H. A.: Improving Antarctic tide models by assimilation of ICESat laser altimetry over ice shelves, Geophysical Research Letters, 35, L22 504, doi:10.1029/2008GL035592, 2008.

Paolo, F. S., Fricker, H. A., and Padman, L.: Volume loss from Antarctic ice shelves is accelerating., Science, 348, 327–331, doi:10.1126/science.aaa0940, 2015.

Pattyn, F., Perichon, L., Durand, G., Favier, L., Gagliardini, O., Hindmarsh, R. C., Zwinger, T., Albrecht, T., Cornford, S., Docquier, D., Fürst, J. J., Goldberg, D., Gudmundsson, G. H., Humbert, A., Hütten, M., Huybrechts, P., Jouvet, G., Kleiner, T., Larour, E., Martin, D., Morlighem, M., Payne, A. J., Pollard, D., Rückamp, M., Rybak, O., Seroussi, H., Thoma, M., and Wilkens, N.: Grounding-line migration in plan-view marine ice-sheet models: results of the ice2sea MISMIP3d intercomparison, Journal of Glaciology, 59, 410–422, doi:10.3189/2013JoG12J129, 2013.

Pritchard, H. D., Ligtenberg, S. R. M., Fricker, H. A., Vaughan, D. G., van den Broeke, M. R., and Padman, L.: Antarctic ice-sheet loss driven by basal melting of ice shelves., Nature, 484, 502–5, doi:10.1038/nature10968, 2012.

Rignot, E. and Steffen, K.: Channelized bottom melting and stability of floating ice shelves, Geophysical Research Letters, 35, 2008.

Rignot, E., Mouginot, J., and Scheuchl, B.: Antarctic grounding line mapping from differential satellite radar interferometry, Geophysical Research Letters, 38, doi:10.1029/2011GL047109, 2011a.

Rignot, E., Mouginot, J., and Scheuchl, B.: Ice flow of the Antarctic ice sheet, Science, 333, 1427–1430, doi:10.1126/science.1208336, 2011b.

Rignot, E., Jacobs, S., Mouginot, J., and Scheuchl, B.: Ice-shelf melting around Antarctica, Science, 341, 266–270, doi:10.1126/science.1235798, 2013.

Rignot, E., Mouginot, J., Morlighem, M., Seroussi, H., and Scheuchl, B.: Widespread, rapid grounding line retreat of Pine Island, Thwaites, Smith, and Kohler glaciers, West Antarctica, from 1992 to 2011, Geophysical Research Letters, 41, 3502–3509, doi:10.1002/2014GL060140, 2014.

Ritz, C., Edwards, T. L., Durand, G., Payne, A. J., Peyaud, V., and Hindmarsh, R. C. A.: Potential sea-level rise from Antarctic ice-sheet instability constrained by observations, Nature, 528, 115–118, doi:10.1038/nature16147, 2015.

Scambos, T. A., Bohlander, J. A., Shuman, C. A., and Skvarca, P.: Glacier acceleration and thinning after ice shelf collapse in the Larsen B embayment, Antarctica, Geophysical Research Letters, 31, L18 402, doi:10.1029/2004GL020670, 2004.

Schoof, C.: Ice sheet grounding line dynamics: Steady states, stability, and hysteresis, Journal of Geophysical Research, 112, F03S28, doi:10.1029/2006JF000664, 2007.

Sergienko, O. V.: Basal channels on ice shelves, Journal of Geophysical Research: Earth Surface, 118, 1342–1355, 2013.

Shean, D. E., Christianson, K., Larson, K. M., Ligtenberg, S. R., Joughin, I. R., Smith, B. E., and Stevens, C. M.: In situ GPS records of surface mass balance and ocean-induced basal melt for Pine Island Glacier, Antarctica, The Cryosphere Discussions, pp. 1–30, doi:10.5194/tc-2016-288, 2017.

Stanton, T. P., Shaw, W. J., Truffer, M., Corr, H. F. J., Peters, L. E., Riverman, K. L., Bindschadler, R., Holland, D. M., and Anandakrishnan, S.: Channelized ice melting in the ocean boundary layer beneath Pine Island Glacier, Antarctica, Science, 341, 1236–1239, doi:10.1126/science.1239373, 2013.

Tsai, V. C., Stewart, A. L., and Thompson, A. F.: Marine ice-sheet profiles and stability under Coulomb basal conditions, Journal of Glaciology, 61, 205–215, doi:10.3189/2015JoG14J221, 2015.

Vaughan, D. G., Corr, H. F. J., Bindschadler, R. A., Dutrieux, P., Gudmundsson, G. H., Jenkins, A., Newman, T., Vornberger, P., and Wingham, D. J.: Subglacial melt channels and fracture in the floating part of Pine Island Glacier, Antarctica, Journal of Geophysical Research, 117, doi:10.1029/2012jf002360, 2012.

Wilson, N., Straneo, F., and Heimbach, P.: Submarine melt rates and mass balance for Greenland's remaining ice tongues, The Cryosphere Discussions, pp. 1–17, doi:10.5194/tc-2017-99, 2017.

Wouters, B., Martin-Español, A., Helm, V., Flament, T., van Wessem, J. M., Ligtenberg, S. R. M., van den Broeke, M. R., and Bamber, J. L.: Dynamic thinning of glaciers on the Southern Antarctic Peninsula, Science, 348, 899–903, doi:10.1126/science.aaa5727, 2015.

1 TanDEM-X frames

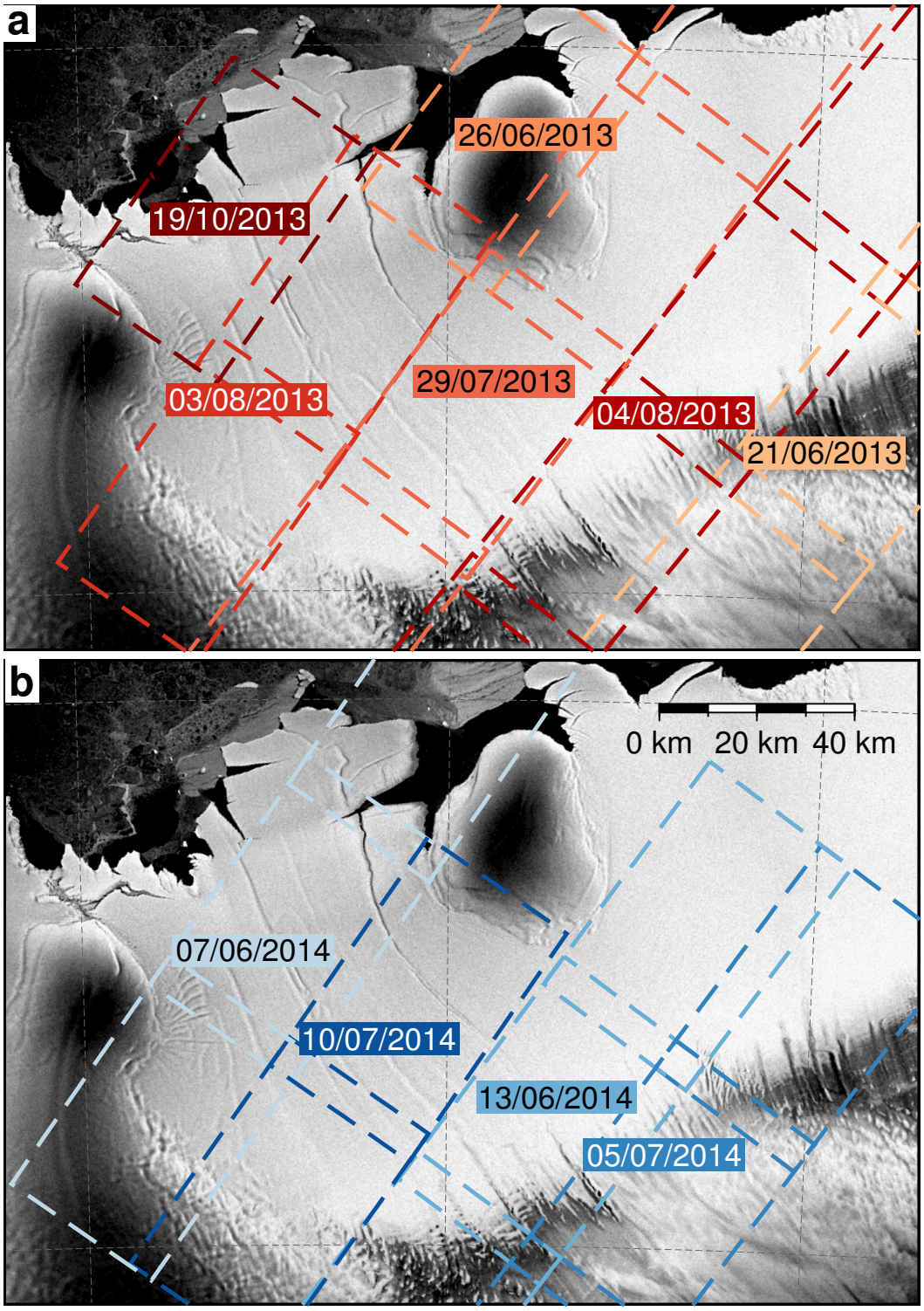

Figure S1: Frame location and dates of the TanDEM-X scenes from 2013 (a) and 2014 (b). The same color is used to represent different scenes acquired on the same day and satellite path that have been concatenated together with a linear taper and subsequently treated as one scene in our study (Sect. 2)

2 Gaussian filtering of TanDEM-X

Comparison between the GNSS profile from Drews (2015) and 2013 TanDEM-X DEM. Filtering the TanDEM-X elevations with a gaussian filter with a standard deviation of 7 pixels minimizes the mean and standard deviation of the difference between the GNSS and TanDEM-X elevations: which are -0.41±0.38 m and -0.41±0.64 m for the filtered and unfiltered case, respectively.

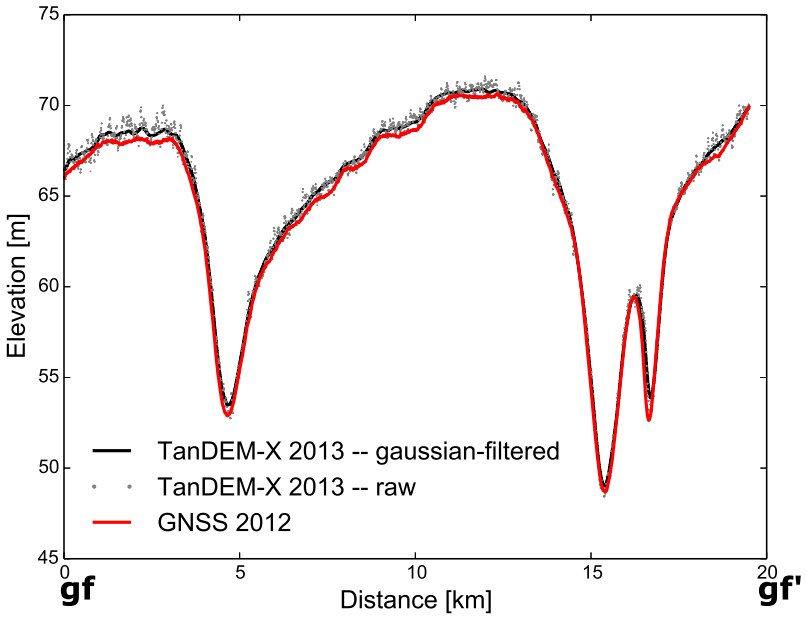

Figure S2: Comparison of unfiltered (raw) TanDEM-X 2013 , Gaussian-filtered TanDEM-X 2013 ($\sigma = 7$) and 2012 GNSS elevations. The profile gf-gf' is shown in Fig. 1. The Gaussian-filtering is discussed in Sect. 2.4.

3 TanDEM-X validation

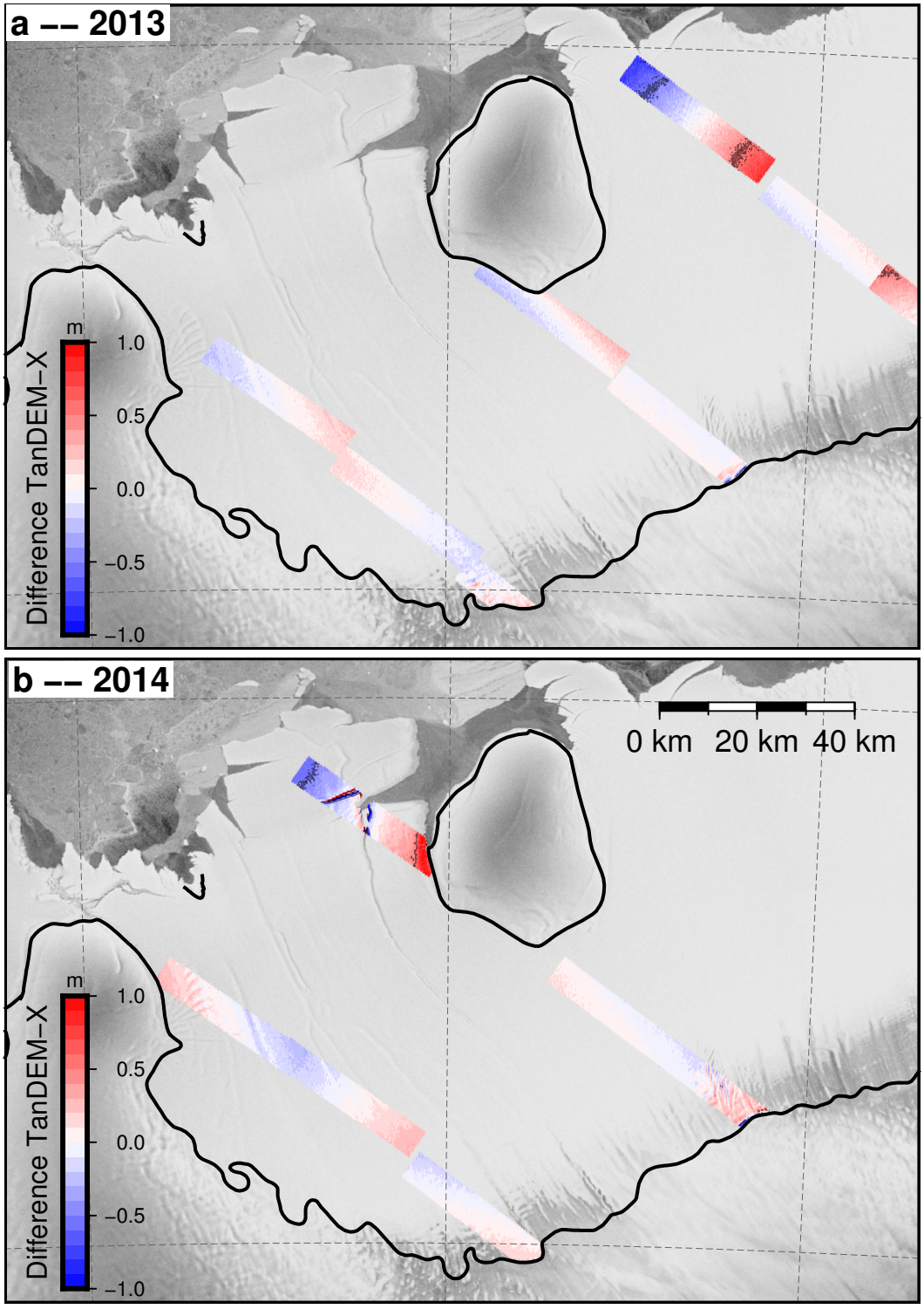

Figure S3: Elevation difference in the overlapping areas of consecutive (filtered) TanDEM-X scenes acquired the same day. The -0.5 and 0.5 contour lines have been added. This figure is discussed in Sect. 2.4 and 4.1

References

Drews, R.: Evolution of ice-shelf channels in Antarctic ice shelves, The Cryosphere, 9, 1169–1181, doi:doi: 10.5194/tc-9-1169-2015, 2015.

Chapter 4

Combining observations and modelling to study the impact of pinning points

This standalone chapter is taken from a paper published in *Journal of Glaciology* :

Berger, S., Favier, L., Drews, R., Derwael, J. J., and Pattyn, F. (2016). The control of an uncharted pinning point on the flow of an Antarctic ice shelf. *Journal of Glaciology*, 62(231):37–45

This article – which provides specific details about the processing of the velocity mosaic of the Roi Baudouin Ice Shelf – combines observations and modelling to study how the misrepresentation of a pinning point in observations impacts the initialisation of ice-sheet models. Initialisation consists in feeding in an ice-sheet model with all the information it needs like: values for the variables and parameters it uses, boundary conditions, etc. Because some variables are difficult to observe (e.g. conditions at the bed and ice rheology, here), initialisation commonly relies on inverse modelling, whereby unknown parameters used by the model (e.g. basal friction coefficient and stiffening factor) are calculated from a set of observations (e.g. ice velocity and ice thickness). Compared to the previous chapter, this study therefore goes one step further in combining observations and modelling.

The modelling performed here is diagnostic, in the sense that temporal changes are not considered. Impact of our findings on prognostic modelling have nevertheless been investigated in a follow-up study (Favier et al., 2016) and are presented in Section 5.3.2.

Journal of Glaciology (2016), Page 1 of 9 doi: 10.1017/jog.2016.7

The control of an uncharted pinning point on the flow of an Antarctic ice shelf

SOPHIE BERGER,[1] LIONEL FAVIER,[1] REINHARD DREWS,[1] JEAN-JACQUES DERWAEL,[2] FRANK PATTYN[1]

[1]*Laboratoire de Glaciologie, Université libre de Bruxelles, Brussels, Belgium*
[2]*Faculty of Applied Engineering, University of Antwerp, Antwerp, Belgium*
Correspondence: Sophie Berger <sberger@ulb.ac.be>

ABSTRACT. Antarctic ice shelves are buttressed by numerous pinning points attaching to the otherwise freely-floating ice from below. Some of these kilometric-scale grounded features are unresolved in Antarctic-wide datasets of ice thickness and bathymetry, hampering ice flow models to fully capture dynamics at the grounding line and upstream. We investigate the role of an 8.7 km^2 pinning point at the front of the Roi Baudouin Ice Shelf, East Antarctica. Using ERS interferometry and ALOS-PALSAR speckle tracking, we derive, on a 125 m grid spacing, surface velocities deviating by -5.2 ± 4.5 m a^{-1} from 37 on-site global navigation satellite systems-derived velocities. We find no evidence for ice flow changes on decadal time scales and we show that ice on the pinning point virtually stagnates, deviating the ice stream and causing enhanced horizontal shearing upstream. Using the BISICLES ice-flow model, we invert for basal friction and ice rigidity with three input scenarios of ice velocity and geometry. We show that inversion results are the most sensitive to the presence/absence of the pinning point in the bathymetry; surface velocities at the pinning point are of secondary importance. Undersampling of pinning points results in erroneous ice-shelf properties in models initialised by control methods. This may impact prognostic modelling for ice-sheet evolution in the case of unpinning.

KEYWORDS: ice rheology, ice shelves, ice velocity, ice-sheet modelling, remote sensing

1. INTRODUCTION

Almost three quarters of the Antarctic grounded ice is discharged into floating ice shelves (Bindschadler and others, 2011). Thinning of ice shelves, as observed by Paolo and others (2015), imprints the current mass loss by reducing the restraint (i.e. buttressing), which the ice shelves exert on the inland flow, subsequently causing acceleration of tributary glaciers (Scambos and others, 2004; Dupont and Alley, 2005; Joughin and others, 2014; Mouginot and others, 2014; De Rydt and others, 2015). Ice-shelf buttressing originates from lateral friction of embayments and/or from rigid obstacles emerging from the bathymetry and attaching to the ice-shelf from below.

Localized grounded areas within ice shelves form ice rumples and ice rises (Smith, 1986; Matsuoka and others, 2015). Ice rumples, on the one hand, decelerate ice flow, but are still overrun by the ice-shelf (e.g. Schmeltz and others, 2001; Humbert and Steinhage, 2011). Ice rises, on the other hand, develop a local flow regime isolated from the surrounding ice shelf (e.g. Drews and others, 2015; references therein). Distinguishing an ice rise from an ice rumple based on the (non-)locality of the flow pattern is not always straightforward, especially for smaller features that extend over only a few square kilometres; in those cases we will use the generic term *pinning point*.

Because ice rises (Goldberg and others, 2009; Favier and others, 2014; Favier and Pattyn, 2015) and ice rumples (Favier and others, 2012) affect the dynamics of the grounding line and that of the upstream catchment area, it is important to better understand what role these features play in defining the buttressing strength of ice shelves.

Although small pinning points (e.g. inset; Fig. 1) are common features of ice shelves in Dronning Maud Land (e.g. Matsuoka and others, 2015), they are often not covered by airborne or ground-based radars and hence not resolved in Antarctic-wide ice thickness datasets such as Bedmap2 (Fretwell and others, 2013; Fürst and others, 2015). Moreover, their surface elevation is often erroneous since satellite-altimeters tracks are too widely spaced. Antarctic-wide ice velocity maps, on the other hand, typically show the deceleration of ice flow near pinning points, but are not necessarily trustworthy at the pinning points themselves (for instance, regrounding necessitates a specific calibration for interferometric synthetic aperture radar).

Ice thickness, surface elevation and ice velocity are the primary input variables for ice flow model initialisation. A typical approach for initialising ice flow models is to invert observed surface velocities for poorly known parameters such as basal friction and ice rigidity (e.g MacAyeal, 1993; Fürst and others, 2015). As a result, if pinning points are insufficiently resolved in the observational datasets, their impact on ice-shelf dynamics may erroneously propagate to the ice-shelf rigidity during the inversion, leading to erroneous predictions in prognostic ice sheet modelling. To address this point, we analyse a small pinning point in the Roi Baudouin Ice Shelf (RBIS), Dronning Maud Land, East Antarctica, by combining radar remote sensing and inverse modelling.

The western part of the Roi Baudouin Ice Shelf (26°E and 71°S), referred to hereafter as the RBIS, extends over 8500 km^2 and presents several ice-shelf channels (i.e. along-flow features

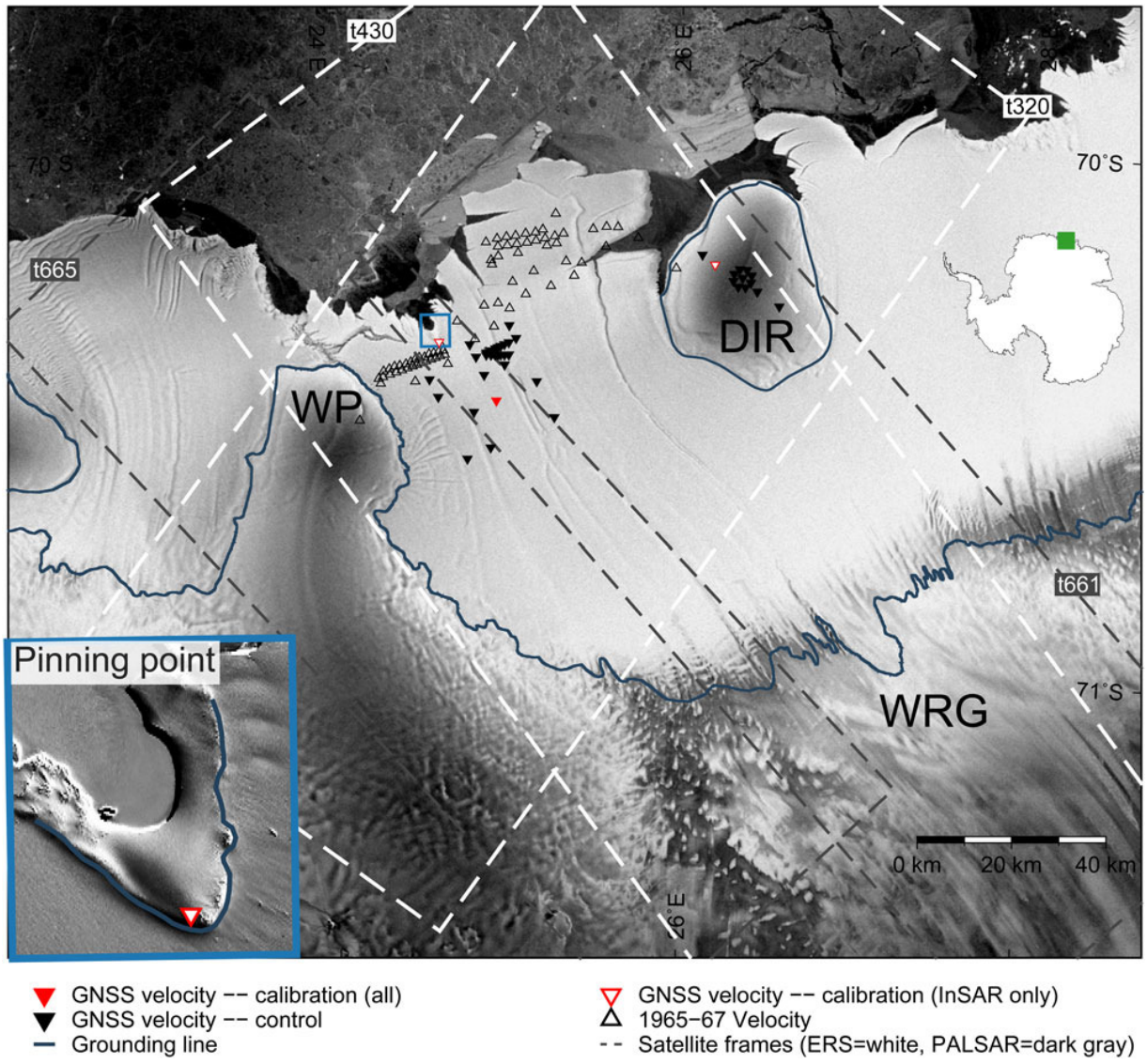

Fig. 1. Overview of the Roi Baudouin Ice Shelf (Dronning Maud Land, East Antarctica). The map locates ground-truth velocity data and the satellite scenes. WP, DIR and WRG indicate the western promontory, Derwael Ice Rise and the West Ragnhild Glacier, respectively. The blue rectangle locates the inset that displays the pinning point and the dark blue curve shows the grounding line from Bindschadler and others (2011), except in the inset where the curve designates the break in slope at the pinning point. The background images are from Radarsat mosaic (Jezek and RAMP-Product-Team, 2002) and Landsat 8 of September 2014 (inset).

of diminished thickness, expressed both at the base and at the top surface of the ice shelf). The RBIS is fed by the West Ragnhild Glacier and constrained by an ice promontory on its western side, Derwael Ice Rise towards the East, and an 8.7 km^2 pinning point at the ice-shelf front (Fig. 1). This pinning point is absent in the bathymetry, ice thickness and surface elevation of Bedmap2 (Fretwell and others, 2013). The West Ragnhild Glacier drains ~10% of the ice in Dronning Maud Land (13–14 Gt a^{-1}; Callens and others, 2014) and is therefore among the major contributors to the ice discharge of Dronning Maud Land. Compared with ice shelves of other major outlet glaciers (e.g. Jutulstraulmen and Shirase Glacier), the RBIS flows more slowly (maximum speed ≈345 m a^{-1}) and ice is discharged through a comparatively wide gate at the grounding line (Callens and others, 2014).

Using interferometric synthetic aperture radar (InSAR) and speckle tracking, we first derive an ice-flow map, which is calibrated and validated with Global Navigation Satellite System (GNSS) ground-truth data (Section 2.1). We then modify the bed topography and ice thickness from Bedmap2 to account for the missing pinning point. This modified dataset is further referred to as *mBedmap2*. To assess the impact of the pinning point on ice flow models, we perform three inverse experiments based on three different scenarios (Section 2.2): (1) the *Standard* scenario using Antarctic-wide velocities (Rignot and others, 2011b) and ice thickness from Bedmap2 (Fretwell and others, 2013); (2) the *Intermediate* scenario combining Rignot and others (2011b)'s velocities with *mBedmap2*; (3) the *High-resolution* scenario using the high-resolution flow field derived here and in *mBedmap2*. We validate and discuss our results (Sections 3 and 4) and close by drawing conclusions with respect to the role of small pinning points on ice-shelf buttressing (Section 5).

Table 1. Characteristics of the satellite data; ΔT, λ and $B_\perp$ are the temporal baseline, the wavelength of the sensor and the perpendicular spatial baseline between the master and slave images, respectively. The satellite frames are shown in Figure 1

Processing	Sensor	ΔT	λ	Track	Date (master)	$B_\perp$	Orbit
		d	cm			m	
InSAR	ERS 1/2	1	5.6	320	21 May 1996	37	Descending
				430	28 May 1996	62	Ascending
Speckle tracking	ALOS-PALSAR	46	23	661	1 August 2010	520	Ascending
				661	16 September 2010	437	Ascending
				661	1 November 2010	453	Ascending
				665	8 October 2010	588	Ascending

2. DATA AND METHODS

2.1. Derivation of surface velocities

We derived surface velocities performing InSAR and speckle tracking on data from the European Remote Sensing satellites (ERS-1 and 2 from 1996) and from the Advanced Land Observation Satellite – Phased Array type L-band synthetic aperture radar (ALOS-PALSAR from 2010), respectively. Both techniques compare two co-registered images of the same area, acquired at different times. InSAR evaluates phase differences to derive ice flow, whereas speckle tracking tracks random, but deterministic, amplitude variations. Assuming steady state, velocities were mosaicked and calibrated with ground-control points collected in 2012/13 (Fig. 1).

2.1.1. Interferometric SAR using ERS-1/2

The individual frames of the ERS-1/2 scenes (Fig. 1; Table 1) were pre-processed to single-look complex images with Gamma's Modular SAR processor (Werner and others, 2000). Pairs with 1-day time intervals were co-registered and differenced in phase forming interferograms (Goldstein and others, 1993) with lines of constant phase-differences (a. k. a. fringes). The fringe pattern depends on the satellite orbits, surface topography and ice flow. Orbital effects were removed using the precise orbits provided by Technical University Delft (Scharroo and Visser, 1998) and the topographic contribution was cancelled using a DEM (Bamber and others, 2009). Phase differences were unwrapped using a minimum cost-flow algorithm (Costantini, 1998), transformed into a line-of-sight velocity map, and calibrated with the ground-control points marked in red in Figure 1. For the latter, the floating parts were discriminated using the dense fringe pattern caused by the tidal uplift in the grounding zone (e.g. Goldstein and others, 1993; Gray and others, 2002; Fricker and others, 2009; Rignot and others, 2011a). Calibration on the floating areas presupposes only vertical movement by tides (i.e. without tilting).

2.1.2. Speckle tracking using ALOS-PALSAR

Because the available InSAR data do not entirely cover the RBIS, we also used speckle tracking (Strozzi and others, 2002; Luckman and others, 2003; Werner and others, 2005) on ALOS-PALSAR images of 2010 (Fig. 1; Table 1). Each pair of PALSAR images was treated separately to generate independent flow fields. Co-registration was done solely on Derwael Ice Rise, the western promontory and the pinning point because ice flow in those areas is <15 m a^{-1} (Drews, 2015; Drews and others, 2015), leading to a negligible displacement of the ice-sheet surface in the 46-day interval of the PALSAR images.

Offsets caused by ice flow were tracked every 12 and 36 pixels in range and azimuth, using a normalised cross-correlation of image patches (64×192 pixels), with a signal-to-noise-ratio threshold of 7 and an over-sampling factor of 2 (cf. Rankl and others, 2014). Range and azimuth offsets were georeferenced and converted to horizontal velocity fields with 125 m spacing. Mismatched pixels were removed (following Mouginot and others, 2012) and the flow fields were finally smoothed by averaging within 9×9 diamond-shaped windows. Because speckle tracking is insensitive to tides, only one of the InSAR ground-control points was used for the entire area (filled red triangle; Fig. 1).

2.1.3. Mosaicking

The four PALSAR flow fields (Table 1) were mosaicked and then blended with the ERS velocities. To reduce cutting edges, velocity maps were feathered by applying a linear taper ranging from 0 to 1 in the overlapping areas. Data gaps on the western promontory and Derwael Ice Rise were filled with Rignot and others (2011b)'s flow field and feathered over 4.5 km.

2.1.4. On-site ice-flow measurements

To measure ice flow, 3 m long markers were placed on the ice-shelf and revisited the next year (Fig. 1). The 42 stakes were positioned using geodetic, dual-phase GNSS receivers with an antenna mounted on top of the stakes, measuring for at least 30 min. The data were post-processed using Precise Point Positioning (PPP) from the Canadian Spatial Reference System. Measurements were collected over a 3 a period. The wider-spaced markers (average distance 5 km) were measured in 2012/13, and a denser network crossing an ice-shelf channel (defined in Section 1) was measured in 2013/14 (Drews, 2015). In 2012/13 some markers were tilted, leading to a maximum uncertainty of ~2 m in the horizontal position. This error is larger than the uncertainty acquainted with the PPP, which is typically within cm (Kouba and Héroux, 2001). Because the average ice velocity in this area is ~265 m a^{-1}, this error is <1%. We used the GNSS-derived velocities to calibrate and validate the satellite-based surface velocities (Sections 2.1 and 3.1).

Another set of ice-flow measurements stems from a triangulation network of 74 stakes measured multiple times with theodolites between 1965 and 1967 (Derwael, 2014; Fig. 1). We use this set of measurements to investigate the steady state assumption (Section 4.1).

2.2. Numerical modelling

Ice-sheet response to environmental conditions depends on the ice rheology and the conditions at the bed. These variables, however, are difficult to estimate experimentally and often parametrised in ice sheet and ice-shelf models. Inverse methods enable us to infer these model parameters from observed surface velocities and ice sheet thickness.

2.2.1. Ice-flow model

We used the adaptive mesh finite-volume ice sheet model BISICLES (http://BISICLES.lbl.gov) (Cornford and others, 2013), which solves the Schoof-Hindmarsh approximation (L1L2) of the full-Stokes equations on an adaptive horizontal two-dimensional (2-D) grid rendered by the Chombo adaptive mesh refinement toolkit. The L1L2 solution is based on the Shallow Shelf Approximation (SSA); vertical shearing is computed from the Shallow Ice Approximation (SIA) and represented within the effective strain-rate in Glen's flow law. BISICLES compares well with the Elmer/Ice ice sheet model, which solves the full Stokes set of equations. Both models yield similar results for ideal (Pattyn and others, 2013) and real-case Antarctic outlet glaciers (Favier and others, 2014), both in terms of ice dynamics and inversion.

In the BISICLES model, the ice rheology is given by Glen's flow law:

$$\boldsymbol{S} = 2\phi\eta\dot{\boldsymbol{\varepsilon}} \tag{1}$$

where $\boldsymbol{S}$ is the deviatoric stress tensor; $\dot{\boldsymbol{\varepsilon}}$ is the strain-rate tensor; η is the effective viscosity depending on the temperature field of the ice mass (updated from Pattyn, 2010) and on the effective strain rate (Wright and others (2014) and Cornford and others (2013) provide a detailed description of η); ϕ is a stiffening factor that can be tuned to account for effects such as ice damage and anisotropy, along with uncertainties for ice temperature. Equation (1) is the constitutive relation used by the forward model to calculate ice flow velocities from the stress-balance equations.

For the grounded part of the ice sheet, a linear friction law governs resistance to basal sliding:

$$\tau_\mathrm{b} = -Cu_\mathrm{b} \tag{2}$$

where τ_b is the basal traction, u_b is the velocity of ice at the bottom interface and C is an estimate of the friction coefficient. The magnitude of C depends on different factors such as subglacial hydrology, the presence of subglacial till, etc. (MacAyeal and others, 1995).

2.2.2. Inverse method

To solve inverse problems, BISICLES uses the control method described by Cornford and others (2015), which is comparable with those of MacAyeal (1993) and Morlighem and others (2010). A nonlinear conjugate gradient method is used to seek a minimum of the cost function J, by expressing its gradient in terms of the adjoint equations constructed from the stress-balance equations, and defined as:

$$J = J_\mathrm{m} + J_\mathrm{p} \tag{3}$$

where J_m is the misfit between observed and modelled velocities. The Tikhonov penalty function J_p is:

$$J_\mathrm{p} = \lambda_C J_C^{reg} + \lambda_\phi J_\phi^{reg} \tag{4}$$

where λ_C and λ_ϕ are the Tikhonov parameters and J_C^{reg} and J_ϕ^{reg}, respectively, represent the spatial gradients of C and ϕ integrated over the domain (Cornford and others (2015) provide the detailed formalism). A L-curve analysis (as in Fürst and others, 2015) was performed on the *High-resolution* scenario to calibrate λ_C and λ_ϕ, subsequently used in all the scenarios. Figure 2 presents the results of the L-curve analysis and highlights the chosen values of $\lambda_C = 5 \times 10^2$ Pa^{-2} m^6 a^{-4} and $\lambda_\phi = 5 \times 10^9$ m^4 a^{-2}.

2.2.3. Inverse experiments

We inverted simultaneously the stiffening factor (ϕ) and the basal friction coefficient (C) for the three scenarios as

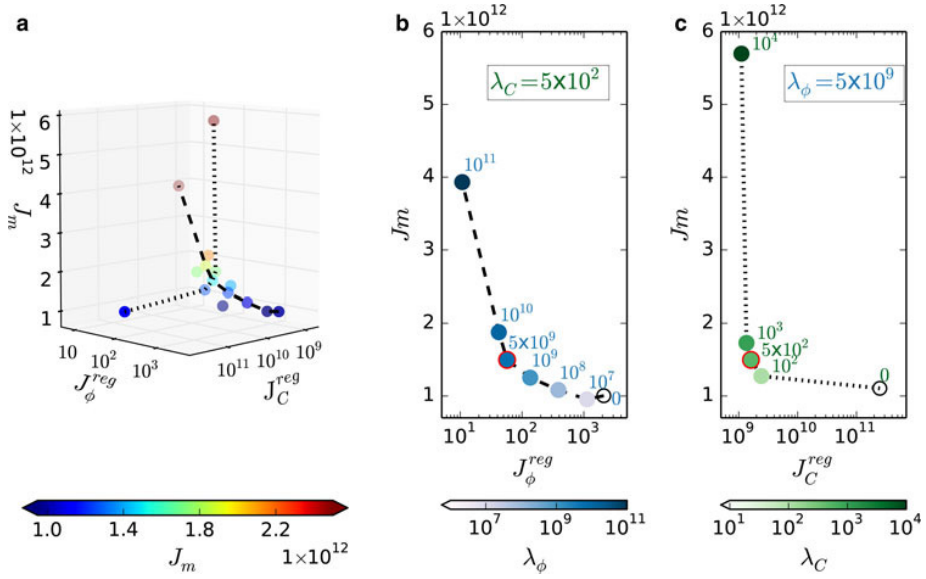

Fig. 2. L-curve analysis to select the Tikhonov parameters λ_ϕ and λ_C: (a) 3-D scatter plot of the model-data misfit J_m as a function of the regularisation terms J_C^{reg} and J_ϕ^{reg}. (b) 2-D cross section for variable λ_ϕ and λ_C fixed to 5×10^2 Pa^{-2} m^6 a^{-4}. (c) Reverse case where λ_ϕ is fixed to 5×10^9 m^4 a^{-2} and λ_C varies. The units of J_m and J_C^{reg} are m^{4}a^{-2} and Pa^2 m^{-2} a^2, respectively. J_ϕ^{reg} has no unit.

described in Section 1. For the *mBedmap2* dataset, used in the *Intermediate* and *High-resolution* scenarios, we modified the surface elevation and bathymetry of Bedmap2 by incorporating a pinning point with a Gaussian shape, with dimensions based on radar and GNSS profiles crossing the observed pinning point on the RBIS (Drews, 2015). Figure 4a shows the modifications for an along-flow cross section. We imposed a stress-free upper surface, water pressure at the calving front and the observed surface velocities at the other lateral boundaries. On the considered domain, all the inversions were performed at a 1 km spatial gridding.

2.2.4. *Sensitivity of the inversion to the initial guesses*

The inverse method is sensitive to the initial guesses of ϕ and C. To dampen this sensitivity, we chose physically justified initial fields for C and ϕ, called hereafter *basis fields*. The *basis* initial friction coefficient was computed from the SIA assuming balance between the driving stress and the basal friction. The *basis* initial stiffening factor was 1.

The former assumption is valid for most of the Antarctic ice sheet (Morlighem and others, 2014), but may not be applicable for ice streams where basal friction is low. We addressed this uncertainty by multiplying the SIA-based friction by 0.6, 0.8 and 1.2. As the inversion was robust under those different fields (<1% change of the RMS difference for the observed and modelled velocities), the model was initialised with the SIA-based friction fields.

The *basis* initial stiffening factor of 1 corresponds to an ice-creep parameter from Pattyn's (2010) updated temperatures only. In the ice sheet, no strong simplifications were applied (apart from neglecting horizontal diffusion) to calculate those temperatures, so we assumed they have sufficient physical meaning to be kept as initial conditions. However, in the ice-shelf, the temperature calculation neglected horizontal advection and internal strain heating, according to the analytical solution due to Holland and Jenkins (1999), so we investigated the sensitivity to an initial stiffening factor on the ice-shelf, ranging from 0.6 to 1.4. Increasing the initial value of ϕ decreased the velocity misfits (~20% difference between 0.6 and 1.4), and stiffened the ice shelf. Ice shelves are generally stiffer than an isotropic reference, because of their strain-induced anisotropy (Ma and others, 2010). However, since the corresponding results are quantitatively almost similar and did not give qualitative differences with the highest values of the initial ϕ, we chose to initialise the stiffening factor to 1 for the ice shelf.

3. RESULTS

3.1. Satellite-derived velocities on the RBIS and strain rates

Velocities in Figure 3a show how Derwael Ice Rise and the pinning point form a flux gate through which most of the ice of the RBIS is directed. Ice-shelf velocities average 205 m a^{-1} and reach 345 m a^{-1} at the front. Velocities decrease down to 0.5 m a^{-1} on the pinning point, which is comparable with the flow velocities near the ice divides of Derwael Ice Rise and the Western Promontory.

The flow field deviates by -5.2 ± 4.5 m a^{-1} and 7.5 ± 16.5 m a^{-1} from the GNSS-derived velocities and Derwael's (2014) triangulation network of 1965–67, respectively. The deviations for both ground-truth datasets do not show any spatial trend. Differences between the ERS and PALSAR mosaics decrease more or less linearly from positive values (~25 m a^{-1}) in the northern part of the overlapping area to negative values (~−25 m a^{-1}) in the southernmost parts. Mean ± standard deviation of the difference field is -5.6 ± 12.9 m a^{-1}. This systematic error likely reflects uncertainties in the baseline estimation of the ERS satellites and/or a systematic phase residual from SAR focusing (Drews and others, 2009). Strain rates were computed for a local coordinate system aligned with the main flow directions (y along- and x across-flow). Horizontal shear-strain rates reveal a number of features (Fig. 3b), which are discussed in Section 4.2.

3.2. Inversion results

The three inversion schemes all adequately reproduce the observed velocities: the RMSD between the modelled and observed velocities are 11.51, 11.25 and 12.33 m a^{-1} for the *Standard, Intermediate* and *High-resolution* scenarios

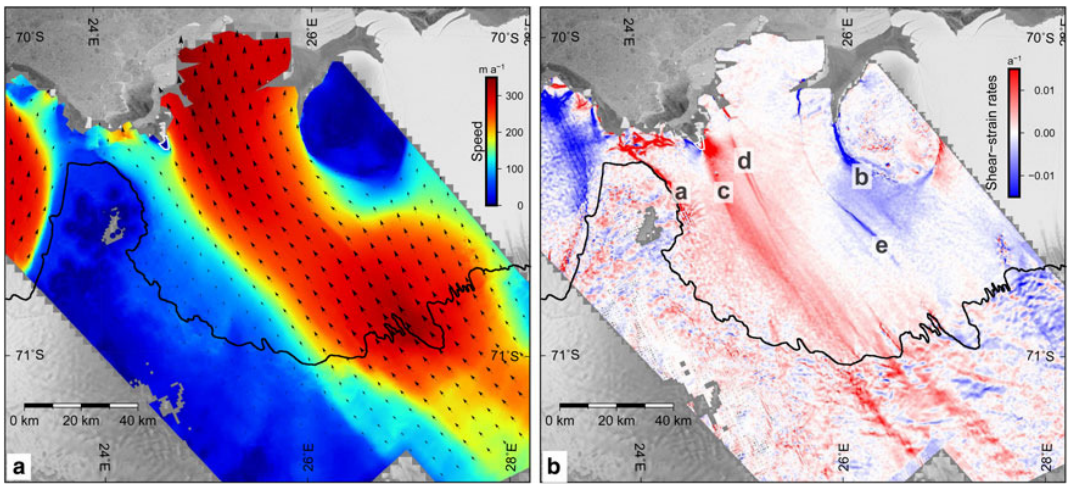

Fig. 3. (a) Horizontal surface velocities and (b) associated shear-strain rates. The grounding line (Bindschadler and others, 2011) is overlaid in black and the pinning point is marked in white. The labels a–e locate the areas of interest discussed in the text. The background image is from Radarsat mosaic (Jezek and RAMP-Product-Team, 2002).

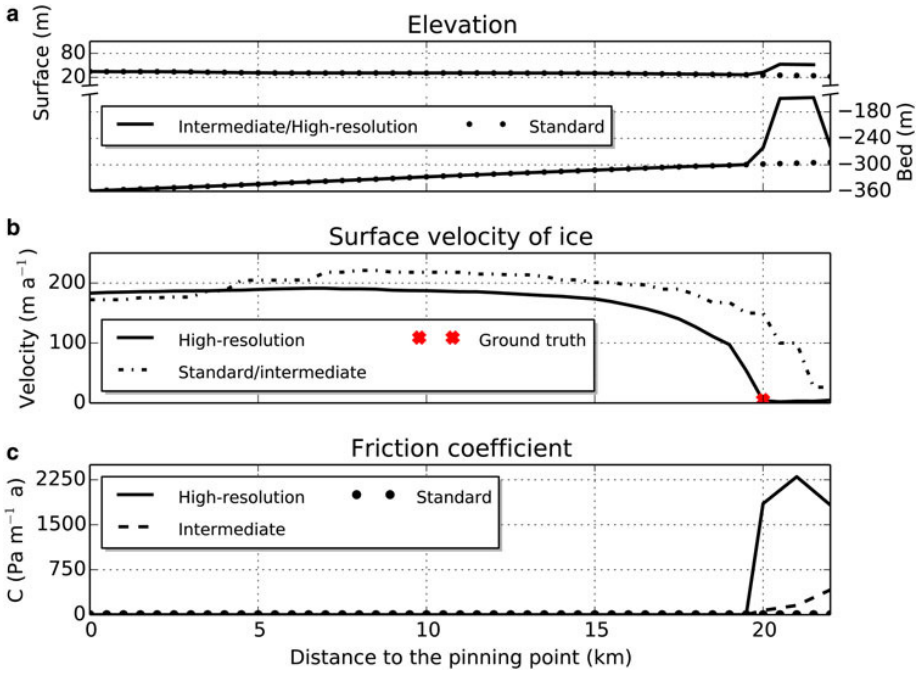

Fig. 4. Profiles along the straight line shown in Figure 5b, d and f. (a) Bed and surface elevations relative to the EIGEN-GL04 geoid. (b) Comparison of the high-resolution flow field and velocities from Rignot and others (2011b). The red cross shows the ground-truth velocity measured on the pinning point. (c) Inverted friction coefficient.

on the whole domain and fall to 8.48, 8.22 and 6.38 m a^{-1}, respectively, on the ice-shelf.

Excluding the vicinity of the pinning point, the inverted basal friction displays the same general pattern for the three scenarios (Fig. 5b, d and f). The slowly flowing western promontory and Derwael Ice Rise are sticky at the bed (C peaks at around 6200 and 5900 Pa m^{-1}a, respectively), whereas the fastest trunk of the West Ragnhild Glacier, upstream of the grounding line, is slippery with a basal friction coefficient ten times lower. The *Standard, Intermediate*, and *High-resolution* scenarios differ at the pinning point (insets in Fig. 5b, d and f). Because the pinning point is absent from the *Standard* scenario (Fig. 4a), the corresponding area is frictionless. In the *Intermediate* experiment, the pinning point is more slippery (mean $C \approx 485$ Pa m^{-1}a, for the pinning point) than the bed beneath the main stream of West Ragnhild Glacier, while in the *High-resolution* scenario it is on average 3.5 times stickier (mean $C \approx 1700$ Pa m^{-1}a, for the pinning point) than in the *Intermediate* scenario.

All the experiments display four similar features in the stiffening factor ϕ (labelled 1–4 in Fig. 5a, c and e). Two wide patches of stiffened ice appear in the centre of the ice-shelf: one, a few km downstream of the grounding line (label 1 in Fig. 5; max $(\phi) \simeq 2.50$) and the other, dozens of kilometres upstream of the calving front (label 4 – max $(\phi) \simeq 2.50$). The most softened ice appears directly upstream of Derwael Ice Rise (label 2 – min $(\phi) \simeq 0.14$) and, to a lesser extent, upstream of the pinning point (label 3 – min $(\phi) \simeq 0.40$), in its shear band (Fig. 3b; label c). The *Standard* experiment stands out from the *Intermediate* and *High-resolution* cases and exhibits another patch with the most stiffened ice (label 5 – max $(\phi) \approx 2.75$). Compared with the *Standard* scenario, the ice-shelf is, on average, 4.0 and 4.6% softer in the *Intermediate* and *High-resolution* simulations, respectively.

4. DISCUSSION

4.1. Is the Roi Baudouin Ice Shelf in steady state?

We mosaicked two different flow fields (1996 and 2010), both of which were calibrated on the ice-shelf with the same ground-control point collected in 2012/13 (Section 2.1). This approach holds if the RBIS is in steady state. To validate this hypothesis, we compared the mosaicked flow field with 74 ground-truth measurements collected in 1965–67 (Derwael, 2014; Section 2.1; Fig. 1). The deviations are not larger than the uncertainty of our high-resolution flow field and we conclude that the RBIS has not undergone prominent changes in average ice flow over the last five decades. This justifies our steady-state assumption in Section 2.1.

4.2. Velocities and strain rates

Our flow field (Fig. 3a) shows that ice virtually stagnates on the pinning point with a flow regime resembling more an ice rise than that of an ice rumple. This implies that the pinning point is stickier than what is suggested by the Antarctic-wide velocities (~150 m a^{-1} vs. 5 m a^{-1} for the ground truth; Fig. 4b) and that size alone is an insufficient criteria to classify ice rumples. Over a distance of only 5 km, ice from upstream is decelerated from 180 m a^{-1} to 0.5 m a^{-1}. The horizontal shear band upstream of the pinning point (label c; Fig. 3b) separates the stagnant part on the west of the ice-shelf from the fast flowing centre and attests to the importance of buttressing on the Western part of the RBIS. Although it is difficult to discriminate the buttressing of the western promontory from the contribution of the pinning point, the alignment between the horizontal shear band and the location of the pinning point suggests a connection. Preliminary transient simulations indicate that unpinning repositions this shear band westwards for about two-thirds

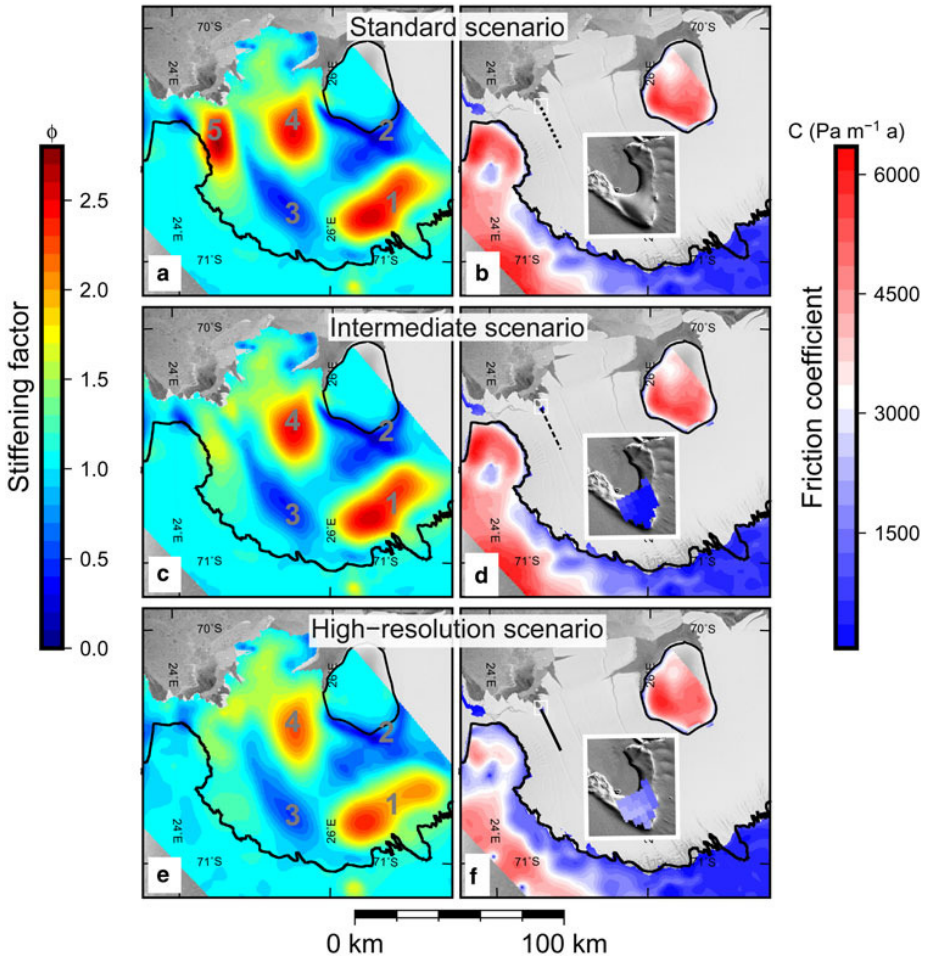

Fig. 5. (left: a, c and e) Stiffening factor ϕ and (right: b, d and f) friction coefficient C inverted for the *Standard* (top: a and b), *Intermediate* (middle: c and d) and *High-resolution* (bottom: e and f) scenarios. The grounding line (Bindschadler and others, 2011) is overlaid in black. A profile upstream/on top of the pinning point is shown in dotted, dashed and plain lines for the *Standard, Intermediate* and *High-resolution* scenarios, respectively. Theses profiles are plotted in Figure 4. The labels 1–5 locate areas of interest. Background images are from Radarsat Mosaic (Jezek and RAMP-Product-Team, 2002) and Landsat 8 of September 2014 (inset).

of the ice shelf upstream of the pinning point. In addition to horizontal shearing at the lateral boundaries of the RBIS (labels a and b; Fig. 3b), other remarkable features of the *High-resolution* flow field are the enhanced velocity gradients in the vicinity of ice-shelf channels (labels d and e; Fig. 3b). At the channels locations, the shearing reproduces the same pattern as that from the synthetic melting case of Drews (2015).

4.3. Inversion for the stiffening factor and basal friction

The *High-resolution* scenario has the highest averaged misfit between the observed and model velocities. However, the magnitudes of the misfits are primarily determined by the slow-flowing areas of Derwael Ice Rise and the Western Promontory, where the observations are correspondingly poor. Zooming in on the ice-shelf, the misfit of the *High-resolution* scenario is more than 20% lower compared with the two other scenarios.

The basal friction coefficient at the outlet of the West Ragnhild Glacier agrees with previous results (Callens and others, 2014), based on a different inversion method. Callens and others (2014) showed that the downstream part of the West Ragnhild Glacier bed is wide, flat and covered by wet sediments, which induces basal sliding, thus a low coefficient C. At that place, the *High-resolution* scenario indicates a more slippery bed because of slightly higher (+50 m a^{-1}) surface velocities between our flow field and that of Rignot and others (2011b). The sticky bed on Derwael Ice Rise and the western promontory concurs with low velocities and the negligible basal sliding in those areas.

The stiffening factor is used for fitting the modelled to the observed velocities. This means that it accounts for both physical approximations in the model and imperfections in the input data (e.g. missing factors such as damage, anisotropy and uncertainties in ice temperature); it is, however, not straightforward to distinguish between those different mechanisms. We will discuss hereafter the five patches of stiffened and softened ice (labels 1–5; Fig. 5a, c and e).

Patch 1 shows stiffened ice downstream from the grounding line, which we attribute to thermal effects. Our model uses the temperature field from Pattyn (2010), which neither accounts for horizontal advection nor horizontal shear-strain heating in the ice shelf (Holland and Jenkins, 1999). This means that the local stiffening at least partially accounts for the cold ice that is advected from the tributary glacier to the ice shelf. The softened ice in patches 2 and 3

can be explained along the same lines, since in these areas (close to Derwael Ice Rise and upstream of the pinning point, respectively) horizontal strain heating probably occurs; moreover these areas are crevassed. The inverse model does not reveal weak margins of softer ice on the side of the ice stream, in contrast with what has been shown for faster ice shelves (e.g. Favier and others, 2014; Larour and others, 2014; Fürst and others, 2015). We have no conclusive evidence for patch 4, and a full thermomechanical coupling will be required to draw more solid conclusions.

Patches 1–4 occur in all model runs, whereas patch 5 only appears in the *Standard* scenario. In this scenario, the ice slows down a few kilometres upstream of the pinning point but the latter is ignored in the bathymetry. To match the observed velocities, the inverse method must stiffen the ice in patch 5, while in the two other scenarios the inverse method can also increase the friction at the pinning point. The value of the surface velocity at the pinning point is of secondary importance : the pinning point is stickier and the ice is less stiffened in the *High-resolution* scenario than in the *Intermediate* scenario. Changing the boundary condition of the ice leads to qualitative differences, while using different velocity values only quantitatively changes the results.

Predictive simulations of the Antarctic ice sheet generally determine initial state and parameters by inverting observational data. Therefore, unresolved pinning points in the latter can result in spurious ice dynamics for transient simulations of unpinning. In the case of the *Standard* scenario, for example, the unpinned RBIS is erroneously buttressed by the stiff ice around the pinning point. This is not the case for the other two scenarios, i.e. softer ice near the pinning point presumably leads to higher flow velocities in unpinning experiments. Our results show that it is more important to incorporate the pinning point in the bathymetry than to resolve the velocities at the pinning point (and correspondingly the inverted basal friction coefficient), even though both may influence transient simulations of the RBIS.

Pinning points such as that presented here are features small enough to be neglected/undersampled in observational datasets but important enough to impact the ice dynamics of their surroundings. Few kilometres-wide features can have larger-scale implications, although the gridding of Antarctic-wide datasets is too coarse to capture them in a modelling framework. For instance, the pinning point of the RBIS only extends over ~8 pixels when the spacing is 1 km (vs. 458 with 125 m) and can thus easily be missed out. The results derived here accord with the findings of Durand and others (2011), demonstrating that it is important to better resolve pinning points in the bathymetry around the Antarctic coastline.

5. CONCLUSION

We derived a flow field for the Roi Baudouin Ice Shelf, combining satellite-based InSAR and speckle tracking techniques. The velocities deviate by -5.2 ± 4.5 m a^{-1} compared with a set of 37 independent ground-control points. Comparison of our flow field with ground-truth measurements collected in 1965–67 provides no evidence for ice flow changes on decadal time scales. With its 125 m gridding, the derived flow field currently has the highest resolution available for the RBIS and shows that ice on top of a 8.7 km^2 pinning point is virtually stagnant, contrary to what is indicated in other datasets. Despite its small size, this feature corresponds to a shear zone across the entire ice shelf.

Using different input scenarios of ice geometries/velocities we inverted for the stiffening factor (determining the ice rheology) and for the basal friction coefficient (determining the basal drag) using the BISICLES model. Surface velocities were adequately reproduced in all scenarios even in the one where the pinning point was omitted. However, including the pinning point in the bathymetry/ice thickness led to the best results on the ice shelf. The inversion for both ice rheology and basal conditions is the most sensitive to presence/absence of the pinning point in ice thickness and bathymetry. Neglecting basal drag at the pinning point is compensated by stiffened ice in its surrounding and overestimating the surface velocities at the pinning point results in too low basal friction coefficients. Both effects can cause errors in transient simulations. Our results emphasize that ice-flow models require high-resolution for observational datasets (especially bed topography) in coastal areas to fully capture the role of pinning points and their impact on the buttressing strength of ice shelves.

ACKNOWLEDGEMENTS

This paper forms a contribution to the Belgian Research Programme on the Antarctic (Belgian Federal Science Policy Office), Project SD/SA/06A Constraining ice mass changes in Antarctica (IceCon) as well as the FNRS-FRFC (Fonds de la Recherche Scientifique) project IDyRA. We thank the InBev Baillet Latour Antarctica Fellowship for partially financing fieldwork and the International Polar Foundation for providing all required logistics in the field. ERS1/2 and ALOS data were provided by the European Space Agency (Project C1P.10754) and further processed with the help of Wolfgang Rack at the Gateway Antarctica, Canterbury University, New Zealand. Ms. S. Berger is supported by a FRS-FNRS (Fonds de la Recherche Scientifique) PhD fellowship. Support and development of BISICLES from S. Cornford and D. Martin is greatly appreciated. We finally wish to thank A. Khazendar and an anonymous reviewer for constructive comments on this manuscript.

REFERENCES

Bamber JL, Gomez-Dans JL and Griggs JA (2009) A new 1 km digital elevation model of the Antarctic derived from combined satellite radar and laser data Part 1: data and methods. *Cryosphere*, **3**(1), 101–111

Bindschadler R and 17 others (2011) Getting around Antarctica: new high resolution mappings of the grounded and freely-floating boundaries of the Antarctic ice sheet created for the International Polar Year. *Cryosphere*, **5**(3), 569–588

Callens D and 5 others (2014) Transition of flow regime along a marine-terminating outlet glacier in East Antarctica. *Cryosphere*, **8**(3), 867–875

Cornford SL and 8 others (2013) Adaptive mesh, finite volume modeling of marine ice sheets. *J. Comput. Phys.*, **232**(1), 529–549

Cornford SL and 14 others (2015) Century-scale simulations of the response of the West Antarctic Ice Sheet to a warming climate. *Cryosphere*, **9**(4), 1579–1600

Costantini M (1998) A novel phase unwrapping method based on network programming. *IEEE Trans. Geosci. Remote Sens.*, **36** (3), 813–821

Derwael JJ (2014) *Snow accumulation data: Princess Ragnhild Coast, Antarctica. Belgian – Netherlands Antarctic Expeditions 1964 – 1965 – 1966. Technical Report*. Belgian Antarctic Archives, Brussels

De Rydt J, Gudmundsson GH, Rott H and Bamber JL (2015) Modelling the instantaneous response of glaciers after the collapse of the Larsen B Ice Shelf. *Geophys. Res. Lett.*, **42**(13), 5355–5363

Drews R (2015) Evolution of ice-shelf channels in Antarctic ice shelves. *Cryosphere*, **9**(3), 1169–1181

Drews R, Rack W, Wesche C and Helm V (2009) A spatially adjusted elevation model in Dronning Maud Land, Antarctica, based on differential SAR interferometry. *IEEE Trans. Geosci. Remote Sens.*, **47**(8), 2501–2509

Drews R and 5 others (2015) Evolution of Derwael Ice Rise in Dronning Maud Land, Antarctica, over the last millennia. *J. Geophys. Res.: Earth Surf.*, **120**(3), 564–579

Dupont TK and Alley RB (2005) Assessment of the importance of ice-shelf buttressing to ice-sheet flow. *Geophys. Res. Lett.*, **32**, L04503

Durand G, Gagliardini O, Favier L, Zwinger T and le Meur E (2011) Impact of bedrock description on modeling ice sheet dynamics. *Geophys. Res. Lett.*, **38**(20), L20501

Favier L and Pattyn F (2015) Antarctic ice-rise formation, evolution and stability. *Geophys. Res. Lett.*, **42**(11), 4456–4463

Favier L, Gagliardini O, Durand G and Zwinger T (2012) A three-dimensional full Stokes model of the grounding line dynamics: effect of a pinning point beneath the ice shelf. *Cryosphere*, **6** (1), 101–112

Favier L and 8 others (2014) Retreat of Pine Island Glacier controlled by marine ice-sheet instability. *Nat. Clim. Change*, **4**(2), 117–121

Fretwell P and 9 others (2013) Bedmap2: improved ice bed, surface and thickness datasets for Antarctica. *Cryosphere*, **7**(1), 375–393

Fricker HA and 5 others (2009) Mapping the grounding zone of the Amery Ice Shelf, East Antarctica using InSAR, MODIS and ICESat. *Antarct. Sci.*, **21**(5), 515

Fürst JJ and 7 others (2015) Assimilation of Antarctic velocity observations provides evidence for uncharted pinning points. *Cryosphere*, **9**(4), 1427–1443

Goldberg D, Holland DM and Schoof C (2009) Grounding line movement and ice shelf buttressing in marine ice sheets. *J. Geophys. Res.: Earth Surf.*, **114**(F4), F04026

Goldstein RM, Engelhardt H, Kamb B and Frolich RM (1993) Satellite radar interferometry for monitoring ice sheet motion: application to an Antarctic Ice Stream. *Science*, **262**(5139), 1525–1530

Gray L and 6 others (2002) RADARSAT interferometry for Antarctic grounding-zone mapping. *Ann. Glaciol.*, **34**(1), 269–276

Holland DM and Jenkins A (1999) Modeling thermodynamic Ice Ocean interactions at the base of an Ice Shelf. *J. Phys. Oceanogr.*, **29**(8), 1787–1800

Humbert A and Steinhage D (2011) The evolution of the western rift area of the Fimbul Ice Shelf, Antarctica. *Cryosphere*, **5**(4), 931–944

Jezek K and RAMP-Product-Team (2002) *RAMP AMM-1 SAR image mosaic of Antarctica*. Fairbanks, AK: Alaska Satellite Facility, in Association with the National Snow and Ice Data Center, Boulder, CO. Digital media

Joughin I, Smith BE and Medley B (2014) Marine ice sheet collapse potentially under way for the Thwaites Glacier Basin, West Antarctica. *Science*, **344**(6185), 735–738

Kouba J and Héroux P (2001) Precise point positioning using IGS orbit and clock products. *GPS Solutions*, **5**(2), 12–28

Larour E and 5 others (2014) Representation of sharp rifts and faults mechanics in modeling ice shelf flow dynamics: application to Brunt/Stancomb-Wills Ice Shelf, Antarctica. *J. Geophys. Res.: Earth Surf.*, **119**(9), 1918–1935

Luckman A, Murray T, Jiskoot H, Pritchard H and Strozzi T (2003) ERS SAR feature-tracking measurement of outlet glacier velocities on a regional scale in East Greenland. *Ann. Glaciol.*, **36**(1), 129–134

Ma Y and 5 others (2010) Enhancement factors for grounded ice and ice shelves inferred from an anisotropic ice-flow model. *J. Glaciol.*, **56**(199), 805–812

MacAyeal DR (1993) A tutorial on the use of control methods in ice sheet modeling. *J. Glaciol.*, **39**(131), 91–98

MacAyeal DR, Bindschadler RA and Scambos TA (1995) Basal friction of ice stream E, West Antarctica. *J. Glaciol.*, **41**(138), 247–262

Matsuoka K and 19 others (2015) Antarctic ice rises and rumples: their properties and significance for ice-sheet dynamics and evolution. *Earth-Sci. Rev.*, **150**, 724–745

Morlighem M and 5 others (2010) Spatial patterns of basal drag inferred using control methods from a full-Stokes and simpler models for Pine Island Glacier, West Antarctica. *Geophys. Res. Lett.*, **37**(14)

Morlighem M, Rignot E, Mouginot J, Seroussi H and Larour E (2014) Deeply incised submarine glacial valleys beneath the Greenland ice sheet. *Nat. Geosci.*, **7**(6), 18–22

Mouginot J, Scheuchl B and Rignot E (2012) Mapping of ice motion in Antarctica using synthetic-aperture radar data. *Remote Sens.*, **4** (9), 2753–2767

Mouginot J, Rignot E and Scheuchl B (2014) Sustained increase in ice discharge from the Amundsen Sea Embayment, West Antarctica, from 1973 to 2013. *Geophys. Res. Lett.*, **41**(5), 1576–1584

Paolo FS, Fricker HA and Padman L (2015) Volume loss from Antarctic ice shelves is accelerating. *Science*, **348**(6232), 327–331

Pattyn F (2010) Antarctic subglacial conditions inferred from a hybrid ice sheet/ice stream model. *Earth Planet. Sci. Lett.*, **295** (3–4), 451–461

Pattyn F, L and 27 others 2013) Grounding-line migration in plan-view marine ice-sheet models: results of the ice2sea MISMIP3d intercomparison. J. Glaciol., 59(215), 410–422

Rankl M, Kienholz C and Braun M (2014) Glacier changes in the Karakoram region mapped by multimission satellite imagery. *Cryosphere*, **8**(3), 977–989

Rignot E, Mouginot J and Scheuchl B (2011a) Antarctic grounding line mapping from differential satellite radar interferometry. *Geophys. Res. Lett.*, **38**(10)

Rignot E, Mouginot J and Scheuchl B (2011b) Ice flow of the Antarctic ice sheet. *Science*, **333**(6048), 1427–1430

Scambos TA, Bohlander JA, Shuman CA and Skvarca P (2004) Glacier acceleration and thinning after ice shelf collapse in the Larsen B embayment, Antarctica. *Geophys. Res. Lett.*, **31**(18), L18402

Scharroo R and Visser P (1998) Precise orbit determination and gravity field improvement for the ERS satellites. *J. Geophys. Res.*, **103**(C4), 8113

Schmeltz M, Rignot E and MacAyeal DR (2001) Ephemeral grounding as a signal of ice-shelf change. *J Glaciol.*, **47**(156), 71–77

Smith AM (1986) Ice rumples on Ronne Ice Shelf Antarctica. *Brit. Antarct. Surv. Bull.*, (72), 47–52

Strozzi T, Luckman A, Murray T, Wegmuller U and Werner CL (2002) Glacier motion estimation using SAR offset-tracking procedures. *IEEE Trans. Geosci. Remote Sens.*, **40**(11), 2384–2391

Werner C, Wegmüller U, Strozzi T and Wiesmann A (2000) Gamma SAR and interferometric processing software. In *Proc. ERS-Envisat Symposium*.

Werner C, Wegmuller U, Strozzi T and Wiesmann A (2005) Precision estimation of local offsets between pairs of SAR SLCs and detected SAR images, Geoscience and Remote Sensing Symposium, 2005 In *IGARSS '05. Proceedings. 2005 IEEE International*, vol. 7, 4803–4805

Wright AP and 10 others (2014) Sensitivity of the Weddell Sea sector ice streams to sub-shelf melting and surface accumulation. *Cryosphere*, **8**(6), 2119–2134

MS received 31 July 2015 and accepted in revised form 17 December 2015

Chapter 5

Discussion

This chapter is structured as follows: we first discuss the limitations and opportunities for methodological improvements in deriving ice-shelf flow fields (Section 5.1.1) and (ii) basal mass balance fields (Section 5.1.2). We then briefly explore the ocean circulation under the Roi Baudouin Ice Shelf (Section 5.2). And finally, we close this chapter with a broader discussion about the stability of the RBIS and other ice shelves in Dronning Maud Land (Section 5.3).

5.1 Methodological considerations and outlook

5.1.1 Velocities

Here, we address the two major limitations that we encountered while deriving the velocity field of the RBIS, namely the co-registration and the lack of coherent SAR images (Section 2.1).

Co-registration
Co-registering SAR images from former satellites (e.g. ERS 1 & 2, ENVISAT, ALOS, etc.) can be tricky because their orbits are not sufficiently constrained (e.g. Strozzi et al., 2002, Mouginot et al., 2012). As a result, co-registration cannot solely rely on information about satellites' position but, instead, is typically based on cross-correlation of intensity images to find and remove a global offset (by fitting a polynomial) (Section 2.1.4). This technique works perfectly well with InSAR, as displacement is retrieved from phase information, itself unrelated to intensity. However, this kind of co-registration becomes challenging for speckle tracking. In that case, orbital offsets need to be discriminated from displacement offsets, whereas both main processing steps (co-registration and offset tracking) rely on the same approach (i.e. 2D-cross-correlation).

Take, for instance, the calving front of the RBIS, which advances between two calving events. Two accurately co-registered images for InSAR must show the front at the same position. On the other hand, for speckle tracking, the calving front must be slightly shifted between the two co-registered images. For speckle tracking, intensity-based co-registration should therefore only be performed on the fixed parts of the scene. As rocky outcrops are lacking at the RBIS, we have based the co-registration of the PALSAR images only on the slow-moving grounded parts of the scene, namely Derwael Ice Rise, the western promontory and the pinning point. To account for possible loss of precision due to this kind of co-registration, we have also calibrated the flow fields with GNSS measurements.

The issue of imprecise orbits has however been addressed in the new generation of satellites (e.g. TanDEM-X, Sentinel-1a & 1b), which carry GNSS receivers on-board (Krieger et al., 2007, Nagler et al., 2015) that are able to estimate the relative position of the satellites with an accuracy of 1-2 mm (Kroes et al., 2005). This means that orbital information has become enough con-

strained to achieve precise co-registration (with the help from an external DEM in case of strong topography, Sansosti et al., 2006, Nagler et al., 2015).

Data suitability

Problems of data availability have been gradually overcome over the last decade. For instance, while the first Antarctic-wide velocity mosaic was not published until 2011 (Rignot et al., 2011, Mouginot et al., 2012), today such mosaics are released on a yearly basis (e.g. Mouginot et al., 2017). Such a drastic change has been initiated by the 2007-2009 International Polar Year, which saw a concerted effort from the European, Canadian, Japanese and US space agencies to acquire a vast amount of data over Antarctica and map continent-wide ice velocities for the very first time (Rignot et al., 2011, Mouginot et al., 2012). Building on the success of the International Polar Year, recent SAR satellite missions now regularly acquire data over Antarctica, considerably increasing the amount of SAR observations over the ice sheet.

Launched in 2014 and 2013, Sentinel-1 and Landsat-8 satellite missions are of particular interest, as they have arguably revolutionised the mapping of Antarctic velocities (Nagler et al., 2015, Mouginot et al., 2017, Jeong and Howat, 2015, Fahnestock et al., 2016). Data from both missions are openly and freely accessible and regularly, if not continuously, acquired over the ice sheet.

The Sentinel-1 mission is part of the broader European Copernicus Programs, which aims at systematically and continuously monitoring the Earth System on the long-term (Berger et al., 2012, Malenovský et al., 2012). Sentinel-1 is a constellation of two SAR satellites (Sentinel-1a &-1b) with a repeat period of 12 days each and separated by 6 days. The Sentinel-1 mission has adopted a specific strategy to monitor the AIS with at least one yearly campaign of 4-6 repeat cycles to monitor the ice-sheet margins, and continuous coverage of fast changing regions such as the Amundsen Sea sector and the Antarctic Peninsula. Besides, the 6-day time separation between Sentinel-1a and 1b acquisitions might be sufficiently short to retain coherence on the ice-sheet's surface, hence enabling InSAR processing or intermediary solutions between InSAR and speckle tracking, such as coherence tracking (Derauw, 2000, Pattyn and Derauw, 2002) – a variant of speckle tracking that also uses the phase information – or a combination of interferometric offsets in range and speckle-tracking offsets in azimuth (from one pair of SAR images) (Joughin, 2002).

Unlike the sensors previously considered in this thesis, the Operational Land Imager (OLI) on-board Landsat-8 is an optical sensor that therefore images the earth in the visible and infrared[1]. Thanks to its improved capabilities compared to its predecessors (Landsat 1-7), it has become possible to successfully perform feature tracking with Landsat-8, with a precision comparable to that from SAR speckle tracking (Jeong and Howat, 2015, Fahnestock et al., 2016, Mouginot et al., 2017). Such improvements include (Irons et al., 2012): (i) a fine spatial resolution (15 m for the panchromatic band); (ii) a large amount of data acquired so frequently (16-day repeat cycle) that it overcomes data lost to cloud cover and lack of illumination (Section 2.1.1); and (iii) a better radiometric resolution (12-bit compared to 8-bit before, Morfitt et al., 2015) that now shows subtle details of surfaces as bright as snow and ice, which were saturated in previous Landsat 1-7 images (Winsvold et al., 2016).

Of course Sentinel-1 and Landsat-8 are not the only satellites currently operational, but we have deliberately not treated the other missions because data-access is restricted (e.g. with the SAR mission : Radarsat-2, TerraSAR-X, Cosmo-Skymed, ALOS-PALSAR-2) or because Antarctica does not belong to their regular acquisition plan (as with Sentinel-2, the European optical counterpart to Landsat-8).

[1] Landsat-8 OLI is therefore a passive sensor, recording the energy coming from the sun and backscattered towards the satellite.

To sum up, the new generation of satellite missions such as Sentinel-1 and Landsat-8 have sharply increased the amount of observations over Antarctica, enabling us to understand the ice sheet like never before. This new wealth of data is paving the way towards a better monitoring of the entire ice sheet, for which regular, if not continuous, data acquisition is ensured in the long term (at least until 2030). If the proliferation of observations is now opening up the possibility for a better incorporation of observations in ice-sheet models, ultimately improving their performance, it also poses new challenges to process such large amounts of data. Overall, we can expect that the new open data policy of these satellite missions will spur improvements and new applications, as it has been the case with the opening of Landsat archives (Wulder et al., 2012).

5.1.2 Lagrangian basal mass balance

As we have seen in Chapter 3, the method we have developed to detect the basal mass balance of ice shelves performs well, or rather, performs well at the Roi Baudouin Ice Shelf. With the idea of temporal and/or spatial upscaling of the technique, this section first discusses the main weaknesses of our LBMB-detecting method at the RBIS. This includes the poor resolution of atmospheric-modelling outputs, the calibration of the DEMs and other issues with small-scale features. Whenever it is possible, we provide some hints on how to address major hurdles and then we explicitly discuss the upscaling possibilities.

Atmospheric-modelling outputs

Outputs from atmospheric modelling – firn-air content and surface mass balance (from Lenaerts et al., 2017) – are gridded with 5.5 km, which is a spacing 550 times coarser than that of the TanDEM-X DEMs. Firn-air content and SMB fields are therefore unable to resolve 1-2 km-wide variations over small-scale features (e.g. ice-shelf channels), for which field data indicate small-scale variability in the SMB and firn-air content (Langley et al., 2014a, Drews et al., 2016). This lack of resolution can introduce biases in the resulting LBMB fields either by underestimating the SMB in surface depressions or because of erroneous absolute thickness. However, alternative techniques to estimate the SMB and firn-air content all have drawbacks that prevent their use in our LBMB method.

Surface mass balance can be inferred from various in situ techniques, either along lines by ground-penetrating radars or at single points by stakes, ice/firn cores and ultrasonic sounders (Eisen et al., 2008, and references therein). Similarly, radio-echo sounding can yield profiles of firn-air content (e.g. Holland et al., 2011) or point measurements (e.g. Drews et al., 2016, and references therein). Unfortunately, all of the aforementioned techniques require substantial logistics to provide only sparse measurements, which renders them unsuitable for broader application of our LBMB method.

While firn-air content is undetectable with satellites, spaceborne remote sensing can provide SMB fields with comprehensive spatial coverage, but (i) their gridding is currently even coarser than high-resolution atmospheric modelling (e.g. 25 km spacing in Arthern et al., 2006), and (ii) none of the existing techniques are currently totally operational (Koenig et al., 2015, and references therein).

As a result, the 5.5 km gridding from atmospheric modelling, albeit imperfect, present therefore the least worst solution to obtain firn-air content and SMB, as it currently provides the finest resolution and the most exhaustive spatial coverage among the existing techniques.

Furthermore, unlike many ground-based measurements, temporal evolution is captured by atmospheric modelling and could, in theory, be implemented in the methodology described in this thesis. Considering temporal changes would improve the quality of the final LBMB field as atmospheric processes vary strongly between years (Section 1.2.3).

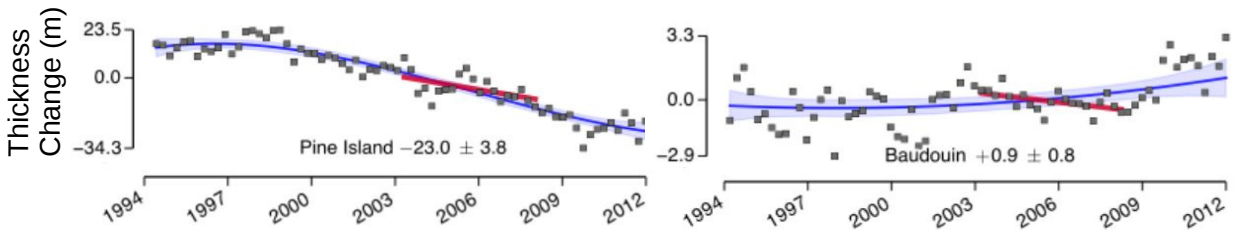

Figure 5.1: Time series of cumulative thickness change for the Pine Island and Roi Baudouin Ice shelves. Black dots are 3-month-average thickness changes (from radar altimetry) relative to series mean, the blue curve is the 18-year polynomial trend with the 95% confidence band, and the red line shows the regression line for the period 2003-2008 (which corresponds to the ICESat period analysed by Pritchard et al., 2012). Average rates (in m/decade) are annotated and derived from the end points of the polynomial models. Credit: subset of Fig. S1 from Paolo et al. (2015) [Reprinted with the American Association for the Advancement of Science].

The relatively coarse resolution of atmospheric modelling acts therefore as the most limiting factor in finely resolving LBMB fields, but remains nevertheless the least worst data source currently at hands, in addition to accounting for temporal variability (neglected in here).

Calibration of digital elevation models

We have also seen that the relative accuracy of the DEMs is so critical that we had to apply a number of adjustments to the DEMs (calibration, plane-correction), to avoid small elevation trends translating in huge melting trends.

However, the fact that the DEMs from 2014 are plane-fitted to the ones from 2013 hampers the detection of absolute melt-rates. In our case, the impact is minimal because the overall thickness change at the RBIS over 1 year is smaller than the precision of DEMs (0.09 m a^{-1}, Fig. 5.1), and can thus be neglected. This effect should nevertheless be accounted for if the time-span increases or if the ice shelf changes rapidly (e.g. Pine Island ice shelf, which thins at rate of 2.3 m a^{-1}, Fig. 5.1). Accounting for thickness changes requires therefore the DEMs to be calibrated independently. Ways to do so include (i) using stable points like rocky outcrops (which would require to explicitly correct for tidal uplift and inverse barometer effect); (ii) calibrating the DEMs with precise concurrent data from satellite altimeters (e.g. CryoSat-2, Sentinel-3, (upcoming) ICESat-2), although obtaining the required accuracy from the latter might be challenging (e.g. Helm et al., 2014, Nilsson et al., 2016); (iii) relying on concurrent GNSS data points. Furthermore, if the DEMs were to be calibrated independently, processing would need to get rid of residual trends in the DEMs, otherwise the effect of independent calibration would probably be removed by the plane-correction.

Small-scale features

Another limitation arises because hydrostatic thickness assumes freely floating ice. This is however not the case close to the grounding line – where basal melting is the strongest (Section 1.2.4) – and where bridging stresses (lateral stress transfer) prevent a full hydrostatic adjustment of small-scale features (Dutrieux et al., 2013, Vaughan et al., 2012, Drews, 2015). Bridging stresses, which are larger in narrower channels (Drews, 2015), should therefore be accounted for to improve the method.

Finally, Drews (2015) has shown that formation of ice-shelf channels characteristically imprints flow fields of buttressed ice shelves (i.e. when longitudinal stretching is not too dominant). Bottom melting induces lateral convergence into channels (Dutrieux et al., 2013), which in turn increases the effective strain rates, locally softens the ice and makes the velocities increase in a step-wise fashion. At the RBIS, channels are not linear but merge at several junctions (Fig. 1.13),

clearly visible in the velocity gradients (Fig 3. in Chapter 4). As the channels and their junctions are advected with the flow, a too long time lag between acquisitions of the velocity and thickness fields introduces therefore biases because channel's mark in the velocity and thickness fields are not aligned any more. Fortunately, this issue is easily addressed with increasingly available satellite observations (Section 5.1.1). This effect is also mitigated by the low velocity divergence at the RBIS.

Upscaling opportunities

The methodology developed in Chapter 3 can be seen as a proof of concept that could be easily be upscaled spatially and temporally, provided that (some of) the issues aforementioned are accounted for.

To illustrate this point, we have applied the same methodology to the Petermann ice shelf, North-West Greenland, to derive the LBMB at two different times: before and after a massive calving event in 2012, which was followed by a significant acceleration of velocities (Munchow et al., 2016, Neckel et al, in prep). Conditions at the Petermann ice shelf are completely different from those of the RBIS: the ice shelf is laterally confined within a 16 km-wide fjord, the surface mass balance is largely negative, firn-air content is very low and velocities range between 400 and 1200 m a^{-1}. Yet, preliminary results (Fig. 5.2) are in line with other estimates (e.g. Wilson et al., 2017).

Those results imply that (i) our methodology is directly transferable to other ice shelves, provided that the input data exist; and (ii) that the processing can be repeated to produce time-series and investigate temporal changes in basal melting. The proliferation of satellite observations should therefore provide a better picture of ice-ocean interactions, their spatial variability, thereby opening up the possibility for monitoring those interactions and their changes in the long term.

In the next section, we discuss the ice-ocean interactions that take place in the cavity of the RBIS.

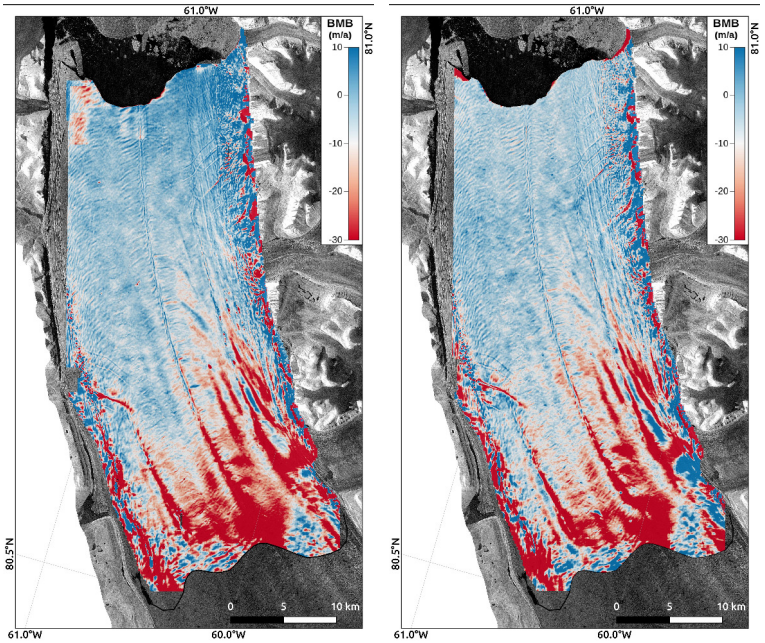

(a) Before calving event (b) After calving event

Figure 5.2: Lagrangian basal mass balance of the Petermann ice shelf, before and after a major calving event. Credit: Neckel et al (in prep).

5.2 Ocean circulation beneath the Roi Baudouin ice shelf

With very few oceanographic measurements and a little known bathymetry, the ocean circulation beneath the Roi Baudouin Ice Shelf is largely unknown and hard to model. The spatial pattern of our basal mass balance field, which shows significant spatial variability on both large and sub-kilometre scales, provides therefore valuable information about ice-ocean interaction in the cavity of the RBIS. Here, we discuss the large-scale ocean circulation beneath the RBIS, deliberately ignoring the small-scale interactions, which are discussed in the next section (Section 5.3.1).

The lack of oceanographic measurements at the RBIS can be partially circumvented with information about the much better-studied Fimbul Ice Shelf. There are a number of similarities with both ice shelves. For instance, Fimbul and Roi Baudouin ice shelves are both fed by major outlet glaciers of Dronning Maud Land (Callens et al., 2014, Fig. 1.12) and contain a number of ice-shelf channels (Langley et al., 2014a). Both ice shelves present melt-rates of the same order of magnitude (Rignot et al., 2013), with similar levels of melting found at the grounding line (~15 m a^{-1}) (Hattermann et al., 2014).

Furthermore, the oceanographic conditions at the Fimbul ice shelf are typical of coastal Dronning Maud Land[2] (Hattermann et al., 2014). There, ice shelves stretch over most of the continental shelf and their cavities are mainly filled by the relatively cold and fresh *Eastern Shelf Water*, which causes low melt rates. The Eastern Shelf Water also prevents (most of the time) the warmer and saltier *Warm Deep Water*, located off-shore, from penetrating the ice-shelf cavities (Fig. 5.3, Nøst et al., 2011). Note that Warm Deep Water is the regional version of the Circumpolar Deep water, after the cooling and freshening of the latter by the Weddell Gyre (Nicholls et al., 2009, Fig. 1.7, Section 1.2.4). For its part, the less dense Eastern Shelf Water is formed by mixing between cold winter water, glacial meltwater and incursions of warm deep water (Nicholls et al., 2009). This oceanographic configuration is overlain at the end of summer by a layer *Antarctic Surface Water*, a fresh warm water mass produced by solar heating and sea-ice melting nearby the ice-shelf front (Hattermann et al., 2014).

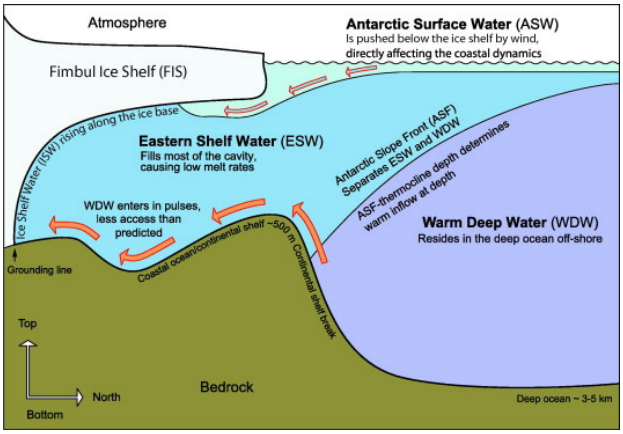

Figure 5.3: Schematic cross-section across and ice-shelf cavity and continental shelf-slope in Dronning Maud Land. The specific case of Fimbul Ice Shelf is illustrative of other ice shelves in the area. Credit: Fig. 1 from Hattermann et al. (2014).

Based on this oceanographic configuration, Hattermann et al. (2012) explain the relatively low basal melting at Fimbul Ice Shelf by a combination of the 3 melting modes (Jacobs et al., 1992, Section 1.2.4). They show that Fimbul ice shelf has a cold cavity (mode 1) where most oceanic heat for basal melting comes from (i) pulses of Warm Deep Water that intrude in the cavity under the form of eddies[3] (mode 2) and (ii) summer-heated Antarctic Surface Water pushed below the ice-shelf front by wind (mode 3) (Nøst et al., 2011, Hattermann et al., 2012, 2014). Given the similarities between the configurations of the Fimbul and the Roi Baudouin ice shelves, it is fair to consider that part of those processes could also be at play at the RBIS. In what comes next, we gather the information we have about the RBIS and discuss how the 3-melting modes could interact in its cavity.

[2]Often referred to as Eastern Weddell Sea by oceanographers.

[3]An *eddy* is a temporary loop of swirling water that detaches from a main current.

Two sets of evidences suggest that the RBIS undergoes melt-mode 1, whereby melt and re-freezing is controlled by reduction of the melting-point with depth. First, the dominance of this mode matches with the overall low melting at the RBIS, which is consistent with a cavity mainly filled with the cold Eastern Shelf Water, too cold to vigorously warm the ice shelf (except nearby the grounding line). Second, Mode 1 is also supported by significant layers of marine ice (>10 m), which are (i) evidenced by ice cores and optical televiewer from a rift area on the western part of the ice-shelf front (Pattyn et al., 2012, Hubbard et al., 2012), and (ii) suggested by conflicting thickness from ground-penetrating radar and hydrostatic inversion of GNSS elevations (Gossart, 2014). Marine-ice accretion could reconcile the discrepancy (that exceeds error) between the sets of thickness, as the penetrating radar is insensitive to marine ice, unlike the hydrostatic thickness. Furthermore, Gossart (2014) also used the flux-gate method (a mass conservation variant of the method outlined in Section 2.2) to calculate the mass balance of different boxes. This technique also hinted at slight accumulation of marine ice beneath the RBIS.

Evidence for melt-mode 3 at the RBIS stems from 1-year time series of basal melt-rates from a phase-sensitive radar installed 25 km upstream of the calving front (Sun et al, in prep). Figure 5.4 shows a strong seasonal variability in a shallow part of the ice shelf. Sharp increase of summer melt-rates, close to the ice front, is consistent with measurements at Fimbul ice shelf (Hattermann et al., 2012, Langley et al., 2014b) and suggests that ice directly upstream of the RBIS front is melted by solar-heated Antarctic Surface Water pushed on-shore by the combined action of Easterly winds and Coriolis (i.e. Ekman transport).

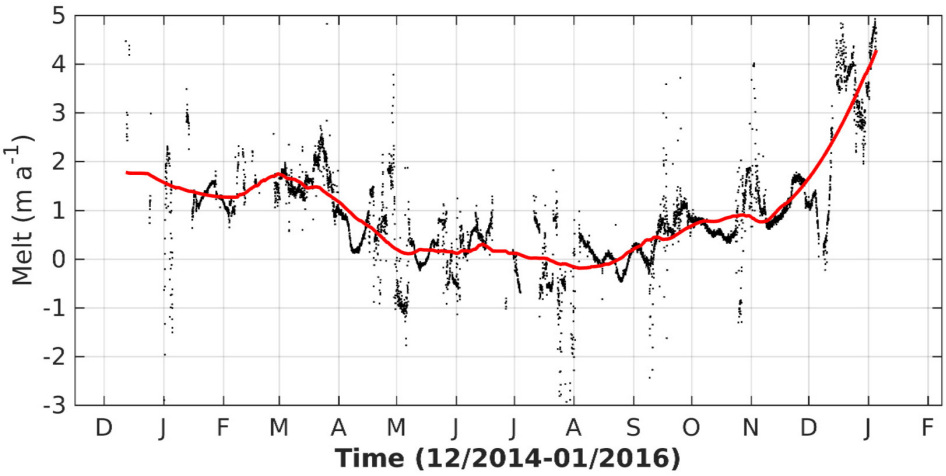

Figure 5.4: 1-year time series of sub-shelf melt-rates, 25 km upstream of the calving front, measured by phase-sensitive radar between December 2014 and January 2016. The red curve shows the filtered results. Credit: Sun et al, (in prep).

Finally, there is also evidence for melt-mode 2. We have seen that Eastern Shelf Water protects ice-shelf cavities from incursions of Warm Deep Water and hence limits basal melting in Dronning Maud Land. It has been suggested that, from time to time, short pulses or *eddies* of Warm Deep Water penetrate the Fimbul-ice-shelf cavity and provide heat that temporally enhances melting (Nøst et al., 2011, Hattermann et al., 2012, 2014). The same mechanism could occur at the RBIS. Oceanographic measurements at the front of the ice shelf have not only revealed the existence of a 850 m-deep marine trough directly downstream of the outlet of the West Ragnhild Glacier, but also that a warm and saline water mass that can enter the RBIS cavity (K. Leonard, pers. Com, Fig. 5.5). This water mass is (i) characteristic of modified Warm Deep Water (mix between Warm Deep and Eastern Shelf Waters), (ii) is located at the same depth as the grounding line of the West Ragnhild Glacier and (iii) is 1.7°C warmer than the in-situ freezing point at that depth. These measurements therefore imply that that the trough constitutes a potential gateway

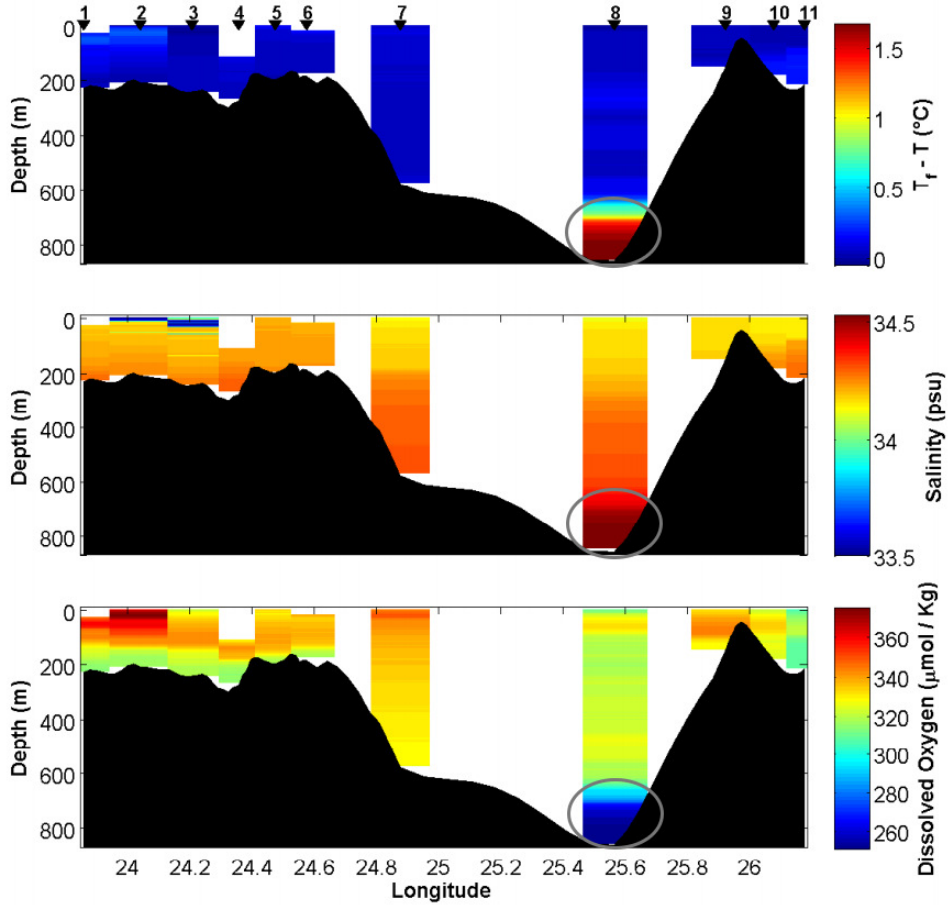

Figure 5.5: Conductivity-temperature-depth measurements made at the RBIS front in 2011. East-West profile showing the bathymetry below the ice front with (top): water temperature above in situ freezing point, (middle): salinity, and (bottom): dissolved oxygen. The grey ellipse show the presence of modified Warm Deep Water. Credit: Fig. 5.4 from Callens (2014).

for Warm Deep Water incursions in the RBIS cavity, whose inlet has been, at least once, occupied by modified Warm Deep Water.

Following the parametrization from Rignot and Jacobs (2002), the water mass observed at the bottom of the trough could lead to grounding line melt-rates as high as 20 m a^{-1}, which is consistent with the ice-shelf profile in the vicinity of the grounding line (Fig. 5.6). The rapid thinning of ice directly downstream of the grounding line (200 m in 5 km) cannot be explained by flow divergence alone. Those melt-rates estimates are however much larger than the melt-rates of ~5 m a^{-1} observed over a two-week period with phase-sensitive radar at the grounding line (Sun et al., in prep). The observed incursions of modified Warm Deep Water might therefore be driven by intermittent eddies, like it is the case at Fimbul ice shelf.

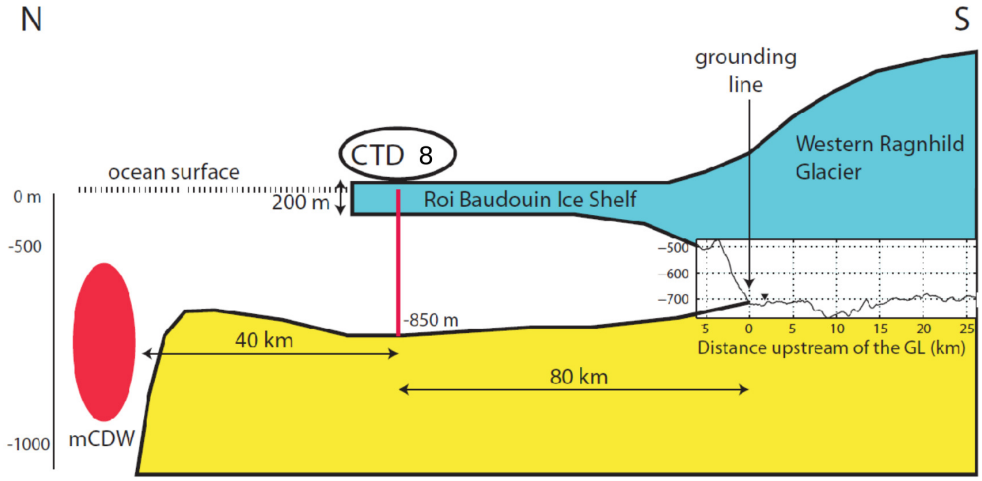

Figure 5.6: Along-flow profile of the continental shelf, the Roi Baudouin Ice Shelf and the West Ragnhild Glacier. Modified Warm Deep Water from the deeper ocean has been observed in the RBIS cavity (CTD 8), at the same depth as the grounding line (radar profile). Credit: F. Pattyn

5.3 Ice-shelves stability in Dronning Maud Land

Finally, we could not close this chapter without specifically discussing the stability of Roi Baudouin Ice Shelf and that of other ice shelves in Dronning Maud Land. This section presents an ideal opportunity to bring together previous studies focusing on the RBIS and to incorporate the following co-authored papers in this thesis:

- Drews, R., Pattyn, F., Hewitt, I. J., Ng, F. S. L., **Berger, S.**, Matsuoka, K., Helm, V., Bergeot, N., Favier, L., and Neckel, N. (2017). Actively evolving subglacial conduits and eskers initiate ice shelf channels at an Antarctic grounding line. *Nature Communications*, 8:15228
- Favier, L., Pattyn, F., **Berger, S.**, and Drews, R. (2016). Dynamic influence of pinning points on marine ice-sheet stability: a numerical study in Dronning Maud Land, East Antarctica. *The Cryosphere*, 10(6):2623–2635
- Lenaerts, J. T. M., Lhermitte, S., Drews, R., Ligtenberg, S. R. M., **Berger, S.**, Helm, V., Smeets, C. J. P. P., van den Broeke, M. R., van de Berg, W. J., van Meijgaard, E., Eijkelboom, M., Eisen, O., and Pattyn, F. (2017). Meltwater produced by wind–albedo interaction stored in an East Antarctic ice shelf. *Nature Climate Change*, 7(1):58–62

After having dealt with the methodological aspects of the LBMB-technique (Section 5.1.2) and having explored the ocean circulation under the RBIS (Section 5.2), we now take a closer look at small-scale basal-melt features, namely ice-shelf channels (Section 5.3.1). We next focus on the pinning point analysed in Chapter 4 and explore its impact on prognostic modelling (Section 5.3.2). We then review the relative stability of the Roi Baudouin Ice Shelf in the past, present and future (Section 5.3.3), before closing with a note on two potential mechanisms that could threaten the instability of the RBIS from below and above: (i) the bathymetric trough highlighted in the previous section (Section 5.3.4) and (ii) surface meltwater and its storage on the ice shelf (Section 5.3.5).

5.3.1 Ice-shelf channels

Ice-shelf channels are intriguing features at the surface and base of ice shelves, whose formation and impact on ice-shelf stability are still debated in the literature. On the one hand, ocean

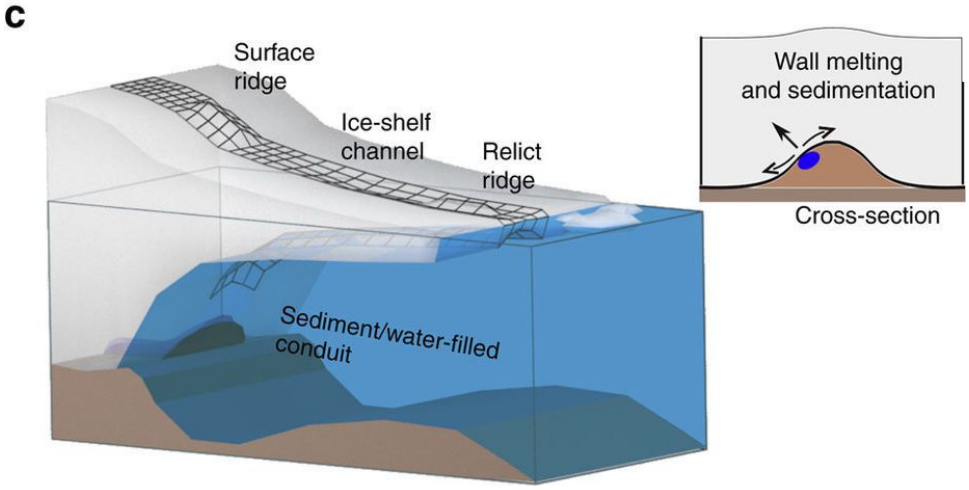

Figure 5.7: Esker formation and ice-shelf initiation at the grounding line of the RBIS. Credit: Fig. 2c from Drews et al. (2017).

modelling suggests that channels stabilise their ice shelves as they prevent ice-shelf-wide basal melting and reduce the average melt-rates (Gladish et al., 2012, Millgate et al., 2013). However, other studies suggest that channels can destabilise ice shelves in two ways. First, ice at channels can be up to 75% thinner than in their surroundings (Rignot and Steffen, 2008, Alley et al., 2016), making such channels potential weak spots. Second, flexural stresses associated with channel's carving fracture the ice to form basal and surface crevasses (Vaughan et al., 2012, Sergienko, 2013), which can soften the ice and subsequently reduce the buttressing strength of the ice shelf (Albrecht and Levermann, 2014, Borstad et al., 2016).

Different theories of channels formation exist but they all explain channels deepening or continuation by freshwater plumes, whereby buoyant and fresh meltwater entrains warmer ocean water, which provides heat to sustain melting (Jenkins, 2011). As a result, those theories only differ in their initiation mechanism. There are currently three mechanisms that explain the formation of channels, which, like those of the RBIS, start at the grounding line and extend downstream. First, Sergienko (2013) has suggested that strong lateral shearing at an ice-shelf's lateral boundary leads to transverse variability in ice flow that can initiate a meltwater plume that leads to channels formation where the ice-shelf base is steeper. Second, meltwater plume and channels can also be initiated by discharge of subglacial meltwater at the grounding line (Jenkins, 2011). Although Le Brocq et al. (2013), Marsh et al. (2016) have detected ice-shelf channels where subglacial water discharge is predicted, they did not observe subglacial conduits, presumably because of their size, too small to be detected by ice-penetrating radar (Le Brocq et al., 2013). The last option is that topographic highs in the bed upstream of the grounding line incise the ice from below and that these gashes can initiate the meltwater plume needed to form channels (Gladish et al., 2012, Sergienko, 2013, Dallaston et al., 2015).

Despite their apparent distinctions, Drews et al. (2017) have recently linked the second and third processes at the RBIS (Fig. 5.7). As subglacial conduits approach the ocean, the overburden pressure on their top progressively decreases to totally disappear when the ice starts to float. In reaction, conduits widen considerably with the vanishing pressure, water inside subsequently slows down, and sediments it carries are deposited. In stable conditions, this process promotes the growth of sediment-ridges named *eskers*, which push the ice upwards, causing surface ridges. This theory is supported by ice-penetrating radar showing large conduits (up to 250 m high) on the grounded ice and explained by modelling (Drews et al., 2017).

The implications of this study are threefold. First, the RBIS channels are already widely carved upstream of the grounding line, which not only means that subglacial processes on the

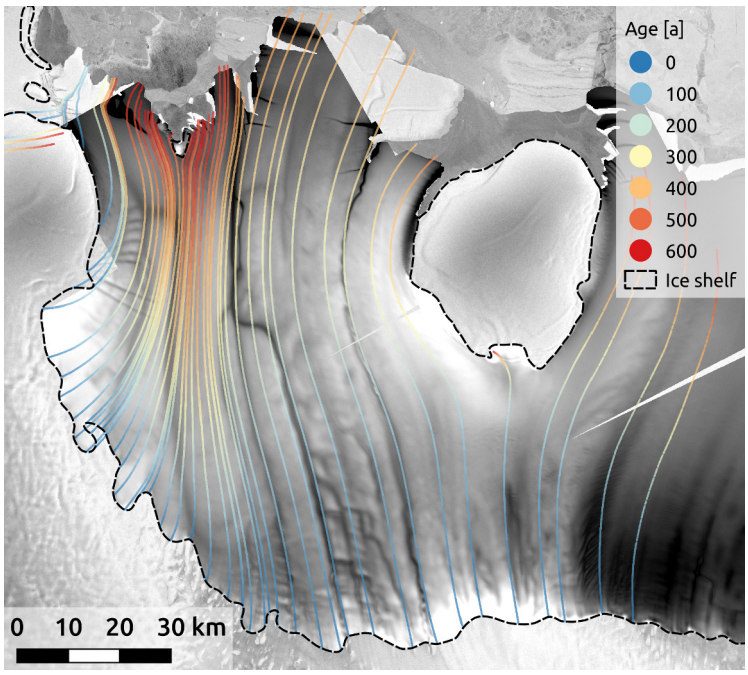

Figure 5.8: Advection time from the grounding line. Coloured dots: pathlines of the velocity mosaic, coloured with advection time from the grounding line. Grey: TanDEM-X elevation mosaic of 2013. Background: Radarsat mosaic (Jezek and RAMP-Product-Team, 2002).

grounded ice sheet (i.e. hydrology and sedimentation) are linked with ocean processes beneath the ice shelf (localised ocean melting at the channels), but also implies that channels can already weaken the ice inland. Second, eskers can potentially stabilise the grounding line, acting as sediment wedges (Alley et al., 2007). Third, those findings support the idea that ice-shelf channels archive the history of subglacial hydrology (Marsh et al., 2016, Le Brocq et al., 2013), meaning that changes in channels tracts (e.g. convergence, meandering) reflect changes in subglacial hydrology (e.g. conduit blockage and subsequent splitting or re-routing). Therefore, the alignment between the pathlines from our velocity field and the ice-shelf channels suggests that both the subglacial hydrological system beneath the West Ragnhild Glacier and the velocities of the RBIS have remained stable for the last 300-600 years (Fig. 5.8). This agrees with the the concept of eskers, which requires stability to develop.

Before discussing the stability of the grounding line in more details in Section 5.3.3, we now focus on the pinning point in front of the RBIS and discuss more specifically what the findings from Chapter 4 imply.

5.3.2 Influence of pinning points

We know from Chapter 4 that data assimilation with observations neglecting/misrepresenting a pinning point leads to spurious ice properties (ice viscosity and basal friction). Unfortunately, the study does not investigate how the small pinning point impacts prognostic modelling. Those questions have however been addressed in a follow-up study. Starting from the scenarios presented Chapter 4, Favier et al. (2016) have, amongst other things, investigated (i) the impact of spurious initialisation on prognostic modelling , together with (ii) the effect of sudden unpinning of the small pinning point in front of the RBIS. The main results are exposed below.

Initialisation without the pinning point

Omitting the pinning point during the initialisation of the ice-sheet model leads to excessive

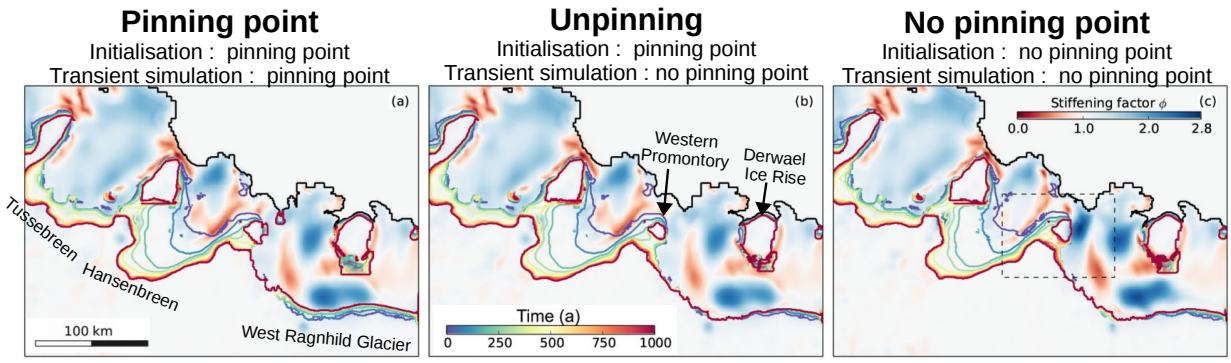

Figure 5.9: Grounding-line migration of the RBIS and neighbouring ice shelves for the next 1000 years (with linear sliding law and present-day melt-rates parametrised as in Gong et al. (2014)). The stiffening factor field is shown in background (colour scale in c), overlain with the grounding line mapped every 100 years (colour scale in b). The subfigures (**a-c**) represent different experiments including or not the pinning point in initialisation and/or prognostic simulation. Note: as explained in Favier et al. (2016), slightly re-advancing grounding lines at RBIS must be cautiously interpreted, due to poorly known bathymetry. Credit: subset of Fig. 7 from Favier et al. (2016).

stiffening in its vicinity (Fig. 5.9c). When this over-stiffened ice field is used in prognostic simulations, the total sea-level contribution is decreased by 10%, compared to simulations considering the pinning point. Furthermore, if spurious initialisation only affects the grounding-line migration locally, it nevertheless delays by 500 years the transition of the Western promontory into an ice rise (referred to as "ice risation" hereafter). Omitting the pinning point in initialisation additionally prevents the model from simulating any effect from unpinning, which is discussed in the following section.

Unpinning

To understand how a sudden de-grounding of the pinning point (unpinning) would impact the dynamics of the RBIS and its surroundings, Favier et al. (2016) have included the pinning point in their initialisation (*High-resolution scenario* in Chapter 4) but have ignored it in their prognostic simulations (*Standard scenario* in Chapter 4).

Unpinning leads to an instantaneous acceleration of the ice-shelf of 300 m a^{-1} at the former pinning-point location, which forces the central flowline of the ice-shelf system to relocate westward, half-way between the western promontory and Derwael Ice Rise. The speed-up gradually propagates upstream and reaches the grounding line of the West Ragnhild Glacier after 50 years but does not affect the neighbouring ice shelves (Fig. 5.10). In contrast with spurious initialisation, unpinning increases the total sea-level contribution by 10% and hurry the "ice risation" of the western promontory by 200 years.

Those results confirm that the pinning point in front of the RBIS significantly buttresses the West Ragnhild Glacier but unpinning does not sufficiently destabilise the system to push the grounding line to the inland-sloping trough, 50 km upstream of the current grounding line.

To sum up, spurious initialisation and unpinning mildly decreases and increases sea-level contribution, respectively. They mainly affect the timing of deglaciation, by delaying or advancing the "ice risation" of the West promontory by a few hundred years and their effect is spatially localised, affecting the Roi Baudouin Ice Shelf and its outlet glacier but not the neighbouring ice shelves.

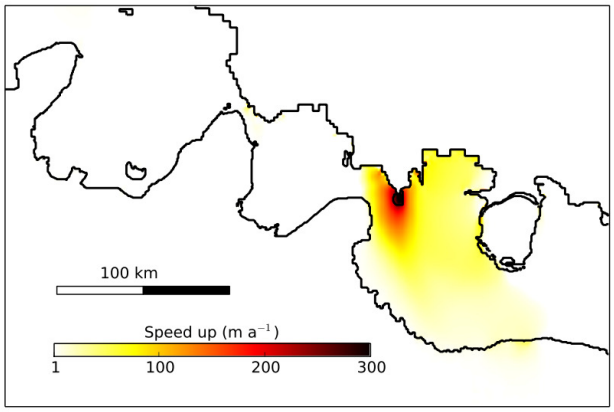

Figure 5.10: Speed-up of the RBIS 50 years after unpinning. Absolute velocity difference between the "unpinning" and "pinning point" scenarios in Fig. 5.9 with present-day melt-rates parametrised as in Gong et al. (2014). Credit: subset of Fig. 5 from Favier et al. (2016).

5.3.3 Grounding-line stability of the Roi Baudouin Ice Shelf

Many studies of the RBIS indicate that its grounding line has remained stable for decades, if not millennia. Here we present the different signs for grounding-line stability. We proceed as follows: we start with direct observations acquired over the last decades, we then look at past reconstructions from geophysical datasets and finish with future predictions from ice-sheet modelling.

Contemporary observations

Observations show that ice velocities and the grounding-line position at the RBIS have changed little over the last decades. First, small differences between our satellite-based flow field (Section 2.1) and 74 ground-truth measurements collected in 1965-67 (Derwael, 2014), has led us to conclude, in Chapter 4, that the RBIS has not undergone prominent flow changes over the last five decades.

Second, in Drews et al. (2017) we have mapped the grounding-line position of the RBIS between 1996 and 2016, using ground-penetrating radar profiling and quadruple differential InSAR with satellite data from Sentinel-1a, ALOS-PALSAR and ERS[4] 1/2. Figure 5.11 excludes a systematic migration of the grounding line during the last 2 decades, indicating temporal stability of the ice shelf.

Direct observations suggest therefore that Roi Baudouin Ice Shelf has remained relatively stable over, at least, 50 years.

Past reconstructions over millennial time-scale

Similarly, reconstructions from ground-penetrating radar on Derwael Ice Rise also point to the stability of the RBIS over the past millennia. Numerical simulations of deglaciation have shown that ice rises form when the grounding line retreats over a topographic high in the bed and then stay stable for thousands of years, because ice rises buttress and subsequently delay grounding-line retreat by several millennia (Favier and Pattyn, 2015). As ground-penetrating radar can map the internal stratigraphy (layering) of ice, radar profiling on Derwael Ice Rise therefore provides information over its past stability and, by extension, that of the RBIS (Drews et al., 2015, Callens et al., 2016).

Combining geophysical data with ice-flow modelling, Drews et al. (2015) concluded that

[4]As only one ERS interferogram was available, horizontal motion could not be removed from the interferogram (Section 2.1.3). The latter is however most sensitive to vertical uplift of the ice shelf, due to the steep look angle of ERS sensor.

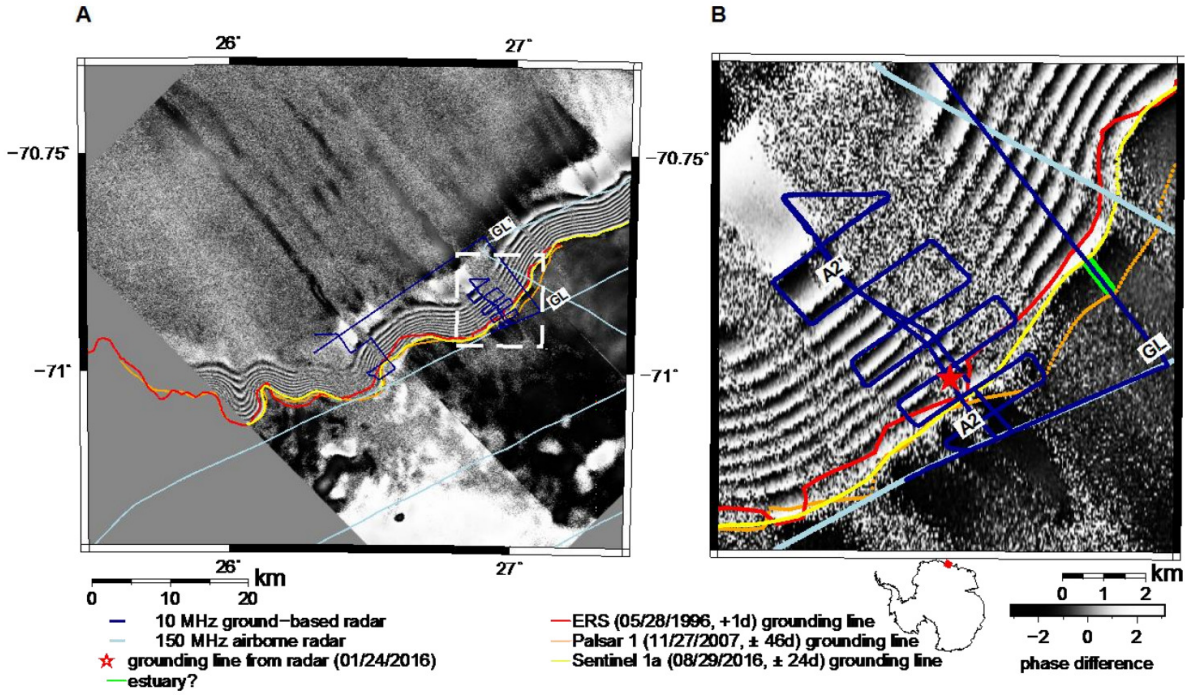

Figure 5.11: Grounding-line position at RBIS between 1996 and 2016 from satellite interferometry and ground-penetrating radar (**a**) Landward limit of the tidal flexure zone from radar interferometry in 1996, 2007 and 2016 with double-differenced Sentinel-1a interferogram (2016) shown in the background and radar profiles in blue (**b**) Close-up view of the white box delineated in (a).
Credit: Suppl. Fig. 1 from Drews et al. (2017).

Derwael Ice Rise is close to steady state and has remains stable as an ice rise for at least 5000 years .

Additionally, Callens et al. (2016) have used a similar approach to reconstruct past variations in the surface mass balance across Derwael Ice Rise. They found that the SMB asymmetry that currently exists across the ice rise – caused by orographic uplift of moist air and subsequent increase in precipitation on the upwind side (Lenaerts et al., 2014) – has persisted for the last thousand years, substantiating the stability hypothesis.

Future stability

Prognostic ice-sheet modelling[5] predicts that the RBIS grounding line will remain relatively stable in the next millennium, regardless of the scenario considered (Fig. 5.9, Favier et al., 2016). (Note that the slight re-advance of the grounding line of the RBIS should be treated with caution as the bathymetry under the RBIS is poorly-known, unlike the bed beneath the West Ragnhild Glacier). If the RBIS is predicted to remain stable in the future, it is however not the case of its neighbouring ice shelf. Favier et al. (2016) predicts a scenario-independent retreat of Hansenbreen over the next hundreds years (Figs. 5.9 and 5.12). The simulations indicate that the fast (up to 0.5-1 km a^{-1}) and unstable retreat of Hansenbreen's grounding line is driven by the marine ice sheet instability (Section 1.2.5 and Fig. 5.12) and sub-shelf melting.

[5]Without drastic changes in atmospheric and ocean forcings.

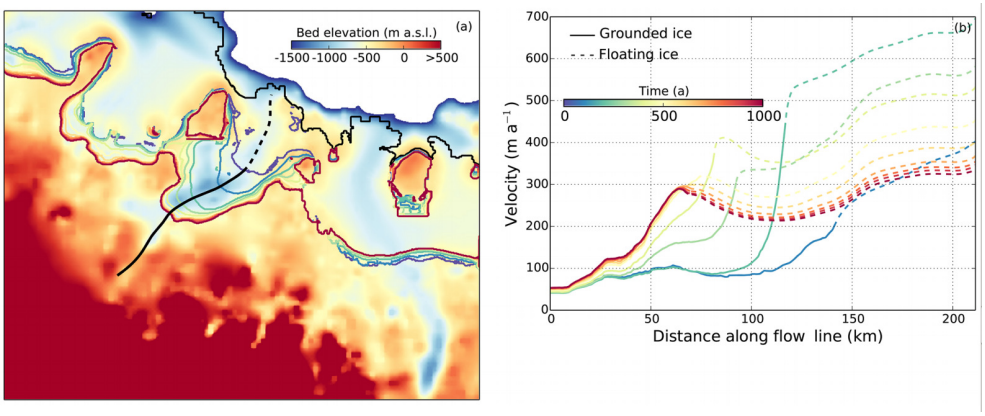

Figure 5.12: Grounding-line migration of the RBIS and neighbouring ice shelves for the next 1000 years, and with present-day melt-rates parametrised as in Gong et al. (2014). (**a**) Bed elevation and grounding-line migratation every 100 years (see colour scale in b). (**b**) Ice velocity along the central flowline shown in (a). Note: as explained in Favier et al. (2016) advancing grounding lines must be cautiously interpreted, due to poorly known bathymetry. Credit: Fig. 6 from Favier et al. (2016)

On the whole, various evidences (remote-sensing and geophysical observations, ice-sheet modelling) indicate that the RBIS has remained a stable sheet-shelf system for the last decades-to-millennia and predict that it should remain so in the next millennium, in the absence of ocean or atmospheric forcing. Two elements could however unsettle the stability of the ice shelf : (i) the bathymetric trough highlighted in Section 5.2 and (ii) surface meltwater. Both threats are discussed in the following sections (Sections 5.3.4 and 5.3.5).

5.3.4 Implications of the bathymetric trough

Fast thinning of ice shelves in West Antarctica has been linked to easy intrusion of Circumpolar Deep Water in their cavity, via bathymetric troughs (Pritchard et al., 2012). As a result, the presence of the RBIS trough potentially threatens the ice-shelf stability. It is not clear whether the warm water at the inlet of the trough can make its way to the grounding line, nor what causes this incursion (exceptional eddy vs regular situation). What is more evident, however, is the fact that this trough makes the RBIS more vulnerable to future circulation changes that would bring more warm waters in the cavity (Hellmer et al., 2012).

5.3.5 Surface meltwater and ice-shelf integrity

Similarly, a recent study (Lenaerts et al., 2017) has started to question the future vulnerability of the Roi Baudouin Ice Shelf to atmospheric warming. In their paper, Lenaerts et al. (2017) provide in situ evidence for large quantities of surface meltwater and its subsequent storage at the (sub)surface of the RBIS.

The paper reports a large number and variety of surface melt features around the grounding zone of the RBIS, including 55 (sub)surface lakes, meltwater streams, *moulins* (sinkhole where the water drains) and *dolines* (surface depressions associated with drained lakes) (Fig. 5.13). Lakes and rivers had been observed before on other East Antarctic ice shelves (e.g. Phillips, 1998, Langley et al., 2016) and have existed for at least 70 years at RBIS (Kingslake et al., 2017). However, Lenaerts et al. (2017) are the first to document englacial storage of this meltwater and to provide a cause: the *katabatic winds*.

Katabatic winds (Fig. 5.14) are cold and dense air masses that form in the ice sheet's interior

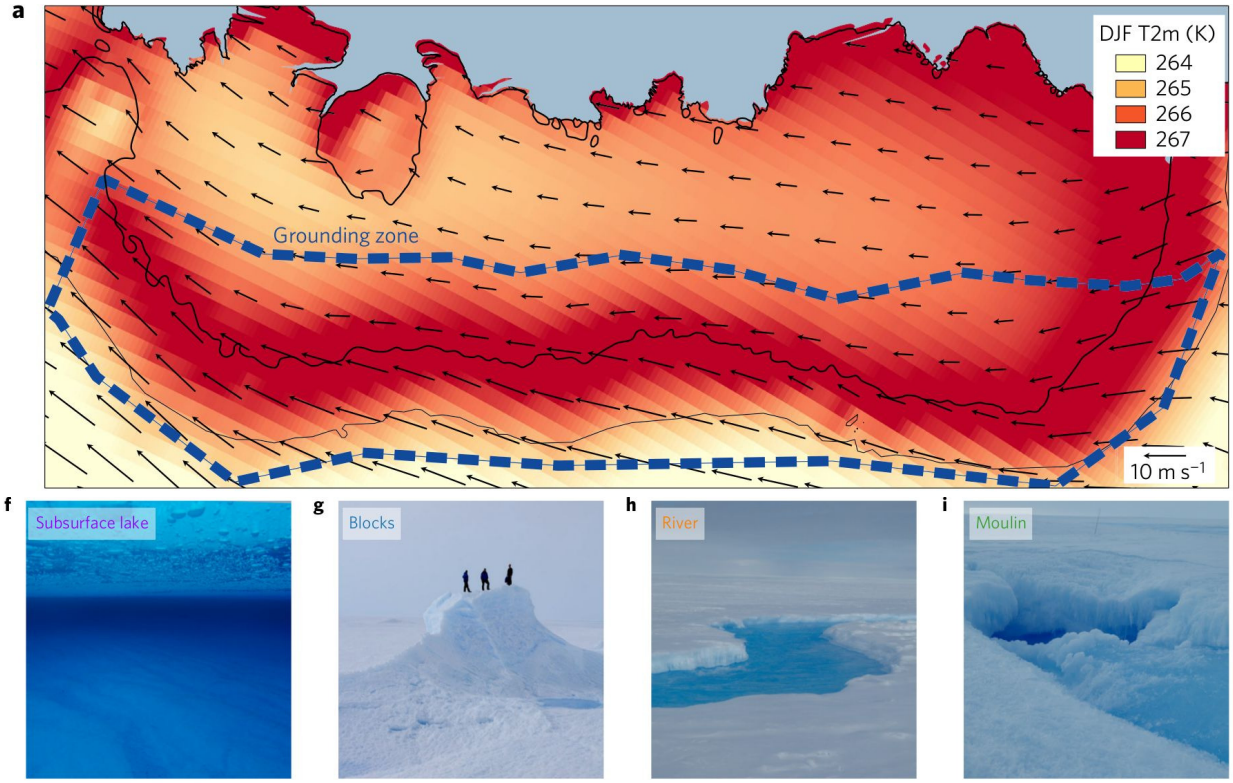

Figure 5.13: Summer near-surface climate and (sub)surface meltwater features at the RBIS. (**a**) Summer (December, January, February (DJF)) near-surface temperature (colours) and wind speed (vectors), averaged over 1979–2015 from RACMO 2.3. (**f**) englacial lake, (**g**) 10 m-high ice block, (**h**) meltwater stream (**i**) ice moulin (drainage). Credit: Figs. 2a and 1f-i from Lenaerts et al. (2017).

and flow down towards the coast, driven by gravity. On descent, katabatic winds (i) warm the surface (by air mixing and decreased atmospheric pressure) (Fig. 5.13a) and (ii) accelerate, scouring (Das et al., 2013) and hence darkening the surface. As a result, katabatic winds efficiently melt the surface in the grounding zone, helped by an albedo feedback whereby darker surfaces – from melt and wind scouring – absorb more energy, which enhances and sustains melting. This process depletes the firn from its air and produces large quantities of meltwater that flows downwards to accumulate in surface depressions, where it gets progressively buried under snowfalls and carried away by ice flow.

Because the Roi Baudouin is not the only ice shelf experiencing katabatic-driven melting, implications of this study are concerning for five reasons. First, surface melting in East Antarctica concentrates in the grounding zone, which is, as we have seen (Section 1.2), a critical area for ice-shelves stability and Antarctic contribution to sea-level rise. Second, the driver of this melting – katabatic winds – are far more relentless than episodic Foehn winds, responsible for intense surface melting on the East Antarctic Peninsula (Kuipers Munneke et al., 2012b, Luckman et al., 2014, Cape et al., 2015). Third, ice moulins and dolines link the accumulation of surface water to its drainage. This has two consequences (i) drained meltwater can influence subshelf ocean properties such as stratification or ocean circulation (Jenkins, 2011, Le Brocq et al., 2013); and (ii) drainage is also linked to structural integrity of the ice shelf (Banwell et al., 2013, Section 1.2.5). Fourth, the refreezing of thick layers of ice impacts ice-shelf properties such as viscosity and resistance to fracturing (Hubbard et al., 2016, Section 1.2.3). Fifth, and more broadly, Lenaerts et al. (2017) point out that some of the conditions for ice-shelves collapse – firn-air depletion and meltwater production and ponding – are already met in numerous parts of East Antarctica. As firn-air depletion and meltwater production are predicted to intensify with future warming

(Ligtenberg et al., 2014, Trusel et al., 2015) while katabatic winds are expected to only slightly diminish (Bintanja et al., 2014), ice-shelf collapse could therefore become a real threat for East Antarctic ice shelves that are either already thin or that are/will be thinning from oceanic melting (Paolo et al., 2015, Depoorter et al., 2013).

The only modelling study that has, so far, accounted for hydrofracturing predicts an Antarctic contribution to sea-level rise that is much higher than previous projections (Section 1.1 and DeConto and Pollard, 2016, Pollard et al., 2015). However, scientific knowledge and understanding of surface hydrology are still incomplete. For instance, DeConto and Pollard (2016)'s predictions ignore (i) that surface water can travel over large distances (up to 120 km), bringing meltwater to potential weak spots (Kingslake et al., 2017) and (ii) that all the meltwater is not necessarily stored on the ice shelve but can also be exported to the ocean by surface river at the ice-shelf front (Bell et al., 2017).

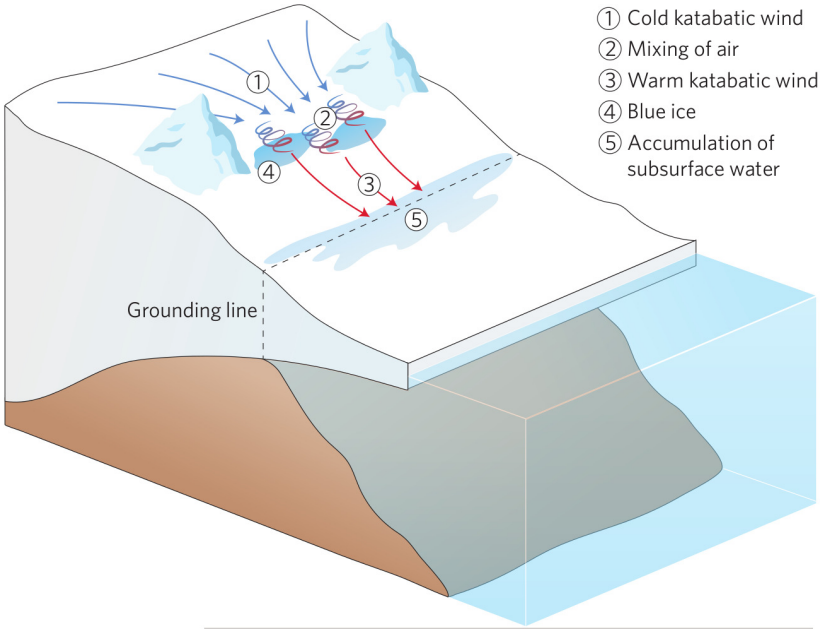

Figure 5.14: Meltwater production by wind-albedo interaction in an East Antarctic ice shelf. Credit: Fig. 1 from Siegert (2017). [Reprinted with permission from Nature Publishing Group]

In conclusion, if ocean forcing is currently driving Antarctic contribution to sea-level rise and will probably continue to do so, recent findings suggest that surface melting and hydrology are likely to become a deciding factor in ice-shelves stability. If that were the case, it would make the Antarctic ice sheet more vulnerable to atmospheric forcing, thus to anthropogenic greenhouse gases emissions. As a result, incorporating those processes in climate and ice sheet models has become crucial if we want to improve future sea-level projections.

Chapter 6

Beyond science: outreach

"***Science is not finished until it's communicated***" – Sir Mark Walport.

In the world of academia, this statement is largely agreed upon. A large majority of scientists realise the importance of publishing their results in peer-review journals or presenting their findings at scientific conferences.

However, a significant number of researchers remain reluctant to actively and regularly engage with their non-peers, be it the general public, the media or policy-makers. Despite regularly criticising the general public's lack of scientific literacy or complaining about misreporting in the media, many scientists are not willing to put in their own time to bridge the gap between science and society (Funk et al., 2015). They do not engage with the public for all kinds of reasons. Many believe that engaging in outreach activities is a waste of their time as long as they are not valuable professionally. Some even think that public engagement can be harmful to their career, because they consider outreach is what mediocre scientists do to compensate their lacking research (Royal Society, 2006).

It is precisely because I do not agree with these statements that I have decided to include here this unusual chapter about public outreach, which I would like to be considered as an integral part of my PhD. I genuinely believe that outreach is essential and can benefit all parties involved: scientists, science and society, and should therefore be more valued in the assessment of the quality of a scientist's work. Unfortunately outreach does not yet receive the recognition it fully deserves.

The rest of this chapter is divided into two parts. I start by explaining why it is crucial for cryospheric researchers to communicate their science to the public. I then focus more specifically on group blogging, using the case of the cryosphere blog of the European Geosciences Union (EGU), which is the outreach activity I am most familiar with. Appendix A lists all the outreach activities I have undertaken during this thesis (including communication with the media) and provides certifications from the EGU.

6.1 Why is it important to communicate cryospheric sciences?

From my point of view, it is important to communicate specifically in the field of cryospheric sciences because (i) they are not well understood by the general public and (ii) they provide crucial understanding of climate change.

6.1.1 The cryosphere as a fundamental part of the Earth system

The Earth System can be understood as a set of different envelopes in interaction with each other's: the atmosphere, the hydrosphere, the lithosphere, the biosphere and the cryosphere.

Among these envelopes, the cryosphere (the frozen part) is arguably the least well-known. One clear example is for instance the fact that it is the only word in the previous sentence that is not recognised by spelling checkers. Despite being crucial to the Earth system – e.g. by storing/releasing greenhouse gases, controlling the albedo of cold regions, driving global ocean circulation, to name just a few – many people do not realise how important the cryosphere is and how it is impacted by climate change.

6.1.2 The cryosphere as a climate-related science

Climate change perhaps illustrates the best the gap that exists between scientists and the public. While the vast majority of climate scientists (97%) agree that humans are changing the climate (Cook et al., 2016), the public still perceives a non-existent and vigorous scientific debate on the topic (Fig. 6.1).

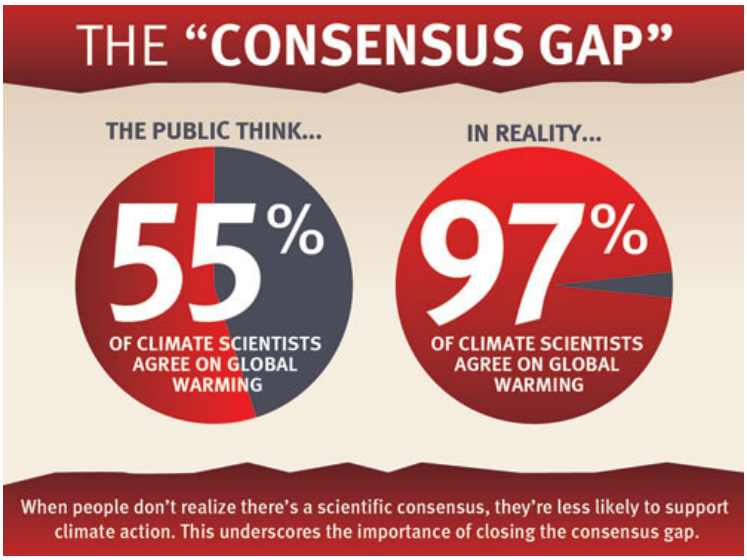

Figure 6.1: Consensus gap in climate sciences. Public perception of the scientific consensus on human-induced climate change vs the actual scientific consensus. Credit: Skeptical Science

This public misperception is rooted in several factors on which scientists have little grip, not least because of psychological reasons (Markowitz and Shariff, 2012), but also well-organised and well-funded disinformation campaigns by powerful groups like Exxon Mobil (Supran and Oreskes, 2017). One can wonder however to what extent the scientific community is responsible for this gap, by failing to appropriately communicate their science to the media, the general public and policy makers.

If (climate) science communication is essential, research has however shown that a same message can be perceived differently, depending on its audience and its format (Bosetti et al., 2017). To effectively communicate scientists should therefore move along with their time, adapt to new technologies and adjust the way they convey their message to their targeted audience.

6.2 Group blogging as an effective way to communicate

6.2.1 The internet era

The internet is key for outreach as it both threatens and offers opportunities for science communication. On the one hand, the development of the internet has largely eroded science coverage in

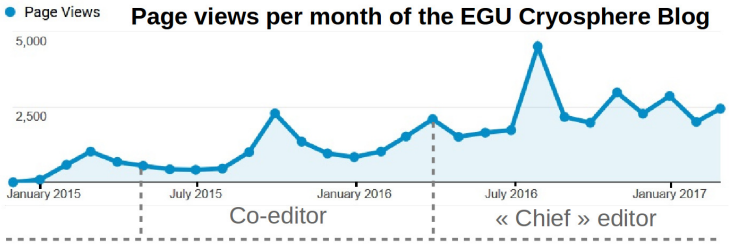

Figure 6.2: Time line of my involvement with the EGU cryosphere blog

the traditional media (Brossard and Scheufele, 2013). But, at the same time, the internet provides scientists with a unique opportunity to directly engage with the public and hence avoid misreporting of their science in the media. Actively engaging on twitter and contributing to group blogs are two of the least demanding outreach activities that enable researchers to reconnect with society and adapt to current societal changes.

6.2.2 The advantages of group blogging

With the emergence of social media and the so-called web 2.0[1], scientific blogs have become increasingly popular and present many advantages. Indeed, blogging is free and easy, it poses little logistical challenges and can be done at any time and from anywhere. Besides, blogging does not face geographical boundaries and can potentially reach out to a large audience.

Personal blogs can however consume a lot of time and efforts and this is why I am convinced that group blogging is more suited to communicating scientists. Collaborative blogs enable their contributors to :

- Benefit from already well established readership
- Save time as the momentum of the blog is collaboratively maintained
- Transform blogging into a social activity
- Improve the quality of content they post through internal reviews

These criteria all apply to the EGU cryosphere bog.

6.2.3 The case of the EGU cryosphere blog

The EGU cryosphere blog was launched in December 2014 and originally run by one person. In March 2015, I agreed to temporarily join the team and have then become increasingly involved until I took over as the blog's chief editor, in March 2016.

Since its launch, the blog has continuously expanded (Fig. 6.2) to become the second most-read division blog of the EGU, catching up with older and better-established blogs of bigger divisions (Fig. 6.3). I explain this positive readership figures based on 4 factors which I will describe now.

First, we have taken up the challenge of publishing at least one relatively short post per week, complemented by more sporadic but longer posts. Consistency and posting regularly are key to build a steady and faithful readership.

[1]The second generation of the world wide web, more focused on interactivity and information sharing between users.

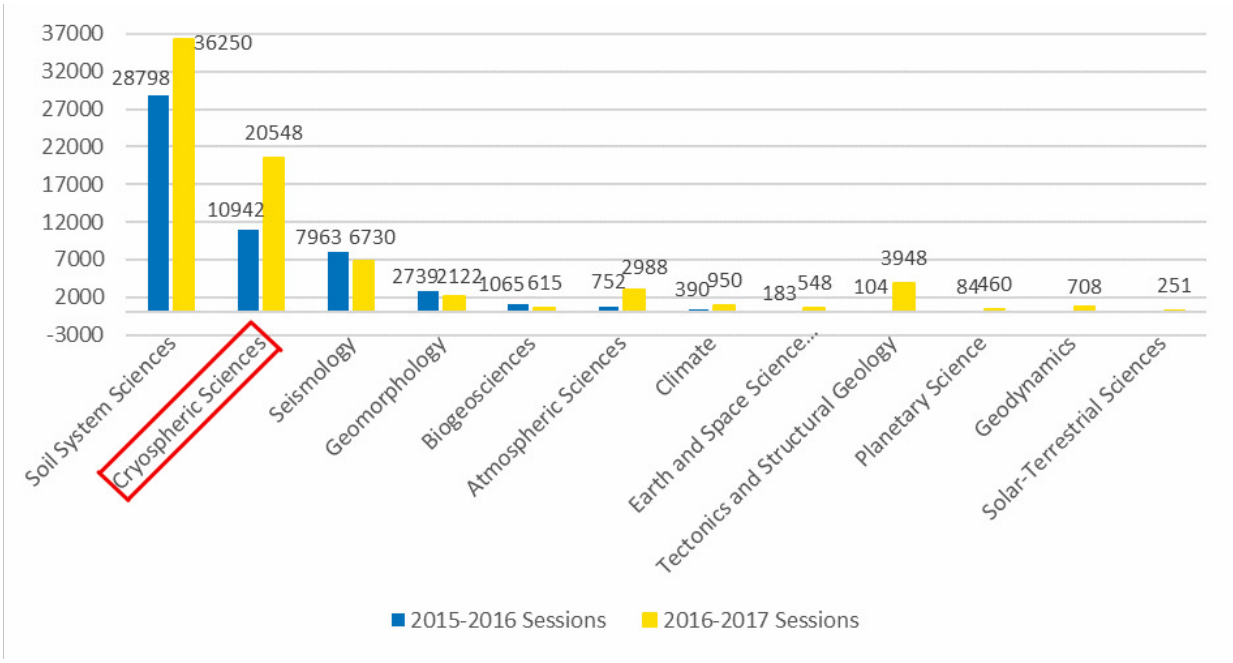

(a) Absolute yearly traffic to each EGU division blog.

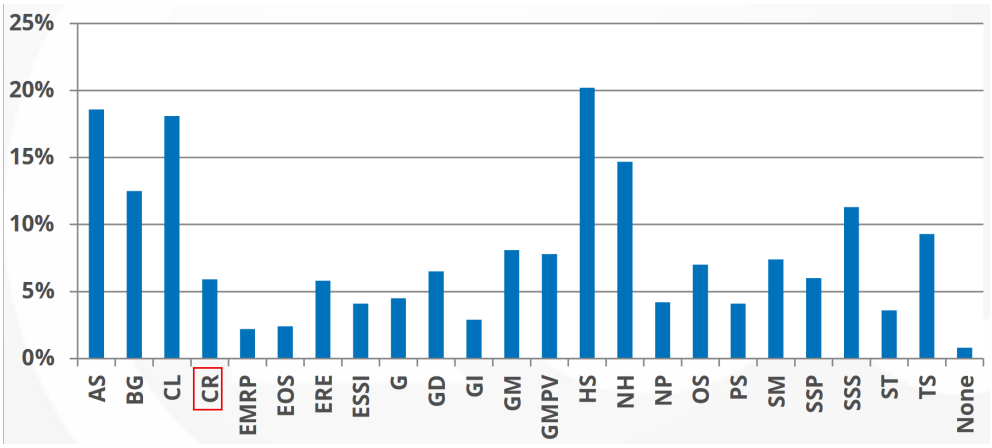

(b) Relative weight of each EGU division in 2016.

Figure 6.3: Importance of blogs and divisions within the EGU. The cryospheric division attracts 27% of the total traffic to the (division) blogs while it represents only ~6% of the EGU headcounts. Credit:(a) EGU communication officer and (b) Survey results of EGU 2016 General Assembly feedbacks.

Second, we have established a network of regular contributors, complemented by guest (one-off) authors. This network is made of early-career scientists (totalling 17 today) who are involved to different degrees (chief editors, editors, authors). This structure has the advantage of being flexible enough to accommodate everyone's constraints, keeping up with a high publishing rate and providing support and motivation to the team members. The network has additionally enabled us to make ourselves better known by outsourcing part of the blog promotion to regular and external contributors.

Third, we have complemented our blog activities with the implementation of a strong social media strategy for the EGU cryosphere division.

And fourth, we are paying a lot of attention to the form and the content of our posts, to make them understandable and engaging. To do so, we vary the types of content (explainers, interviews, historical facts, scientists' life stories, cryospheric news, etc.) and the topics covered (sea ice, permafrost, datasets, Greenland, etc.). We also try to keep an approachable language, understandable by non-scientists. But, perhaps most importantly when it comes to blogging:

while we talk about science, we don't stick to the "scientific etiquette", but instead we do not hesitate to frame our posts as stories, to use puns and to be informal. That helps the public understand that science does not have to be boring and made of specialised, impermeable jargon.

Those are, I think, the key ingredients for the success of the cryosphere blog, which overall contributes to promoting multi-disciplinarity across subfields of the cryosphere and cryospheric sciences in general. In the political times of Trump and Brexit – which feed on economical austerity and where facts are overlooked and experts despised – scientists must break free from their ivory tower and re-engage with the public, the media and policy-makers. This is the only way for them to reconnect with society and therefore regain support for their science. Researchers must learn how to communicate more effectively and this implies that they should be trained, supported and valued for their outreach activities.

Chapter 7

Synthesis and Conclusions

The work presented here has aimed to improve our understanding of ice-shelf stability using the Roi Baudouin Ice Shelf, Dronning Maud Land, East Antarctica, as a case study.

First, we have derived direct observations of velocities. Starting from this velocity field we have then addressed two key processes for ice-shelf stability in two standalone studies: (i) the basal mass balance, the current driver of Antarctic ice losses; and (ii) the buttressing, the mechanism by which ocean melting leads to Antarctic ice losses. Those two studies increasingly combine observations towards modelling: the first one combine many observational datasets with various assumptions to derive secondary observations, whereas the second relies on observations for ice-sheet model initialisation. In the following, we outline our main findings before discussing the necessity to combine observations and modelling. We conclude with quick notes on ice-shelf stability and outreach.

The velocity field has been obtained from satellite synthetic aperture radar, applying interferometry to ERS 1/2 images from 1996 and speckle tracking to ALOS-PALSAR images from 2010. With its 125 m gridding, this dataset represents the most finely resolved velocities currently available for the RBIS. Compared to continent-wide data, our flow field better resolves small-scale features like the small pinning point and ice-shelf channels that we observe in our area of interest. First, velocities gradually slow down upstream of the pinning point to become stagnant at its top, as observed on site. Second, flow convergence, step-wise velocity increase and enhanced shearing are all observed at ice-shelf channels, as predicted by ice-sheet modelling (Drews, 2015).

In the first standalone study (Chapter 3), we have combined the flow field with finely resolved TanDEM-X elevations and high-resolution outputs from atmospheric modelling to derive the Basal Mass Balance of the RBIS, using mass conservation in a Lagrangian framework. The technique we have developed/refined seems successful at detecting ice-ocean interactions on short spatial scales, even with low-melting ice shelves like the RBIS. In addition to showing a large-scale pattern that is consistent with previous studies (Rignot et al., 2013), our method agrees reasonably well with ground-truth measurements. Overall, we find a low average mass loss of -0.8 m a^{-1} for the RBIS, with highest melt rates where the ice draft is the deepest and the steepest, notably close to the grounding line. The large-scale pattern is overlain with sub-kilometre variability in the basal mass balance. Our basal mass balance field indicates locally elevated melting at an elliptical surface depression and at the flanks of an ice-shelf channel. We have also shown that processing the same data in a – more traditional – Eulerian frame produces similar BMB pattern on the large scale, but locally corrupts the pattern in areas where advection of thickness gradients is strong.

With increasingly available satellite data, the methodology developed for the RBIS could easily be spatially and temporally upscaled, as preliminary results of the Petermann Ice Shelf in Greenland indicate. Unfortunately, the coarse resolution of atmospheric-modelling output will likely remain the main limiting factor of the methodology over the coming years.

In the second standalone study (Chapter 4), we have investigated how a pinning point overlooked in observations (velocity and bathymetry) affects model initialisation, through data assimilation. To do so, we have combined different sets of velocities and bathymetry to form 3 scenarios resolving the pinning point to diverse degrees. We have subsequently inverted these three scenarios to determine parameters poorly constrained in the ice-sheet model BISICLES, namely the stiffening factor (determining the ice rheology) and the basal friction coefficient (determining the basal drag). We have found that it is more important to accurately account for the pinning point in the bathymetry than in the velocities. When omitted in the bathymetry, the data assimilation cannot account for the pinning point with basal drag, which yields over-stiffened ice in its surroundings. On the other hand, when velocities on top of the pinning are largely overestimated but the pinning point is included in the bathymetry, assimilation only underestimates basal friction. Those findings call for a better mapping of the bathymetry around Antarctica, to account for pinning point in ice-sheet modelling and improve sea-level predictions.

We have therefore seen that kilometres-wide features can impact ice shelves more strongly than what would be suggested by their limited size. The most striking examples developed here are (i) the 2 kilometres-wide pinning point that impacts the ice-shelf flow dozens of kilometres upstream of it and (ii) the elliptical surface depression, which shows basal mass balance rates one order magnitude higher than its surroundings. Because small-scale features/processes can have much larger-scale impacts, resolving them in Antarctic-wide datasets – albeit challenging – has become of paramount importance to fully understand how the ice-sheet behaves and interacts with its environment.

Overall, the datasets from contemporary observations and past reconstructions consistently indicate that the RBIS has remained relatively stable over millennial time scales, strongly buttressed by the Derwael Ice Rise, the western ice promontory and the pinning point. This agrees with ice-sheet modelling, which predicts only minor grounding line migration over the coming millennium and contrasts with the neighbouring ice shelf fed by Hansenbreen predicted to destabilise and quickly retreat in the next thousand years.

Nevertheless, this predicted stability of the RBIS neglects potential destabilisation from three processes: ice-shelf channelling, accumulation of surface meltwater and incursions of warm deep water in a bathymetric trough. These three processes can potentially weaken the RBIS at a crucial area : its grounding zone.

First, contrary to what was originally thought, the channels of the RBIS are initiated upstream of the grounding line, close to the outlet of predicted subglacial conduits, and have been associated with building-up of eskers (Drews et al., 2017). Downstream of the grounding line, the discharged freshwater initiates a buoyant plume that entrains warmer ocean water and effectively melt ice below the channels and maintains them. Evidences about channel's impact on the stability are conflicting. On the one hand, it has been argued that channels structurally weaken ice shelves through fracturing (crevasses and rifts) but, on the other hand, studies have suggested that (i) eskers pin and therefore stabilise the grounding line and (ii) the presence of channels reduce

the overall melting of ice shelves.

Second, surface melting and its storage can weaken ice shelves through hydrofracturing and are thought to be involved in the abrupt collapses of ice shelves in the Antarctic Peninsula. If, unlike their peninsular counterparts, ice shelves like the RBIS are not currently thinning, surface melting from katabatic winds is far more relentless than episodic melting due to Foehn winds in the Peninsula. Because latest ice-sheet modelling (DeConto and Pollard, 2016) suggests that surface hydrology on ice shelves will impact their future stability, it has therefore become essential to better understand and represent those processes in models. This suggests that the future integrity of the ice shelf is potentially sensitive to atmospheric warming.

Third, the bathymetric trough beneath the RBIS means that if the ocean circulation were to change or if the ocean were to warm, the grounding line of the RBIS would be easily accessed by warm deep waters. Ocean forcing could even initiate a marine-ice sheet instability if sufficient heat were to be supplied to the ice-shelf base to push the grounding on its retrograde slope, 50 km upstream of the current grounding line.

As a result, oceanic warming or future changes in ocean circulation, together with a warmer atmosphere have the potential to affect the predicted stability of the Roi Baudouin Ice Shelf and other ice shelves in Dronning Maud Land, which have been considered as stable until now. Unfortunately, current understanding is still incomplete (e.g. marine ice cliff instability) or knowledge is lacking (e.g. pinning point and bathymetric troughs) to fully understand the implications of those processes and to incorporate them in ice-sheet models.

Last but not least, societal impact of current and future scientific advances will be determined by researchers' ability to communicate their science to the public, the media and policy-makers. After all, public outreach is (arguably) to climate science what an ice shelf is to an ice sheet. Like an ice shelf, science outreach and communication will ultimately regulate the transfers of science to the ocean of public knowledge. As a result, I do believe that scientists have a critical role to play communicating their expertise, effectively bridging the gap between science and society, something critically needed in a post-truth politics era where facts are rejected and experts distrusted.

Bibliography

Abram, N. J., Mulvaney, R., Wolff, E. W., Triest, J., Kipfstuhl, S., Trusel, L. D., Vimeux, F., Fleet, L., and Arrowsmith, C. (2013). Acceleration of snow melt in an Antarctic Peninsula ice core during the twentieth century. *Nature Geoscience*, 6(5):404–411.

Albrecht, T. and Levermann, A. (2014). Fracture-induced softening for large-scale ice dynamics. *Cryosphere*, 8(2):587–605.

Alley, K. E., Scambos, T. A., Siegfried, M. R., and Fricker, H. A. (2016). Impacts of warm water on Antarctic ice shelf stability through basal channel formation. *Nature Geoscience*, 9(4):290–293.

Alley, R. B., Anandakrishnan, S., Dupont, T. K., Parizek, B. R., and Pollard, D. (2007). Effect of Sedimentation on Ice-Sheet Grounding-Line Stability. *Science*, 315(5820):1838–1841.

Arndt, J. E., Schenke, H. W., Jakobsson, M., Nitsche, F. O., Buys, G., Goleby, B., Rebesco, M., Bohoyo, F., Hong, J., Black, J., Greku, R., Udintsev, G., Barrios, F., Reynoso-Peralta, W., Taisei, M., and Wigley, R. (2013). The international bathymetric chart of the Southern Ocean (IBCSO) version 1.0-A new bathymetric compilation covering circum-Antarctic waters. *Geophysical Research Letters*, 40(12):3111–3117.

Arthern, R. J., Winebrenner, D. P., and Vaughan, D. G. (2006). Antarctic snow accumulation mapped using polarization of 4.3-cm wavelength microwave emission. *Journal of Geophysical Research*, 111(D6):D06107.

Bamber, J. L. and Aspinall, W. P. (2013). An expert judgement assessment of future sea level rise from the ice sheets. *Nature Climate Change*, 3(4):424–427.

Bamber, J. L., Gomez-Dans, J. L., and Griggs, J. a. (2009). A new 1 km digital elevation model of the Antarctic derived from combined satellite radar and laser data – Part 1: Data and methods. *The Cryosphere*, 3(1):101–111.

Bamler, R. and Hartl, P. (1998). Synthetic Aperture Radar Interferometry. *Inverse Problems*, 14(4):1–54.

Banwell, A. F. and Macayeal, D. R. (2015). Ice-shelf fracture due to viscoelastic flexure stress induced by fill/drain cycles of supraglacial lakes. *Antarctic Science*, 27(06):587–597.

Banwell, A. F., MacAyeal, D. R., and Sergienko, O. V. (2013). Breakup of the Larsen B Ice Shelf triggered by chain reaction drainage of supraglacial lakes. *Geophysical Research Letters*, 40(22):5872–5876.

Bassis, J. N., Fricker, H. A., Coleman, R., and Minster, J. B. (2008). An investigation into the forces that drive ice-shelf rift propagation on the amery ice shelf, East Antarctica. *Journal of Glaciology*, 54(184):17–27.

Bassis, J. N. and Jacobs, S. (2013). Diverse calving patterns linked to glacier geometry. *Nature Geoscience*, 6(10):833–836.

Bell, R. E., Chu, W., Kingslake, J., Das, I., Tedesco, M., Tinto, K. J., Zappa, C. J., Frezzotti, M., Boghosian, A., and Lee, W. S. (2017). Antarctic ice shelf potentially stabilized by export of meltwater in surface river. *Nature*, 544(7650):344–348.

Berger, M., Moreno, J., Johannessen, J. A., Levelt, P. F., and Hanssen, R. F. (2012). ESA's sentinel missions in support of Earth system science. *Remote Sensing of Environment*, 120:84–90.

Berthier, E., Scambos, T. A., and Shuman, C. A. (2012). Mass loss of Larsen B tributary glaciers (Antarctic Peninsula) unabated since 2002. *Geophysical Research Letters*, 39(13):L13501.

Bindoff, N. L., Rosenberg, M. A., and Warner, M. J. (2000). On the circulation and water masses over the Antarctic continental slope and rise between 80 and 150°E. *Deep Sea Research Part II: Topical Studies in Oceanography*, 47(12):2299–2326.

Bindschadler, R., Choi, H., Wichlacz, A., Bingham, R., Bohlander, J., Brunt, K., Corr, H., Drews, R., Fricker, H., Hall, M., Hindmarsh, R., Kohler, J., Padman, L., Rack, W., Rotschky, G., Urbini, S., Vornberger, P., and Young, N. (2011a). Getting around Antarctica: New high-resolution mappings of the grounded and freely-floating boundaries of the Antarctic ice sheet created for the International Polar Year. *The Cryosphere*, 5(3):569–588.

Bindschadler, R., Vaughan, D. G., and Vornberger, P. (2011b). Variability of basal melt beneath the Pine Island Glacier ice shelf, West Antarctica. *Journal of Glaciology*, 57(204):581–595.

Bindschadler, R. A., Nowicki, S., Abe-OUCHI, A., Aschwanden, A., Choi, H., Fastook, J., Granzow, G., Greve, R., Gutowski, G., Herzfeld, U., Jackson, C., Johnson, J., Khroulev, C., Levermann, A., Lipscomb, W. H., Martin, M. A., Morlighem, M., Parizek, B. R., Pollard, D., Price, S. F., Ren, D., Saito, F., Sato, T., Seddik, H., Seroussi, H., Takahashi, K., Walker, R., and Wang, W. L. (2013). Ice-sheet model sensitivities to environmental forcing and their use in projecting future sea level (the SeaRISE project). *Journal of Glaciology*, 59(214):195–224.

Bintanja, R., Severijns, C., Haarsma, R., and Hazeleger, W. (2014). The future of Antarctica's surface winds simulated by a high-resolution global climate model: 2. Drivers of 21st century changes. *Journal of Geophysical Research: Atmospheres*, 119(12):7160–7178.

Boening, C., Lebsock, M., Landerer, F., and Stephens, G. (2012). Snowfall-driven mass change on the East Antarctic ice sheet. *Geophysical Research Letters*, 39(21):L21501.

Borstad, C., Khazendar, A., Scheuchl, B., Morlighem, M., Larour, E., and Rignot, E. (2016). A constitutive framework for predicting weakening and reduced buttressing of ice shelves based. *Geophysical Research Letters*, 43(5):2027–2035.

Bosetti, V., Weber, E., Berger, L., Budescu, D. V., Liu, N., and Tavoni, M. (2017). COP21 climate negotiators' responses to climate model forecasts. *Nature Climate Change*, (February):1–7.

Brossard, D. and Scheufele, D. A. (2013). Science, New Media, and the Public. *Science*, 339(6115):40–41.

Callens, D. (2014). *Impact of improved basal and surface boundary conditions on the mass balance of the Sr Rondane Mountains glacial system, Dronning Maud Land, Antarctica*. PhD thesis, Université libre de Bruxelles.

Callens, D., Drews, R., Witrant, E., Philippe, M., and Pattyn, F. (2016). Temporally stable surface mass balance asymmetry across an Ice rise derived from radar internal reflection horizons through inverse modeling. *Journal of Glaciology*, 62(233):525–534.

Callens, D., Matsuoka, K., Steinhage, D., Smith, B., Witrant, E., and Pattyn, F. (2014). Transition of flow regime along a marine-terminating outlet glacier in East Antarctica. *The Cryosphere*, 8(3):867–875.

Cape, M. R., Vernet, M., Skvarca, P., Marinsek, S., Scambos, T., and Domack, E. (2015). Foehn winds link climate-driven warming to ice shelf evolution in Antarctica. *Journal of Geophysical Research: Atmospheres*, 120(21):11037–11057.

Carter, L., McCave, I. N., and Williams, M. J. M. (2008). Chapter 4 Circulation and Water Masses of the Southern Ocean: A Review. *Developments in Earth and Environmental Sciences*, 8:85–114.

Church, J. A., Clark, P. U., Cazenave, A., Gregory, J. M., Jevrejeva, S., Levermann, A., Merrifield, M. A., Milne, G. A., Nerem, R. S., Nunn, P. D., Payne, A. J., Pfeffer, W. T., Stammer, D., and Unnikrishnan, A. S. (2013). Sea Level Change. In Stocker, T. F., Qin, D., Plattner, G.-K., Tignor, M., Allen, S. K., Boschung, J., Nauels, A., Xia, Y., Bex, V., and Midgley, P. M., editors, *Climate Change 2013 - The Physical Science Basis*, book section 13, pages 1137–1216. Cambridge University Press, Cambridge, United Kingdom and New York, NY, USA.

Cook, A. J. and Vaughan, D. G. (2010). Overview of areal changes of the ice shelves on the Antarctic Peninsula over the past 50 years. *The Cryosphere*, 4(1):77–98.

Cook, J., Oreskes, N., Doran, P. T., Anderegg, W. R. L., Verheggen, B., Maibach, E. W., Carlton, J. S., Lewandowsky, S., Skuce, A. G., Green, S. A., Nuccitelli, D., Jacobs, P., Richardson, M., Winkler, B., Painting, R., and Rice, K. (2016). Consensus on consensus: a synthesis of consensus estimates on human-caused global warming. *Environmental Research Letters*, 11(4):048002.

Curlander, J. C. and McDonough, R. N. (1991). *Synthetic Aperture Radar: Systems and Signal Processing*. Wiley Series in Remote Sensing Series. Wiley.

Dallaston, M. C., Hewitt, I. J., and Wells, A. J. (2015). Channelization of plumes beneath ice shelves. *Journal of Fluid Mechanics*, 785:109–134.

Das, I., Bell, R. E., Scambos, T. A., Wolovick, M., Creyts, T. T., Studinger, M., Frearson, N., Nicolas, J. P., Lenaerts, J. T. M., and van den Broeke, M. R. (2013). Influence of persistent wind scour on the surface mass balance of Antarctica. *Nature Geoscience*, 6(5):367–371.

DeConto, R. M. and Pollard, D. (2016). Contribution of Antarctica to past and future sea-level rise. *Nature*, 531(7596):591–597.

Depoorter, M. A., Bamber, J. L., Griggs, J. a., Lenaerts, J. T. M., Ligtenberg, S. R. M., van den Broeke, M. R., and Moholdt, G. (2013). Calving fluxes and basal melt rates of Antarctic ice shelves. *Nature*, 502(7469):89–92.

Derauw, D. (2000). DInSAR and coherence tracking applied to glaciology: The example of Shirase Glacier. In *FRINGE '99 Workshop : Advancing ERS SAR Interferometry from Applications towards Operations, 10-12 November 1999, Liège, Belgium*.

Derwael, J.-J. (2014). Snow accumulation data: Princess Ragnhild Coast, Antarctica. Belgian

- Netherlands Antarctic Expeditions 1964 - 1965 - 1966. Technical report, Belgian Antarctic Archives, Brussels.

Deschamps, P., Durand, N., Bard, E., Hamelin, B., Camoin, G., Thomas, A. L., Henderson, G. M., Okuno, J., and Yokoyama, Y. (2012). Ice-sheet collapse and sea-level rise at the Bølling warming 14,600years ago. *Nature*, 483(7391):559–564.

Dinniman, M., Asay-Davis, X., Galton-Fenzi, B., Holland, P., Jenkins, A., and Timmermann, R. (2016). Modeling Ice Shelf/Ocean Interaction in Antarctica: A Review. *Oceanography*, 29(4):144–153.

Drews, R. (2015). Evolution of ice-shelf channels in Antarctic ice shelves. *The Cryosphere*, 9(3):1169–1181.

Drews, R., Brown, J., Matsuoka, K., Witrant, E., Philippe, M., Hubbard, B., and Pattyn, F. (2016). Constraining variable density of ice shelves using wide-angle radar measurements. *The Cryosphere*, 10(2):811–823.

Drews, R., Matsuoka, K., Martín, C., Callens, D., Bergeot, N., and Pattyn, F. (2015). Evolution of Derwael Ice Rise in Dronning Maud Land, Antarctica, over the last millennia. *Journal of Geophysical Research: Earth Surface*, 120(3):564–579.

Drews, R., Pattyn, F., Hewitt, I. J., Ng, F. S. L., Berger, S., Matsuoka, K., Helm, V., Bergeot, N., Favier, L., and Neckel, N. (2017). Actively evolving subglacial conduits and eskers initiate ice shelf channels at an Antarctic grounding line. *Nature Communications*, 8:15228.

Dupont, T. K. and Alley, R. B. (2005). Assessment of the importance of ice-shelf buttressing to ice-sheet flow. *Geophysical Research Letters*, 32:L04503.

Dutrieux, P., Vaughan, D. G., Corr, H. F. J., Jenkins, A., Holland, P. R., Joughin, I., and Fleming, A. (2013). Pine Island Glacier ice shelf melt distributed at kilometre scales. *The Cryosphere*, 7:1591–1620.

Dutton, A., Carlson, A. E., Long, A. J., Milne, G. A., Clark, P. U., DeConto, R., Horton, B. P., Rahmstorf, S., and Raymo, M. E. (2015). Sea-level rise due to polar ice-sheet mass loss during past warm periods. *Science*, 349(6244).

Eisen, O., Frezzotti, M., Genthon, C., Isaksson, E., Magand, O., Broeke, V. D., Michiel, R., Dixon, D. a., Ekaykin, A., Holmlund, P., Kameda, T., Karlöf, L., Kaspari, S., Lipenkov, V. Y., Oerter, H., Takahashi, S., and Vaughan, D. G. (2008). Ground-based measurements of spatial and temporal variability of snow accumulation in East Antarctica. *Reviews of*, 46(2006):RG2001.

Fahnestock, M., Scambos, T., Moon, T., Gardner, A., Haran, T., and Klinger, M. (2016). Rapid large-area mapping of ice flow using Landsat 8. *Remote Sensing of Environment*, 185:84–94.

Favier, L., Durand, G., Cornford, S. L., Gudmundsson, G. H., Gagliardini, O., Gillet-Chaulet, F., Zwinger, T., Payne, A. J., and Le Brocq, A. M. (2014). Retreat of Pine Island Glacier controlled by marine ice-sheet instability. *Nature Climate Change*, 4(2):117–121.

Favier, L., Gagliardini, O., Durand, G., and Zwinger, T. (2012). A three-dimensional full Stokes model of the grounding line dynamics: effect of a pinning point beneath the ice shelf. *The Cryosphere*, 6(1):101–112.

Favier, L. and Pattyn, F. (2015). Antarctic ice-rise formation, evolution and stability. *Geophysical Research Letters*, 42(11):4456–4463.

Favier, L., Pattyn, F., Berger, S., and Drews, R. (2016). Dynamic influence of pinning points on marine ice-sheet stability: a numerical study in Dronning Maud Land, East Antarctica. *The Cryosphere*, 10(6):2623–2635.

Foldvik, A. and Kvinge, T. (1974). Conditional instability of sea water at the freezing point. *Deep Sea Research and Oceanographic Abstracts*.

Förste, C., Bruinsma, S., Abrikosov, O., Flechtner, F., Marty, J.-C., Lemoine, J.-M., Dahle, C., Neumayer, H., Barthelmes, F., König, R., and Biancale, R. (2014). EIGEN-6C4 - The latest combined global gravity field model including GOCE data up to degree and order 1949 of GFZ Potsdam and GRGS Toulouse. In *EGU General Assembly Conference Abstracts*, volume 16 of *EGU General Assembly Conference Abstracts*, page 3707.

Fretwell, P., Pritchard, H. D., Vaughan, D., Bamber, J. L., Barrand, N. E., Bell, R., Bianchi, C., Bingham, R. G., Blankenship, D. D., Casassa, G., and Others (2013). Bedmap2: improved ice bed, surface and thickness datasets for Antarctica. *The Cryosphere*, 7(1):375–393.

Frezzotti, M., Urbini, S., Proposito, M., Scarchilli, C., and Gandolfi, S. (2007). Spatial and temporal variability of surface mass balance near Talos Dome, East Antarctica. *Journal of Geophysical Research*, 112(F2):F02032.

Fricker, H. A., Coleman, R., Padman, L., Scambos, T. A., Bohlander, J., and Brunt, K. M. (2009). Mapping the grounding zone of the Amery Ice Shelf, East Antarctica using InSAR, MODIS and ICESat. *Antarctic Science*, 21(05):515.

Fricker, H. A. and Padman, L. (2006). Ice shelf grounding zone structure from ICESat laser altimetry. *Geophysical Research Letters*, 33(15):L15502.

Fricker, H. A., Young, N. W., Allison, I., and Coleman, R. (2002). Iceberg calving from the Amery Ice Shelf, East Antarctica. *Annals of Glaciology*, 34(1):241–246.

Funk, C., Rainie, L., and Page, D. (2015). Public and Scientists' Views on Science and Society. *Pew Research Center*, pages 1–111.

Fürst, J. J., Durand, G., Gillet-Chaulet, F., Tavard, L., Rankl, M., Braun, M., and Gagliardini, O. (2016). The safety band of Antarctic ice shelves. *Nature Climate Change*, 6(5):479–482.

Furuya, M. (2011). SAR Interferometry. In Gupta, H., editor, *Encyclopedia of Solid Earth Geophysics*, Encyclopedia of Earth Sciences Series, pages 1041–1049. Springer Netherlands.

Gagliardini, O., Durand, G., Zwinger, T., Hindmarsh, R. C. A., and Le Meur, E. (2010). Coupling of ice-shelf melting and buttressing is a key process in ice-sheets dynamics. *Geophysical Research Letters*, 37(14):L14501.

Gladish, C. V., Holland, D. M., Holland, P. R., and Price, S. F. (2012). Ice-shelf basal channels in a coupled ice/ocean model. *Journal of Glaciology*, 58(212):1227–1244.

Goldberg, D., Holland, D. M., and Schoof, C. (2009). Grounding line movement and ice shelf buttressing in marine ice sheets. *Journal of Geophysical Research*, 114(F4):F04026.

Goldstein, R. M., Engelhardt, H., Kamb, B., and Frolich, R. M. (1993). Satellite Radar Interferometry for Monitoring Ice Sheet Motion: Application to an Antarctic Ice Stream. *Science*, 262(5139):1525–1530.

Gong, Y., Cornford, S. L., and Payne, A. J. (2014). Modelling the response of the Lambert

Glacier-Amery Ice Shelf system, East Antarctica, to uncertain climate forcing over the 21st and 22nd centuries. *Cryosphere*, 8(3):1057–1068.

Gossart, A. (2014). *Basal mass balance of the Roi Baudouin ice shelf , using GPS and Radar*. Master's thesis, Université Libre de Bruxelles.

Gray, A. L., Mattar, K. E., Vachon, P. W., Bindschadler, R., Jezek, K. C., Forster, R., and Crawford, J. P. (1998). InSAR results from the RADARSAT Antarctic Mapping Mission data: estimation of glacier motion using a simple registration procedure. In *Geoscience and Remote Sensing Symposium Proceedings, 1998. IGARSS'98. 1998 IEEE International*, volume 3, pages 1638–1640. IEEE.

Gray, A. L., Short, N., Mattar, K. E., and Jezek, K. C. (2001). Velocities and flux of the Filchner Ice Shelf and its tributaries determined from speckle tracking interferometry. *Canadian Journal of Remote Sensing*, 27(3):193–206.

Gray, L., Short, N., Bindschadler, R., Joughin, I., Padman, L., Vornberger, P., and Khananian, A. (2002). RADARSAT interferometry for Antarctic grounding-zone mapping. *Annals of Glaciology*, 34(1):269–276.

Greenbaum, J. S., Blankenship, D. D., Young, D. a., Richter, T. G., Roberts, J. L., Aitken, a. R. a., Legresy, B., Schroeder, D. M., Warner, R. C., van Ommen, T. D., and Siegert, M. J. (2015). Ocean access to a cavity beneath Totten Glacier in East Antarctica. *Nature Geoscience*, 8(March):1–5.

Hanna, E., Navarro, F. J., Pattyn, F., Domingues, C. M., Fettweis, X., Ivins, E. R., Nicholls, R. J., Ritz, C., Smith, B., Tulaczyk, S., and Others (2013). Ice-sheet mass balance and climate change. *Nature*, 498(7452):51–59.

Harig, C. and Simons, F. J. (2015). Accelerated West Antarctic ice mass loss continues to outpace East Antarctic gains. *Earth and Planetary Science Letters*, 415:134–141.

Hattermann, T., Nst, O. A., Lilly, J. M., and Smedsrud, L. H. (2012). Two years of oceanic observations below the Fimbul Ice Shelf, Antarctica. *Geophysical Research Letters*, 39(12):1–6.

Hattermann, T., Smedsrud, L., Nøst, O., Lilly, J., and Galton-Fenzi, B. (2014). Eddy-resolving simulations of the Fimbul Ice Shelf cavity circulation: Basal melting and exchange with open ocean. *Ocean Modelling*, 82:28–44.

Hellmer, H. H., Kauker, F., Timmermann, R., Determann, J., and Rae, J. (2012). Twenty-first-century warming of a large Antarctic ice-shelf cavity by a redirected coastal current. *Nature*, 485(7397):225–8.

Helm, V., Humbert, A., and Miller, H. (2014). Elevation and elevation change of Greenland and Antarctica derived from CryoSat-2. *The Cryosphere*, 8(4):1539–1559.

Helsen, M. M., van den Broeke, M. R., van de Wal, R. S. W., van de Berg, W. J., van Meijgaard, E., Davis, C. H., Li, Y., and Goodwin, I. (2008). Elevation changes in Antarctica mainly determined by accumulation variability. *Science (New York, N.Y.)*, 320(5883):1626–1629.

Hogg, A. E., Shepherd, A., Gourmelen, N., and Engdahl, M. (2016). Grounding line migration from 1992 to 2011 on Petermann Glacier, North-West Greenland. *Journal of Glaciology*, 62(236):1104–1114.

Holland, P. R., Brisbourne, A., Corr, H. F. J., McGrath, D., Purdon, K., Paden, J., Fricker, H. A., Paolo, F. S., and Fleming, A. H. (2015). Oceanic and atmospheric forcing of Larsen C Ice-Shelf thinning. *Cryosphere*, 9(3):1005–1024.

Holland, P. R., Corr, H. F. J., Pritchard, H. D., Vaughan, D. G., Arthern, R. J., Jenkins, A., and Tedesco, M. (2011). The air content of Larsen Ice Shelf. *Geophysical Research Letters*, 38(10):L10503.

Hubbard, B., Luckman, A., Ashmore, D. W., Bevan, S., Kulessa, B., Kuipers Munneke, P., Philippe, M., Jansen, D., Booth, A., Sevestre, H., Tison, J.-L., O'Leary, M., and Rutt, I. (2016). Massive subsurface ice formed by refreezing of ice-shelf melt ponds. *Nature Communications*, 7(5):11897.

Hubbard, B., Tison, J. L., Pattyn, F., Dierckx, M., Boereboom, T., and Samyn, D. (2012). Optical-televiewer-based identification and characterization of material facies associated with an antarctic ice-shelf rift. *Annals of Glaciology*, 53(60):137–146.

Hubbard, B., Tison, J.-L., Philippe, M., Heene, B., Pattyn, F., Malone, T., and Freitag, J. (2013). Ice shelf density reconstructed from optical televiewer borehole logging. *Geophysical Research Letters*, 40(22):5882–5887.

Irons, J. R., Dwyer, J. L., and Barsi, J. A. (2012). The next Landsat satellite: The Landsat Data Continuity Mission. *Remote Sensing of Environment*, 122:11–21.

Jacobs, S. S., Hellmer, H. H., Doake, C. S. M., Jenkins, A., and Frolich, R. M. (1992). Melting of ice shelves and the mass balance of Antarctica. *Journal of Glaciology*, 38(130):375–387.

Jenkins, A. (2011). Convection-driven melting near the grounding lines of ice shelves and tidewater glaciers. *Journal of Physical Oceanography*, 41(12):2279–2294.

Jenkins, A., Dutrieux, P., Jacobs, S. S., McPhail, S. D., Perrett, J. R., Webb, A. T., and White, D. (2010). Observations beneath Pine Island Glacier in West Antarctica and implications for its retreat. *Nature Geoscience*, 3(7):468–472.

Jeong, S. and Howat, I. M. (2015). Performance of Landsat 8 Operational Land Imager for mapping ice sheet velocity. *Remote Sensing of Environment*, 170(8):90–101.

Jezek, K. and RAMP-Product-Team (2002). RAMP AMM-1 SAR Image Mosaic of Antarctica. *Fairbanks, AK: Alaska Satellite Facility, in association with the National Snow and Ice Data Center, Boulder, CO. Digital media.*

Joughin, I. (2002). Ice-sheet velocity mapping: a combined interferometric and speckle-tracking approach. *Annals of Glaciology*, 34(1):195–201.

Joughin, I. and MacAyeal, D. R. (2005). Calving of large tabular icebergs from ice shelf rift systems. *Geophysical Research Letters*, 32(2):1–4.

Joughin, I. and Padman, L. (2003). Melting and freezing beneath Filchner-Ronne Ice Shelf, Antarctica. *Geophysical Research Letters*, 30(9):1477.

Joughin, I., Smith, B. E., and Medley, B. (2014). Marine ice sheet collapse potentially under way for the Thwaites Glacier Basin, West Antarctica. *Science*, 344(6185):735–8.

Joughin, I. R., Kwok, R., and Fahnestock, M. A. (1998). Interferometric estimation of three-dimensional ice-flow using ascending and descending passes. *IEEE Transactions on Geoscience and Remote Sensing*, 36(1):25–37.

Kearns, D. A. (2005). *Where Hell Freezes Over: A Story of Amazing Bravery and Survival*. St. Martin's Press.

Khazendar, A., Rignot, E., and Larour, E. (2009). Roles of marine ice, rheology, and fracture in the flow and stability of the Brunt/Stancomb-Wills Ice Shelf. *Journal of Geophysical Research: Earth Surface*, 114(4):F04007.

Khazendar, A., Rignot, E., Schroeder, D. M., Seroussi, H., Schodlok, M. P., Scheuchl, B., Mouginot, J., Sutterley, T. C., and Velicogna, I. (2016). Rapid submarine ice melting in the grounding zones of ice shelves in West Antarctica. *Nature Communications*, 7:13243.

Kingslake, J., Ely, J. C., Das, I., and Bell, R. E. (2017). Widespread movement of meltwater onto and across Antarctic ice shelves. *Nature*, 544(7650):349–352.

Knudsen, P., Bingham, R., Andersen, O., and Rio, M.-H. (2011). A global mean dynamic topography and ocean circulation estimation using a preliminary GOCE gravity model. *Journal of Geodesy*, 85(11):861–879.

Koenig, L., Forster, R., Brucker, L., and Miller, J. (2015). Remote sensing of accumulation over the Greenland and Antarctic ice sheets. In *Remote Sensing of the Cryosphere*, pages 157–186. John Wiley & Sons, Ltd, Chichester, UK.

Krieger, G., Moreira, A., Fiedler, H., Hajnsek, I., Werner, M., Younis, M., and Zink, M. (2007). TanDEM-X: A Satellite Formation for High-Resolution SAR Interferometry. *IEEE Transactions on Geoscience and Remote Sensing*, 45(11):3317–3341.

Kroes, R., Montenbruck, O., Bertiger, W., and Visser, P. (2005). Precise GRACE baseline determination using GPS. *GPS Solutions*, 9(1):21–31.

Kuipers Munneke, P., Ligtenberg, S. R. M., Van Den Broeke, M. R., and Vaughan, D. G. (2014). Firn air depletion as a precursor of Antarctic ice-shelf collapse. *Journal of Glaciology*, 60(220):205–214.

Kuipers Munneke, P., Picard, G., Van Den Broeke, M. R., Lenaerts, J. T. M., and Van Meijgaard, E. (2012a). Insignificant change in Antarctic snowmelt volume since 1979. *Geophysical Research Letters*, 39(1):L01501.

Kuipers Munneke, P., Van Den Broeke, M. R., King, J. C., Gray, T., and Reijmer, C. H. (2012b). Near-surface climate and surface energy budget of Larsen C ice shelf, Antarctic Peninsula. *The Cryosphere*, 6(2):353–363.

Kwok, R., Kwok, R., Fahnestock, M. a., and Fahnestock, M. a. (1996). Ice-Sheet Motion and Topography from Radar Interferometry. *IEEE Transactions on Geoscience and Remote Sensing*, 34(1):189–200.

Lacomme, P., Marchais, J. C., Hardange, J. P., and Normant, E. (2001). *Air and Spaceborne Radar Systems: An Introduction*. Press Monograph, No 108. Elsevier Science.

Langley, E. S., Leeson, A. A., Stokes, C. R., and Jamieson, S. S. R. (2016). Seasonal evolution of supraglacial lakes on an East Antarctic outlet glacier. *Geophysical Research Letters*, 43(16):8563–8571.

Langley, K., Deschwanden, A., Kohler, J., Sinisalo, A., Matsuoka, K., Hattermann, T., Humbert, A., Nøst, O. A., and Isaksson, E. (2014a). Complex network of channels beneath an Antarctic ice shelf. *Geophysical Research Letters*, 41(4):1209–1215.

Langley, K., Kohler, J., Sinisalo, A., Øyan, M. J., Hamran, S. E., Hattermann, T., Matsuoka, K., Nøst, O. A., and Isaksson, E. (2014b). Low melt rates with seasonal variability at the base of Fimbul Ice Shelf, East Antarctica, revealed by in situ interferometric radar measurements. *Geophysical Research Letters*, 41(22):8138–8146.

Le Bars, D., Drijfhout, S., and de Vries, H. (2017). A high-end sea level rise probabilistic projection including rapid Antarctic ice sheet mass loss. *Environmental Research Letters*, 12(4):044013.

Le Brocq, A. M., Ross, N., Griggs, J. A., Bingham, R. G., Corr, H. F. J., Ferraccioli, F., Jenkins, A., Jordan, T. A., Payne, A. J., Rippin, D. M., and Others (2013). Evidence from ice shelves for channelized meltwater flow beneath the Antarctic Ice Sheet. *Nature Geoscience*, 6(11):945–948.

Lenaerts, J., Brown, J., Van Den Broeke, M. R., Matsuoka, K., Drews, R., , Callens, D., Philippe, M., Gorodetskaya, I. V., Van Meijgaard, E., Reijmer, C. H., and Others (2014). High variability of climate and surface mass balance induced by Antarctic ice rises. *Journal of Glaciology*, 60(224):1101.

Lenaerts, J. T. M., Lhermitte, S., Drews, R., Ligtenberg, S. R. M., Berger, S., Helm, V., Smeets, C. J. P. P., van den Broeke, M. R., van de Berg, W. J., van Meijgaard, E., Eijkelboom, M., Eisen, O., and Pattyn, F. (2017). Meltwater produced by wind–albedo interaction stored in an East Antarctic ice shelf. *Nature Climate Change*, 7(1):58–62.

Lenaerts, J. T. M., van den Broeke, M. R., van de Berg, W. J., van Meijgaard, E., and Kuipers Munneke, P. (2012). A new, high-resolution surface mass balance map of Antarctica (1979-2010) based on regional atmospheric climate modeling. *Geophysical Research Letters*, 39(4):L04501.

Lenaerts, J. T. M., van Meijgaard, E., van den Broeke, M. R., Ligtenberg, S. R. M., Horwath, M., and Isaksson, E. (2013). Recent snowfall anomalies in Dronning Maud Land, East Antarctica, in a historical and future climate perspective. *Geophysical Research Letters*, 40(11):2684–2688.

Lenaerts, J. T. M., Vizcaino, M., Fyke, J., van Kampenhout, L., and van den Broeke, M. R. (2016). Present-day and future Antarctic ice sheet climate and surface mass balance in the Community Earth System Model. *Climate Dynamics*, 47(5-6):1367–1381.

Ligtenberg, S. R. M., Helsen, M. M., and van den Broeke, M. R. (2011). An improved semi-empirical model for the densification of Antarctic firn. *The Cryosphere*, 5(4):809–819.

Ligtenberg, S. R. M., Kuipers Munneke, P., and van den Broeke, M. R. (2014). Present and future variations in Antarctic firn air content. *The Cryosphere*, 8(5):1711–1723.

Liu, Y., Moore, J. C., Cheng, X., Gladstone, R. M., Bassis, J. N., Liu, H., Wen, J., and Hui, F. (2015). Ocean-driven thinning enhances iceberg calving and retreat of Antarctic ice shelves. *Proceedings of the National Academy of Sciences of the United States of America*, 112(11):3263–8.

Luckman, A., Elvidge, A., Jansen, D., Kulessa, B., Kuipers Munneke, P., King, J., and Barrand, N. E. (2014). Surface melt and ponding on Larsen C Ice Shelf and the impact of föhn winds. *Antarctic Science*, 26(06):625–635.

MacAyeal, D. R., Scambos, T. A., Hulbe, C. L., and Fahnestock, M. A. (2003). Catas-

trophic ice-shelf break-up by an ice-shelf-fragment-capsize mechanism. *Journal of Glaciology*, 49(164):22–36.

MacAyeal, D. R. and Sergienko, O. V. (2013). The flexural dynamics of melting ice shelves. *Annals of Glaciology*, 54(63):1–10.

Malenovský, Z., Rott, H., Cihlar, J., Schaepman, M. E., García-Santos, G., Fernandes, R., and Berger, M. (2012). Sentinels for science: Potential of Sentinel-1, -2, and -3 missions for scientific observations of ocean, cryosphere, and land. *Remote Sensing of Environment*, 120(February):91–101.

Markowitz, E. M. and Shariff, A. F. (2012). Climate change and moral judgement. *Nature Climate Change*, 2(4):243–247.

Marsh, O. J., Fricker, H. A., Siegfried, M. R., Christianson, K., Nicholls, K. W., Corr, H. F. J., and Catania, G. (2016). High basal melting forming a channel at the grounding line of Ross Ice Shelf, Antarctica. *Geophysical Research Letters*, 43(1):1–6.

Martín-Español, A., Zammit-Mangion, A., Clarke, P. J., Flament, T., Helm, V., King, M. A., Luthcke, S. B., Petrie, E., Rémy, F., Schön, N., Wouters, B., and Bamber, J. L. (2016). Spatial and temporal Antarctic Ice Sheet mass trends, glacio-isostatic adjustment, and surface processes from a joint inversion of satellite altimeter, gravity, and GPS data. *Journal of Geophysical Research F: Earth Surface*, 121(2):182–200.

Massom, R. and Lubin, D. (2006). *Polar Remote Sensing*, volume II- Ice Sh of *Springer Praxis Books. Geophysical Sciences Series*. Springer.

Massonnet, D. and Feigl, K. L. (1998). Radar interferometry and its application to changes in the Earth's surface. *Reviews of Geophysics*, 36(4):441.

Massonnet, D., Rossi, M., Carmona, C., Adragna, F., Peltzer, G., Feigl, K., and Rabaute, T. (1993). The displacement field of the Landers earthquake mapped by radar interferometry. *Nature*, 364(6433):138–142.

Matsuoka, K., Hindmarsh, R. C., Moholdt, G., Bentley, M. J., Pritchard, H. D., Brown, J., Conway, H., Drews, R., Durand, G., Goldberg, D., Hattermann, T., Kingslake, J., Lenaerts, J. T., Martín, C., Mulvaney, R., Nicholls, K., Pattyn, F., Ross, N., Scambos, T., and Whitehouse, P. L. (2015). Antarctic ice rises and rumples: their properties and significance for ice-sheet dynamics and evolution. *Earth-Science Reviews*, 150:724–745.

McMillan, M., Shepherd, A., Sundal, A., Briggs, K., Muir, A., Ridout, A., Hogg, A., and Wingham, D. (2014). Increased ice losses from Antarctica detected by CryoSat-2. *Geophysical Research Letters*.

Mengel, M. and Levermann, A. (2014). Ice plug prevents irreversible discharge from East Antarctica. *Nature Climate Change*, 4(6):451–455.

Mercer, J. H. (1978). West Antarctic ice sheet and CO2 greenhouse effect: a threat of disaster. *Nature*, 271(5643):321–325.

Michel, R. and Rignot, E. (1999). Flow of Moreno Glaciar, Argentina, from repeat-pass Shuttle Imaging Radar images: Comparison of the phase correlation method with radar interferometry. *Journal of Glaciology*, 45(149):93–100.

Millgate, T., Holland, P. R., Jenkins, A., and Johnson, H. L. (2013). The effect of basal channels on oceanic ice-shelf melting. *Journal of Geophysical Research: Oceans*, 118(12):6951–6964.

Morfitt, R., Barsi, J., Levy, R., Markham, B., Micijevic, E., Ong, L., Scaramuzza, P., and Vanderwerff, K. (2015). Landsat-8 Operational Land Imager (OLI) radiometric performance on-orbit. *Remote Sensing*, 7(2):2208–2237.

Mouginot, J., Rignot, E., and Scheuchl, B. (2016). MEaSURES Antarctic Boundaries for IPY 2007-2009 from Satellite Radar, Version 1.

Mouginot, J., Rignot, E., Scheuchl, B., and Millan, R. (2017). Comprehensive annual ice sheet velocity mapping using Landsat-8, Sentinel-1, and RADARSAT-2 data. *Remote Sensing*, 9(4):364.

Mouginot, J., Scheuch, B., and Rignot, E. (2012). Mapping of ice motion in antarctica using synthetic-aperture radar data. *Remote Sensing*, 4(9):2753–2767.

Munchow, A., Padman, L., and Nicholls, K. W. (2016). The Ice Shelf of Petermann Gletscher, North Greenland, and Its Connection to the Arctic and Atlantic Oceans. *Oceanography*, 29(4):84–95.

Nagler, T., Rott, H., Hetzenecker, M., Wuite, J., and Potin, P. (2015). The Sentinel-1 Mission: New Opportunities for Ice Sheet Observations. *Remote Sensing*, 7(7):9371.

Neckel, N. (2010). Surface velocities in the hinterland of the Neumayer III station (Antarctica) derived from SAR-Interferometry. Master's thesis, Universitat Heidelberg.

Nicholls, K. W., Corr, H. F., Stewart, C. L., Lok, L. B., Brennan, P. V., and Vaughan, D. G. (2015). A ground-based radar for measuring vertical strain rates and time-varying basal melt rates in ice sheets and shelves. *Journal of Glaciology*, 61(230):1079–1087.

Nicholls, K. W., Østerhus, S., and Makinson, K. (2009). Ice-ocean processes over the continental shelf of the southern Weddell Sea, Antarctica: A review. *Reviews of Geophysicsof Geophysics*, 47(2007):RG3003.

Nilsson, J., Gardner, A., Sandberg Sørensen, L., and Forsberg, R. (2016). Improved retrieval of land ice topography from CryoSat-2 data and its impact for volume-change estimation of the Greenland Ice Sheet. *The Cryosphere*, 10(6):2953–2969.

Nishio, F. and Uratsuka, S. (1991). Subglacial water layer and grounding line derived from backscattering coefficients of radio echo sounding in the Shirase Glacier and Roi Baudouin Ice Shelf, East. 4:93–102.

Nøst, O., Biuw, M., Tverberg, V., Lydersen, C., Hattermann, T., Zhou, Q., Smedsrud, L. H., and Kovacs, K. M. (2011). Eddy overturning of the Antarctic Slope Front controls glacial melting in the Eastern Weddell Sea. *Journal of Geophysical Research: Oceans*, 116(11):1–17.

Nowicki, S., Bindschadler, R. A., Abe-Ouchi, A., Aschwanden, A., Bueler, E., Choi, H., Fastook, J., Granzow, G., Greve, R., Gutowski, G., Herzfeld, U., Jackson, C., Johnson, J., Khroulev, C., Larour, E., Levermann, A., Lipscomb, W. H., Martin, M. A., Morlighem, M., Parizek, B. R., Pollard, D., Price, S. F., Ren, D., Rignot, E., Saito, F., Sato, T., Seddik, H., Seroussi, H., Takahashi, K., Walker, R., and Wang, W. L. (2013). Insights into spatial sensitivities of ice mass response to environmental change from the SeaRISE ice sheet modeling project II: Greenland. *Journal of Geophysical Research: Earth Surface*, 118(2):1025–1044.

Palerme, C., Genthon, C., Claud, C., Kay, J. E., Wood, N. B., and L'Ecuyer, T. (2017). Evaluation of current and projected Antarctic precipitation in CMIP5 models. *Climate Dynamics*, 48(1-2):225–239.

Paolo, F. S., Fricker, H. A., and Padman, L. (2015). Volume loss from Antarctic ice shelves is accelerating. *Science*, 348(6232):327–331.

Pattyn, F. and Derauw, D. (2002). Ice-dynamic conditions of Shirase Glacier, Antarctica, inferred from ERS SAR interferometry. *Journal of Glaciology*, 48:559–565.

Pattyn, F., Favier, L., Sun, S., and Durand, G. (2017). Progress in Numerical Modeling of Antarctic Ice-Sheet Dynamics. *Current Climate Change Reports*, pages 1–11.

Pattyn, F., Matsuoka, K., Callens, D., Conway, H., Depoorter, M., Docquier, D., Hubbard, B., Samyn, D., and Tison, J. L. (2012). Melting and refreezing beneath Roi Baudouin Ice Shelf (East Antarctica) inferred from radar, GPS, and ice core data. *Journal of Geophysical Research*, 117(F4):F04008.

Philippe, M., Tison, J., Fjøsne, K., Hubbard, B., Kjær, H., Lenaerts, J., Drews, R., Sheldon, S., De Bondt, K., Claeys, P., and Pattyn, F. (2016). Ice core evidence for a 20th century increase in surface mass balance in coastal Dronning Maud Land, East Antarctica. *The Cryosphere*, 10(5):2501–2516.

Phillips, H. A. (1998). Surface meltstreams on the Amery Ice Shelf, East Antarctica. *Annals of Glaciology*, 27:177–181.

Pollard, D., DeConto, R. M., and Alley, R. B. (2015). Potential Antarctic Ice Sheet retreat driven by hydrofracturing and ice cliff failure. *Earth and Planetary Science Letters*, 412:112–121.

Pritchard, H. D., Ligtenberg, S. R. M., Fricker, H. A., Vaughan, D. G., van den Broeke, M. R., and Padman, L. (2012). Antarctic ice-sheet loss driven by basal melting of ice shelves. *Nature*, 484(7395):502–5.

Rankl, M., Fürst, J. J., Humbert, A., and Braun, M. H. (2017). Dynamic changes on the Wilkins Ice Shelf during the 2006–2009 retreat derived from satellite observations. *The Cryosphere*, 11(3):1199–1211.

Richards, J. A. (2009). *Remote Sensing with Imaging Radar*. Signals and Communication Technology. Springer-Verlag Berlin Heidelberg.

Rignot, E. (1996). Tidal motion, ice velocity and melt rate of Petermann Gletscher, Greenland, measured from radar interferometry. *Journal of Glaciology*, 42(142):476–485.

Rignot, E. (1998a). Hinge-line migration of Petermann Gletscher, north Greenland, de- tected using satellite radar interferometry. *Journal of Glaciology*, 44:469–476.

Rignot, E. (1998b). Radar Interferometry Detection of Hinge Line Migration on Rutford Ice Stream and Carkon Inlet , Antarctica. *Annals of Glaciology*, 27:25–32.

Rignot, E., Casassa, G., Gogineni, P., Krabill, W., Rivera, A., and Thomas, R. (2004). Accelerated ice discharge from the Antarctic Peninsula following the collapse of Larsen B ice shelf. *Geophysical Research Letters*, 31(18):2–5.

Rignot, E., Jacobs, S., Mouginot, J., and Scheuchl, B. (2013). Ice-shelf melting around Antarctica. *Science*, 341(6143):266–270.

Rignot, E. and Jacobs, S. S. (2002). Rapid Bottom Melting Widespread near Antarctic Ice Sheet Grounding Lines. *Science*, 296(5575).

Rignot, E., Mouginot, J., Morlighem, M., Seroussi, H., and Scheuchl, B. (2014). Widespread, rapid grounding line retreat of Pine Island, Thwaites, Smith, and Kohler glaciers, West Antarctica, from 1992 to 2011. *Geophysical Research Letters*, 41(10):3502–3509.

Rignot, E., Mouginot, J., and Scheuchl, B. (2011). Ice flow of the Antarctic ice sheet. *Science*, 333(6048):1427–1430.

Rignot, E. and Steffen, K. (2008). Channelized bottom melting and stability of floating ice shelves. *Geophysical Research Letters*, 35(2).

Rintoul, S., Hughes, C., and Olbers, D. (2001). The Antarctic Circumpolar Current System. In *Ocean Circulation and Climate*, chapter 4.6, pages 271–301.

Ritz, C., Edwards, T. L., Durand, G., Payne, A. J., Peyaud, V., and Hindmarsh, R. C. A. (2015). Potential sea-level rise from Antarctic ice-sheet instability constrained by observations. *Nature*, 528(7580):115–118.

Rosen, P., Hensley, S., Joughin, I., Li, F., Madsen, S., Rodriquez, E., and Goldstein, R. (2000). Synthetic Aperture Radar Interferometry. *Proceedings of the IEEE*, 88(3):333–382.

Rott, H. (2009). Advances in interferometric synthetic aperture radar (InSAR) in earth system science. *Progress in Physical Geography*, 33(6):769–791.

Rott, H., Müller, F., Nagler, T., and Floricioiu, D. (2011). The imbalance of glaciers after disintegration of Larsen-B ice shelf, Antarctic Peninsula. *The Cryosphere*, 5(1):125–134.

Royal Society (2006). Factors affecting science communication: A survey of scientists and engineers: The Royal Society. Technical report.

Sansosti, E., Berardino, P., Manunta, M., Serafino, F., and Fornaro, G. (2006). Geometrical SAR image registration. *IEEE Transactions on Geoscience and Remote Sensing*, 44(10):2861–2870.

Scambos, T., Fricker, H. A., Liu, C.-C., Bohlander, J., Fastook, J., Sargent, A., Massom, R., and Wu, A.-M. (2009). Ice shelf disintegration by plate bending and hydro-fracture: Satellite observations and model results of the 2008 Wilkins ice shelf break-ups. *Earth and Planetary Science Letters*, 280(1-4):51–60.

Scambos, T., Hulbe, C., and Fahnestock, M. (2003). Climate-induced ice shelf disintegration in the Antrctic Peninsula. In *Antarctica Peninsula climate variability: a historical and paleoenvironmental perspective*, pages 79–92. American Geophysical Union.

Scambos, T. and Shuman, C. (2016). Comment on 'mass gains of the Antarctic ice sheet exceed losses' by H. J. Zwally and others. *Journal of Glaciology*, 62(233):599–603.

Scambos, T. A., Hulbe, C., M.Fahnestock, and J.Bohlander (2000). The link between climate warming and break-up of ice shelves in the Antarctica Peninsula. *Journal of Glaciology*, 46(154):516–530.

Schodlok, M. P., Menemenlis, D., and Rignot, E. J. (2016). Ice shelf basal melt rates around Antarctica from simulations and observations. *Journal of Geophysical Research: Oceans*, 121(2):1085–1109.

Schoof, C. (2007). Ice sheet grounding line dynamics: Steady states, stability, and hysteresis. *Journal of Geophysical Research*, 112(F3):F03S28.

Schrama, E. J. O., Wouters, B., and Rietbroek, R. (2014). A mascon approach to assess ice sheet and glacier mass balances and their uncertainties from GRACE data. *Journal of Geophysical Research: Solid Earth*, 119(7):6048–6066.

Sergienko, O. V. (2013). Basal channels on ice shelves. *Journal of Geophysical Research: Earth Surface*, 118(3):1342–1355.

Shepherd, A., Ivins, E. R., A, G., Barletta, V. R., Bentley, M. J., Bettadpur, S., Briggs, K. H., Bromwich, D. H., Forsberg, R., Galin, N., Horwath, M., Jacobs, S., Joughin, I., King, M. a., Lenaerts, J. T. M., Li, J., Ligtenberg, S. R. M., Luckman, A., Luthcke, S. B., McMillan, M., Meister, R., Milne, G., Mouginot, J., Muir, A., Nicolas, J. P., Paden, J., Payne, a. J., Pritchard, H., Rignot, E., Rott, H., Sorensen, L. S., Scambos, T. a., Scheuchl, B., Schrama, E. J. O., Smith, B., Sundal, a. V., van Angelen, J. H., van de Berg, W. J., van den Broeke, M. R., Vaughan, D. G., Velicogna, I., Wahr, J., Whitehouse, P. L., Wingham, D. J., Yi, D., Young, D., and Zwally, H. J. (2012). A Reconciled Estimate of Ice-Sheet Mass Balance. *Science*, 338(6111):1183–1189.

Shepherd, A., Wingham, D., Payne, T., and Skvarca, P. (2003). Larsen ice shelf has progressively thinned. *Science (New York, N.Y.)*, 302(5646):856–9.

Siegert, M. (2017). Vulnerable Antarctic ice shelves. *Nature Climate Change*, 7(1):11–12.

Silvano, A., Rintoul, S., and Herraiz-Borreguero, L. (2016). Ocean-ice shelf interaction in East Antarctica. *Oceanography*, 29(4):130–143.

Stanton, T. P., Shaw, W. J., Truffer, M., Corr, H. F. J., Peters, L. E., Riverman, K. L., Bindschadler, R., Holland, D. M., and Anandakrishnan, S. (2013). Channelized ice melting in the ocean boundary layer beneath Pine Island Glacier, Antarctica. *Science*, 341(6151):1236–1239.

Strozzi, T., Luckman, A., Murray, T., Wegmuller, U., and Werner, C. L. (2002). Glacier motion estimation using SAR offset-tracking procedures. *IEEE Transactions on Geoscience and Remote Sensing*, 40(11):2384–2391.

Supran, G. and Oreskes, N. (2017). Assessing ExxonMobil's climate change communications (1977–2014). *Environmental Research Letters*, 12(8):084019.

Tedesco, M. (2015). *Remote sensing of the cryosphere*. The Cryosphere Science Series. Wiley-Blackwell, Chichester, first edition.

Trusel, L. D., Frey, K. E., Das, S. B., Karnauskas, K. B., Kuipers Munneke, P., van Meijgaard, E., and van den Broeke, M. R. (2015). Divergent trajectories of Antarctic surface melt under two twenty-first-century climate scenarios. *Nature Geoscience*, advance on.

Trusel, L. D., Frey, K. E., Das, S. B., Munneke, P. K., and Van Den Broeke, M. R. (2013). Satellite-based estimates of Antarctic surface meltwater fluxes. *Geophysical Research Letters*, 40(23):6148–6153.

Van Autenboer, T. (1964). The Geomorphology and Glacial Geology of the S: or-Rondane, Droning Mayd Land, Antarctica. *Mededelingen van de Koninklijke Vlaamse Academie voor Wetenschappen, Letteren en Schone Kunsten van België, Klasse der Wetenschappen*, 8.

van den Broeke, M. (2005). Strong surface melting preceded collapse of Antarctic Peninsula ice shelf. *Geophysical Research Letters*, 32(12):1–4.

Vaughan, D. G., Comiso, J. C., Allison, I., Carrasco, J., Kaser, G., Kwok, R., Mote, P., Murray,

T., Paul, F., Ren, J., Rignot, E., Solomina, O., Steffen, K., and Zhang, T. (2013). *Observations: Cryosphere*, book section 4, pages 317–382. Cambridge University Press, Cambridge, United Kingdom and New York, NY, USA.

Vaughan, D. G., Corr, H. F. J., Bindschadler, R. A., Dutrieux, P., Gudmundsson, G. H., Jenkins, A., Newman, T., Vornberger, P., and Wingham, D. J. (2012). Subglacial melt channels and fracture in the floating part of Pine Island Glacier, Antarctica. *Journal of Geophysical Research*, 117(F3).

Vaughan, D. G., Marshall, G. J., Connolley, W. M., Parkinson, C., Mulvaney, R., Hodgson, D. A., King, J. C., Pudsey, C. J., and Turner, J. (2003). Recent Rapid Regional Climate Warming on the Antarctic Peninsula. *Climatic Change*, 60(3):243–274.

Velicogna, I., Sutterley, T. C., and Van Den Broeke, M. R. (2014). Regional acceleration in ice mass loss from Greenland and Antarctica using GRACE time-variable gravity data. *Geophysical Research Letters*, 41(22):8130–8137.

Weber, M. E., Clark, P. U., Kuhn, G., Timmermann, A., Sprenk, D., Gladstone, R., Zhang, X., Lohmann, G., Menviel, L., Chikamoto, M. O., Friedrich, T., and Ohlwein, C. (2014). Millennial-scale variability in Antarctic ice-sheet discharge during the last deglaciation. *Nature*, 510(7503):134–138.

Williams, M. J. M. (2015). *The Southern Ocean*, pages 115–127. Springer International Publishing, Cham.

Williams, S. D. P., Moore, P., King, M. A., and Whitehouse, P. L. (2014). Revisiting GRACE Antarctic ice mass trends and accelerations considering autocorrelation. *Earth and Planetary Science Letters*, 385:12–21.

Wilson, N., Straneo, F., and Heimbach, P. (2017). Submarine melt rates and mass balance for Greenland's remaining ice tongues. *The Cryosphere Discussions*, pages 1–17.

Winsvold, S. H., Kääb, A., and Nuth, C. (2016). Regional Glacier Mapping Using Optical Satellite Data Time Series. *IEEE Journal of Selected Topics in Applied Earth Observations and Remote Sensing*, 9(8):3698–3711.

Winther, M. N., Liston, G. E., Winther, J.-G., Jespersen, M. N., and Liston, G. E. (2001). Blue-ice Areas in Antartica Derived from NOAA AVHRR Satellite Data. *Journal of Glaciology*, 47(157):325–334.

Wouters, B., Martin-Español, A., Helm, V., Flament, T., van Wessem, J. M., Ligtenberg, S. R. M., van den Broeke, M. R., and Bamber, J. L. (2015). Dynamic thinning of glaciers on the Southern Antarctic Peninsula. *Science*, 348(6237):899–903.

Wuite, J. (2006). *Spatial and temporal dynamics of three East Antarctic outlet glaciers and their floating ice tongues*. PhD thesis, The Ohio State University.

Wulder, M. A., Masek, J. G., Cohen, W. B., Loveland, T. R., and Woodcock, C. E. (2012). Opening the archive: How free data has enabled the science and monitoring promise of Landsat. *Remote Sensing of Environment*, 122:2–10.

Zazulie, N., Rusticucci, M., and Solomon, S. (2010). Changes in climate at high southern latitudes: A unique daily record at Orcadas spanning 1903-2008. *Journal of Climate*, 23(1):189–196.

Zebker, H. A., Rosen, P. A., Goldstein, R. M., Gabriel, A. K., and Werner, C. L. (1994). On the derivation of coseismic displacement fields using differential radar interferometry: The Landers eathquake. *Journal of Geophysical Research*, 99(B10):19617–19634.

Zhou, X., Chang, N.-B., and Li, S. (2009). Applications of SAR Interferometry in Earth and Environmental Science Research. *Sensors*, 9(3):1876–1912.

Appendix A

Outreach activities and certifications

A.1 Outreach activities

We have listed here all the outreach activities undertaken during the completion of this thesis.

A.1.1 Recurring role

Since Apr. 2017 : **Outreach officer** of the cryosphere division the European Geosciences Union (EGU)

- promoting the cryospheric sciences
- setting up and co-running the twitter and facebook accounts for the Cryosphere division of the EGU

Since Sept. 2016 : **Board member** of the Belgian branch of the Association of Polar Early-Career Scientist (APECS-Belgium)

- scope : promoting polar sciences and fostering networking (especially for early-career scientists)
- co-running the twitter and facebook accounts
- organising outreach events *(e.g : a photo competition for Antarctica Day)*

Since Sept. 2015 : **Member** of the cryospheric early-career scientists team of the European Geosciences Union

- scope : promoting cryospheric sciences and fostering networking (especially for early-career scientists)
- organising social events at the EGU general assembly
- coordinating short courses

Since Mar. 2015 : **Blog editor** of the Cryosphere Blog for the European Geosciences Union

- writing, editing and publishing blog posts
- establishing and managing a network of regular and guest contributors
- promoting the blog on social media and building a strong readership

A.1.2 Engagement with the media

2017 : **Skype interview** for "Grist", an American online environmental magazine, 12.06.2017
Article: A trillion-ton iceberg just broke off Antarctica.

Co-writing of a press release for Drews et al. (2017)'s paper, May 2017
Release: *Oversized landforms discovered beneath the Antarctic ice sheet*

2016 : **45 min radio interview** for "Radio Campus", a local radio, 19.12.2016
Article: *Antarctique Oriental et fonte des glaces* [East Antarctica and melting ice].

Phone interview for "Le Soir", a Belgian national newspaper, 13.12.2016
Article: *Un cratère menace l'Antarctique* [A crater threatens Antarctica].

Television interview for "RTBF", Belgian national newscast, 12.12.2016
Report: *Antarctique: un inlandsis plus vulnérable que prévu* [Antarctica: an ice sheet more vulnerable than assumed]

A.1.3 Engagement with the general public

2016 : **Drafting of policy-related webpage**, *Polar Research (Policy-related science for policy workers)* on the European Geosciences Website, June 2016.

Co-writing of a popular piece : *La fonte de glace et hausse du niveau marin* [Melting ice and sea-level rise], published in "Science connection", 50, pp. 10-11, March-April 2016.

A.1.4 Engagement with peers

2017 : **Co-Convener** of "Communicating Climate Change - blogging as a group"
Short course at EGU General Assembly, Vienna (Austria), 26.04.2017

2016 : **Panellist** of "Se faire entendre sur le web" [Getting heard on the web],
Panel discussion about the use of social media as a scientist, at the Université libre de Bruxelles, Brussels, 17.11.2016.

Convener of "The Cryosphere – Publishing Your Work: Meet The Editor"
short course at EGU General Assembly, Vienna (Austria), 22.04.2016

Co-Convener of "Working at the science policy interface"
Short course at EGU General Assembly, Vienna (Austria), 21.04.2016

Panellist of "The communicating geoscientist"
Short course at EGU General Assembly, Vienna (Austria), 19.04.2016

A.2 EGU cryosphere blog: letters of certification

European Geosciences Union • Luisenstr. 37 • 80333 München • Germany

Ms. Sophie Berger
Université libre de Bruxelles (ULB)
Glaciology unit CP160/03
50 av F.D. Roosevelt
1050 Brussels
Belgium

Your contact

Dr. Philippe Courtial

EGU Executive Secretary

Phone +49-89-2180-6549
Fax +49-89-2180-17855

info@egu.eu
www.egu.eu

1. June 2017

Letter of Certification

To whom it may concern,

EGU, the European Geosciences Union, is Europe's premier geosciences union, dedicated to the pursuit of excellence in the Earth, planetary, and space sciences for the benefit of humanity. It is a non-profit international association of scientists (over 12,000 members from all over the world).
The EGU has a current portfolio of 17 diverse scientific journals, which use an innovative open-access format, and organises a number of meetings, and education and outreach activities. Its annual General Assembly is the largest and most prominent European geosciences event, attracting over 14,000 scientists from all over the world.

This letter is to certify that Sophie Berger is an editor of the EGU blog of Cryospheric sciences since March 2015 (as a temporary editor before she became a permanent editor in September 2015).
The EGU Blogs aim to share accurate information about geoscientific research, in a language understandable not only to fellow scientists but also to the broader public. With a particular focus on European research, the EGU Blogs offer a place for scientists to interact with each other and the Union.

EGU is very grateful to Sophie Berger for all the efforts she did and the time she invested to promote and communicate cryospheric sciences as part of the EGU outreach programme.
The Cryospheric sciences blog is one of the most successful EGU Division blogs and grew a lot since its launch. That success is largely down to Sophie Berger who has thrown herself into creating a great team of guest bloggers and promoting the blog through effective social media campaigns.

Kind regards,

Philippe Courtial
(EGU Executive Secretary)

ALFRED-WEGENER-INSTITUT
HELMHOLTZ-ZENTRUM FÜR POLAR- UND MEERESFORSCHUNG

Alfred-Wegener-Institut, Postfach 12 01 61, 27515 Bremerhaven

To whom it may concern

Prof. Dr. Olaf Eisen
Sektion Glaziologie
Olaf.Eisen@awi.de
Telefon +49-471-4831-1969
Telefax +49-471-4831-1271

Alfred-Wegener-Institut
Helmholtz-Zentrum für
Polar- und Meeresforschung
BREMERHAVEN

Am Handelshafen 12
27570 Bremerhaven
Telefon 0471 4831-0
Telefax 0471 4831-1149
www.awi.de

Stiftung des öffentlichen Rechts

Sitz der Stiftung:
Am Handelshafen 12
27570 Bremerhaven
Telefon 0471 4831-0
Telefax 0471 4831-1149
www.awi.de

Vorsitzender des Kuratoriums:
MinDir Dr. Karl Eugen Huthmacher
Direktorium:
Prof. Dr. Dr. h.c. Karin Lochte
(Direktorin)
Dr. Karsten Wurr
(Verwaltungsdirektor)
Dr. Uwe Nixdorf
(Stellvertretender Direktor)
Prof. Dr. Karen H. Wiltshire
(Stellvertretende Direktorin)

Bankverbindung:
Commerzbank AG,
Bremerhaven
BIC/Swift COBADEFF292
IBAN DE12292400240349192500
UST-Id-Nr. DE 114707273

HELMHOLTZ GEMEINSCHAFT

2 June 2019
Certification and Appreciation

as the former vice and now president of the European Geosciences Union's Division of Cryospheric Sciences it is a pleasure for me to certify the very active role Sophie Berger played over the last years for the divisions's outreach. In particular, I would like to appreciate her function as an editor of the EGU blog of Cryospheric sciences since March 2015. With her own blog posts as well as part of a team of young scientists to oversee the acquisition of new bloggers she helped to make the Cryospheric Sciences blog one of the most successful EGU Division blogs. The actual blog-writing activity has more over been complemented by social media activity on different channels. Her efforts helped to make complex processes in the cryosphere accessible to non-experts and make young scientists interested in this field across traditional disciplinary boundaries.

I am very grateful to her efforts and am convinced that this voluntary service was of great value to the cryospheric community.

Sincerely,

Olaf Eisen

President of the EGU Division on Cryospheric Sciences
CR contact: cr@egu.eu
CR on Twitter: @EGU_CR
CR blog: http://blogs.egu.eu/divisions/cr/